OPTIMAL TRAJECTORY DESIGN FOR INTERCEPTION AND DEFLECTION OF NEAR EARTH OBJECTS

Camilla Colombo

Submitted in fulfilment of the requirements for
the Degree of Doctor of Philosophy

Department of Aerospace Engineering
Faculty of Engineering
University of Glasgow

NOTE

This thesis contains some figures in .eps. In order to print it out correctely an eps printer is suggested.

Author contact: allimac17@gmail.com

Abstract

Many asteroids and comets orbit the inner solar system; among them Near Earth Objects (NEOs) are those celestial bodies for which the orbit lies close, and sometimes crosses, the Earth's orbit. Over the last decades the impact hazard they pose to the Earth has generated heated discussions on the required measures to react to such a scenario.

The aim of the research presented in this dissertation is to develop methodologies for the trajectory design of interception and deflection missions to Near Earth Objects. The displacement, following a deflection manoeuvre, of the asteroid at the minimum orbit intersection distance with the Earth is expressed by means of a simple and general formulation, which exploits the relative motion equations and Gauss' equations. The variation of the orbital elements achieved by any impulsive or low-thrust action on the threatening body is derived through a semi-analytical approach, whose accuracy is extensively shown. This formulation allows the analysis of the optimal direction of the deflection manoeuvre to maximise the achievable deviation.

The search for optimal opportunities for mitigation missions is done through a global optimisation approach. The transfer trajectory, modelled through preliminary design techniques, is integrated with the deflection model. In this way, the mission planning can be performed by optimising different contrasting criteria, such as the mass at launch, the warning time, and the total deflection. A set of Pareto fronts is computed for different deflection strategies and considering various asteroid mitigation scenarios. Each Pareto set represents a number of mission opportunities, over a wide domain of launch windows and design parameters.

A first set of results focuses on impulsive deflection missions, to a selected group of potentially hazardous asteroids; the analysis shows that the ideal optimal direction of the deflection manoeuvre cannot always be achieved when the transfer trajectory is integrated with the deflection phase. A second set of results

includes solutions for the deviation of some selected NEOs by means of a solar collector strategy. The semi-analytical formulation derived allows the reduction of the computational time, hence the generation of a large number of solutions. Moreover, sets of Pareto fronts for asteroid mitigation are computed through the more feasible deflection schemes proposed in literature: kinetic impactor, nuclear interceptor, mass driver device, low-thrust attached propulsion, solar collector, and gravity tug. A dominance criterion is used to perform a comparative assessment of these mitigation strategies, while also considering the required technological development through a technology readiness factor.

The global search of solutions through a multi-criteria optimisation approach represents the first stage of the mission planning, in which preliminary design techniques are used for the trajectory model. At a second stage, a selected number of trajectories can be optimised, using a refined model of the dynamics. For this purpose, the use of Differential Dynamic Programming (DDP) is investigated for the solution of the optimal control problem associated to the design of low-thrust trajectories. The stage-wise approach of DDP is exploited to integrate an adaptive step discretisation scheme within the optimisation process. The discretisation mesh is adjusted at each iteration, to assure high accuracy of the solution trajectory and hence fully exploit the dynamics of the problem within the optimisation process. The feedback nature of the control law is preserved, through a particular interpolation technique that improves the robustness against some approximation errors. The modified DDP-method is presented and applied to the design of transfer trajectories to the fly-by or rendezvous of NEOs, including the escape phase at the Earth. The DDP approach allows the optimisation of the trajectory as a whole, without recurring to the patched conic approach. The results show how the proposed method is capable of fully exploiting the multi-body dynamics of the problem; in fact, in one of the study cases, a fly-by of the Earth is scheduled, which was not included in the first guess solution.

To my brother Marco

Isaiah 43, 1–3

«Do not be afraid. I've redeemed you.
I've called your name. You're mine.
When you're in over your head, I'll be there with you.
When you're in rough waters, you will not go down.
When you're between a rock and a hard place, it won't be a dead end
Because I am God, your personal God, the Holy One of Israel, your Saviour.
I paid a huge price for you: all of Egypt, with rich Cush and Seba thrown in!
That's how much you mean to me! That's how much I love you!
I'd sell off the whole world to get you back, trade the creation just for you.
So don't be afraid: I am with you»

Richard Feynman, “The Value of Science”, in *Frontiers in Science: A Survey*, Ed. E. Hutchings, Basic Books, New York, 1958.

«The same thrill, the same awe and mystery, comes again and again when we look at any question deeply enough. With more knowledge comes a deeper, more wonderful mystery, luring one on to penetrate deeper still. Never concerned that the answer may prove disappointing, with pleasure and confidence we turn over each new stone to find unimagined strangeness leading on to more wonderful questions and mysteries - certainly a grand adventure!»

Acknowledgments

I would like to acknowledge my advisors, Dr. Gianmarco Radice and Dr. Massimiliano Vasile for making this work possible. Their support and guidance have been precious throughout these years. I would like to thank Max, for conveying to me "*the same thrill, the same awe and mystery*" that make research so beautiful, and for sharing the enthusiasm of working in team. Thank you for the invaluable scientific guidance and the contribution to many of the ideas in this thesis. I would like to thank Gianmarco, for making this extraordinary experience possible. Thank you, for supporting me always e unconditionally, for believing in my abilities and giving me confidence in them. Your positiveness encouraged me and helped me in playing down my worries and insecurities. I am very grateful to each member of the Department of Aerospace Engineering of the University of Glasgow, because the environment has been friendly, supportive and stimulating. I am thankful to the examiners of this thesis, Dr. Victor Becerra and Dr. Jongrae Kim for the fruitful discussion.

For many reasons, my experience of the PhD in Glasgow has been one of the best and strongest in my life, it has changed and extended my visions and strengthened my beliefs. I would like to thank all my colleagues and best friends of the Space Advanced Research Team; you have been wonderful "travel mates", on every day of this experience. Thank you Pau, I have learnt a lot from the close collaboration with you, *saving the Earth from NEOs* has been enjoyable together! Thank you Matteo, for being always available, encouraging and supporting me. Thank you for your splendid friendship, Nico, for listening to my thoughts and for sharing with me yours. A big hug and sincere thank-you to Christie, Daniel, Edmondo, Stuart, Imran, Anna, Giulio, Irene, Paola, Matt, Giangi, Nita, DC, Kiran, Tao, my Scottish supporters, Janice, Celia and James. With each one of you I have shared unforgettable precious moments of my Glaswegian experience.

The biggest thank-you goes to my family: Emilia, Giorgio, Riccardo, Marco and Fabrizio, because their love and unconditional support is always with me,

even at 1,912 km far away. I am grateful to my parents, for teaching me that good results come from strong commitment and for raising me to chase my dreams. Grazie papi, because with your morning phone calls I experienced that distances are nothing, if you believe so. Grazie mamma, for your constant care, for sharing my feelings and anxieties, and sometimes not sleeping because of them. A big hug to Richi, who shows me his love with no needs for words! Marco, I feel you close to me in every single moment.

Fabri, living so far during these years has been difficult, but we only know how that made us close. Thank you for your patience, presence and love. You are the one who completes me.

I declare that, except where explicitly stated, the work contained in this dissertation is my own.

November 2009, Camilla Colombo

Contents

Abstract iii
Acknowledgments vii
Contents x
List of figures xiii
List of tables xx
Nomenclature xxii
List of symbols xxii
List of constants xxx
List of acronyms xxx
Chapter 1. Introduction 1
1.1. Near Earth Objects and problem definition 1
1.2. Research motivations and objectives 3
1.3. Background 5
1.3.1. Impact hazard 5
1.3.2. NEO deflection strategies 7
1.3.3. Asteroid deviation 10
1.3.4. NEO interception and trajectory optimisation 13
1.4. Methodologies developed and implemented 16
1.5. Dissertation organisation 20
1.6. Contributions 21
Chapter 2. Impulsive NEO deflection 24
2.1. Asteroid deviation problem 24
2.1.1. Maximum deviation strategies 28
2.1.2. Accuracy analysis 32
2.1.3. Representation on the *b*-plane 35
2.2. Mission options for impulsive deviation 50
2.2.1. Targets selection 50
2.2.2. Impact model and optimisation problem definition 53

2.2.3. Results 56
2.3. Summary 63
Chapter 3. Low-thrust NEO deflection 65
3.1. Asteroid deviation problem 66
3.1.1. Analysis of the optimal thrust direction 70
3.2. Semi-analytical formulae for low-thrust deviation action 72
3.2.1. Latitude formulation 73
3.2.2. Periodic variation of the orbital parameters 78
3.2.3. Time formulation 82
3.3. Mission options for low-thrust deviation 89
3.3.1. Targets selection 90
3.3.2. Spacecraft model and optimisation problem definition 91
3.3.3. Results 95
3.4. Summary 109
Chapter 4. Comparison of mitigation strategies for hazardous NEOs 111
4.1. NEO deflection strategies model 112
4.1.1. Impulsive action 113
4.1.2. Low-thrust action 116
4.2. Transfer trajectory 119
4.3. Multi-criteria optimisation problem formulation 120
4.4. Objective function definition 123
4.5. Deflection mission options 126
4.5.1. Targets selection 127
4.5.2. Pareto fronts 128
4.5.3. Multi-criteria analysis 138
4.6. Summary 142
Chapter 5. Optimal low-thrust trajectories to asteroids through an algorithm based on differential dynamic programming 144
5.1. Differential Dynamic Programming 145
5.1.1. Differential dynamic programming for trajectory optimisation.... 145
5.2. Modified DDP method 160
5.2.1. Discretisation scheme 160

5.2.2. Mesh definition 162
5.3. Algorithm 165
5.3.1. Heuristics to improve the convergence rate 170
5.4. Local refinement of low-thrust trajectories 172
5.5. Asteroid rendezvous and fly-by missions 177
5.5.1. Rendezvous with asteroid Apophis 180
5.5.2. Rendezvous with asteroid Apophis from a geostationary transfer orbit 187
5.5.3. Fly-by of asteroid 2002 AA29 195
5.6. Summary 203
Chapter 6. Conclusions 204
6.1. Summary and findings of the thesis 204
6.2. Limitations 211
6.3. Remarks for future work 213
References 216
Appendix A. Secular variation of orbital elements due to low-thrust manoeuvre 232
A.1. Secular variation of eccentricity over one orbital revolution 232
A.2. Secular variation of semi-major axis over one orbital revolution 235
A.3. Secular variation of anomaly of the pericentre over one orbital revolution 236
A.4. Secular variation of the mean anomaly over one orbital revolution 237
Appendix B. Influence of the technology readiness level on the multi-criteria analysis 242

List of figures

Figure 2.1: Impulsive NEO deviation. 25

Figure 2.2: Components of the optimal δv direction for a) asteroid 2000SG344 and b) asteroid 1979XB. 30

Figure 2.3: Deviation achieved with $||\delta v||$=0.07 m/s for a) asteroid 2000SG344 and b) asteroid 1979XB. 31

Figure 2.4: Relative error calculated by orbit propagation for asteroid 2000SG344. 32

Figure 2.5: Relative error for the deviation of a) asteroid 2000SG344 and b) asteroid 1979XB..... 33

Figure 2.6: Deviation of a) asteroid 2000SG344 and b) asteroid 1979XB. 34

Figure 2.7: Maximum relative error for different asteroids. 34

Figure 2.8: Earth-centred local reference system: a) *b*-plane representation and b) geometry of hyperbolic passage. 35

Figure 2.9: Impact parameter and magnitude of the deviation for 1979XB with δv = 0.07 m/s; b*-parameter (bold lines), and deviation (thin lines). 37

Figure 2.10: Impact parameter for asteroid 1979XB $\Delta t<1T_{NEO}$: a) strategy of maximum deviation and b) strategy of maximum b*-parameter. 37

Figure 2.11: Impact parameter for asteroid 2000SG344 $\Delta t<0.5T_{NEO}$. Strategy of maximum deviation (solid line) and maximum b*-parameter (bold line). 39

Figure 2.12: Deviation (dashed line) and its projection (bold line) on the *b*-plane calculated through the two-body problem and minimum deviation computed through the three-body problem (continuous thin line): a) maximum deviation strategy for asteroid 1979XB and b) maximum b*-parameter strategy for asteroid 1979XB. 41

Figure 2.13: Projection of the deviation (continuous line) on the *b*-plane calculated through the two-body problem and minimum deviation computed through the three-body problem (dashed line) for asteroid 1979XB. The bold lines represent the results of the maximum-b* strategy, the thin lines represent the result for the maximum-deviation strategy. 41

Figure 2.14: Components of the deviation in the *b*-plane for asteroid 1979XB... 42

Figure 2.15: Fly-by representation in the *b*-plane reference system. a) case A: the asteroid is approaching the fly-by of the Earth and b) case B: the asteroid is at the end of the fly-by. 43

Figure 2.16: Projection on the *b*-plane of the deviation for asteroid 2000SG344 (left) and asteroid 1979XB (right) with δv = 0.07 m/s applied a) along the tangent to the motion, b) along the normal to the motion, and c) along the *h*-direction. 45

Figure 2.17: Projection on the *b*-plane, function of Δ*t* for a) asteroid 2000SG344 and b) asteroid 1979XB. 46

Figure 2.18: Projection on the *b*-plane of the deviation. δv = 0.07 m/s applied along the optimal (normal line), the tangent to the motion (dark grey normal line), the normal to the motion (black bold line), and the *h* (light grey bold line) directions for a) asteroid 2000SG344 and b) asteroid 1979XB..... 46

Figure 2.19: Distribution of the components of δv, represented through the Gaussian membership function, with $3\sigma = \delta v_{t,\,mean}/100$. a) Tangential component, b) normal component, and c) component along the *h* direction..... 48

Figure 2.20: Projection on the *b*-plane of the deviation. $\delta v_{t,\,mean} = 0.07$ m/s applied along the tangent direction with $3\sigma = \delta v_{t,\,mean}/100$ for a) asteroid 2000SG344 and b) asteroid 1979XB. 48

Figure 2.21: Distribution of the components of δv, represented through the Gaussian membership function, with $3\sigma = \delta v_{t,\,mean}/10$. a) Tangential component, b) normal component, and c) component along the *h* direction..... 49

Figure 2.22: Projection on the *b*-plane of the deviation. $\delta v_{t,\,mean} = 0.07$ m/s applied along the tangent direction with $3\sigma = \delta v_{t,\,mean}/10$ for a) asteroid 2000SG344 and b) asteroid 1979XB. 49

Figure 2.23: Optimal interception of a) asteroid 1979XB and b) asteroid 1996TC1..... 57

Figure 2.24: Optimal interception arguments of latitude for a) asteroid 1979XB and b) asteroid 1996TC1. 57

Figure 2.25: Optimal interception of a) asteroid 2000SB45 and b) asteroid 2002TX55. 58

Figure 2.26: Impact velocity function a) of the eccentricity and b) of the inclination (*h*-component). 58

Figure 2.27: Pareto front for a) asteroid 2000SG344 and b) asteroid 2002GJ8. .. 59

Figure 2.28: Pareto front for asteroid 2002VU17. 62

Figure 2.29: Optimal impact Δv distribution for direct impacts: a) results of the single-objective optimisation and b) results of the multi-objective optimisation. 62

Figure 3.1: Low-thrust NEO deviation. 66

Figure 3.2: Relative error on the deviation of a) asteroid Apophis and b) asteroid 1979XB. 78

Figure 3.3: Semi-analytical expression of the eccentricity for asteroid Apophis. 80

Figure 3.4: Relative error between the numerical and semi-analytical integration of a) the eccentricity, b) the semi-major axis, and c) anomaly of the pericentre for asteroid Apophis (left) and asteroid 1979XB (right)... 81

Figure 3.5: Relative error between the numerical and semi-analytical integration of the mean anomaly for a) asteroid Apophis and b) asteroid 1979XB. 82

Figure 3.6: Time-formulation algorithm. 85

Figure 3.7: Relative error of the time formulation for a) asteroid Apophis ($k_a=2.2\times10^5$ km^3/s^2) and b) asteroid 1979XB ($k_a=2\times10^4$ km^3/s^2). 87

Figure 3.8: Relative error on δM for a) asteroid Apophis and b) asteroid 1979XB. 88

Figure 3.9: Percentage of savings in computational time by using the semi-analytical time formulation with respect to the numerical integration of Gauss' equations. a) Asteroid Apophis and b) asteroid 1979XB. . 89

Figure 3.10: Magnitude of the acceleration for Apophis. 92

Figure 3.11: Launch opportunities for a deviation mission to Apophis. The colour scale represents the value of the achieved deviation at the MOID. ... 96

Figure 3.12: Deviation mission to Apophis: a) Pareto front. Launch mass, warning time and magnitude of the deviation are represented on the three axes. b) Achieved deviation as a function of the time length of the thrust arc. 97

Figure 3.13: Orbit and MOID characteristics for different values of semi-major axis starting from Apophis case: a) asteroid orbits and b) true anomaly of the MOID. 98

Figure 3.14: Sensitivity of the deviation to the semi-major axis: a) deviation achieved for orbits with different values of semi-major axis and for increasing values of thrust interval and b) relative error for different values of semi-major axis. The white line represents Apophis case (a = 0.922 AU). 99

Figure 3.15: Orbit and MOID characteristics for different values of eccentricity starting from Apophis case: a) asteroid orbits and b) true anomaly of the MOID. 100

Figure 3.16: Sensitivity of the deviation to the eccentricity: a) deviation achieved for orbits with different values of eccentricity and for increasing values of thrust interval and b) relative error for different values of eccentricities. The white line represents Apophis case (e = 0.191). 101

Figure 3.17: Launch opportunities for a deviation mission to 1979XB. The colour scale represents the value of the achieved deviation at the MOID. . 102

Figure 3.18: Deviation mission to 1979XB: a) Pareto front. Launch mass, warning time and magnitude of the deviation are represented on the three axes. b) Achieved deviation as a function of the time length of the thrust arc. 102

Figure 3.19: Orbit and MOID characteristics for different values of semi-major axis starting from 1979XB case: a) asteroid orbits and b) true anomaly of the MOID. 103

Figure 3.20: Sensitivity of the deviation to the semi-major axis: a) deviation achieved for orbits with different values of semi-major axis and for increasing values of thrust interval and b) relative error for different values of semi-major axis. The white line represents 1979XB case (a = 2.350 AU). 104

Figure 3.21: Orbit and MOID characteristics for different values of eccentricity starting from 1979XB case: a) asteroid orbits and b) true anomaly of the MOID. 105

Figure 3.22: Sensitivity of the deviation to the eccentricity: a) deviation achieved for orbits with different values of eccentricity and for increasing values of thrust interval and b) relative error for different values of eccentricity. The white line represents 1979XB case (e = 0.726).... 106

Figure 3.23: Launch opportunities for a deviation mission to Castalia. The colour scale represents the value of the achieved deviation at the MOID. . 106

Figure 3.24: Deviation mission to Castalia: a) Pareto front. Launch mass, warning time and magnitude of the deviation are represented on the three axes. b) Achieved deviation as a function of the time length of the thrust arc. 107

Figure 3.25: Launch opportunities for a deviation mission to Itokawa. The colour scale represents the value of the achieved deviation at the MOID. . 108

Figure 3.26: Deviation mission to Itokawa: a) Pareto front. Launch mass, warning time and magnitude of the deviation are represented on the three axes. b) Achieved deviation as a function of the time length of the thrust arc. 108

Figure 4.1: Orbit of the selected asteroids: a) 2D view, and b) 3D view. 128

Figure 4.2: Pareto front for the deviation of asteroid Apophis through different strategies: a) kinetic impactor, b) nuclear interceptor, c) mass driver, d) attached spacecraft propulsion, e) solar collector, and e) gravity tractor. 132

Figure 4.3: Pareto front for the deviation of asteroid Itokawa through different strategies: a) kinetic impactor, b) nuclear interceptor, c) mass driver, d) attached spacecraft propulsion, e) solar collector, and e) gravity tractor. 134

Figure 4.4: Pareto front for the deviation of asteroid Castalia through different strategies: a) kinetic impactor, b) nuclear interceptor, c) mass driver, d) attached spacecraft propulsion, e) solar collector, and e) gravity tractor. 136

Figure 4.5: Pareto front for the deviation of asteroid 1979XB through different strategies: a) kinetic impactor, b) nuclear interceptor, c) mass driver, d) attached spacecraft propulsion, e) solar collector, and e) gravity tractor. 137

Figure 5.1: Dynamic programming approach. 147

Figure 5.2: Control law schedule according to Jacobson's algorithm. 150

Figure 5.3: Trajectory associated to the control law in Eq. (5.12). 150

Figure 5.4: Control law during the convergence process. Direct transfer Earth to Mars, with a time of flight of 200 days. 151

Figure 5.5: Trajectory discretisation within the optimisation problem. 161

Figure 5.6: Trajectory discretisation in the Static/Dynamic Control approach. The grey arrows show that the control is kept constant within a segment. 162

Figure 5.7: Modified DDP algorithm. 169

Figure 5.8: Pareto front for a deviation mission to asteroid Apophis. 174

Figure 5.9: Points of the Pareto front locally optimised through the DDP method. 175

Figure 5.10: Percentage of propellant mass saved through the local optimisation of the solutions. 176

Figure 5.11: Thrust magnitude. The dashed line represents the first guess solution provided to the DDP algorithm, the continuous line is the optimal thrust profile. a) Entire trajectory and b) close-up on the escape phase. 181

Figure 5.12: Time evolution of the thrust components. 181

Figure 5.13: Mass. The dashed line represents the first guess solution; the continuous line is the optimal profile. 182

Figure 5.14: Rendezvous trajectory to Apophis represented in the Earth inertial reference frame. a) Entire trajectory and b) close-up on the escape phase. 183

Figure 5.15: Trajectory to Apophis rendezvous. Transfer in the Sun inertial reference frame. The dashed line represents the first guess transfer solution; the continuous line is the optimal trajectory. Apophis and Earth orbit are represented respectively in red and blue continuous lines. 184

Figure 5.16: Evolution of the Keplerian elements during the escape phase. The dashed line represents the first guess solution; the continuous line is the optimal profile. a) Semi-major axis expressed in Earth radii, b) eccentricity and c) inclination. 185

Figure 5.17: Time of flight sensitivity. The integral term of the cost function (normalised to the weight parameter w) is represented on the y axis. Each point represents an optimised transfer (with final constraints satisfied) with a given time of flight. The cross shows the result corresponding to the solution fully presented in this section. 186

Figure 5.18: Thrust magnitude for the mission with $m_0 = 1350$ kg. The dashed line represents the first guess solution provided to the DDP algorithm, the continuous line is the optimal thrust profile. a) Entire trajectory and b) close-up on the escape phase. 187

Figure 5.19: Mass for the mission with m_0 = 1350 kg. The dashed line represents the first guess solution; the continuous line is the optimal profile... 187

Figure 5.20: Mass. The dashed line represents the first guess solution; the continuous line is the optimal profile. 189

Figure 5.21: Thrust magnitude. The dashed line represents the first guess solution provided to the DDP algorithm, the continuous line is the optimal thrust profile. a) Entire trajectory and b) close-up on the escape phase. 189

Figure 5.22: Time evolution of the thrust components. 190

Figure 5.23: Evolution of the instantaneous eccentricity with time during the spiralling-out phase. The dashed line represents the first guess, the continuous line is the optimal solution. 190

Figure 5.24: Close-up on the escape phase. The dashed line represents the first guess, the continuous line is the optimal solution. 191

Figure 5.25: Trajectory to Apophis rendezvous. The dashed line represents the first guess transfer solution; the continuous line is the optimal trajectory. a) Transfer in the Earth inertial reference frame. The circle represents the target position, the cross is the final state of the optimal trajectory. b) Transfer in the Sun inertial reference frame. Apophis and Earth orbit are represented respectively in red and blue continuous lines. 192

Figure 5.26: Fly-by of the Earth. The cross represents the pericentre of the hyperbola with respect to the Earth. a) Fly-by phase and b) close-up of the passage from the pericentre of the hyperbola. 193

Figure 5.27: Evolution of the thrust and velocity magnitude during the fly-by. The dashed line represents the first guess solution; the continuous line is the optimal profile. The cross symbol is in correspondence of the pericentre passage. a) Thrust magnitude and b) velocity magnitude with respect to the Earth. 194

Figure 5.28: Evolution of the angles of the velocity vector with respect to the Earth inertial reference frame, during the fly-by. The dashed line represents the first guess solution; the continuous line is the optimal profile. The cross symbol is in correspondence of the pericentre passage. a) In-plane angle of the velocity vector and b) out-of-plane angle of the velocity vector. 195

Figure 5.29: Trajectory of asteroid 2002 AA29 relative motion with respect to the Earth. 196

Figure 5.30: Transfer trajectory to 2002 AA29 fly-by in the Sun inertial reference frame. The dashed line represents the first guess transfer solution; the continuous line is the optimal trajectory. 2002 AA29 and Earth orbit are represented respectively in red and blue continuous lines. 196

Figure 5.31: Thrust magnitude. The dashed line represents the first guess solution provided to the DDP algorithm, the continuous line is the optimal thrust profile. a) Entire trajectory and b) close-up on the escape phase. 197

Figure 5.32: Time evolution of the thrust components. 197

Figure 5.33: Mass. The dashed line represents the first guess solution; the continuous line is the optimal profile 198

Figure 5.34: Trajectory to 2002 AA29 fly-by represented in the Earth inertial reference frame. a) Entire trajectory and b) close-up on the escape phase. 199

Figure 5.35: Evolution of the Keplerian elements during the escape phase. The dashed line represents the first guess solution; the continuous line is the optimal profile. a) Semi-major axis, b) eccentricity, c) inclination, and d) anomaly of the ascending node. 200

Figure 5.36: Lagrange point passage. The cross highlights the position of the Lagrange point L2 when the trajectory changes its inclination. 201

Figure 5.37: Angles of the thrust vector. The dashed line represents the first guess solution; the continuous line is the optimal profile. a) Right ascension and b) declination. 201

Figure 5.38: Acceleration components. The dashed line represents the first guess solution, the continuous line is the optimal solution. The black line indicates the acceleration due to the Earth's gravity field, the black bold line indicates the disturbing acceleration due to the Sun and the bold grey line indicates the thrust acceleration. a) Acceleration magnitude, b) x component of the acceleration, c) y component of the acceleration, and d) z component of the acceleration. 202

Figure 6.1: Comparison between the approximated low-thrust model and the numerical integration in the three-body problem (Earth inertial system): a) transfer to Apophis, and b) Earth escape phase. 214

List of tables

Table 2.1: Physical parameters for considered NEOs. 52
Table 2.2: Optimal launch opportunities for a direct transfer to selected asteroids as a result of the multi-objective optimisation. 60
Table 2.3: Optimal launch opportunities for transfers to selected asteroids via a single Venus swing-by as a result of the single-objective optimisation. 63
Table 3.1: Computational time of the analytical and numerical approach. 78
Table 3.2: Maximum relative error between the numerical and semi-analytical integration. 80
Table 3.3: Asteroids orbital and physical parameters. 90
Table 3.4: Mission characteristics. 91
Table 3.5: Acceleration constant and average of the accelerations acting on the asteroid. 92
Table 4.1: Margins on the wet mass into orbit for the different deviation strategies. 124
Table 4.2: Search domain for the multi-objective optimisation. 126
Table 4.3: Asteroids orbital and physical parameters. 127
Table 4.4: Strategy dominance for asteroid Apophis. 140
Table 4.5: Strategy dominance for asteroid Itokawa. 140
Table 4.6: Strategy dominance for asteroid Castalia. 140
Table 4.7: Strategy dominance for asteroid 1979XB. 141
Table 5.1: Mission characteristics. 173
Table 5.2: Mission characteristics. 180
Table 5.3: Parking orbit parameters. 188
Table 5.4: Mission characteristics. 188
Table 5.5: Mission characteristics. 195

Table B.1 : Technology readiness levels. 243
Table B.2 : TRL for the different mitigation schemes. 243
Table B.3 : TRL mapping into required time to fully develop the required technology. 245
Table B.4 : Strategy dominance for asteroid Apophis considering the technology readiness level. 246

Table B.5 : Strategy dominance for asteroid Itokawa considering the technology readiness level. 246

Table B.6 : Strategy dominance for asteroid Castalia considering the technology readiness level. 247

Table B.7 : Strategy dominance for asteroid 1979XB considering the technology readiness level. 247

Nomenclature

List of symbols

Latin symbols

$\mathbf{A}_k$	Matrix of the DDP algorithm at stage k.
$\mathbf{A}_{\text{MOID}}$	Matrix form of the proximal motion equations.
a	Acceleration vector, km/s^2, or coefficient matrix of the Runge-Kutta-Fehlberg integration scheme.
a	Semi-major axis, km.
AU	Astronomical unit, km.
$\mathbf{B}_k$	Matrix of the DDP algorithm at stage k.
b	Coefficient matrix of the Runge-Kutta-Fehlberg integration scheme.
b	Semi-minor axis, km.
b^*	Impact parameter, km.
b^l	Lower boundary for the solution vector of the global optimisation.
b^u	Upper boundary for the solution vector of the global optimisation.
$\mathbf{C}_k$	Matrix of the DDP algorithm at stage k.
C	Constraint.
c	Coefficient matrix of the Runge-Kutta-Fehlberg integration scheme.
c	Constant.
$\mathbf{D}_k$	Matrix of the DDP algorithm at stage k.
D	Domain.
d	Hovering distance, m.
d_m	Diameter of the mirror, km.
d_{tr}	Index associated to the transfer trajectory.
$\mathbf{E}_k$	Matrix of the DDP algorithm at stage k.
E	Incomplete elliptic integral of the second kind.

e	Eccentricity.
e_r	Relative error.
F	Incomplete elliptic integral of the first kind.
$\mathbf{f}$	Discrete-time state transition function.
$\tilde{\mathbf{f}}$	Function containing the continuous dynamics equations.
$\mathbf{G}_d$	Matrix form of the Gauss' equations, considering an impulsive change in the velocity.
$\mathbf{G}_t$	Matrix form of the Gauss' equations, considering an impulsive change in the velocity at time t.
G	Universal gravity constant, $km^3/(kg \cdot s^2)$.
g	Scalar stage-wise loss function.
g_0	Standard free-fall, km/s^2.
$\mathbf{H}_k$	Matrix of the DDP algorithm at stage k.
$\hat{\mathbf{h}}$	Unit vector in the direction of the angular momentum.
h	Angular momentum, km^2/s.
h_k	Discretisation step.
I_d	Dominance index.
I_{sp}	Specific impulse of the spacecraft engine, s.
$\mathrm{I}(m)$	Identity matrix of size m.
i	Inclination, rad or deg, or integer number.
id_{NEO}	Near Earth object identification number.
$\mathbf{J}$	Vectorial (multi-criteria) cost function of the optimisation problem.
J	Cost function of the optimisation problem.
j	Integer number.
$\mathbf{K}_k$	Matrix of the DDP algorithm at stage k.
k	Integer number or integer number indicating the generic stage of DDP and the decision time of the trajectory at which the control law is allowed to change.
k_a	Proportionality constant of the acceleration, km^3/s^2.

k_{lim}	State from which the new control law is adopted for the integration of the dynamics.
L	True longitude, rad.
l	Number of components of the Lagrange multiplier vector.
M	Mean anomaly, rad or deg.
m	Mass of the spacecraft, kg, or number of components of the objective function, or number of components of the control vector.
m_0	Mass of the spacecraft into space, kg.
m_d	Dry mass or mass of the spacecraft at the asteroid interception, kg.
m_p	Propellant mass, kg.
m_{NEO}	Mass of the near Earth object, kg.
$m_{\text{shot},j}$	Mass expelled per shot j by the mass driver strategy, kg.
N	Total number of decision times or control stages of the DDP algorithm.
N_p	Set of indices of feasible solutions in the population in the global optimisation problem.
n	Angular velocity, s^{-1}, or number of components of the state vector.
n_{rev}	Number of revolutions around the central body.
$\hat{\mathbf{n}}$	Unit vector in the normal direction in the orbital plane.
$\mathbf{P}_k$	Matrix of the DDP algorithm at stage k.
$P(\mathbf{x})$	Property of $\mathbf{x}$.
p	Semilatus rectum, km.
$\mathbf{Q}_k$	Matrix of the DDP algorithm at stage k.
$\mathbf{R}$	General rotation matrix.
$\mathbf{R}_k$	Matrix of the DDP algorithm at stage k.
R_{Earth}	Radius of the Earth, km.
$R_{\text{Earth-Moon}}$	Earth–Moon distance, km.
$\mathbf{r}$	Position vector, km.
r	Norm of the position (orbital radius), km.
r_a	Apocentre distance, km.

r_p	Pericentre distance, km.
$reltol$	Relative tolerance.
$reltol_{mesh}$	Relative tolerance on the mesh selection.
$\mathbf{S}_k$	Matrix of the DDP algorithm at stage k.
$\mathbf{s}$	State vector.
s	Deviation strategy.
$\mathbf{T}$	Thrust vector, N.
T_{NEO}	Orbital period of the NEO, days.
$\hat{\mathbf{t}}$	Unit vector in the tangential direction in the orbital plane.
t	Time, s or days.
t_0	Departure time from the Earth, s or days.
t_d	Time at which the impulsive deviation manoeuvre is performed, s or days.
t_e	Time when the low-thrust arc ends, s or days.
t_f	Final time of the transfer trajectory, s or days.
t_i	Interception time and time when the low-thrust deflection manoeuvre is performed, s or days.
t_{MOID}	Time at the minimum orbit intersection distance point, s or days.
t_w	Warning time, s or days.
ToF	Time of flight, s or days.
tol_r	Absolute tolerance on the position error.
tol_v	Absolute tolerance on the velocity error.
$\mathbf{U}_{\mathrm{NEO}}$	Unperturbed velocity of the asteroid relative to the Earth, km/s.
$\mathbf{u}$	Control vector.
$\mathbf{v}$	Orbital velocity vector, km/s.
V	Optimal return function of the DDP algorithm.
$\bar{V}$	Average velocity of evaporated particles, m/s.
v	Norm of the orbital velocity, km/s.
v_e	Excess velocity, m/s.

w	Weight parameter.
$\tilde{w}$	Weight parameter.
X	Set of feasible solutions of the global optimisation problem.
$\mathbf{x}$	Generic vector or solution of the Pareto front.
x	Cartesian coordinate along the x axis.
y	Cartesian coordinate along the y axis.
$\mathbf{Z}_k$	Matrix of the DDP algorithm at stage k.
z	Cartesian coordinate along the z axis.

Greek symbols

$\boldsymbol{\alpha}$	Vector of the orbital parameters.
α	In-plane angle of the velocity vector, rad or deg.
$\boldsymbol{\beta}_k$	Coefficient vector of the feedback control law component proportional to the variation of the state vector at stage k.
$\boldsymbol{\gamma}_k$	Coefficient vector of the feedback control law component proportional to the variation of the Lagrange multiplier vector at stage k.
γ	Momentum enhancement factor.
$\Delta\mathbf{r}$	Vector distance of the NEO from Earth at the minimum orbit intersection distance, km.
Δr	Norm of $\Delta\mathbf{r}$, km.
Δt_{TR}	Time interval required to develop a technology, y or days.
$\Delta\mathbf{v}$	Relative velocity vector, km/s.
δ	Out-of plane angle of the velocity vector, rad or deg.
$\delta\mathbf{r}$	Deviation vector, km.
δr	Norm of $\delta\mathbf{r}$, km.
δs	Component of the deviation vector, km.
$\delta\mathbf{v}$	Impulsive manoeuvre vector, km/s.
δv	Norm of $\delta\mathbf{v}$, km/s.
$\delta\hat{\mathbf{v}}_{opt}$	Optimal impulse unit vector.
$\delta\boldsymbol{\alpha}$	Orbital elements difference between the perturbed and the nominal orbit.
ε	Constant between 0 and 1.

$\hat{\boldsymbol{\zeta}}$ Unit vector in the direction opposite to the projection of the heliocentric velocity of the planet onto the *b*-plane.

$\hat{\boldsymbol{\eta}}$ Unit vector in the direction perpendicular to the *b*-plane aligned along the unperturbed velocity of the NEO relative to the Earth.

Θ_k Difference between the optimal return function at state *k* applying the new control, and the optimal return function at state *k* applying the nominal control.

θ True anomaly, rad or deg.

θ^* Argument of latitude, rad or deg.

$\boldsymbol{\lambda}$ Vector of Lagrange multipliers.

μ Gravitational constant, km^3/s^2.

$\mathbf{v}$ Eigenvector of the transition matrix.

$\hat{\boldsymbol{\xi}}$ Unit vector in the *b*-plane that completes the reference system $\{\xi \quad \eta \quad \zeta\}$.

ρ Shape parameter of the shape-based method for low-thrust trajectories.

σ Scattering factor.

$\boldsymbol{\Phi}$ Transition matrix.

ϕ Angle between the pointing direction of the engines of the gravity tug, and the line between the spacecraft and the NEO centre of mass, rad.

φ Scalar function representing the constrains on the final stage in the optimal control problem.

Ω Argument of the ascending node, rad of deg.

ω Argument of the perigee, rad or deg.

Subscripts

1 Initial condition of a variable.

d Value calculated at the instant the deviation manoeuvre is performed.

e Value calculated at the time the low-thrust manoeuvre is ended.

h	Vector component in the direction perpendicular to the orbit plane, in the direction perpendicular to the osculating angular momentum of the orbit.
i	Value calculated at the time of the NEO interception.
k	Stage of the DDP procedure.
MOID	Value calculated at the Minimum Orbit Intersection Distance.
mean	Mean value.
n	Vector component in the normal direction in the orbit plane.
out	Threshold value to exit a computational loop.
r	Vector component in the radial direction in the orbit plane.
s	Derivative with respect to the state vector $\mathbf{s}$.
s/c	Spacecraft.
t	Vector component in the tangential direction in the orbit plane.
target	Variable related to the target body.
u	Derivative with respect to the state vector $\mathbf{u}$.
x	Vector component along the Cartesian *x* axis.
y	Vector component along the Cartesian *y* axis.
z	Vector component along the Cartesian *z* axis.
θ	Vector component in the transversal direction in the orbit plane.

Superscripts

*	New nominal control for the DDP algorithm with global variation in control.
k	Stage of the DDP procedure.

Mathematical notation

$\square$	Arbitrary variable.
$\bar{\square}$	Nominal value of $\square$.
$\tilde{\square}$	Value of $\square$ computed on the deviated orbit.
$\frac{d\square}{dt}$	Time derivative of $\square$ over time.
$f(\square)$	Function of $\square$.
$\Delta\square$	(Finite) difference in $\square$.

$\delta\square$	(Differential) variation of $\square$.
$\square^T$	Transposed of $\square$.
$\square^{-1}$	Inverse of $\square$.
$\exp[\square]$	Exponential of $\square$.
$\hat{\square}$	Unit vector in the direction of $\square$.
$\|\square\|$	2-norm of $\square$.
$\|\square\|_\infty$	Norm infinity of the vector $\square$.
$\{\square_k\}$	Sequence of variable $\square$ in time.
$QP[\square]$	Linear quadratic part of the Taylor expansion of the function $\square$.
$\square_s$	Gradient of the scalar function $\square$, or Jacobian of the vector function $\square$ with respect to the state $\mathbf{s}$.
$\square_{ss}$	Block components of the Hessian matrix of the scalar or the vector function $\square$ with respect to the state $\mathbf{s}$.
$\square_{us}$	Block components of the Hessian matrix of the scalar or the vector function $\square$ with respect to the control $\mathbf{u}$ and the state $\mathbf{s}$.
$\square_u$	Gradient of the scalar function $\square$, or Jacobian of the vector function $\square$ with respect to the control $\mathbf{u}$.
$\square_{uu}$	Block components of the Hessian matrix of the scalar or the vector function $\square$ with respect to the control $\mathbf{u}$.
$\succ$	Dominance.
$\ll$	Is much less than.
$\times$	Cross product or symbol used to define the dimension of a vector/matrix.
$\approx$	Equal approximately to.
$<\square_1,\square_2>$	Scalar product between the vectors $\square_1$ and $\square_2$.
$\mid$	Such that.
$\mid\ \mid$	Cardinality of a set.
$\in$	Is an element of.
$\subseteq$	Is a subset of.
$\wedge$	And condition.

$\forall$	For all, for any.
$\Rightarrow$	Material implication.
$\leftarrow$	Assignment (in an algorithm).
$\mathbb{R}$	Set of real numbers.
min	Minimisation problem.
max	Maximisation problem.

List of constants

Astronomical Unit distance	AU	$= 1.495978707 \times 10^{8}$ km
Universal gravity constant	G	$= 6.67259 \times 10^{-20}$ km^3/(kg·s^2)
Standard-free fall	g_0	$= 9.80665$ m/s^2
Radius of the Earth	R_{Earth}	$= 6378.16$ km
Earth–Moon distance	$R_{\text{Earth-Moon}}$	$= 384{,}401$ km
Earth gravitational constant	μ_{Earth}	$= 3.986004461921757 \times 10^{5}$ km^3/s^2
Sun gravitational constant	μ_{Sun}	$= 1.327244876900 \times 10^{11}$ km^3/s^2

List of acronyms

AIAA	American Institute of Aeronautics and Astronautics.
AU	Astronomical Unit.
CPU	Central Processing Unit.
DDP	Differential Dynamic Programming.
ESA	European Space Agency.
JAXA	Japan Aerospace Exploration Agency.
JPL	Jet Propulsion Laboratory.
LEO	Low Earth Orbit.
GEO	Geosynchronous Earth Orbit.
GTO	Geostationary Transfer Orbit.
MJD	Modified Julian Day.

MJD2000	Modified Julian Day since 2000 (counted since 1st of January 2000 at 12:00 pm).
MOID	Minimum Orbit Intersection Distance.
NASA	National Aeronautics and Space Administration.
NEA	Near Earth Asteroid.
NEO	Near Earth Object.
NEODyS	Near Earth Objects - Dynamic Site.
PHO	Potentially Hazardous Object.
PHA	Potentially Hazardous Asteroid.
SDC	Static/Dynamic Control.
TRL	Technology Readiness Level.

Chapter 1.

Introduction

Near Earth Objects (NEOs) interception and hazard mitigation has been recognised as a key issue for the safety of life on Earth. This thesis will respond to this requirement and will develop methodologies to allow the interception and deviation of potentially hazardous asteroids and comets.

In this chapter we will introduce the motivations and objectives of the study. Subsequently, a summary of the current state of the art in asteroid deflection and interception will be given. After a brief overview on the impact hazard, we will present the deflection strategies proposed in literature. In particular, the analysis will focus on methods to compute the variation of the asteroid course following a deflection manoeuvre. In this context, we also review some analytical models for low-thrust trajectory design and investigate their application to the computation of the diverted trajectory of the NEO.

For the study of asteroid interception, an overview of various approaches for low-thrust trajectory optimisation is given. A brief discussion of direct and indirect approaches, in order to highlight the reasons which led us to the selection of the differential dynamic programming technique for the design of interception transfers to NEOs, is also performed.

Finally, a summary of the methodologies developed and implemented in this study is provided.

1.1. Near Earth Objects and problem definition

Asteroids and comets orbit the Sun since the earliest stages of the life of the solar system. The orbits of most asteroids lay between the orbit of Mars and Jupiter, whereas the comets are concentrated in the Kuiper Belt, beyond the orbit of Neptune, up to 55 AU from the Sun. Almost 450,000 known small bodies orbit

in the solar system [1], and the number increases as astronomical surveys continue. Among the family of asteroids and comets, Near Earth Objects* are those bodies that have been attracted by the gravity of the other planets into orbits, which bring them near the Earth's, with a perihelion distance less than 1.3 AU. These celestial bodies, which travel at very high velocity relative to the Earth, range in size from pebbles to kilometres-diameter objects.

Near Earth objects have been generating growing scientific interest because, as primordial remnants of our solar system, they preserve precious information about its formation, composition and evolution; besides, their collision with the early Earth, would have influenced the shape and composition of our planet. Some NEOs are especially attractive targets for low-cost missions, because of their orbital accessibility with current technologies and short flight duration. This suggests their use for the exploitation of raw materials and for the settlement of future bases, to extend the human exploration to Mars and beyond [2],[3].

Nevertheless, NEO collision with the Earth represents a possible risk to mankind. A short-term threat is posed by a large number of small asteroids, which could cause local devastating effects to our planet. On the other hand, impact hazards with global catastrophic consequences could occur, on a long-term, if a larger kilometre-sized body were to hit the Earth [4]. Advances in orbit determination and theoretical studies on hazard characterisation have increased the capability of predicting potential impacts. A subcategory of NEAs is defined Potentially Hazardous Asteroids (PHAs), which have a non-zero probability of collision with the Earth. This is determined accordingly to their orbital parameters and absolute magnitude; specifically, objects with a Minimum Orbit Intersection Distance (MOID) from the Earth's orbit equal or less than 0.05 AU (i.e., approximately 7,480,000 km) and a diameter larger than 150 meters (which is equivalent to an absolute magnitude of 22.0 or less [2]) are considered potentially hazardous objects. There are currently 1105† known PHAs [5].

* The definition of Near Earth Objects includes Near Earth Asteroids (NEAs) and Near Earth Comets, which are comets with a period less than 200 years. Within this dissertation we will often use the term asteroid alone; however, except where explicitly stated, the techniques developed can be applied to either class of celestial bodies.

† Current number of PHAs from NASA Near Earth Object Program homepage: http://neo.jpl.nasa.gov/neo/ [Retrieved: 13 March 2010].

The impact hazard raises major issues, among them the need to increase the present knowledge of the orbits and physical properties of such bodies, to accurately assess (after initial observation) the likelihood of a collision with the Earth well in advance, the inadequacy of current techniques and technologies necessary for mitigation, disaster management, politics and policy of planetary defence, and communication with the public. Moreover, careful thought is required to investigate options for fast and efficient interception of a potentially dangerous NEO and for minimising or removing the threat it poses. Several organisations and governments have recognised the threat of asteroid hazard and have established discussion panels on the state of the art and the issues of NEO discovery and characterisation, available deflection systems, current and future mitigation and study missions and technologies, impact hazard and effects, involvement of the general public, political and policy implications [6]. The outcome of these works is a series of recommendations and steps that should be followed by the international community to undertake a program on planetary defence [7],[8]. In Great Britain a debate took place in the House of Commons in March 1999 and a Task Force to the Minister for Science to report on potentially hazardous near Earth objects was established in January 2002. The Task Force, which released its findings in September 2000, stated that "We recommended that the Government, with other governments, set in hand to studies to look into the practical possibilities of mitigating the results of impact and deflecting incoming objects" [9].

Over the last decades significant efforts have been devoted to the monitoring [10],[11] and cataloguing of potentially hazardous objects, together with a continuous update of the risk assessment related to each potential hazardous object [12]–[15], but little research has been carried out to assess how to act and react in the case of a NEO travelling on a collision course with the Earth.

1.2. Research motivations and objectives

The aim of this research is to find methodologies for the optimal interception and deviation of potentially hazardous near Earth objects.

Several deviation strategies have been proposed and the space community is discussing the current capabilities for NEO mitigation. Therefore, the first objective is to develop a formulation of the asteroid deviation problem, which allows assessing the effectiveness of any proposed mitigation strategy. The general applicability of this formulation is desired to model the effect of various deflection strategies and to accommodate to the wide range of orbital elements of NEOs. Moreover, high accuracy is essential in predicting the variation of the displacement of the asteroid, achieved through the application of a deflection action on it.

The second objective is to study methodologies for the design of optimal transfers to the interception of dangerous NEOs. In fact, in order to assess the effectiveness and efficiency of a mitigation strategy, the complete mission has to be modelled. Moreover, for the selection of optimal launch opportunities, the two main phases of the mission, namely interception and deflection phase, have to be linked into an integrated design. For example, the total mass of the spacecraft into orbit and the warning time (i.e., elapsed time between the date the mission is launched from the Earth and the date of the hazard impact) should be minimal for a given deviation achievable. Instead of designing a single mission scenario, a more general approach hinges on the analysis of families of optimal opportunities, according to different criteria. In computational terms, this translates in exploring a wide domain of design parameters and hence requires the use of preliminary design techniques (usually under the hypothesis of two-body problem dynamics), for fast modelling the transfer leg.

At a second stage, once a set of first guess solutions for the overall mission has been identified, a selected number of refined trajectories can be optimised, using a more accurate model of the system dynamics. In this context, this research aims to study and develop techniques for the solution of the optimal control problem associated to the design of low-thrust trajectories. The principal requirements are accuracy in reproducing the trajectory, in order to fully exploit the dynamics of the problem within the optimisation process, and robustness, to converge even when a poor first guess solution is available.

The last research objective is to define a wide variety of deflection mission opportunities for a number of selected asteroids, over a wide range of possible

launch dates. Moreover, the purpose is to perform a comparative assessment of the more feasible mitigation strategies proposed in literature, in order to evaluate their efficiency and technology readiness. In order to perform a comprehensive analysis, to compare the various deflection strategies according to a wide number of mitigation scenarios, in terms of target NEOs and mission design parameters, a method will be defined.

1.3. Background

1.3.1. Impact hazard

The Earth, as with most of the planets of the solar system, from its formation up to recent times, has experienced a strong interaction with minor celestial bodies such as asteroids and comets. This is testified by the numerous craters on the Moon and other planets [16].

The over 170 impact structures or craters recognised around the globe provide scientific evidence that such astronomical events have repeatedly occurred in the past [17], though in many cases the erosion and the movement of the terrestrial plates cancelled their sign.

These impact events have had effects on the geological, climate and biosphere evolution of our planet, sometimes with global and dramatic consequences. A catastrophic impact during the Cretaceous-Tertiary period, about 65 millions years ago, has been suggested by Alvarez et al. [18] as the cause for the extinction of many species among which the dinosaurs, observed in the paleontological record. The asteroid impact hypothesis has been widely acknowledged since the identification of the Chicxulub Crater on the coast of Yucatan, Mexico [19],[20], which is estimated to have been caused by a celestial body of about ten km in diameter. In fact, the potential impact of such a large and massive object, though statistically unlikely, having a probability of one event over millions of years, would certainly pose a critical threat to most of the population of the planet, mainly because dust material from the impact would be injected into the stratosphere, preventing sunlight to reach the surface for several years [18]. The size of an object that could pose a threat to the global ecosystem

has been estimated to be larger than 1 km and is estimated that the number of such objects is around 1000 [21].

If these large size bodies are extremely rare, on the other hand objects with diameter greater than 40 m, which is considered the critical threshold above which the Earth's atmosphere is no longer disintegrating an object, are estimated to be more than one million in number, with a statistical frequency of impact of one hundred years or even less. An example of such an event happened at the beginning of the twentieth century in Siberia, where an object of few tens of meters, though disintegrating before hitting the ground, pulverised many square kilometres of the Siberian forest [22],[23]. An equivalent impact in a densely populated area would have locally devastating effects [4].

Though the concern for hazard from impact of comets was first expressed by Halley in 1705 [24], the threat of an asteroid hitting the Earth has been recognised and accepted only over the last decades, and sometimes brought to the attention of a wider public, for example through spectacular events such as the collision of fragments of the comet Shoemaker-Levy 9 with Jupiter in 1994 [25]. The discovery of Apophis (for which an impact in 2029 has been definitively excluded, through a passage in a keyhole during the 2029 fly-by could still lead to an impact in 2036[‡] [26]) has drawn the attention of public and media to the issue of potentially hazardous objects, and, consequently, to the technological and detection capabilities that nations have in order to implement a mitigation and prevention policy.

At the same time, space agencies have started widening their scope to comets and asteroids not only to improve the current knowledge of these small celestial bodies, but also to develop the technological capabilities required in case an object should pose a serious threat to the Earth. Several fly-by, rendezvous or sample return missions to asteroids and comets have been scheduled to track their position and velocities, map the surface, determine size, shape, mass, rotation rate, density, gas and dust emission and characterise their chemical composition and structure. Past missions such as Giotto (ESA) [27], Deep Impact (NASA) [28], NEAR-Shoemaker (NASA) [29], Deep Space 1 (NASA) [30],[31], Galileo

[‡] 99942 Apophis risk page, available at http://neo.jpl.nasa.gov/risk/a99942.html [Retrieved 14 September 2009].

(NASA) [32], Stardust (NASA) [33], present missions like Rosetta (ESA) [34], Hayabusa (JAXA) [35], and future missions like Dawn (NASA) [36] testify the interest of space agencies in scientific exploration of the solar system. In particular, the European Space Agency is now assessing the feasibility of Don Quijote asteroid deflection precursor mission [37],[38], which plans to impact a spacecraft with a high relative velocity onto an asteroid and measure its deflection. Should this mission launch, this would be the first technological demonstration of our capability to deviate an asteroid if needed.

1.3.2. NEO deflection strategies

During the last decades a number of possible strategies to prevent a collision of a potentially hazardous object with Earth have been proposed [39],[6]. Most of them consider a change in linear momentum of the asteroid, with a consequent variation in its nominal orbit, this resulting in an increase of the distance of minimum displacement of the object from the Earth. The mitigation strategies reviewed in the literature can be catalogued depending on their interaction with the asteroid, as:

- Strategies producing an impulsive change in the linear momentum of the asteroid, such as kinetic impactors or nuclear interceptors;
- Strategies producing a multi-impulsive change in the linear momentum of the NEO by ejection of material, such as mass drivers;
- Strategies actively producing a low-thrust, such as attached propulsion devices, ablation-based technologies, gravity tractors;
- Strategies passively producing a low-thrust by inducing thermo-optical changes of the asteroid surface.

Deflection by kinetic impactor is the simplest technology: a spacecraft acts as a projectile and hits the NEO at high relative velocity [40]–[43]. As an alternative, nuclear explosion devices can be adopted [44],[45], in three different forms: 1) stand-off, the explosion occurs at a certain distance from the asteroid surface; 2) the explosion takes place on the surface of the asteroid; 3) the nuclear warhead is placed under the asteroid surface. If the explosion takes place on or under the asteroid surface, the ejected mass from the body is bigger. However,

stand-off explosion, occurring at a certain distance from the NEO, is more robust against the uncertainties on asteroid materials, components, shape, etc. On the other hand, the use of nuclear explosives in space is banned by the Outer Space Treaty [46] and the misuse of this deflection system could pose a higher risk than the probability of NEO collision with Earth [47].

Systems like kinetic impactors and nuclear interceptors will deliver an impulse that will change the asteroid orbit or break it into fragments [48],[49]. Strategies relying on kinetic impact or nuclear explosion can achieve the threat mitigation either by diverting the asteroid or comet course, or by destroying it in space with a single explosive charge on, or, below the surface. This latter option, however, is a critical strategy, as the asteroid could only fragment and still impact the Earth and potentially cause more damage [50],[51].

Mass drivers deliver a multi-impulsive change in the linear momentum of the NEO by collecting material from the asteroid surface and ejecting it away from the asteroid. The effect is equivalent to the steam of an engine device; the only difference is the use of in-situ material (material from the asteroid surface) as propellant [52].

Other mitigation strategies produce a continuous low-thrust action on the asteroid; concepts include attached propulsion devices, gravity tugs or strategies making use of ablation of the NEO surface. In the first case a propulsion system is anchored to the body and operates along the desired direction, determined accordingly to the rotation of the asteroid. The anchored device can adopt any conventional or advanced propulsion system (e.g. electrical, chemical or nuclear propulsion, solar sails, etc.) [53]. The technical problem related to this scheme is the connection between the device and the rotating asteroid. The gravity tractor consists of a spacecraft hovering above the asteroid; the gravitational attraction between the two bodies is exploited to pull the asteroid and move it [54]. This strategy has the advantage of not being affected by the uncertainties on the asteroid surface and composition, because it does not need physical contact with the NEO. Another option deflects the threatening object from its nominal orbit, by provoking the ablation of its surface. For example a mirror collects the solar radiation and, through a system of lenses, it focuses it onto the asteroid's surface [55]–[58]. The same principle is exploited by a spacecraft-based laser beam,

which is concentrated onto the asteroid surface, producing the vaporisation of the surface [59],[60]. Ablation-based strategies produce a beam of ejected material that would act as a thrust according to the Newton's third law.

Coating the surface of the asteroid is used to alter the albedo and modify the induced Yarkovsky acceleration [61]. The resulting thrust is small compared to other schemes, especially for increasing NEO size.

A small number of authors have performed a partial comparative assessment of the numerous proposed mitigation strategies. Some of these emphasise a classification system based on effectiveness in acting near instantaneously on the hazard, or producing a long duration continuous effect [62]. Some considerations on the capabilities of current technologies (i.e., near-term, medium-term or long-term strategies) were also included in the discussion; however, simplified dynamics model were used to asses the required velocity increment for the deflection (for example, the deflection manoeuvre is assumed applied at the pericentre of the NEO's orbit). Other authors classified various mitigation strategies on the basis of the coupling between the dynamics of the deflection of the object and the guidance of the spacecraft [63]. The approximation of the control delivered by the spacecraft to the NEO depends on the motion of the two bodies and on the deflection mechanism capabilities. Three main categories of strategies are identified, respectively based on cratering of the NEO, continuous mass ejection or on action at distance, such as exploiting solar pressure, with solar sails or paint.

In recent years several studies have been performed at NASA [64], to analyse possible alternatives for NEO deflection, evaluate their effectiveness and identify recommended options for further studies. Several potential mitigation strategies were modelled with inputs from other studies. Unlike previous work, a complete mission design was performed, including a first approximation of the required Δv (i.e., velocity change) for the interception or rendezvous of the asteroid. Some mitigation options were analysed with the purpose of building a parametric model and quantifying the relation between required system mass, mission time and size of the object deflected, however, a procedure for comparing the different technologies was not defined. In a subsequent report [6] an attempt was made to graphically compare alternatives for NEO deflection; five scenarios

were identified, representing different sizes of threat. The system performance was described as the "effective momentum change" (i.e., Δv required for the deflection multiplied by the NEO's mass) and the launch performance (i.e., deflection vehicle launch mass) to place the payload into an intercept trajectory.

Finally Rogers and Izenberg [65] used the normalised specific impulse of the divert technology (defined as the ratio of the impulse imparted to the weight-on-Earth of the strategy) as a qualitative way of comparing the efficiency of various mitigation strategies.

1.3.3. Asteroid deviation

In order to determine the variation of the displacement of the NEO, following the application of any of the proposed strategies, it is convenient to classify them according to the equivalent action they deliver to the body. The effect all the proposed deflection strategies have on the asteroid can be distinguished either as an impulsive or nearly instantaneous variation of the velocity of the asteroid, or as a low-thrust, if they act on the asteroid over an extended period of time, with a continuous momentum change [6]. Hence in the following of this study, they will be distinguished between *impulsive* strategies (e.g., kinetic impactor, nuclear interceptor. Mass driver can be considered as a multi-impulsive strategy, even if its effect is comparable to the deviation produced by a continuous action) or *low-thrust* strategies (e.g., solar collector, pulsed laser, gravity tractor, enhanced Yarkovsky effect, etc.).

The consequent variation of the orbit of the asteroid can be computed through a numerical procedure, and the result has to be validated through orbit tracking and astronomical observations. Carusi et al. [40] studied the δv requirement for deflecting a hazardous near Earth object at different epochs. The orbital course of the asteroid following a deflection impulse along its velocity is computed through the numerical propagation of the full n-body dynamics. They show that when an encounter occurs before the impact epoch, the required deflection manoeuvre is noticeably lower if given before rather than after the encounter itself. Kahle et al. [66] extended this study by removing the assumption of a manoeuvre along-track; they show that using a different direction for the deflection manoeuvre in the vicinity of a planetary encounter significantly

increases the performance. The issue with numerical approaches is the computational time, which becomes a limit when the trajectory has to be integrated over a long period without losing accuracy. Of course, in the case of a real event, the CPU time would not be an issue; nonetheless, a number of authors have developed analytical formulations to make extensive investigations and gather useful lessons from the computation of a wide range of solutions. In this case the simplification of the two-body problem is often adopted.

Ahrens and Harris [67] gave an estimation of the δv required for deflecting an asteroid from an Earth-crossing orbit, by perturbation either perpendicular or along the direction of motion, and Scheeres and Schweickart [68] derived an analytical expression of the shift in the position of the asteroid, under the assumption of a circular orbit and a constant acceleration aligned with the velocity of the NEO. This strategy, which yields a change in the mean motion of the asteroid, is proposed for long lead time until the impact. Subsequently, Izzo [69] proposed a similar solution, but extended it to non circular orbits. However, this formulation introduces an integral term that was solved analytically only in the case of an impulsive deflection manoeuvre. Furthermore, the effect of the deviation strategy is translated in a change of mean motion and hence in a phase shift; other changes in the orbital geometry are not included.

A more general approach was used by Conway [70] to determine the near-optimal direction in which an impulsive manoeuvre should be given. The modified orbital course was propagated analytically forward in time by means of Lagrange coefficients expressed through universal formulae [71]. An analysis on the minimum δv and the optimal impulse angle was performed also by Park and Ross [72], who used Lagrange coefficients to propagate the deviated orbit of the asteroid rather than only its displacement with respect to the nominal course. They also included the effects of the Earth's gravity [73],[74], obtaining a more accurate estimation of the optimal impulse. Song et al. [75] investigated the deflection of asteroids and comets using a power-limited laser beam. They used the same technique proposed by Park and Ross [72] to solve the heliocentric two-body motion after the laser is shut off, whereas when the laser is on, the trajectory of the Earth-crossing object is numerically integrated. They found that the optimal operating angle between the asteroid velocity and the thrust acceleration vector

remains in the range 150–180 deg for warning times longer than one asteroid period, regardless of the orbital elements of the asteroid.

Low-thrust analytical models

The attention is now focused on NEO deviation by technologies delivering a continuous low-thrust action. In particular, when the objective is the identification of many mission opportunities (i.e., favourable conditions for deflection), global optimisation techniques can be employed, to perform an extensive search for optimal solution over a search space. In this case, the evaluation of several tens of thousands of trajectories is required, thus the numerical computation of the deflected course of the asteroid would be impractical.

Since 1950 [76]–[78], several authors have proposed analytical solutions for some particular cases of low-thrust control problems. Tsien [77] and Benney [78] developed a solution for escape trajectories, respectively, subject to radial and tangential continuous thrust acceleration. Following a similar formulation, Boltz [79],[80] proposed a solution in case the ratio between the thrust and the gravity acceleration is kept constant. In both cases, the orbit is assumed to be circular or nearly circular.

Kechichian [81] used an averaging technique to compute analytical solutions for orbit-raising with constant tangential acceleration in the presence of Earth shadow. Kechichian's equations, which contain some terms expanded in power of the eccentricity, are accurate for small-to-moderate values of the eccentricity up to 0.2. The effects of the Earth oblateness are also considered. Gao and Kluever [82] adopted an averaging technique with respect to the eccentric anomaly for continuous-tangential-thrust trajectories, also accounting for the Earth oblateness and the Earth shadow. The value of the elliptic integrals in the solution of Gao and Kluever is approximated and the accuracy of the solution depends on the eccentricity.

Other analytical solutions for low-thrust trajectories were studied by Petropoulos [83], who presented a general overview of the approximated solutions derived so far. In his work, Petropoulos developed some analytical integrals to describe the secular evolution of the orbit of a spacecraft subject to different thrust control laws. The rate of change of the orbital energy and the eccentricity are

time-averaged and reformulated, introducing some elliptic integrals, which are valid for all initial eccentricity from slightly above zero.

1.3.4. NEO interception and trajectory optimisation

Asteroids are nowadays appealing targets for space missions. The orbit of those asteroids classified as Near Earth Objects comes close to the Earth's orbit around the Sun; this makes their exploration viable with current technologies. In particular, as testified by some missions like Dawn [36] and Hayabusa [35], the use of low-thrust propulsion showed in the last decade to be a valuable option to decrease propellant consumption, at the expense of longer times of flight.

The design of low-thrust trajectories requires the solution of an optimal control problem, the difficulty of which increases with the complexity of the transfer and the fidelity of the trajectory model. Multi-body dynamics, gravity assist manoeuvres, capture or escape phases concur to increase the complexity of a trajectory design problem [84]. Furthermore, the low level of thrust implies long transfer times and a low control authority because the thrust level is comparable to the gravitational forces. Moreover, the design of interplanetary transfers involves dynamics of variable scales, i.e., from planetocentric phases (e.g., during gravity assist manoeuvres) to heliocentric legs.

In order to properly handle the different scales, it would be desirable to have an optimisation method that can adaptively change the discretisation of the numerical integration of the dynamics, during the optimisation itself. Additionally, it should be robust enough to converge even when a poor first guess solution is available and accurate enough to reproduce the trajectory with high fidelity, hence exploiting a full dynamical model.

Direct and indirect methods

In general, methods for trajectory optimisation are classified under direct or indirect approaches [85],[86]. Directs methods are known to be quite robust, convergence being reached even if a poor first guess solution is available; however, collocation method efficacy is bounded by the definition of the discretisation of the state variables prior to the optimisation [87]–[89]. Direct shooting methods overcome the disadvantage of collocating the states, but still

need the a priori collocation of the control [90],[91] and tend to be less robust than collocation methods.

On the contrary, indirect methods guarantee the accuracy of the solution, which satisfies Pontryagin's maximum principle [92], but, on the other hand, they require a good first guess for the adjoint variables. Common applications usually focus on a single phase of the mission, in which the primary body does not change, such as Earth centred transfers [93] or heliocentric leg [94],[95].

When direct and indirect methods are applied to the design of transfers which involve multi-body dynamics (i.e., include escape and capture phases) or gravity assist manoeuvres (not simplified as impulsive change of velocity), a patched conic approach is usually adopted. The overall trajectory is divided in a sequence of problems, each of them expressed in the primary body reference frame; different segments are then patched together, through boundary constraints at the edge of each segment (direct methods), or through conditions on states and costates (indirect methods). Many applications have been presented, making use of direct methods [96]–[99], indirect methods [100]–[103], or hybrid methods [104],[105].

The patched conic approach allows handling different time and distance scales over different segments of the trajectory, hence avoiding numerical sensitivity; however, since the transition conditions from one segment to the following one are defined a priori, the solution may not fully exploit the multi-body dynamics nature of a transfer.

Previous works attempted to optimise multi-body low-thrust problems, treating the trajectory as a whole, without resorting to the patched conic approach; Whiffen et al. presented many interplanetary trajectories, including escape, capture and fly-bys, computed with the Static/Dynamic Control (SDC) algorithm [106]–[108], Lantoine and Russel [109] proposed a hybrid differential dynamic programming algorithm and applied it to a LEO to GEO orbital transfer and Olympio [110] developed a gradient-based method to address the problem of interplanetary transfers with escape and capture phases.

Differential dynamic programming

In this work we investigate the use of Differential Dynamic Programming (DDP) (introduced by Jacobson and Mayne in 1969 [111]) for designing interplanetary trajectories to the rendezvous and fly-by of near Earth objects, including the escape phase at the Earth. This technique can be classified among direct methods, but, unlike the other approaches, the time dependence is not removed from the parameterisation.

DDP is derived from the theory of dynamic programming [112], and overcomes its inherent "curse of dimensionality" (see Yakowitz and Rutherford, [113]) by replacing the cost function of the problem with its quadratic expansion in the neighbourhood of a nominal non-optimal trajectory. The optimisation process is based on successive iterations, in which the coefficients for a feedback control law are generated through the stage-wise solution, backward in time, of Bellman's partial differential equation, and the consequent improved trajectory and control policy are then propagated forward in time.

Because the minimisation is performed through successive approximations around a nominal solution, the large scale problem, associated with the optimisation of a low-thrust trajectory, is translated into a series of problems of small dimensions. In other words, the stage-wise approach allows to efficiently handle problems with a large number of stages; this overcomes the limit of direct transcription methods, which lead to the solution of systems of nonlinear programming problems of increasing dimension with the number of discretisation steps (or stages). For example the trajectory representative of SMART-1 mission, computed by Betts and Erb [88] required the solution of a sparse optimisation problem with 211,031 variables and 146,285 constraints.

Moreover, DDP is based on Bellman's principle of optimality which is a necessary and sufficient condition for a solution to be locally optimal [114]; hence the solution of the optimal control problem preserves the accuracy of indirect methods, without requiring a first guess solution for the adjoint variables.

1.4. Methodologies developed and implemented

The present research focuses on the orbital dynamics of the asteroid deviation problem and studies the design and optimisation of interplanetary trajectories for the interception and rendezvous of potentially hazardous NEOs.

The effect on the asteroid of any deflection strategy can be modelled either as an impulsive action or as a low-thrust continuous manoeuvre. In both cases, a semi-analytical formulation is derived to compute the displacement of the position of an asteroid at the MOID point, after a deviation manoeuvre.

This approach makes use of the proximal motion equations [115] expressed as a function of the orbital elements, through Gauss' planetary equations [71]. This formulation provides a very simple and general means to compute the variation of the MOID with good accuracy, without the need for further analytical developments. It is worth underlying that the computation of the deflection distance through proximal motion equations can be adopted for any deviation strategy (low-thrust and impulsive) and represents an extension and a generalisation of the methodologies proposed in previous works [40],[68],[69], in which analytical formulae were derived to compute the deviation due to a variation in the orbital mean motion, i.e., due to an action applied along the direction of the motion of the asteroid.

In this work, near-optimal directions for the deviation impulse are derived using a simple restricted two-body dynamic model. The gravitational effect of the Earth is accounted for by looking at the obtained deviation on the *b*-plane. This allows the computation of the correct estimate of the minimum intersection distance between the asteroid and the Earth. The accuracy of the result is then assessed using a numerical propagation of the post deviation conditions within a full three-body dynamic model, which includes the Sun and the Earth.

If low-thrust mitigation options are selected, the computation of the achieved deviation requires, in the general case, the numerical integration of the diverted trajectory. To overcome the issue of computational time, a set of semi-analytical formulae is developed, under the assumption that the deflection strategy uses the Sun as a power source, and therefore the thrust acceleration is inversely proportional to the square of the distance from the Sun. The reason for this choice

is that, as will be shown in Chapter 4, the solar collector mitigation strategy showed to be the most efficient among the low-thrust deflection options. Furthermore, the attention is focused on the case in which the thrust is aligned with the tangent to the osculating orbit of the asteroid. To obtain an analytical solution for the variation of the orbital elements, Gauss' equations are averaged over one orbital revolution. However, the required accuracy for the computation of the deflection distance is higher than for the design of a generic low-thrust trajectory; hence, unlike other works [81]–[83], the periodic variation of the orbital elements is also taken into account. In addition, the analytic integrals are updated with a one-period step to further improve the accuracy. The general applicability of the proposed formulation and its accuracy is demonstrated through a number of test cases. Furthermore, some analyses are presented on the sensitivity of the deviation to the in-plane orbital elements of the nominal orbit of the asteroid.

The second research objective is to study methodologies for the design of transfer trajectories that intercept and rendezvous with PHAs. A NEO mitigation mission requires the integrated design of the two phases of the mission, namely interception and deflection phase. In fact, the mission performance is determined by contrasting drivers, such as the total mass of the spacecraft into orbit and the total time of the mission, which should be minimal for a given deviation. In this work, the search for different transfer options is performed with a particular global optimisation procedure based on an automatic branch and prune of the solution space combined with an agent-based search technique [116],[117]. In particular, an extensive search for all mission opportunities is carried out, over a wide range of launch dates that are Pareto-optimal with respect to three criteria: the achievable displacement of the asteroid at the point of MOID, the time between the launch and the hypothetical impact, and the propellant mass for the transfer trajectory. The use of high fidelity models of the trajectory (i.e., characterised by a complete dynamics and a full and accurate description of all the singular events, such as gravity assist manoeuvres) would be impractical; hence, at this stage, preliminary design techniques are used to model the trajectory (shape-based approach for low-thrust transfer [118] and Lambert's algorithm for impulsive transfer [71],[119]).

The proposed formulation of NEO deviation through impulsive and low-thrust action, together with the model of the transfer trajectory, by means of existent preliminary design techniques, provides a way to fully model a generic mitigation mission. In order to give some insight into the NEO deviation problem, the formulae developed are applied to the design of a set of mitigation scenarios. Instead of using a single hypothetical mission case, a set of hundreds of solutions is found, each one representing a complete mission with a specific launch date and transfer time.

Firstly, the attention is focused on the analysis of impact strategies for the deflection of asteroids. Because ideal optimal deflection conditions cannot always be achieved, a characterisation of optimal mission opportunities is performed for a restricted group of selected PHAs over a very wide range of possible launch dates. The result of this analysis demonstrates that with a small spacecraft and very simple transfer strategies, it is possible to obtain considerable deviations for the majority of the threatening asteroids.

Moreover a set of mitigation missions through a solar collector strategy is designed by means of the semi-analytical low-thrust formulae and a shape-based approach for the transfer trajectory. Families of Pareto-optimal solutions, for different asteroids, that minimise the warning time and the spacecraft mass, while maximising the orbital deviation, are presented. The warning time is defined as the time difference between the impact epoch and the launch date that is required to achieve a given deviation; hence it gives quantitative information on the time to react, once the impact hazard has been confirmed.

Another result of this research is a comparison of deflection technologies, proposed in literature, according to different criteria. A set of NEOs, differing in physical characteristics (i.e. size, mass and spin properties) and orbital parameters, was selected for this analysis. A group of different mitigation strategies is then applied to these asteroids, and evaluated in terms of four figures of merit: achieved deflection distance at the MOID, warning time, total mass into orbit and technology readiness level, i.e., the required technological development to implement a given mitigation strategy. The deflection distance between the asteroid and the Earth is the displacement of the position of the asteroid at the MOID, achieved by a deviation manoeuvre applied before the encounter. The first

three criteria (deflection distance, warning time and mass into orbit) express quantitatively how easy deflecting an asteroid with a given strategy is, and whether a given deviation strategy can be implemented with present launch capabilities. A multi-criteria optimisation is used, to provide a preliminary and relative measure of the effectiveness of one deviation over another according to the selected criteria. The novelty of this study is the use of the dominance criterion (borrowed from multi-objective optimisation) to make a comparative assessment of all the various mitigation options, over a wide range of initial masses and warning times.

In order to address the second research objective, the trajectory design process is performed on two levels. Once a large number of optimal interception options have been identified over a wide solution domain, high fidelity models are used to locally refine some solutions. In light of the strength and drawbacks of traditional direct and indirect methods, it was decided to investigate the use of differential dynamic programming for designing low-thrust interplanetary trajectories to the rendezvous and fly-by of near Earth objects, including the escape phase at the Earth.

In this research, the stage-wise feature of DDP (discussed in Section 1.3.4), is exploited to integrate an adaptive variable step discretisation scheme within the optimisation process. The discretisation grid is adjusted at each iteration, to better adapt to the non-linear dynamics of the problem. A Runge-Kutta explicit method is selected for the numerical integration and the derivatives of the dynamics scheme are analytically derived. The stage-wise approach also allows handling a multi-phase trajectory as a whole, without recurring to the patched conic approximation.

A particular interpolation technique is used to preserve the feedback nature of the control law, thus improving robustness against some approximation errors introduced during the adaptation process. The algorithm developed applies global variation of the control law [111], through the use of DDP and non-linear programming techniques; this ensures a further increase in robustness. The constraints on the target state at the end of the trajectory are included in the optimisation problem as an additional term of the cost objective, through a time invariant vector of Lagrange multipliers, whose value is modified along the

convergence process [120]. The results presented show how the proposed approach is capable of fully exploiting the multi-body dynamics of the problem; in fact, in one of the study cases, a fly-by of the Earth is scheduled, which was not included in the first guess solution.

1.5. Dissertation organisation

This dissertation is divided into six chapters, which introduce different aspects of the research on optimal interception and deflection of near Earth objects. The first part of each chapter explains the theoretical development and the method adopted, subsequently some results are presented as the application of the theory. The thesis is organised as follows.

Chapter 2 introduces the reader to the asteroid deviation problem. The analytical formulation for an impulsive deflection manoeuvre is derived and its accuracy is assessed. The chapter continues with an analysis of the optimal manoeuvres in order to maximise the achievable deviation and a study on including the gravitational effect of the Earth, through the *b*-plane representation. In Section 2.2 a characterisation of optimal mission opportunities is performed, applying a kinetic impact to a number of selected potentially hazardous asteroids.

In Chapter 3, the attention is focused on deviation techniques that make use of a continuous low-thrust action. A semi-analytical solution is derived for the asteroid deviation problem when a selected control-acceleration profile is used (Appendix A contains some mathematical developments left aside in Chapter 3). The accuracy and computational time of this approach are shown, together with a sensitivity analysis on the orbital elements of the asteroid. In Section 3.3 we perform an extensive search for mission opportunities to rendezvous with the asteroid by means of a low-thrust spacecraft and a solar collector device for the deflection.

Chapter 4 presents a comparative assessment of six deflection strategies: kinetic impactor, nuclear interceptor, mass driver, low-thrust attached propulsion, solar collector, and gravity tug. A multi-criteria optimisation is used to compute a set of optimal solutions for the mitigation of four different asteroids. A dominance criterion is defined to compare the set of solutions and a technology readiness

level is associated to each one of the deviation system to asses the required technological development (Appendix B).

Following the formalisation of the deflection problem and the identification of a wide number of optimal mitigation mission opportunities in Chapter 2 to 4, Chapter 5 focuses on the low-thrust transfer problem. An optimisation method based on differential dynamic programming is studied and applied to the design of rendezvous and fly-by trajectories to near Earth objects. The classical DDP approach is introduced in Section 5.1, whereas Sections 5.2 and 5.3 present the modified method, which was adopted for designing trajectories to asteroids. Sections 5.4 and 5.5 present some interesting cases of transfer trajectories, aimed at highlighting the strengths of the proposed approach.

Finally Chapter 6 summarises the finding of this research and gives an insight into possible further developments of this study that will be subject of future work.

1.6. Contributions

The contents of this dissertation have been published in four stand-alone but highly related journal papers.

The study on optimal impact strategies for asteroid deflection was published in the AIAA Journal of Guidance, Control and Dynamics in 2008 [121]. The low-thrust formulation was presented at the 2007 Planetary Defense Conference in Washington, D.C. An extended version was presented at the 58th International Astronautical Congress in Hyderabad, India [122] and was published in the AIAA Journal of Guidance, Control and Dynamics [123].

The results on the comparative assessment of different deflection strategies are the outcome of a joined work with Dr. Joan Pau Sanchez, who developed the model of the deflection devices and were presented in 2007 at New Trends in Astrodynamics and Applications III conference in Princeton, New Jersey [124] and at the 57th International Astronautical Congress, in Valencia, Spain [125]. A more exhaustive version of this study was discussed at the 2007 Planetary Defense Conference in Washington, D.C. and published in the AIAA Journal of Guidance, Control and Dynamics in February 2009 [126].

Finally the algorithm based on differential dynamic programming was presented in Milano, Italy in June 2008 at the conference New Trends in Astrodynamics and Applications V. This study has been published on the journal Celestial Mechanics and Dynamical Astronomy [127]. Some results of Chapter 5 were presented at the 59th International Astronautical Congress, in Glasgow [128].

Journal Publications

- Vasile M. and Colombo C., "Optimal Impact Strategies for Asteroid Deflection", *Journal of Guidance, Control and Dynamics*, Vol. 31, No. 4, July–August 2008, pp. 858–872, doi: 10.2514/1.33432.
- Colombo C., Vasile M. and Radice G., "Semi-Analytical Solution for the Optimal Low-Thrust Deflection of Near Earth Objects", *Journal of Guidance, Control and Dynamics*, Vol. 32, No. 3, May–June 2009, pp. 796–809, doi: 10.2514/1.40363.
- Sanchez J. P., Colombo C., Vasile M. and Radice G., "A Multi-criteria Assessment of Deflection Methods for Dangerous NEOs", *American Institute of Physics*, Conference Proceedings of New Trends in Astrodynamics and Applications III, 16–18 August 2006, Princeton, New Jersey, Vol. 886, 2007, pp. 317–333, doi: 10.1063/1.2710065.
- Sanchez J. P., Colombo C., Vasile M. and Radice G., "Multi-Criteria Comparison among Several Mitigation Strategies for Dangerous Near Earth Objects", *Journal of Guidance, Control and Dynamics*, Vol. 32, No. 1, January–February 2009, pp. 121–142, doi: 10.2514/1.36774.
- Colombo C., Vasile M. and Radice G., "Optimal Low-thrust Trajectories to Asteroids through an Algorithm based on Differential Dynamic Programming", *Celestial Mechanics and Dynamical Astronomy*, Vol. 105, Nos. 1–3, November 2009, pp. 75–112, doi: 10.1007/s10569-009-9224-3.

Conference Publications

- Colombo C., Sanchez J. P., Vasile M. and Radice G., "A Comparative Assessment of Different Deviation Strategies for Dangerous NEO", 57th

International Astronautical Congress, Valencia, 2–6 October, Spain, 2006, IAC-06-A3.5.8.

- Colombo C. and Vasile M., "Optimal Trajectories for NEO Deflection", 58th International Astronautical Congress, Hyderabad, India, 24–28 September 2007, IAC-07-C1.4.02.
- Colombo C., Vasile M. and Radice G., "Interception and Deviation of Near Earth Objects via Solar Collector Strategy", 59th International Astronautical Congress, Glasgow, United Kingdom, 29 September–3 October 2008, IAC-08-A3.I.06.

Presentations (not included in conference publications)

- Colombo C., Sanchez J. P., Vasile M. and Radice G., "Optimal Trajectories for NEO Deflection Missions", 2007 Planetary Defense Conference, 5–8 March 2007, Washington.
- Colombo C., Sanchez J. P., Vasile M. and Radice G., "Comparative Assessment of Deviation Strategies for Dangerous Near Earth Objects", Aero-Mech Seminar, 3 May 2007, University of Glasgow.
- Sanchez J. P., Colombo C., Vasile M. and Radice G., "A Multi-criteria Assessment of Deflection Methods for Dangerous NEOs", New Trends in Astrodynamics and Applications III, 16-18 August 2006, Princeton, New Jersey.
- Colombo C., Vasile M. and Radice G., "An algorithm based on Differential Dynamic Programming for low-thrust trajectories", New Trends in Astrodynamics and Applications V, June 30, 1–2 July 2008, Milano, Italy.

Chapter 2.

Impulsive NEO deflection

This chapter presents an analysis of optimal impact strategies to deflect potentially dangerous NEOs. To compute the increase in the minimum orbit intersection distance of the asteroid due to an impact with a spacecraft, simple analytical formulae are derived from the proximal motion equations. The proposed analytical formulation allows an analysis of the optimal direction of the deviating impulse transferred to the asteroid. This ideal optimal direction cannot be achieved for every asteroid at any time; therefore, an analysis of the optimal launch opportunities for deviating a number of selected asteroids is performed through the use of a global optimisation procedure. The results in this chapter demonstrate that the proximal motion formulation has very good accuracy in predicting the actual deviation and can be used with any deviation strategy since it has general validity. Furthermore, the characterisation of optimal launch opportunities shows that a significant deviation can be obtained even with a small spacecraft.

2.1. Asteroid deviation problem

Given the orbit of a generic near Earth object, identified by its orbital elements, the Minimum Orbit Intersection Distance (MOID) $\Delta\mathbf{r}$ between the NEO and the Earth is defined to be the minimum distance between the osculating orbits of the two bodies[*]. The MOID is used as a warning indicator of hazard collision, because a small $\|\Delta\mathbf{r}\|$ could represent a close encounter, if the two bodies are in phase. As a consequence of the evolution of NEOs' ephemerides

[*] Note that in this thesis we will use the term MOID as the minimum distance between the osculating orbits of the Earth and the NEO, but also to indicate the location along the asteroid's orbit where the minimum distance occurs.

with time, due to planetary gravitational perturbations [129], the MOID also changes in time [5],[13].

The objective is to maximise the deflection of the asteroid at the MOID by applying an impulsive deviation action at a certain time t_d. The impulse acts as a quasi-instantaneous perturbation on the orbit of the NEO and its new orbit can be considered to be proximal to the unperturbed one (see Figure 2.1).

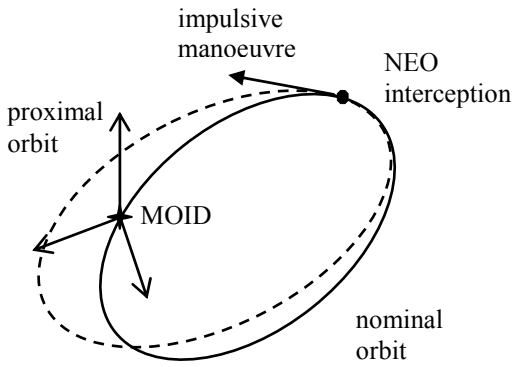

Figure 2.1: Impulsive NEO deviation.

Let *a, e, i,* Ω and ω be respectively the semi-major axis, eccentricity, inclination, anomaly of the ascending node, and anomaly of the pericentre of the nominal orbit of the NEO. If θ_{MOID} is the true anomaly of the NEO at the MOID along the unperturbed orbit, and $\theta^*_{\mathrm{MOID}} = \theta_{\mathrm{MOID}} + \omega$ the corresponding argument of latitude, we can write the variation of the position of the NEO after deviation, with respect to its unperturbed position, by using the proximal motion equations [115]:

$$\begin{aligned}
\delta s_r &\approx \frac{r_{\mathrm{MOID}}}{a}\delta a + \frac{ae\sin\theta_{\mathrm{MOID}}}{\eta}\delta M - a\cos\theta_{\mathrm{MOID}}\delta e \\
\delta s_\theta &\approx \frac{r_{\mathrm{MOID}}}{\eta^3}\left(1+e\cos\theta_{\mathrm{MOID}}\right)^2\delta M + r_{\mathrm{MOID}}\delta\omega + \\
&\quad + \frac{r_{\mathrm{MOID}}\sin\theta_{\mathrm{MOID}}}{\eta^2}\left(2+e\cos\theta_{\mathrm{MOID}}\right)\delta e + r_{\mathrm{MOID}}\cos i\delta\Omega \\
\delta s_h &\approx r_{\mathrm{MOID}}\left(\sin\theta^*_{\mathrm{MOID}}\delta i - \cos\theta^*_{\mathrm{MOID}}\sin i\delta\Omega\right)
\end{aligned} \tag{2.1}$$

where δs_r, δs_θ and δs_h are the displacements in the radial, transversal and perpendicular-to-the-orbit-plane directions, and $\eta = \sqrt{1-e^2}$. The linearising

assumption to compute Eqs. (2.1) is that the variation of relative position $\delta r = \|\delta \mathbf{r}\|$ is small compared to the inertial chief orbit radius r_{MOID}, that is $\delta r \ll r_{\text{MOID}}$ [115], where $\delta \mathbf{r} = \left[\delta s_r \quad \delta s_\vartheta \quad \delta s_h\right]^T$. Moreover, Eqs. (2.1) are limited to elliptical orbits ($e < 1$), because of the term $\sqrt{1-e^2}$.

The variation of the orbital parameters *a, e, i,* Ω and ω are computed through Gauss' planetary equations [71] considering an instantaneous change in the NEO velocity vector $\delta \mathbf{v}$. Let the components of the impulsive variation of the velocity vector $\delta \mathbf{v} = \left[\delta v_t \quad \delta v_n \quad \delta v_h\right]^T$ be along the velocity vector and normal to it, in the plane of the osculating orbit, and perpendicular to it.

$$
\begin{aligned}
\delta a &= \frac{2a^2 v_d}{\mu_{\text{Sun}}}\delta v_t \\
\delta e &= \frac{1}{v_d}\left[2\left(e+\cos\theta_d\right)\delta v_t - \frac{r_d}{a}\sin\theta_d \delta v_n\right] \\
\delta i &= \frac{r_d \cos\theta_d^*}{h}\delta v_h \\
\delta\Omega &= \frac{r_d \sin\theta_d^*}{h\sin i}\delta v_h \\
\delta\omega &= \frac{1}{e v_d}\left[2\sin\theta_d \delta v_t + \left(2e + \frac{r_d}{a}\cos\theta_d\right)\delta v_n\right] - \frac{r_d \sin\theta_d^* \cos i}{h\sin i}\delta v_h \\
\delta M_{t_d} &= -\frac{b}{e a v_d}\left[2\left(1+\frac{e^2 r_d}{p}\right)\sin\theta_d \delta v_t + \frac{r_d}{a}\cos\theta_d \delta v_n\right]
\end{aligned}
\tag{2.2}
$$

where r_d and v_d are respectively the orbital radius and velocity at the point the deflection manoeuvre is given, *h* is the angular momentum, *p* the semilatus rectum, *b* is the semi-minor axis and μ_{Sun} the gravitational constant of the Sun.

The preceding variation on the mean anomaly *M* takes into account only the instantaneous change of the orbit geometry at time t_d. On the other hand, due to the change in the semi-major axis, we have a variation of the mean motion *n* and therefore a change in the mean anomaly at the time of the MOID, given by:

$$\delta M_n = \delta n\left(t_{\text{MOID}} - t_d\right) = \delta n \Delta t \tag{2.3}$$

where t_{MOID} is the time at the MOID along the orbit of the NEO,

$$\delta n = \sqrt{\frac{\mu_{\mathrm{Sun}}}{\left(a+\delta a\right)^3}} - \sqrt{\frac{\mu_{\mathrm{Sun}}}{a^3}}$$

and Δt is the time-to-MOID, defined as $t_{\mathrm{MOID}} - t_d$. Eq. (2.3) takes into account the phase shift between the Earth and the NEO. The total variation in the mean anomaly between the unperturbed and the proximal orbit is therefore:

$$\delta M = -\frac{b}{eav_d}\left[2\left(1+\frac{e^2 r_d}{p}\right)\sin\theta_d \delta v_t + \frac{r_d}{a}\cos\theta_d \delta v_n\right] + \delta n \Delta t \tag{2.4}$$

The result in Eq. (2.4) can be proved as follows, M_{MOID} and $\tilde{M}_{\mathrm{MOID}}$, respectively the mean anomaly at the MOID on the nominal and on the perturbed orbit, can be expressed as:

$$\begin{aligned} \tilde{M}_{\mathrm{MOID}} &= M\left(t_d\right) + \delta M_{t_d} + \left(n+\delta n\right)\Delta t \\ M_{\mathrm{MOID}} &= M\left(t_d\right) + n\Delta t \end{aligned} \tag{2.5}$$

from which Eq. (2.4) can be computed as $\delta M = \tilde{M}_{\mathrm{MOID}} - M_{\mathrm{MOID}}$.

Eqs. (2.2) are limited to $e<1$, because of the term $\sqrt{1-e^2}$. Moreover, this set of equations present singularities for zero inclination and/or zero eccentricity (the terms $\sin i$ and e are at the denominator of the expressions describing the variation of Ω, ω and M). If a NEO with eccentricity or inclination equal to zero is found, the set of equations Eqs. (2.1) and Eqs. (2.2) would have to be rewritten using the non-singular elements [71],[115]. The classical elements representation was used here because it yields a more elegant result.

At this point, if $\Delta\mathbf{r} = \begin{bmatrix}\Delta s_r & \Delta s_\theta & \Delta s_h\end{bmatrix}^T$ is the vector distance of the asteroid from the Earth's orbit at the MOID and $\delta\mathbf{r} = \begin{bmatrix}\delta s_r & \delta s_\theta & \delta s_h\end{bmatrix}^T$ is the variation given by Eqs. (2.1) at t_{MOID}, then the objective function for the maximum deviation problem is the following:

$$J = \left(\Delta s_r + \delta s_r\right)^2 + \left(\Delta s_\theta + \delta s_\theta\right)^2 + \left(\Delta s_h + \delta s_h\right)^2 \tag{2.6}$$

The proposed formulation provides a very fast analytical way of computing the variation of any asteroid's orbit due to any impulsive deviation action. It is both an extension and a generalisation of other approaches [40],[68],[69] that are based on the modification of the orbital period due to an action on the asteroid. In these approaches, only the effect on the orbital mean motion due to a change in the orbital energy was considered, and the variation in the other orbital elements was neglected. As a consequence, the resulting deviation could be maximised only by acting in a direction parallel to the velocity vector of the asteroid. Any other strategy producing an action in a normal direction could not be investigated.

Compared with more general methods that involve analytically propagating the perturbed trajectory by using the Lagrange coefficients [72], the proposed approach does not require any solution of the time equation for every variation of the orbit of the asteroid and is therefore less computationally expensive. On the other hand, it is conceptually and computationally equivalent to those approaches [70] that analytically propagate only the variation of the position and velocity of the asteroid by using the fundamental perturbation matrix [71]. Conversely, the benefit of using proximal motion equations expressed through orbital elements is the explicit relationship between the components of the perturbing action and the variation of the geometric characteristics of the orbit of the asteroid.

2.1.1. Maximum deviation strategies

By combining Eqs. (2.1) and Eqs. (2.2), it is possible to compute the transition matrix $\mathbf{\Phi}$ that links $\delta\mathbf{v}$ at t_d to $\delta\mathbf{r}$ at t_{MOID} for each time t_d. To make explicit the dependence on the impulse components in each of the equations, Eq. (2.3) has to be rewritten as a function of δa as follows:

$$\delta M_n = \delta n \Delta t = -\frac{3}{2}\frac{\sqrt{\mu_{\text{Sun}}}}{a^{\frac{5}{2}}}\Delta t \delta a \tag{2.7}$$

If now Eq. (2.4) is incorporated into system (2.2) and, along with Eqs. (2.1), is expressed in matrix form, we have:

$$\begin{cases}\delta\mathbf{r}\left(t_{\mathrm{MOID}}\right)=\mathbf{A}_{\mathrm{MOID}}\delta\boldsymbol{\alpha}\left(t_{\mathrm{MOID}}\right)\\ \delta\boldsymbol{\alpha}\left(t_{\mathrm{MOID}}\right)=\mathbf{G}_{d}\delta\mathbf{v}\left(t_{d}\right)\end{cases}\Rightarrow\delta\mathbf{r}\left(t_{\mathrm{MOID}}\right)=\mathbf{A}_{\mathrm{MOID}}\mathbf{G}_{d}\delta\mathbf{v}\left(t_{d}\right)=\boldsymbol{\Phi}\delta\mathbf{v}\left(t_{d}\right)\quad(2.8)$$

where $\delta\boldsymbol{\alpha}\left(t_{\mathrm{MOID}}\right)=\left[\delta a\quad\delta e\quad\delta i\quad\delta\Omega\quad\delta\omega\quad\delta M\right]^{T}$ is the orbital element difference, $\mathbf{A}_{\mathrm{MOID}}$ is the matrix

$$\mathbf{A}_{\mathrm{MOID}}{}^{T}=$$

$$\begin{bmatrix}\frac{r_{\mathrm{MOID}}}{a}-\frac{3e\sin\theta_{\mathrm{MOID}}\sqrt{\mu_{\mathrm{Sun}}}\cdot\Delta t}{2\eta a^{\frac{3}{2}}} & -\frac{3r_{\mathrm{MOID}}\sqrt{\mu_{\mathrm{Sun}}}}{2\eta^{3}a^{\frac{5}{2}}}\left(1+e\cos\theta_{\mathrm{MOID}}\right)^{2}\Delta t & 0\\ -a\cos\theta_{\mathrm{MOID}} & \frac{r_{\mathrm{MOID}}\sin\theta_{\mathrm{MOID}}}{\eta^{2}}\left(2+e\cos\theta_{\mathrm{MOID}}\right) & 0\\ 0 & 0 & r_{\mathrm{MOID}}\sin\theta^{*}{}_{\mathrm{MOID}}\\ 0 & r_{\mathrm{MOID}}\cos i & -r_{\mathrm{MOID}}\cos\theta^{*}{}_{\mathrm{MOID}}\sin i\\ 0 & r_{\mathrm{MOID}} & 0\\ \frac{ae\sin\theta_{\mathrm{MOID}}}{\eta} & \frac{r_{\mathrm{MOID}}}{\eta^{3}}\left(1+e\cos\theta_{\mathrm{MOID}}\right)^{2} & 0\end{bmatrix}\quad(2.9)$$

and $\mathbf{G}_{d}$ is the matrix

$$\mathbf{G}_{d}=\begin{bmatrix}\frac{2a^{2}v_{d}}{\mu_{\mathrm{Sun}}} & 0 & 0\\ \frac{2\left(e+\cos\theta_{d}\right)}{v_{d}} & -\frac{r_{d}}{av_{d}}\sin\theta_{d} & 0\\ 0 & 0 & \frac{r_{d}\cos\theta_{d}^{*}}{h}\\ 0 & 0 & \frac{r_{d}\sin\theta_{d}^{*}}{h\sin i}\\ \frac{2\sin\theta_{d}}{ev_{d}} & \frac{2e+\frac{r_{d}}{a}\cos\theta_{d}}{ev_{d}} & -\frac{r_{d}\sin\theta_{d}^{*}\cos i}{h\sin i}\\ -\frac{b}{eav_{d}}2\left(1+\frac{e^{2}r_{d}}{p}\right)\sin\theta_{d} & -\frac{b}{eav_{d}}\frac{r_{d}}{a}\cos\theta_{d} & 0\end{bmatrix}\quad(2.10)$$

The subscript indices, MOID and *d*, indicate that the matrices are calculated respectively at t_{MOID} and t_d. As suggested by Conway [70], in order to maximise

$$\left\|\delta\mathbf{r}\left(t_{\mathrm{MOID}}\right)\right\| = \max\left(\boldsymbol{\Phi}\delta\mathbf{v}\left(t_d\right)\right) \tag{2.11}$$

the associated quadratic form $\delta\mathbf{v}\left(t_d\right)^T\boldsymbol{\Phi}^T\boldsymbol{\Phi}\delta\mathbf{v}\left(t_d\right)$ has to be maximised by choosing an impulse vector $\delta\mathbf{v}\left(t_d\right)$ parallel to the eigenvector $\mathbf{v}$ of $\boldsymbol{\Phi}^T\boldsymbol{\Phi}$, conjugated to the maximum eigenvalue of $\boldsymbol{\Phi}^T\boldsymbol{\Phi}$. Figure 2.2a and 2.2b represent the components of the optimal impulse unit vector $\delta\hat{\mathbf{v}}_{opt}\left(t_d\right)$, projected onto the $\{t,n,h\}$ reference frame (where $\hat{\mathbf{t}}$ is along the direction of motion, $\hat{\mathbf{h}}$ is the direction of the angular momentum, and $\hat{\mathbf{n}}$ is the component normal to the motion, in the orbital plane), as a function of the time-to-MOID Δt expressed as a multiple of the NEO orbital period T_{NEO}. The out-of-plane component *h* of $\delta\hat{\mathbf{v}}_{opt}$ is not shown since it is always less than 10^{-15}. The components of the $\delta\hat{\mathbf{v}}_{opt}\left(t_d\right)$ are shown for asteroid 2000SG344 with small eccentricity and inclination ($e = 0.067$, $i = 0.11$ deg) and asteroid 1979XB, characterised by highly elliptical orbit ($e = 0.73$) and $i = 25.14$ deg. These two asteroids were selected as representative examples of NEOs' orbital parameters (in particular in terms of eccentricity and inclination). Note that the components of the optimal $\delta\mathbf{v}$ direction are represented in Figure 2.2 in terms of components of the unit eigenvector $\mathbf{v}$.

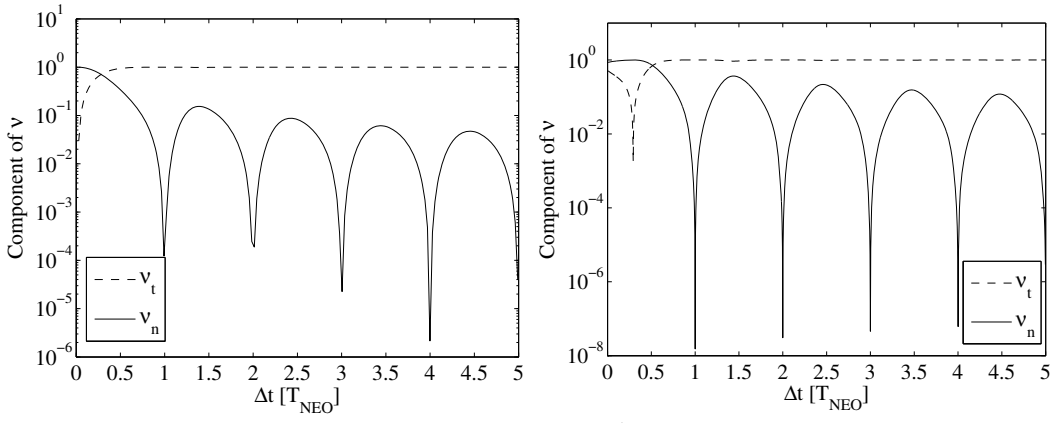

Figure 2.2: Components of the optimal δ*v* direction for a) asteroid 2000SG344 and b) asteroid 1979XB.

As a result of this analysis, we can infer that for a Δt smaller than a specific $\Delta t_{\mathrm{NEO}} < 1 T_{\mathrm{NEO}}$, which is different for every asteroid, the component perpendicular to the motion dominates the other two, whereas for larger Δt, the tangential component becomes dominant. This conclusion is in agreement with the preliminary analysis on the $\delta\mathbf{v}$ direction performed by Ahrens and Harris [67], the numerical verification by Park and Ross [72], and the mathematical demonstration provided by Conway [70]. It can be noted that the value of the normal component of the optimal deviation impulse goes to zero periodically, with a period equal to that of the asteroid. Therefore, a deviation impulse given in the normal direction yields no deviation after an exact number of revolutions. Figure 2.3a and 2.3b emphasise the optimality of the solution: the deviation obtained with $\|\delta\mathbf{v}\| = 0.07$ m/s was calculated, applying the manoeuvre along the optimal direction (solid line), and along the tangent direction (dotted line), the normal direction (dashed-dotted line), and the out-of-plane direction (dashed line). The deviation δr associated to $\delta\hat{\mathbf{v}}_{opt}$ is the maximum displacement and overlaps the deviation achieved with a normal impulse for low Δt, and the deviation obtained with a tangent manoeuvre for longer Δt. An impulsive action at the pericentre is found to be the most effective one, whereas a $\delta\mathbf{v}$ at the apocentre gives a deviation close to the minimum. In fact, the orbital velocity is higher at the pericentre; as a consequence, an impulsive manoeuvre will achieve a higher variation in semi-major axis [see first of Eqs. (2.2)] and hence in the mean motion. The choice of an optimum timing along the orbital period is more significant for highly eccentric orbits (see Figure 2.3b).

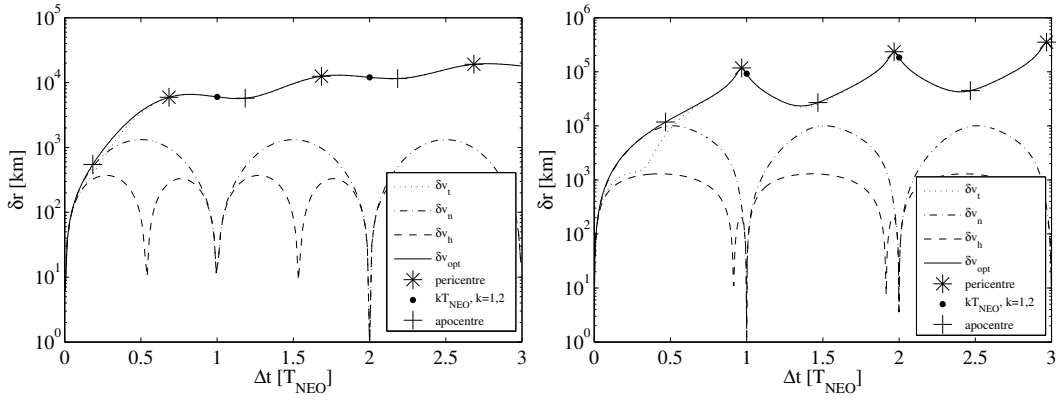

a) **b)**

Figure 2.3: Deviation achieved with ||δv||=0.07 m/s for a) asteroid 2000SG344 and b) asteroid 1979XB.

Although the direction of the optimal impulse is given by the maximisation of the quadratic form associated with the transition matrix, the sign of $\delta\mathbf{v}_{opt}$ at this point of the analysis is completely arbitrary. However, if we define the relative difference $e_{r,\delta\mathbf{v}\text{ direction}}$ between the deviation computed for $\delta\hat{\mathbf{v}}_{opt}$ and for $-\delta\hat{\mathbf{v}}_{opt}$, as

$$e_{r,\delta\mathbf{v}\text{ direction}} = \frac{\left\| \delta\mathbf{r}_{+\hat{\delta}\mathbf{v}_{opt}} - \delta\mathbf{r}_{-\hat{\delta}\mathbf{v}_{opt}} \right\|}{\left\| \delta\mathbf{r}_{-\hat{\delta}\mathbf{v}_{opt}} \right\|}$$

and we plot it as a function of the time-to-MOID (see Figure 2.4), we can conclude that the sign of $\delta\mathbf{v}_{opt}$ does not change the magnitude of the deviation. This can be alternatively demonstrated by changing the sign of $\delta\mathbf{v}$ in Eqs. (2.2). The variation of the orbital parameters is of opposite sign and, consequently, the displacement of the asteroid [described by Eqs. (2.1)] is also in the opposite direction but with the same magnitude. This result confirms the results obtained by Conway [70].

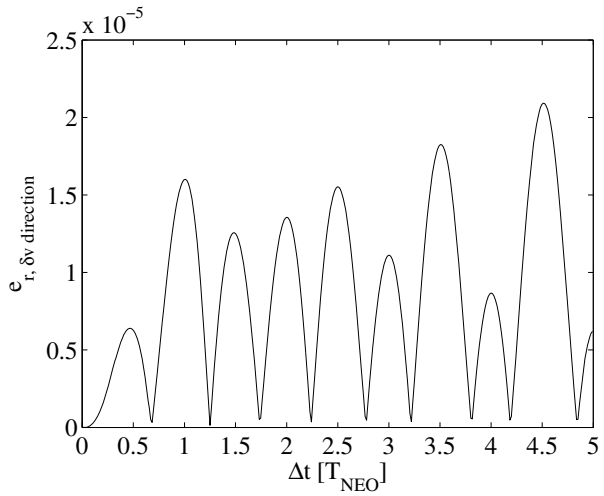

Figure 2.4: Relative error calculated by orbit propagation for asteroid 2000SG344.

2.1.2. Accuracy analysis

The accuracy of Eqs. (2.1) was assessed by numerically propagating forward in time the deviated orbit of the asteroid and comparing the obtained variation in the position vector with the one predicted by Eqs. (2.1). The nominal

trajectory was propagated from the deviation point up to the MOID, for a period up to 15 years, and the deviated trajectory was integrated† starting from the deviation point on the asteroid orbit, with the perturbed velocity vector $\mathbf{v}+\delta\mathbf{v}$. The two-body problem is used as model of the dynamics:

$$\begin{cases} \dfrac{d\mathbf{r}}{dt} = \mathbf{v} \\ \dfrac{d\mathbf{v}}{dt} = -\dfrac{\mu_{\text{Sun}}}{\|\mathbf{r}\|^3}\mathbf{r} \end{cases}$$

As a measure of accuracy, the relative error is computed, between the variation in position after numerical propagation and the analytically estimated deviation:

$$e_r = \frac{\left\|\delta\mathbf{r}_{\text{propagated}} - \delta\mathbf{r}_{\text{estimated}}\right\|}{\left\|\delta\mathbf{r}_{\text{propagated}}\right\|} \tag{2.12}$$

Figure 2.5 shows the relative errors, for asteroid 2000SG344 and for asteroid 1979XB, as a function of the time-to-MOID Δt and the magnitude of $\delta\mathbf{v}_{opt}$. These two asteroids, the former with $e<0.1$ and $i \ll 10$ deg, the latter with $e>0.1$ and $i>10$ deg, were chosen in order to study the impact of the orbital parameters on the relative error. Figure 2.6 reports the deviation value associated to the relative error in Figure 2.5.

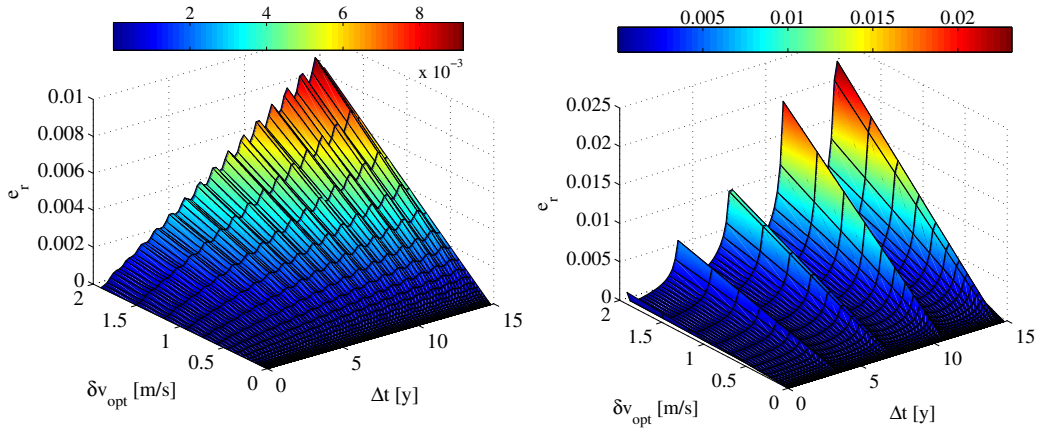

a) **b)**

Figure 2.5: Relative error for the deviation of a) asteroid 2000SG344 and b) asteroid 1979XB.

† An adaptive step-size Runge-Kutta-Fehlberg integration scheme integrator is used, with absolute tolerance of 1×10^{-12} and relative tolerance of 1×10^{-9}.

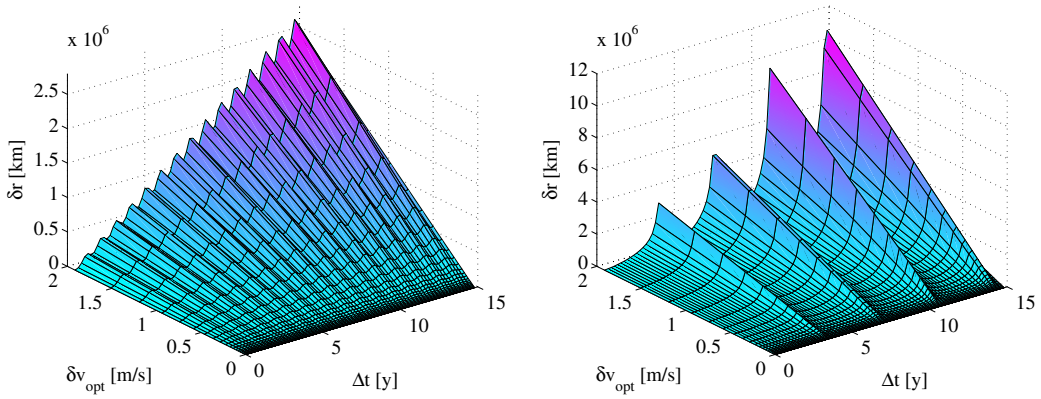

a) **b)**

Figure 2.6: Deviation of a) asteroid 2000SG344 and b) asteroid 1979XB.

For both asteroids, the relative error grows with the time-to-MOID and with $\|\delta \mathbf{v}_{opt}\|$, because the difference between the deviated orbit and the nominal orbit increases significantly and the proximal motion equations become inaccurate when describing the actual motion of the asteroid. In fact, as also stated by Schaub and Junkins [115], the hypotheses under which the equations were derived hold true until the relative orbit radius is small compared to the chief orbit radius. The difference in the maximum relative error between the two asteroids is remarkable. If we compute the maximum relative error (i.e. for $\Delta t \leq 15$ years and $\delta v = 2$ m/s) for a large number of asteroids characterised by different sets of orbital parameters, we can see (Figure 2.7) that its value increases as a function of the eccentricity of the orbit of the asteroid.

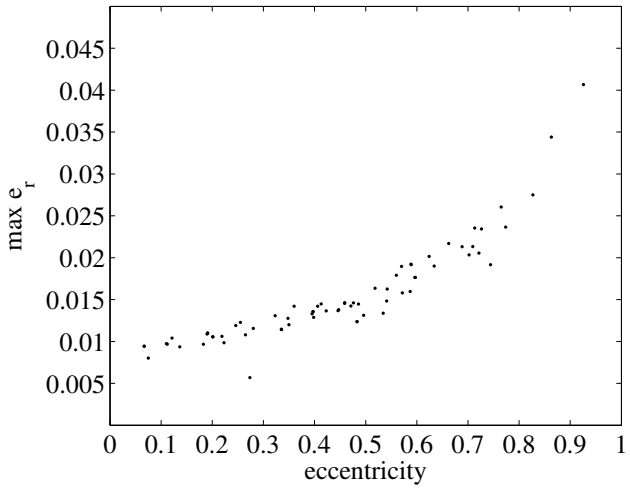

Figure 2.7: Maximum relative error for different asteroids.

2.1.3. Representation on the *b*-plane

To describe the motion of the NEO when entering the Earth's sphere of influence, the achieved deviation can be represented on the plane that is perpendicular to the incoming relative velocity of the small body at the planet arrival (i.e., the *b*-plane) [130]. We can define a local reference system centred on the Earth with the axis η perpendicular to the *b*-plane aligned along the unperturbed velocity of the asteroid relative to the Earth, the axis ζ along the direction opposite to the projection of the heliocentric velocity of the planet onto the *b*-plane, and the axis ξ that completes the reference system (see Figure 2.8a).

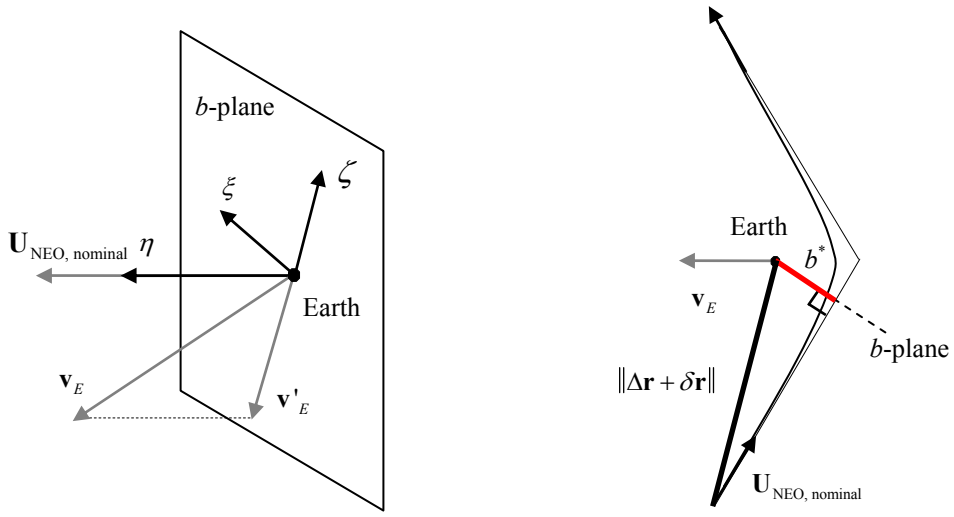

a) **b)**

Figure 2.8: Earth-centred local reference system: a) *b*-plane representation and b) geometry of hyperbolic passage.

The general transformation from the Cartesian to the *b*-plane reference frame is:

$$\mathbf{x}_{b\text{-plane}} = \left[\hat{\boldsymbol{\xi}} \quad \hat{\boldsymbol{\eta}} \quad \hat{\boldsymbol{\zeta}}\right]^T \mathbf{x}_{\text{Cartesian}} \tag{2.13}$$

where $\mathbf{x}$ is a generic vector and $\hat{\boldsymbol{\eta}}$, $\hat{\boldsymbol{\xi}}$, and $\hat{\boldsymbol{\zeta}}$ are column vectors that can be computed as

$$\hat{\boldsymbol{\eta}} = \frac{\mathbf{U}_{\text{NEO,nominal}}}{\left\|\mathbf{U}_{\text{NEO,nominal}}\right\|} \qquad \hat{\boldsymbol{\xi}} = \frac{\mathbf{v}_{\text{Earth}} \times \hat{\boldsymbol{\eta}}}{\left\|\mathbf{v}_{\text{Earth}} \times \hat{\boldsymbol{\eta}}\right\|} \qquad \hat{\boldsymbol{\zeta}} = \hat{\boldsymbol{\xi}} \times \hat{\boldsymbol{\eta}}$$

where $\mathbf{U}_{\mathrm{NEO,nominal}}$ is the unperturbed velocity of the asteroid relative to the Earth, expressed in a Cartesian reference frame, and $\mathbf{v}_{\mathrm{Earth}}$ is the heliocentric velocity of the Earth. The proper representation would be on the *instantaneous* *b*-plane, perpendicular to the *deviated* relative velocity of the asteroid; however, the maximum relative error between the plane perpendicular to the nominal relative velocity and the plane perpendicular to the perturbed relative velocity is around 0.01. Thus in the following, we will use the *b*-plane associated with the nominal relative velocity, which avoids the additional calculation of the velocity of the deflected asteroid. Moreover, for this analysis, the distance at the MOID was set to zero, to have the Earth at the origin of the reference system on the *b*-plane. To this aim, the phase θ and periapsis anomaly ω of the asteroids were modified to have $\Delta r = 0$. This will not change the result of this analysis, because the other geometric properties of the orbit are unchanged.

On the *b*-plane we can represent the distance b^* (called the impact parameter) from the Earth to the intercept of the asymptote of the hyperbola of the deviated orbit of the asteroid:

$$b^* = \sqrt{\xi^2 + \zeta^2}$$

Figure 2.9 shows the impact parameter (bold lines) for a highly elliptic asteroid (1979XB), together with the norm of the deviation $\delta\mathbf{r}$ (thin lines), by applying the deviation manoeuvre in the various directions analysed (i.e., tangential, normal, perpendicular-to-the-orbit-plane directions and optimal direction for the maximisation of the magnitude of the deviation). Although for a time-to-MOID Δt above a specific value, which is different for every asteroid (in the case of 1979XB, $\Delta t_{NEO} > 0.25 T_{NEO}$), the maximisation of the b^*-parameter and the maximisation of the deviation lead to the same conclusion on the optimal deflection strategy, for smaller Δt, the *b*-plane suggests a different strategy. This can be appreciated in Figure 2.10a, which contains a close-up of Figure 2.9 for $\Delta t < 1 T_{NEO}$.

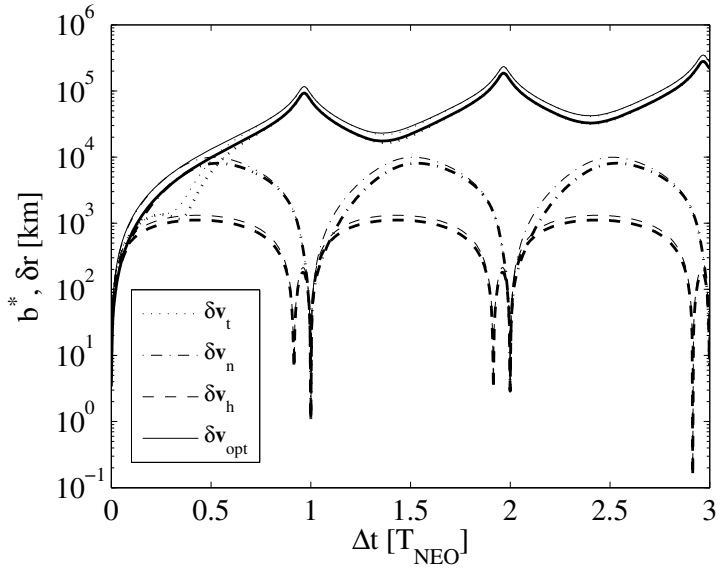

Figure 2.9: Impact parameter and magnitude of the deviation for 1979XB with δv = 0.07 m/s; b*-parameter (bold lines), and deviation (thin lines).

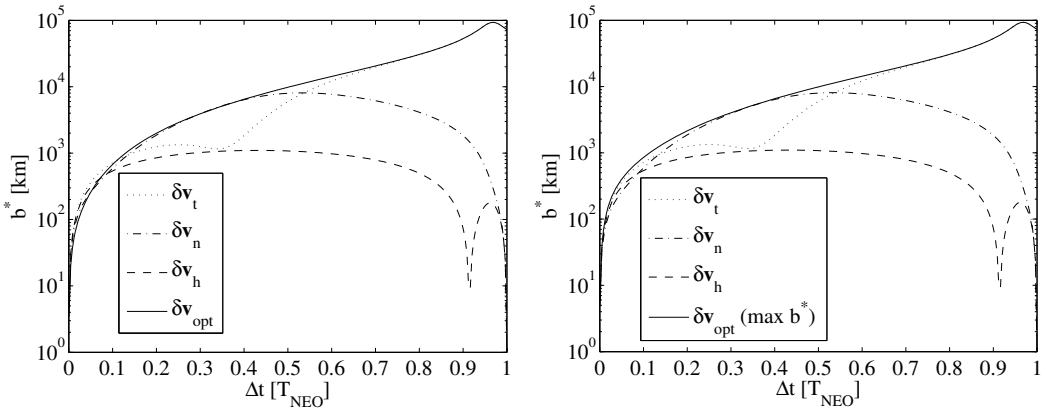

a) **b)**

Figure 2.10: Impact parameter for asteroid 1979XB Δt<1T_{NEO}: a) strategy of maximum deviation and b) strategy of maximum b*-parameter.

The difference between the two results depends on whether or not we consider the Earth to be at the MOID point when the asteroid crosses it.

The formulation of the maximisation problem in Eq. (2.11) is modified to maximise the projection of the deviation in the b-plane instead of the deviation δr. As we want to maximise only the two components of the deviation ξ and ζ, we have:

$$\mathbf{b}^* = \begin{Bmatrix} \xi \\ 0 \\ \zeta \end{Bmatrix} = \begin{bmatrix} 1 & 0 & 0 \\ 0 & 0 & 0 \\ 0 & 0 & 1 \end{bmatrix} \delta\mathbf{r}\left(t_{\mathrm{MOID}}\right)\Big|_{b\text{-plane}}$$

where $\delta\mathbf{r}\left(t_{\text{MOID}}\right)\big|_{b\text{-plane}}$ is the deviation vector $\delta\mathbf{r}\left(t_{\text{MOID}}\right)$ described in the *b*-plane reference frame, computed through the conversion matrix $\mathbf{R}$ [‡]:

$$\delta\mathbf{r}\left(t_{\text{MOID}}\right)\big|_{b\text{-plane}} = \mathbf{R}\boldsymbol{\Phi}\delta\mathbf{v}\left(t_d\right)$$

In this way the system in Eq. (2.8) is replaced by:

$$\mathbf{b}^* = \boldsymbol{\Phi}_{b^*}\delta\mathbf{v}\left(t_d\right) \tag{2.14}$$

with the transition matrix

$$\boldsymbol{\Phi}_{b^*} = \begin{bmatrix} 1 & 0 & 0 \\ 0 & 0 & 0 \\ 0 & 0 & 1 \end{bmatrix}\mathbf{R}\boldsymbol{\Phi}$$

Hence the maximisation of b^* is equivalent to maximising the quadratic form $\delta\mathbf{v}\left(t_d\right)^T\boldsymbol{\Phi}_{b^*}^T\boldsymbol{\Phi}_{b^*}\delta\mathbf{v}\left(t_d\right)$ associated to problem Eq. (2.14). Note that the maximisation problem can be solved even if the transition matrix $\boldsymbol{\Phi}_{b^*}$ is singular.

The result of the maximisation of b^* can be seen in Figure 2.10b. For example, for asteroid 1979XB, we can conclude from the *b*-plane analysis that the direction of the optimal impulse changes from the tangent direction to the normal

---

[‡] The matrix $\mathbf{R}$ converts the deviation vector $\delta\mathbf{r}\left(t_{\text{MOID}}\right)$ computed in the $\{r,\theta,h\}$ reference frame through Eq. (2.1) to the *b*-plane reference frame. Given a generic vector $\mathbf{x}$, the general transformation from $\{r,\theta,h\}$ to the Cartesian reference frame is:

$$\mathbf{x}_{\text{Cartesian}} = \begin{bmatrix}\hat{\mathbf{r}} & \hat{\boldsymbol{\theta}} & \hat{\mathbf{h}}\end{bmatrix}^T\mathbf{x}_{\{r,\theta,h\}}$$

where $\hat{\mathbf{r}}$, $\hat{\boldsymbol{\theta}}$, and $\hat{\mathbf{h}}$ are column vectors that can be computed as

$$\hat{\mathbf{r}} = \frac{\mathbf{r}}{\|\mathbf{r}\|} \qquad \hat{\mathbf{h}} = \frac{\mathbf{r}\times\mathbf{v}}{\|\mathbf{r}\times\mathbf{v}\|} \qquad \hat{\boldsymbol{\theta}} = \hat{\mathbf{h}}\times\hat{\mathbf{r}}$$

In this case $\mathbf{r}$ and $\mathbf{v}$ are respectively the nominal position and velocity of the NEO at the MOID. The general transformation from Cartesian to *b*-plane reference frame is reported in Eq. (2.13). Hence the transformation from $\{r,\theta,h\}$ to the *b*-plane reference frame is:

$$\mathbf{x}_{b\text{-plane}} = \mathbf{R}\,\mathbf{x}_{\{r,\theta,h\}}$$

$$\mathbf{R} = \begin{bmatrix}\hat{\boldsymbol{\xi}} & \hat{\boldsymbol{\eta}} & \hat{\boldsymbol{\zeta}}\end{bmatrix}^T\begin{bmatrix}\hat{\mathbf{r}} & \hat{\boldsymbol{\theta}} & \hat{\mathbf{h}}\end{bmatrix}^T$$

to the motion at $\Delta t \cong 0.15 T_{\mathrm{NEO}}$, whereas for $\Delta t > 0.55 T_{\mathrm{NEO}}$, the tangential component dominates.

In Figure 2.11 the result for the δr-maximisation strategy (thin line) is compared whit that for the b^*-maximisation strategy (bold line), for asteroid 2000SG344 in the range $\Delta t < 0.5 T_{\mathrm{NEO}}$. The maximisation of the impact parameter would lead to choose the *h* direction strategy for very small Δt, the *n* direction for a range of $0.15 T_{\mathrm{NEO}} < \Delta t < 0.25 T_{\mathrm{NEO}}$, and the tangential direction for higher Δt. Note that for small Δt, the angle of the optimal impulse changes, depending on the orbital parameters of the asteroid, but for higher Δt, the optimal strategy is always along the direction of motion.

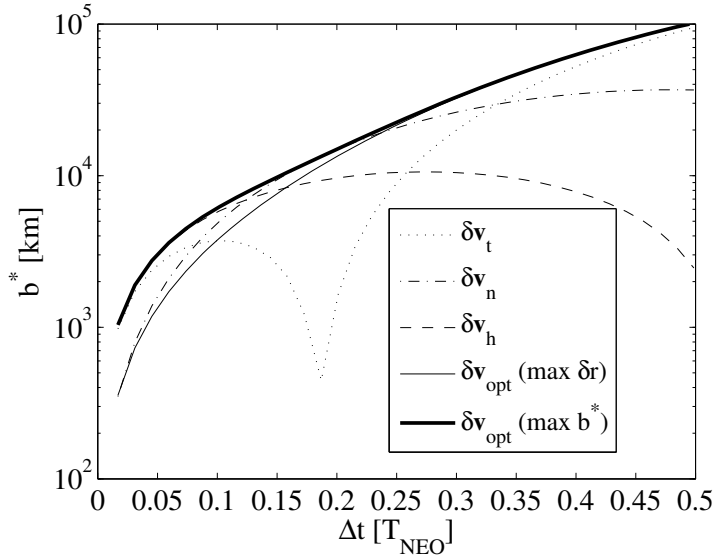

Figure 2.11: Impact parameter for asteroid 2000SG344 $\Delta t<0.5T_{NEO}$. Strategy of maximum deviation (solid line) and maximum *b-parameter (bold line).**

Three-body analysis

The results obtained with the *b*-plane formulation imply an increase of the $\delta \mathbf{v}$-requirement due to the gravitational effects of the Earth, which is consistent with the results found by Ross et al. [73]. Furthermore, they suggest a different optimal strategy for short times-to-MOID. We can verify the reliability of these results by propagating the motion of the asteroid after the deflection manoeuvre for two different cases: the optimal deflection manoeuvre is computed as the result of the maximisation of the deviation, and the optimal deflection manoeuvre

is computed as the result of the maximisation of the b*-parameter. A full three-body dynamic model was used, considering the Sun and the Earth as gravitational bodies:

$$\begin{cases} \dfrac{d\mathbf{r}}{dt} = \mathbf{v} \\ \dfrac{d\mathbf{v}}{dt} = -\dfrac{\mu_{\text{Sun}}}{\|\mathbf{r}\|^3}\mathbf{r} - \mu_{\text{Earth}}\left(\dfrac{\mathbf{r}_{\text{Earth-NEO}}}{\|\mathbf{r}_{\text{Earth-NEO}}\|^3} + \dfrac{\mathbf{r}_{\text{Sun-Earth}}}{\|\mathbf{r}_{\text{Sun-Earth}}\|^3}\right) \end{cases}$$

where μ_{Sun} and μ_{Earth} are respectively the Sun and Earth gravitational constant. $\mathbf{r}$ is the position vector with respect to the Sun inertial reference frame, $\mathbf{r}_{\text{Sun-Earth}}$ is the position vector of the Earth in a Sun-centred inertial reference frame and $\mathbf{r}_{\text{Earth-NEO}}$ is

$$\mathbf{r}_{\text{Earth-NEO}} = \mathbf{r} - \mathbf{r}_{\text{Sun-Earth}}$$

The trajectory was propagated, after a 2 m/s impulse, over the interval $I_p = \left[t_d \quad t_{\text{MOID}} + 0.1T_{\text{NEO}}\right]$; then, the closest point to the Earth was computed as follows, with nonlinear programming techniques:

$$\delta r_{\min,3b} = \min_{t \in I_p} \left\|\mathbf{r}_{\text{Earth}}(t) - \mathbf{r}_{\text{NEO}}(t)\right\| \tag{2.15}$$

As can be seen in Figure 2.12a, a deflection manoeuvre computed maximising the deviation is not an optimal strategy for short times-to-MOID, whereas the one computed maximising the b^*-parameter (see Figure 2.12b) leads to better results. Note that this is true for short times-to-MOID, whereas for longer times the two strategies are equivalent. With both strategies, the projection of the deviation on the b-plane (bold line) is a reliable estimation of the actual deviation computed with the three-body model (thin line). The deviation at the MOID, considering the two-body dynamics (dashed line) instead, does not accurately predict the actual minimum distance from the asteroid in proximity of the Earth. The results of the maximisation of the b^*-parameter and the maximisation of the deviation can be

compared also in Figure 2.13 that represents the projection of the deviation on the b-plane and $\delta r_{\min,3b}$ for the two strategies.

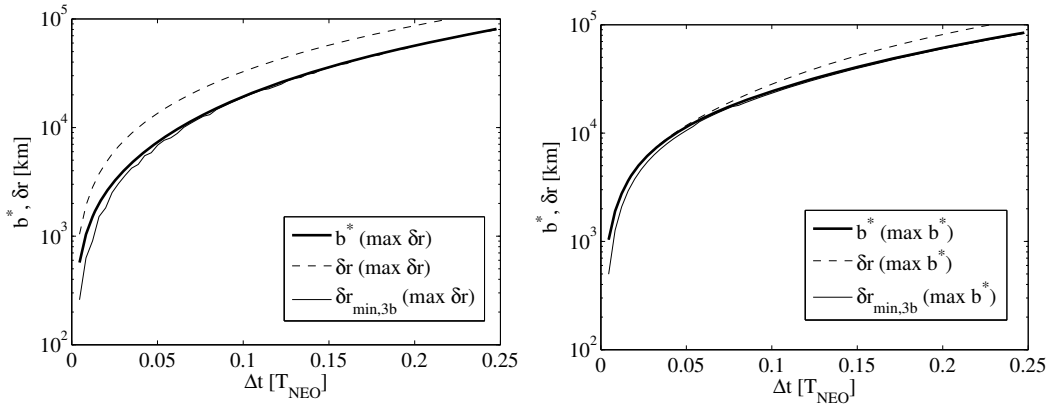

a) **b)**

Figure 2.12: Deviation (dashed line) and its projection (bold line) on the *b*-plane calculated through the two-body problem and minimum deviation computed through the three-body problem (continuous thin line): a) maximum deviation strategy for asteroid 1979XB and b) maximum *b-parameter strategy for asteroid 1979XB.**

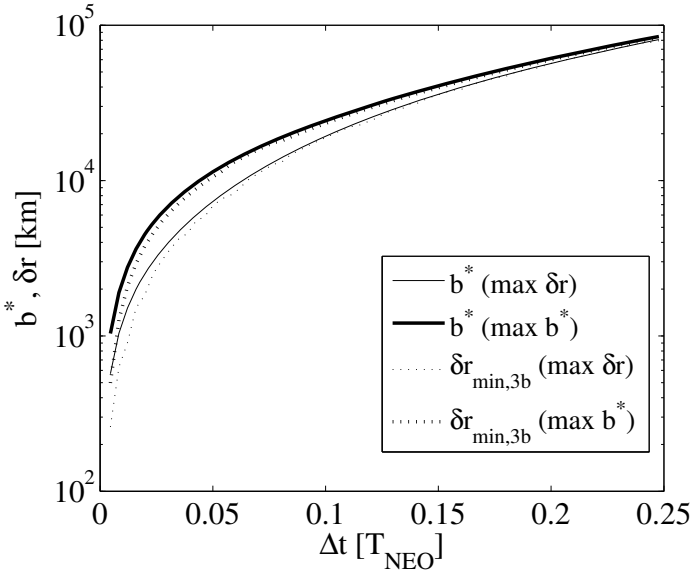

Figure 2.13: Projection of the deviation (continuous line) on the *b*-plane calculated through the two-body problem and minimum deviation computed through the three-body problem (dashed line) for asteroid 1979XB. The bold lines represent the results of the maximum-b* strategy, the thin lines represent the result for the maximum-deviation strategy.

Analysis of the deviation components in the *b*-plane

Figure 2.14 shows the components of the deviation in the *b*-plane as a function of the time-to-MOID, when the optimal strategy is computed by maximising b^*. In the same figure, $t_{\delta r_{\min,3b}}$ is the time corresponding to $\delta r_{\min,3b}$, defined in Eq. (2.15); $t_{\delta r_{\min,3b}} - t_{\mathrm{MOID}}$ represents the difference between the instant when the actual minimum distance from the Earth is reached and the expected time at the unperturbed MOID. This quantity is expressed in days, multiplied by 10^6 to make it comparable in scale with the components of the deviation.

The components of the deviation projected onto the *b*-plane have a discontinuity corresponding to the discontinuity in $t_{\delta r_{\min,3b}} - t_{\mathrm{MOID}}$. In particular when $t_{\delta r_{\min,3b}} - t_{\mathrm{MOID}} > 0$, we have $\eta < 0$; this means that the asteroid at t_{MOID} has not intersected the *b*-plane yet (the component normal to it is negative). This situation is depicted in Figure 2.15a, in which point A represents the asteroid approaching a fly-by of the Earth. When $t_{\delta r_{\min,3b}} - t_{\mathrm{MOID}} < 0$, then $\eta > 0$; this means that the asteroid at t_{MOID} has already intersected the *b*-plane (the component normal to it is positive). This situation is depicted in Figure 2.15b, in which the point B represents the asteroid after the fly-by.

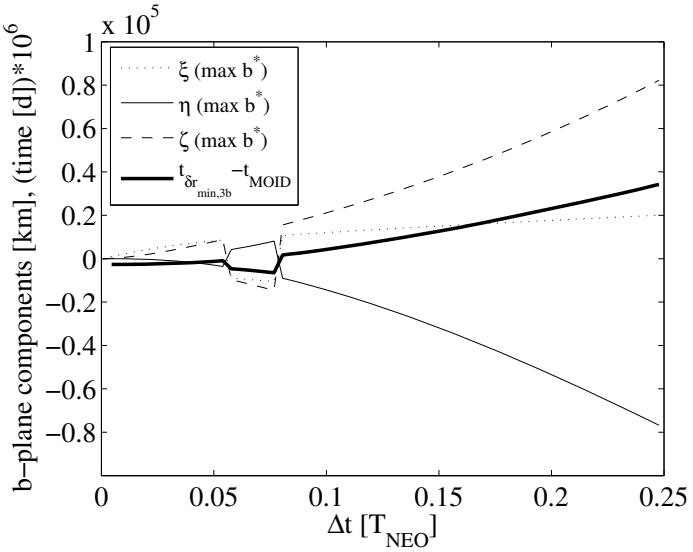

Figure 2.14: Components of the deviation in the *b*-plane for asteroid 1979XB.

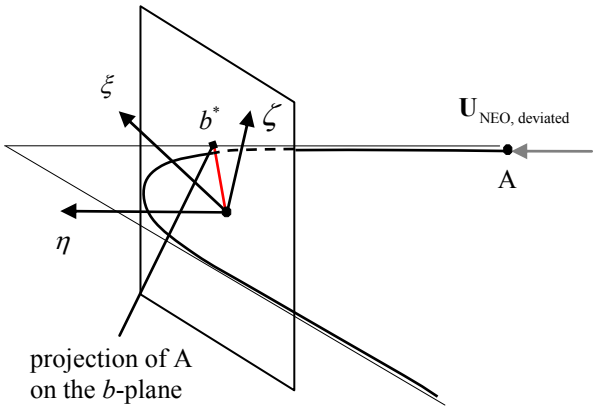

a) The asteroid is approaching the fly-by of the Earth.

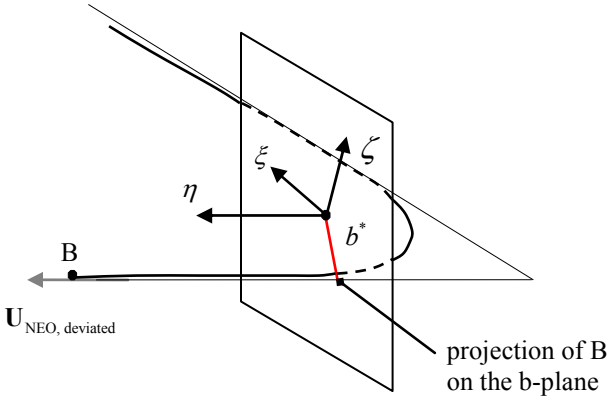

b) The asteroid is at the end of the fly-by of the Earth.
Figure 2.15: Fly-by representation in the *b*-plane reference system. a) case A: the asteroid is approaching the fly-by of the Earth and b) case B: the asteroid is at the end of the fly-by.

The two situations described in Figure 2.15 are a consequence of the sign of the impulsive manoeuvre $\delta\mathbf{v}_{opt}$ obtained from problem (2.8). In fact, for a $+\delta\mathbf{v}$ along the motion, the period of the asteroid is increased; hence at t_{MOID} the asteroid is at point A in Figure 2.15a. On the other hand, for a $-\delta\mathbf{v}$ along the motion, the period of the asteroid is decreased; hence at t_{MOID} the asteroid is at point B in Figure 2.15b. The choice of $+\delta\mathbf{v}$ or $-\delta\mathbf{v}$, which corresponds to case A or B, will lead the asteroid in its subsequent course (i.e., after t_{MOID}) to pass closer or farther from the Earth[§].

The analysis on the *b*-plane demonstrates that, assuming no gravity of the Earth, the b^*-parameter is the correct estimate of the minimum intersection

[§] The switching of $t_{\delta r_{\min,3b}} - t_{\mathrm{MOID}}$ and the components on the *b*-plane in Figure 2.14 is due to the fact that the direction of $\delta\mathbf{v}$ is not univocally determined by the solution of the b^*-maximisation problem.

distance between the asteroid and the Earth. Therefore, in the general case, when the nominal unperturbed MOID is not zero, the total deviation $\|\Delta\mathbf{r} + \delta\mathbf{r}\|$ has to be projected on the *b*-plane. If the Earth's gravity is included in the calculations, the computation of the pericentre of the hyperbolic trajectory (the actual minimum distance from the Earth) can be derived from the b^*-parameter [73]. The minimum distance will occur at an instant of time that precedes or follows the time of the unperturbed MOID passage, whether the deflection action decelerates or accelerates the asteroid ($+\delta\mathbf{v}$ or $-\delta\mathbf{v}$).

Figure 2.16 represents the projection on the *b*-plane of the deviated points for different values of Δt for the deflection of asteroid 2000SG344 (left) and asteroid 1979XB (right). The deviation was calculated by applying the impulsive manoeuvre along the tangent to the motion (Figure 2.16a), the normal (Figure 2.16b) and the out-of-plane directions (Figure 2.16c) respectively. It can be noted that an impulse along the tangent direction produces a substantial variation of the ζ component, with a secular and a periodic term and a small periodic variation of the ξ component. An impulse in the normal direction instead produces a purely periodic variation of both components. To better appreciate Figure 2.16, it is useful to remind a property of Öpik theory [130]: it decouples the two key parameters associated with a planetary encounter, the shift in time and the MOID. As demonstrated by Bourdoux and Izzo, the ξ-component represents the shortest distance between the Earth and the asteroid (hence it is strictly related to the geometrical variation of the MOID), whereas the ζ-component is a measure of the time shift between the asteroid and the Earth passage at the MOID [131]. The difference in the three strategies can be appreciated in Figure 2.17a (asteroid 2000SG344) and Figure 2.17b (asteroid 1979XB), which represent the evolution of the two components in the *b*-plane along the time axis.

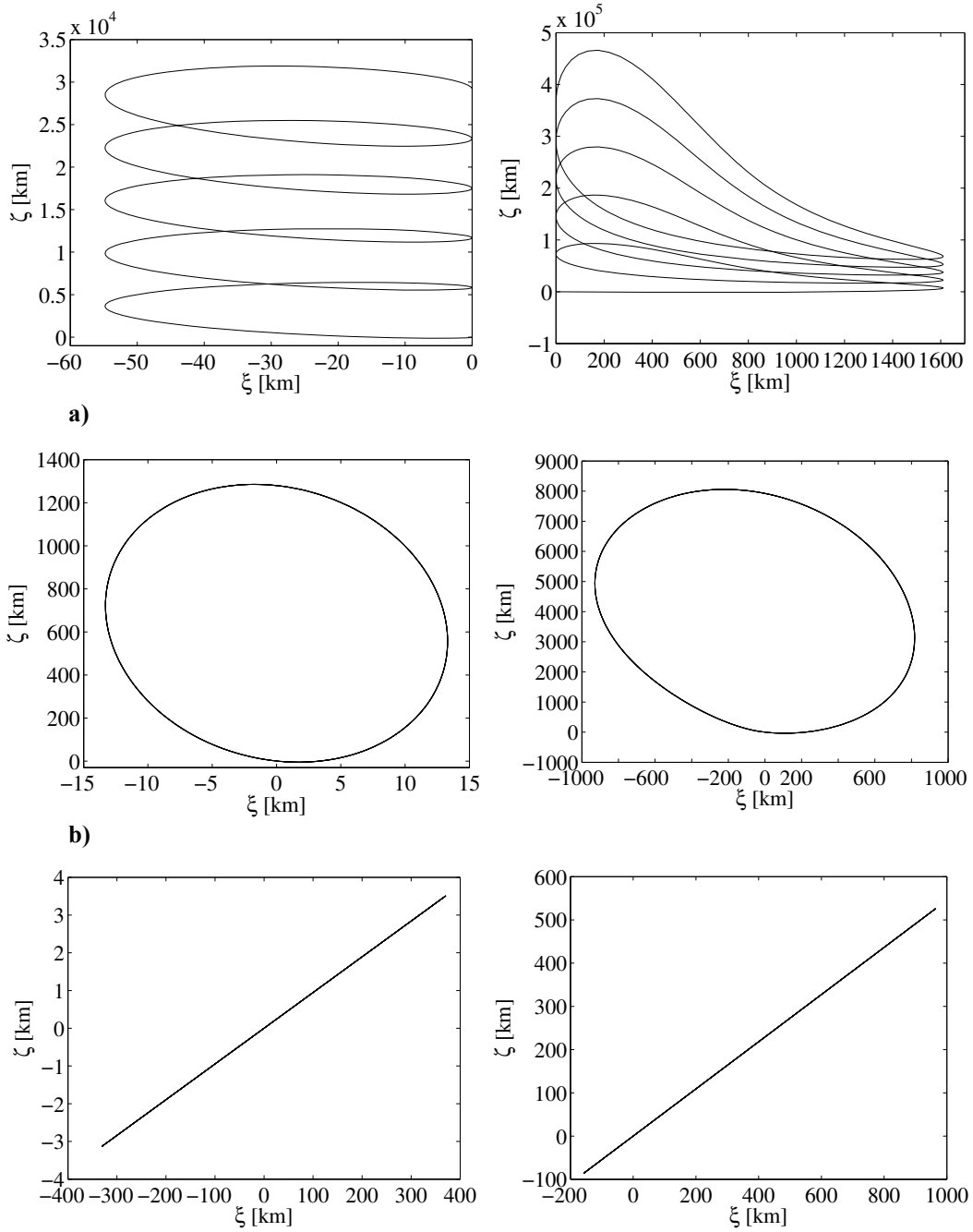

Figure 2.16: Projection on the *b*-plane of the deviation for asteroid 2000SG344 (left) and asteroid 1979XB (right) with δv = 0.07 m/s applied a) along the tangent to the motion, b) along the normal to the motion, and c) along the *h*-direction.

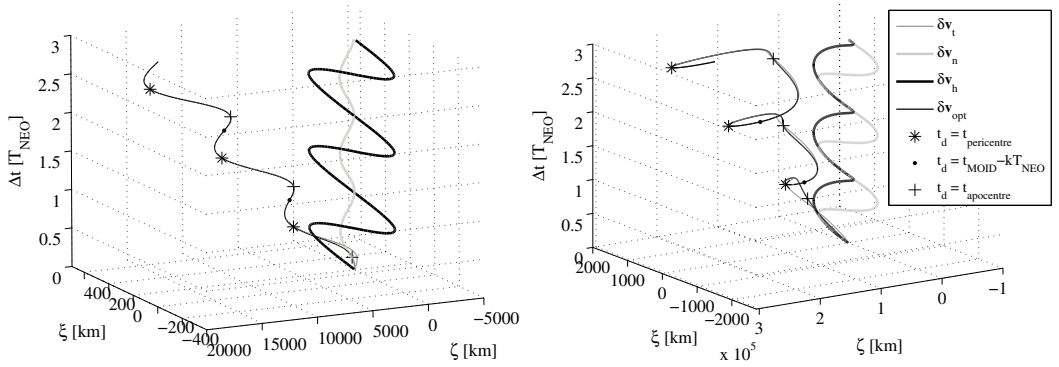

a) **b)**

Figure 2.17: Projection on the *b*-plane, function of Δ*t* for a) asteroid 2000SG344 and b) asteroid 1979XB.

Figure 2.18 shows the result of a deflection action along the three directions and in the optimal direction for a low-eccentric orbit (asteroid 2000SG344) and a highly elliptical orbit (asteroid 1979XB). It can be noted that for highly elliptical orbits, such as asteroid 1979XB (see Figure 2.18b), the best results are achieved if the impulse is given at the pericentre of the orbit. A $\delta\mathbf{v}$ at the apocentre on the other hand is almost the less efficient action, because it changes ξ (related to the MOID) but not ζ. Note that by acting *k* orbital periods before the time at the MOID (where *k* is an integer number), the deviation component along ξ is zero. For an orbit with a low eccentricity (see Figure 2.18a), a deviation manoeuvre at the pericentre is still the most efficient, though it does not maximise ζ.

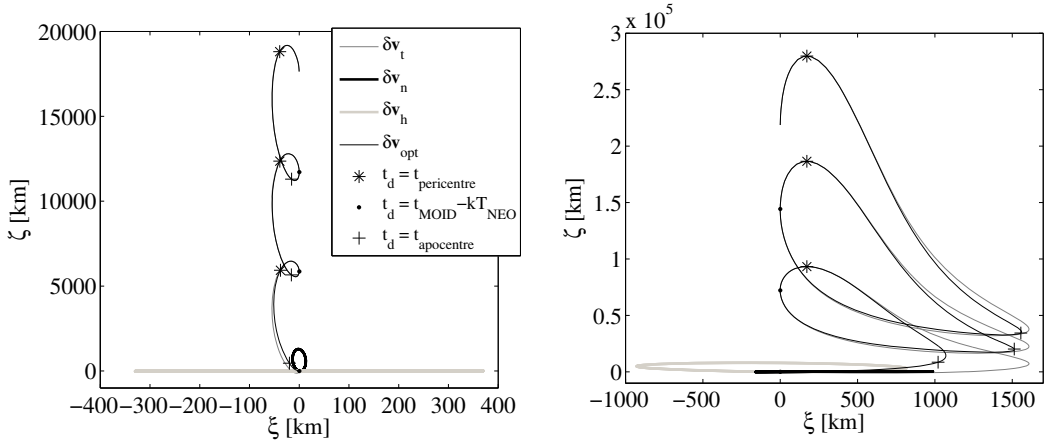

a) **b)**

Figure 2.18: Projection on the *b*-plane of the deviation. δv = 0.07 m/s applied along the optimal (normal line), the tangent to the motion (dark grey normal line), the normal to the motion (black bold line), and the *h* (light grey bold line) directions for a) asteroid 2000SG344 and b) asteroid 1979XB.

Analysis on the uncertainties on the impulsive manoeuvre

An analysis on the uncertainties due to a possible error in the impulsive manoeuvre magnitude and direction can be performed, exploiting the representation on the *b*-plane. The deviation was calculated for increasing values of time-to-MOID Δt, by applying an impulsive manoeuvre along the tangential direction and assuming an error on the direction and the magnitude of the $\delta\mathbf{v}$. A normal distribution was used to model the three component of $\delta\mathbf{v} = \begin{bmatrix} \delta v_t & \delta v_n & \delta v_h \end{bmatrix}^T$, characterised by a mean value δv_{mean} of:

$$\begin{aligned} \delta v_{t,\,\text{mean}} &= 0.07\,\text{m/s} \\ \delta v_{n,\,\text{mean}} &= 0\,\text{m/s} \\ \delta v_{h,\,\text{mean}} &= 0\,\text{m/s} \end{aligned}$$

The analysis was performed with two different values of standard deviation (in each case taken equal for all the three components). Figure 2.19 shows the distribution of the components of $\delta\mathbf{v}$, with a standard deviation equivalent to $3\sigma = \delta v_{t,\,\text{mean}} / 100$ and Figure 2.20 represents the projection of the consequent deviation on the *b*-plane. To the deviation achieved with $\delta v_t = 0.07$ m/s (also represented in Figure 2.18), the projection of the deflection considering an uncertainty on the $\delta\mathbf{v}$ is superimposed. For each nominal point, corresponding to a certain Δt, the shape of the uncertainty region (shape in colour magenta) assumes a roughly elliptical shape, which changes and rotates depending on the value of the time-to-MOID. Figure 2.21 and Figure 2.22 contain the $\delta\mathbf{v}$ distribution and the corresponding projection of the deviation, assuming a standard deviation equivalent to $3\sigma = \delta v_{t,\,\text{mean}} / 10$.

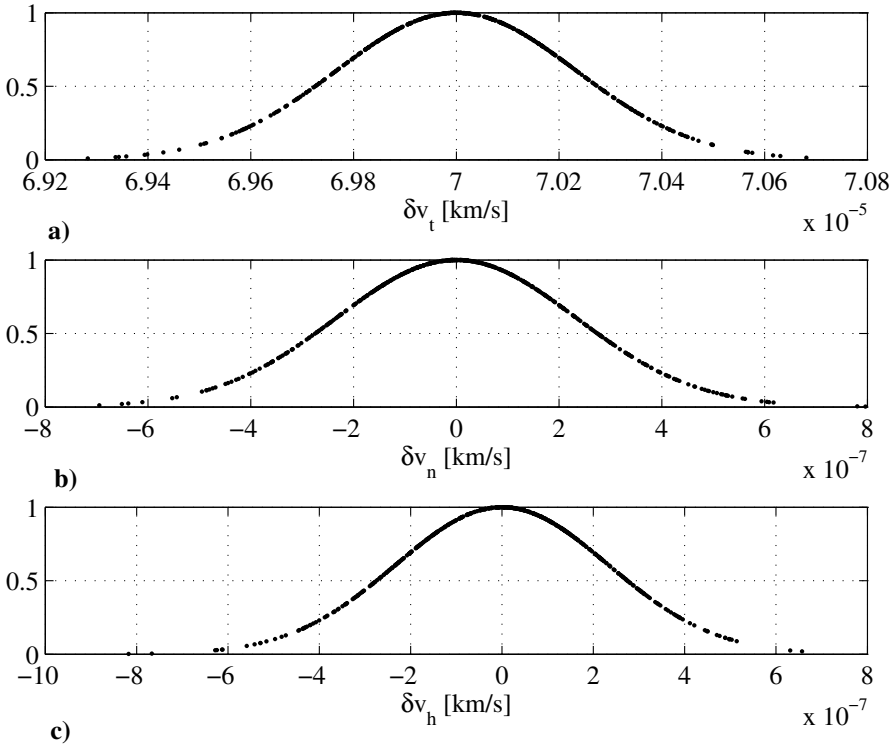

Figure 2.19: Distribution of the components of δv, represented through the Gaussian membership function, with 3σ = $\delta v_{t,\ mean}$/100. a) Tangential component, b) normal component, and c) component along the *h* direction.

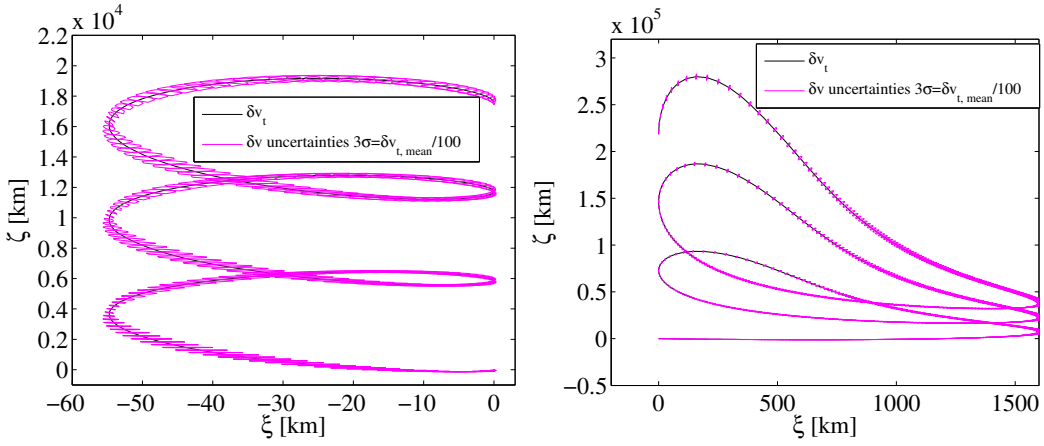

Figure 2.20: Projection on the *b*-plane of the deviation. $\delta v_{t,\ mean}$ = 0.07 m/s applied along the tangent direction with 3σ = $\delta v_{t,\ mean}$/100 for a) asteroid 2000SG344 and b) asteroid 1979XB.

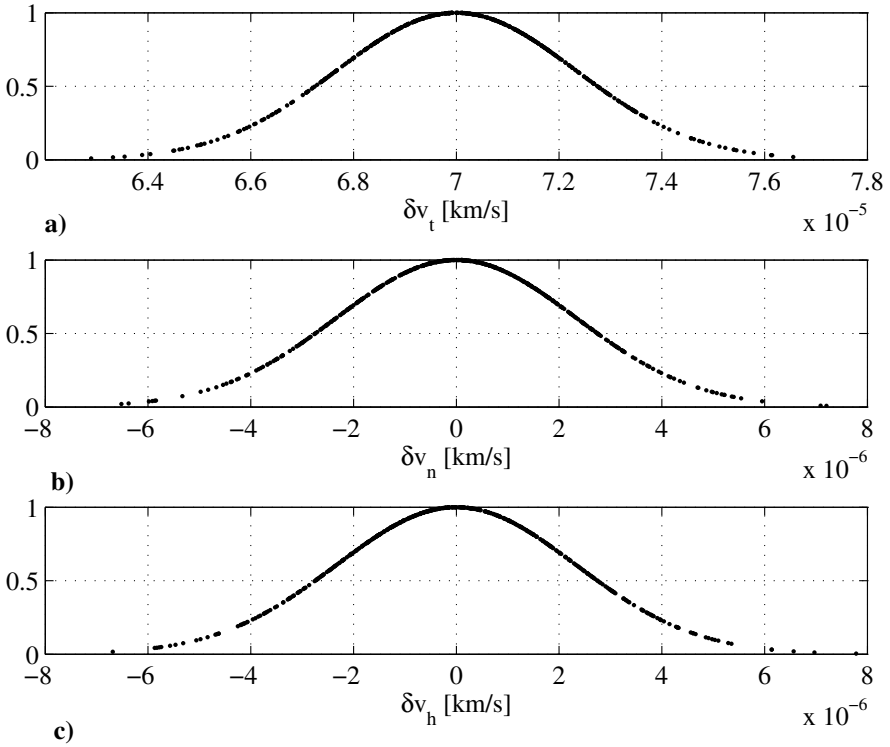

Figure 2.21: Distribution of the components of δv, represented through the Gaussian membership function, with $3\sigma = \delta v_{t,\,mean}/10$. a) Tangential component, b) normal component, and c) component along the *h* direction.

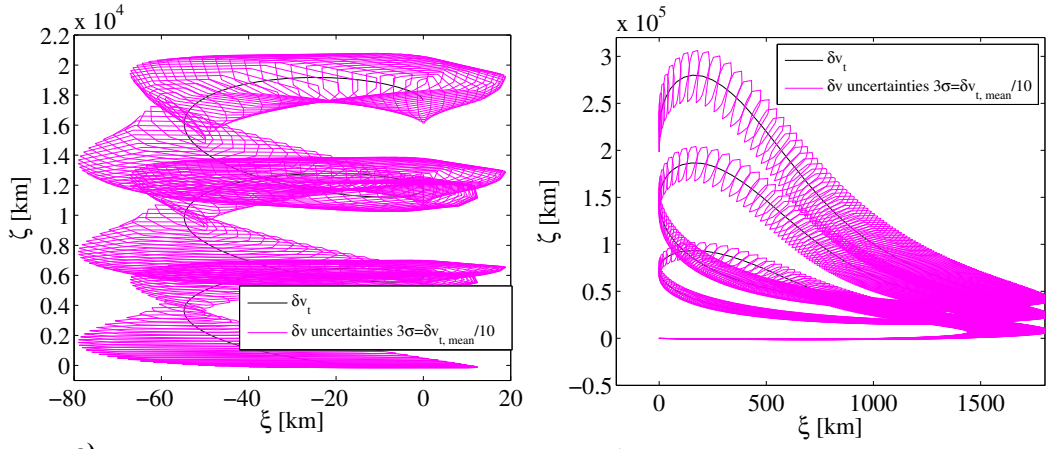

a) b)

Figure 2.22: Projection on the *b*-plane of the deviation. $\delta v_{t,\,mean}$ = 0.07 m/s applied along the tangent direction with $3\sigma = \delta v_{t,\,mean}/10$ for a) asteroid 2000SG344 and b) asteroid 1979XB.

2.2. Mission options for impulsive deviation

In the following section, we focus the attention on the analysis of optimal impact strategies for the deflection of NEOs. Among the different prevention strategies considered against a potential hazardous object in collision route with the Earth, the simplest one is the kinetic impact. In fact, as will be shown, effective kinetic impacts resulting in a variation of the MOID of thousand of kilometres seem to be already achievable with the current launch and spacecraft capabilities, provided that the time difference between the momentum change and the potential Earth impact is large enough.

The ideal optimal deflection conditions, derived in Section 2.1.1, cannot always be achieved, because the transfer trajectory to the asteroid must be included in the design of a generic mitigation mission. The analytical formulation of the maximum deviation problem can be used to find a wide range of launch opportunities. A wide number of target NEOs was selected for this analysis. The idea is to explore, for each one of them, a wide interval of launch dates and transfer times and to collect all the solutions that maximise the deviation and minimise the warning time.

It was decided to look only for mission options with a relatively low transfer time; therefore, only direct transfers and transfers with one single swing-by of Venus are considered. Longer sequences of swing-bys, though improving the deviation, would imply a longer term planning and more complex operations.

2.2.1. Targets selection

Potentially Hazardous Asteroids, a subclass of NEOs, are defined based on parameters that measure the asteroid's potential to make dangerously close approaches to Earth. Different research groups in the world keep updated databases [such as the Sentry system [12] at the Jet Propulsion Laboratory (JPL) or the Near Earth Objects Dynamic Site (NEODyS) [13] at the research centre in Pisa, Italy] that continuously asses the risk posed by these objects. As more ground-based observations become available a more accurate determination of the PHAs orbits will be performed and, as a consequence, some of the asteroids might be removed from the possible-impact-risks list. However, looking at the current

estimate for potential impacts through the next century, there are still a few objects whose impact probability is not negligible in statistical terms.

Table 2.1 shows an extract of 30 objects taken from the JPL catalogue of asteroids[**], with the exception of 2004VD17, which, although foreseen to have its closest approach with the Earth in the years 2102–2104, is currently considered as the most dangerous objects in terms of impact probability, due to its large size relative to the other PHAs listed. Table 2.1 lists the asteroids and their properties, used in the analysis. For simplicity, each asteroid is given a local reference number (instead of using the formal names or international *Id* numbers). The semi-major axis a is given in astronomical units; the inclination i, argument of the ascending node Ω, anomaly of the pericentre ω, and mean motion M are in degrees; the estimated mass is in kilograms, and the epoch is given in Modified Julian Days (MJD). The list considered contains some bodies that have recently become objects of interest for the scientific community: Apophis, 2004VD17, and 2005WY5 are, in fact, reported in the JPL catalogue of the most recently observed objects as the currently most risky, having a Palermo scale [15] ranging between -0.57 and -2.61[††]. Some of the objects in the list are among those not recently observed or even lost, which is a major issue in the current assessment of their risk. Because of the limited capabilities of ground-based observation and limited available resources, most of the hazardous objects can be lost for several years, resulting in the possibility that when new observations of the objects are available again, they could definitely rule out the possibility of an impact or actually turn out to have an increased impact probability, with the additional drawback of a reduced warning time.

The rationale behind the selection presented in Table 2.1 is twofold. We are interested in providing some general considerations on optimal impact trajectories and consequent deviations strategies, and for this reason, we surveyed a set of potential dangerous objects presenting a large variety of orbital and physical characteristics. As can be noticed from Table 2.1, our selection collects objects having semi-major axes ranging between 0.85 and 3 AU, eccentricity as high as 0.92 and orbital inclination up to 28 deg, with estimated masses in a range

[**] Data available online at http://neo.jpl.nasa.gov/risk/ [Retrieved 13 March 2008].
[††] Value from http://neo.jpl.nasa.gov/risk/ [Retrieved 13 March 2008].

between 10^7 and 10^{12} kg. Such substantial differences in both orbital elements and mass will eventually affect the optimal impact and deflection strategy. At the same time, we want to look at some actual sample cases, considering real objects which currently have quite a high impact probability (usually indicated in terms of Palermo scale), to provide a worst-case assessment of the current and short-term future capabilities of deflecting hazardous objects such as Apophis or 2004VD17 if such an unlikely, but highly disastrous, event should ever be faced by our society. The MOID Δr was calculated using the Earth's ephemerides on the 1st of January 2000 at 12:00 hrs (0 MJD since 2000). As a consequence of this approximation, the MOID of asteroid 1997XR2 is less than the Earth's radius. The actual MOID varies with time [132], due to the actual orbit of both the Earth and the asteroid; furthermore, a MOID smaller than the radius of the Earth does not imply an imminent impact, because the Earth and the asteroid could not be at the MOID at the same time. Note that, the aim of this work is not to reproduce a realistic impact scenario, but rather to assess the actual achievable deviation, as opposed to the theoretical deviation, derived in the Section 2.1, depending on the mass and orbital characteristics of the asteroid. In this respect the modulus and direction of the MOID vector play an important role, as will be demonstrated in the following sections. A more accurate calculation of the MOID would produce a more precise estimation of the actual achievable deviation, but would not invalidate the results of this dissertation.

Table 2.1: Physical parameters for considered NEOs.

Id	Name	*a* [AU]	*e*	*i* [deg]	*Ω* [deg]	*ω* [deg]	*M* [deg]	Epoch [MJD]	Mass [kg]	Δr [km]
1	2004VD17	1.50	0.58	4.22	224.2	90.7	286.9	53,800.5	2.7×10^{11}	229,479.20
2	Apophis	0.92	0.19	3.33	204.4	126.3	222.2	53,800.5	4.6×10^{10}	36,651.75
3	2005WY55	2.47	0.72	7.26	248.4	285.9	3.30	53,800.5	1.9×10^{10}	696,520.60
4	1997XR2	1.07	0.20	7.17	250.8	84.6	211.8	53,800.5	1.7×10^{10}	3,277.43
5	1994WR12	0.75	0.39	6.81	62.8	205.8	27.3	53,700.0	2.0×10^{9}	283,313.30
6	1979XB	2.35	0.73	25.14	85.5	75.7	62.0	53,700.0	4.4×10^{11}	3,720,840.42
7	2000SG344	0.97	0.06	0.11	192.3	274.9	132.3	53,800.5	7.1×10^{7}	124,351.73
8	2000QS7	2.68	0.66	3.19	153.5	218.7	84.8	53,800.5	9.9×10^{10}	542,496.18
9	1998HJ3	1.98	0.74	6.54	224.9	92.7	333.6	50,926.5	4.5×10^{11}	1,907,030.74
10	2005TU45	1.97	0.49	28.5	120.2	76.8	34.1	53,651.5	3.3×10^{12}	38,152,163.70
11	2004XK3	1.21	0.25	1.43	58.1	302.2	22.0	53,800.5	1.1×10^{8}	168,758.33
12	1994GK	1.92	0.59	5.60	15.4	111.4	17.3	49,450.5	1.5×10^{8}	445,443.47
13	2000SB45	1.55	0.39	3.67	195.5	216.3	214.4	53,700.0	1.3×10^{8}	199,226.54

Id	Name	*a* [AU]	*e*	*i* [deg]	*Ω* [deg]	*ω* [deg]	*M* [deg]	Epoch [MJD]	Mass [kg]	Δr [km]
14	2001CA21	1.66	0.77	4.93	46.4	218.8	65.5	53,700.0	4.3×10^{11}	5,574,409.52
15	2005QK76	1.40	0.51	22.9	337.6	266.1	36.1	53,613.5	4.1×10^{7}	122,907.28
16	2002TX55	2.23	0.57	4.37	190.2	148.8	16.8	53,800.5	3.4×10^{8}	534,543.89
17	2005EL70	2.27	0.92	16.18	167.5	167.5	12.0	53,438.5	1.9×10^{8}	21,308,100.31
18	2001BB16	0.85	0.17	2.02	122.5	195.5	327.4	53,800.5	1.5×10^{9}	704,667.59
19	2002VU17	2.47	0.61	1.49	55.7	308.8	11.37	52,599.5	7.3×10^{7}	1,500,966.15
20	2000TU28	1.07	0.18	15.64	203.1	280.6	227.0	53,800.5	3.0×10^{10}	166,332.26
21	2001AV43	1.27	0.23	0.27	30.7	43.0	226.9	53,800.5	1.2×10^{8}	632,550.85
22	2002RB182	2.54	0.65	0.22	165.5	254.3	347.4	52,532.5	1.1×10^{9}	302,338.44
23	2002GJ8	2.97	0.82	5.30	144.2	180.3	261.3	53,800.5	1.3×10^{11}	13,925,769.75
24	2001FB90	2.48	0.78	1.92	266.3	14.5	343.3	51,993.5	5.7×10^{10}	4,781,828.50
25	2005NX55	1.52	0.58	26.16	106.4	277.2	327.2	53,563.5	3.8×10^{9}	5,098,118.30
26	1996TC1	1.86	0.72	14.53	5.0	258.8	22.8	50,363.5	2.3×10^{8}	11,305,879.51
27	6344P-L	2.64	0.64	4.66	184.9	232.6	349.8	37,203.5	1.2×10^{10}	4,183,900.25
28	2004ME6	2.36	0.57	9.44	112.2	210.3	346.1	53,182.5	1.5×10^{9}	4,343,813.94
29	2001QJ96	1.59	0.79	5.87	339.1	121.3	333.9	52,147.5	3.3×10^{9}	292,749.39
30	2004GE2	2.04	0.70	2.16	45.1	259.9	341.6	53,112.5	8.0×10^{9}	856,426.32

2.2.2. Impact model and optimisation problem definition

The impact between the spacecraft and the asteroid is considered to be perfectly inelastic; we do not take into consideration additional impulsive effects due to the ejection of mass or gasses. The variation of velocity imparted by the spacecraft to the asteroid is therefore given by the equation:

$$\delta\mathbf{v} = \gamma \frac{m_d}{\left(m_{\mathrm{NEO}} + m_d\right)} \Delta\mathbf{v} \tag{2.16}$$

where the relative velocity $\Delta\mathbf{v}$ of the spacecraft with respect to the asteroid at the impact point is computed from the ephemerides of the asteroid and from the solution of Lambert's problem for the spacecraft, and the parameter γ (representing the momentum enhancement factor) has a value of 1 in this implementation.

The mass of the asteroid m_{NEO} was estimated from its measured magnitude, whereas the mass of the spacecraft m_d at the impact point was computed through the rocket equation as follows:

$$m_d = m_0 \exp\left(-\frac{\Delta v_{\text{tot}}}{g_0 I_{sp}}\right)$$

where the specific impulse I_{sp} was taken equal to 315 s and the total Δv_{tot} is the sum of all the required manoeuvres that the spacecraft has to perform after launch. Note that m_d, at the denominator of Eq. (2.16), can be neglected.

All the celestial bodies are considered to be point masses with no gravity, the ephemerides of the asteroids were computed using the mean orbital elements in Table 2.1, and analytical ephemerides considering the long-term variation of the orbital elements were used for the Earth and for Venus. The model of analytic ephemerides approximates JPL ephemerides de405[‡‡]. In the case of direct Earth–asteroid transfers, Δv_{tot} is the required velocity change at the Earth to reach the asteroid, in the case of Earth–Venus–asteroid transfers, Δv_{tot} accounts for the required velocity change at the Earth to reach Venus, plus the deep space correction required after the Venus swing-by to reach the asteroid (further details on the trajectory model can be found in [119]). The initial mass of the spacecraft is $m_0 = 1000$ kg, and the launcher is assumed to provide an escape velocity of 2.5 km/s. If the required Δv at launch is less than the escape velocity provided by the launcher, a higher effective mass at launch is considered, to fully exploit the launcher capabilities. In this case the initial mass is:

$$m_0 = 1000 \exp\left(\frac{\Delta v_{\text{exc}}}{g_0 I_{\text{sp}}}\right)$$

where $\Delta v_{\text{exc}} = 2.5 - \Delta v_{\text{launch}}$. We consider that a minimum of 20% of the mass of the spacecraft at launch is allocated to structure and subsystems, whereas a minimum of 10% of the propellant mass is allocated to tanks and propulsion system; therefore the quantity $1.1\exp\left(-\frac{\Delta v_{\text{tot}}}{g_0 I_{sp}}\right) - 0.3$ at impact must be positive. Hence, we define a constraint C_m on the residual mass computed at the impact:

[‡‡] Data available online at http://naif.jpl.nasa.gov/naif/pds.html [Retrieved 13 March 2008].

$$C_m = \max\left(\left[\text{sign}\left(1.1\exp\left(-\frac{\Delta v_{\text{tot}}}{g_0 I_{sp}}\right)-0.3\right),0\right]\right)$$

The deviation $\delta\mathbf{r}$ is therefore a function of the mass of the spacecraft at impact and can be written in compact form as follows:

$$\delta\mathbf{r} = \gamma\frac{C_m m_d}{m_{\text{NEO}}}\mathbf{\Phi}\Delta\mathbf{v}$$

where $\mathbf{\Phi}$ is the transition matrix introduced in Section 2.1.1. The square of the modulus of the MOID after deviation then becomes:

$$J = \left(\Delta\mathbf{r} + \gamma\frac{C_m m_d}{m_{\text{NEO}}}\mathbf{\Phi}\Delta\mathbf{v}\right)^T\left(\Delta\mathbf{r} + \gamma\frac{C_m m_d}{m_{\text{NEO}}}\mathbf{\Phi}\Delta\mathbf{v}\right) \tag{2.17}$$

which has to be maximised with respect to the launch date t_0 and the deviation time t_d. Note that, from the analysis presented in Section 2.1.3 the strategies that aims at maximising b^* are more accurate than the ones aiming at the maximisation of $\delta\mathbf{r}$ [§§]. However, in the following, we use the latter strategy, because it provides good and reliable results for medium to long times-to-MOID and requires a lower computational cost.

To better examine the full range of launch opportunities, three different optimisations were run, fixing three different upper limits for the maximum warning time, which is the time from launch to the time the asteroid reaches the MOID: respectively, up to 5, 10, and 15 years. This was obtained by fixing the upper limit for a possible launch date to, respectively, [3650 5475] MJD2000, [3650 7300] MJD2000, and [3650 9125] MJD2000. Because the warning time can be up to 15 years, we computed all the times the asteroid is crossing the MOID for up to 15 years after the upper limit for the launch date, and we took the first date the asteroid reaches the MOID. Because some asteroids in Table 2.1 cannot be

[§§] To have a precise estimate of the miss distance from the Earth, the projection on the *b*-plane of $\|\Delta\mathbf{r} + \delta\mathbf{r}\|$ should be computed. Here, however, we are not interested in computing the minimum distance from the Earth, rather to compute the optimal manoeuvre and we do not consider the Earth to be at the MOID point when the asteroid crosses it.

reached with a low-cost direct transfer, the benefits of a single swing-by manoeuvre with Venus were also analysed. More complex sequences and multi-burn manoeuvres can further improve the deviation in the desired time frame; this will be the subject of future work.

As we are interested in a large number of local minima for the objective function given in Eq. (2.17) rather than only the global minimum, we used a particular global optimisation method that blends a stochastic search with an automatic solution space decomposition technique (see Section 4.3). This method has proven to be particularly effective when compared to common optimisation methods, especially when applied to space trajectory optimisation problems [116],[117].

Furthermore, it is expected that the largest deviations can be obtained with the longest warning time; thus, we performed an additional analysis, minimising the warning time t_w along with objective function (2.17):

$$t_w = t_{\mathrm{MOID}} - t_0$$

For this second analysis, the aim is to find the set of Pareto-optimal solutions (i.e., all those solutions for which there is no other solution that has a better value for both J and t_w). We used the same optimisation method but in its multi-objective version [133] (a more extensive explanation of the multi-criteria optimisation problem formulation will be given in Section 4.3).

2.2.3. Results

Single-objective optimisation

The results of the single-objective optimisation consist of a number of families of mission opportunities for each upper boundary on the maximum warning time. When the asteroid has high inclination, the optimal interception points are concentrated close to the ascending and descending node of the orbit. Two examples are shown in Figure 2.23 (asteroid 1979XB and asteroid 1996TC1), and the value of the argument of latitude at interception is shown in Figure 2.24. As can be seen in Figure 2.23, the interception points, marked with a

dot, are straddling the pericentre. This is the best compromise between an impact at the pericentre, which is the point that ensures the maximum change in the orbital period, and the transfer trajectory to reach the asteroid from the Earth. On the other hand, when the pericentre of the asteroid orbit is close to the Earth orbit, as in the case of asteroid 2000SB45 and 2002TX55 (see Figure 2.25), many optimal solutions are grouped around the pericentre.

The value of the impact velocity is almost a linear function of the eccentricity of the orbit (see Figure 2.26a), and its out-of-plane component increases with the inclination of the orbit (see Figure 2.26b).

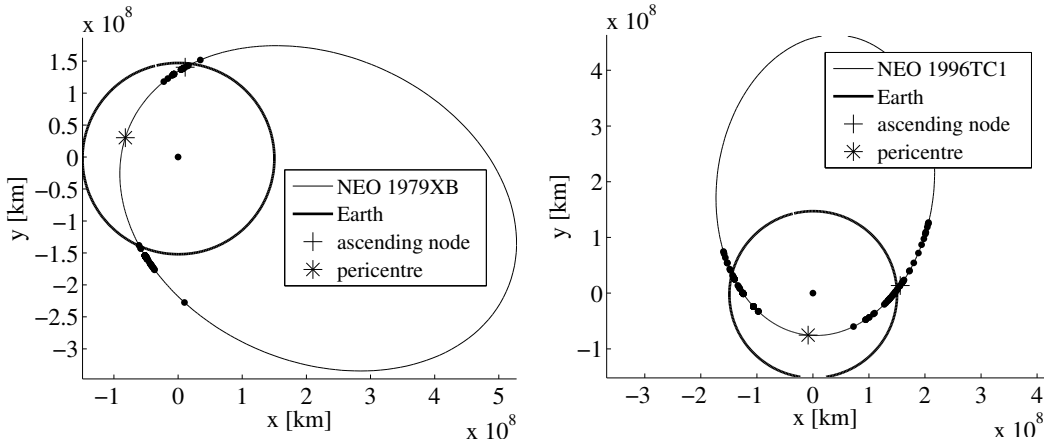

a) **b)**

Figure 2.23: Optimal interception of a) asteroid 1979XB and b) asteroid 1996TC1.

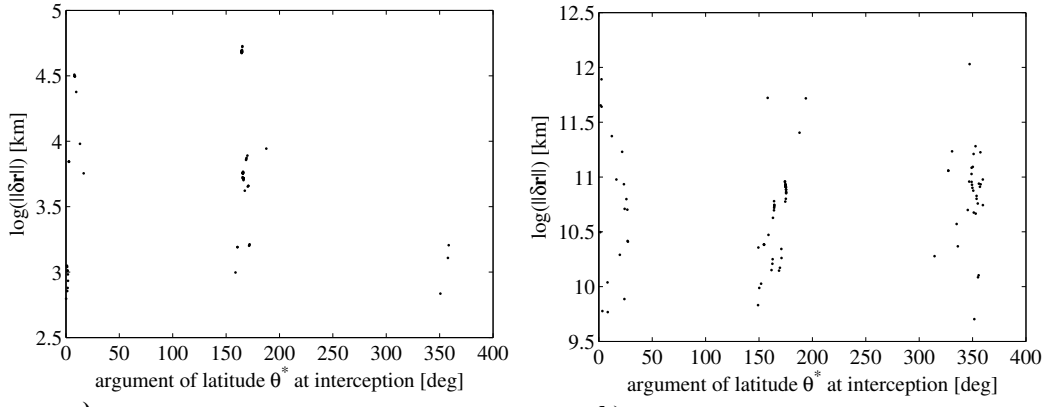

a) **b)**

Figure 2.24: Optimal interception arguments of latitude for a) asteroid 1979XB and b) asteroid 1996TC1.

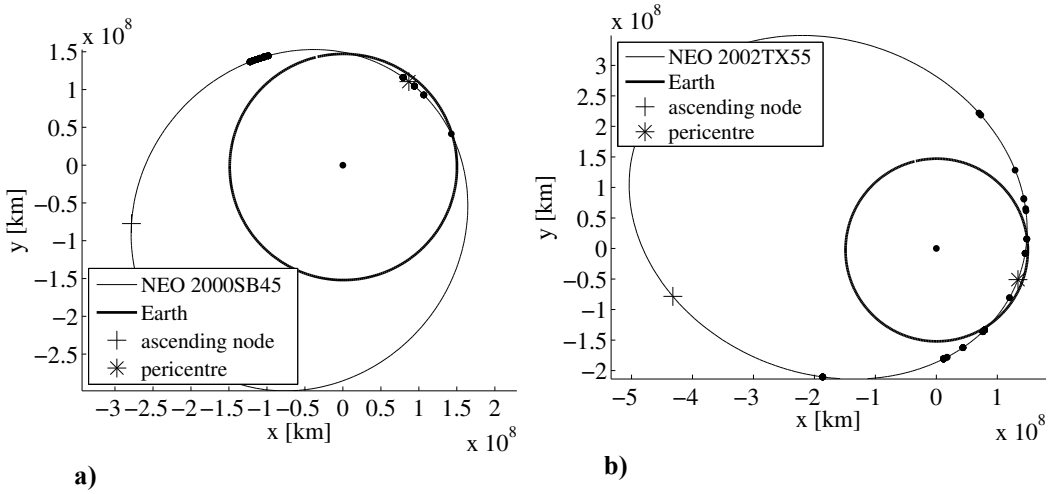

a) b)

Figure 2.25: Optimal interception of a) asteroid 2000SB45 and b) asteroid 2002TX55.

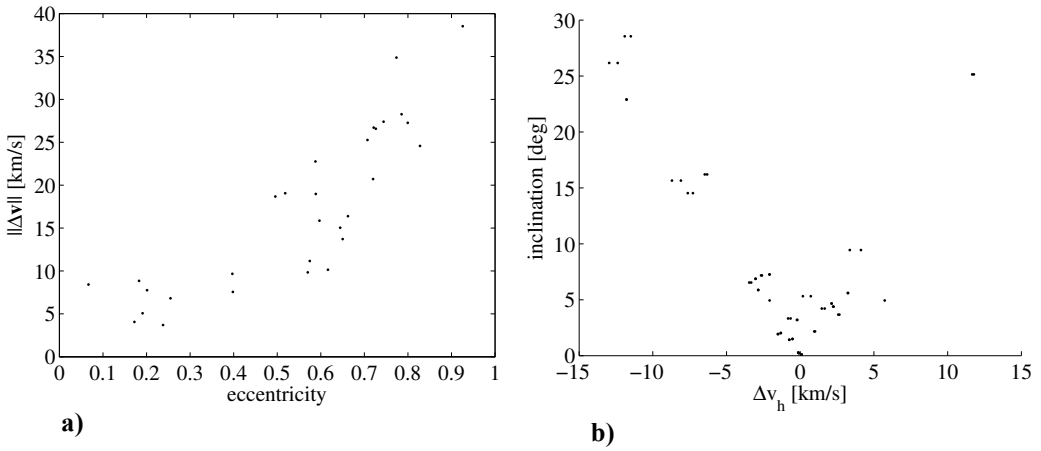

a) b)

Figure 2.26: Impact velocity function a) of the eccentricity and b) of the inclination (*h*-component).

Multi-objective optimisation

For each mitigation scenario (i.e., different upper boundary on the maximum warning time), a number of solutions were found that are Pareto-optimal with respect to the total deviation $\|\Delta\mathbf{r} + \delta\mathbf{r}\|$ and warning time t_w. Two sets of Pareto-optimal solutions are given as an example in Figure 2.27. The former asteroid (2000SG344) has a low-eccentric orbit, whereas the latter asteroid (2002GJ8) has an eccentricity $e = 0.82$. The Pareto front for the low-eccentric case has a more regular shape (see Figure 2.27a); the Pareto front of the high-eccentric case (see Figure 2.27b), instead, is strongly influenced by the synodic period between the asteroid and the Earth, and its shape is driven by the target interception at the orbit nodes.

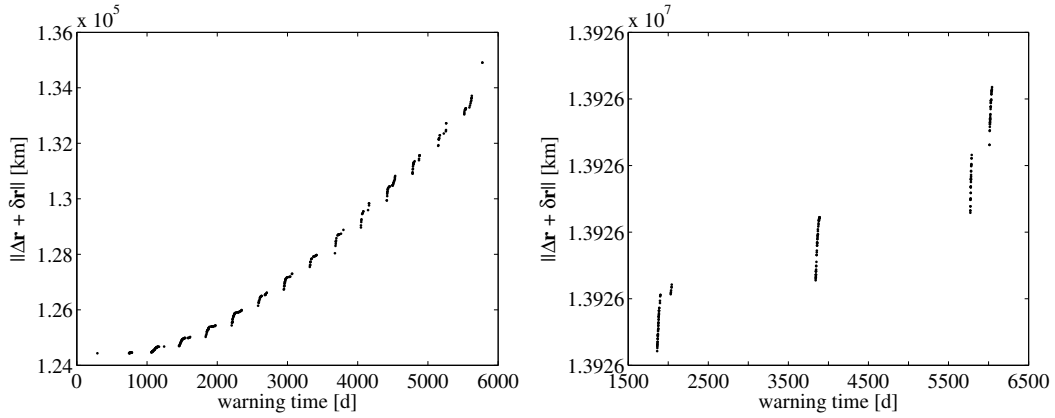

a) **b)**

Figure 2.27: Pareto front for a) asteroid 2000SG344 and b) asteroid 2002GJ8.

Among all the solutions of each Pareto-optimal set for each scenario, we selected (listed in Table 2.2) those that maximise the total deflection. For each mission, details of the optimal trajectory are given: namely the launch date t_0, the time of flight ToF, and the mass of the spacecraft at the interception point with the asteroid m_d. The deflection scenario selected for each case is identified by t_{MOID} (i.e., the asteroid passes through the MOID position along its orbit), which also determines the warning time for that mission t_w. The components of the relative velocity of the spacecraft with respect to the NEO at the interception point are Δv_t, Δv_n, and Δv_h, and δr is the achieved deviation.

The last column of Table 2.2 highlights the net deviation at the MOID (i.e., $\|\Delta\mathbf{r}+\delta\mathbf{r}\|-\|\Delta\mathbf{r}\|$). The table shows that the value of the deviation δr can be significantly higher than the actual modification of the MOID. Furthermore, from the comparison between the actual achieved deviations of asteroids with small and big Δr, we can infer that Δr itself plays an important role and cannot be neglected when dealing with a realistic impact scenario.

Table 2.2: Optimal launch opportunities for a direct transfer to selected asteroids as a result of the multi-objective optimisation.

Id^{***}	t_0 [d]	ToF [d]	t_{MOID} [MJD since 2000]	t_w [d]	m_d [d]	Δv_t [km/s]	Δv_n [km/s]	Δv_h [km/s]	δr [km]	$\|\Delta\mathbf{r}+\delta\mathbf{r}\|-\|\Delta\mathbf{r}\|$ [km]
1	4100.06	408.52	5826.16	1726.10	743.48	-10.48	-19.00	1.27	16.38	1.0
	4836.37	341.55	7855.58	3019.20	962.04	-10.05	-17.83	1.25	42.24	2.2
	4105.08	403.60	9208.52	5103.44	743.74	-10.47	-18.97	1.18	56.84	3.5
2	4165.11	310.87	5842.53	1677.42	1176.78	2.65	-2.75	-1.15	16.67	4.4
	4697.60	62.89	7460.40	2762.80	940.69	3.24	-0.78	-0.82	35.82	10.7
	4697.91	65.67	9401.85	4703.93	965.74	3.17	-0.53	-0.81	62.29	18.6
3	4671.63	507.57	9418.49	4746.86	481.39	-16.60	-20.91	-2.15	1430.33	169.1
4	5448.36	146.33	5618.12	169.75	374.42	-1.64	10.09	0.14	0.48	0.1
	4946.31	245.89	7658.52	2712.20	527.53	-3.63	6.75	-2.63	75.76	12.2
	5369.94	229.44	9290.84	3920.89	968.31	-2.25	7.03	-3.83	128.66	22.6
5	4103.70	334.67	5585.66	1481.96	943.91	6.66	1.81	-2.94	489.45	122.2
	4100.17	338.79	7508.27	3408.10	939.58	6.64	1.98	-3.08	1250.35	319.3
	4100.94	339.59	9190.56	5089.62	919.72	6.59	2.37	-3.07	1874.36	492.9
6	4257.00	356.52	8465.81	4208.81	636.13	-15.60	-17.87	11.55	82.27	11.8
	5590.11	253.95	9781.67	4191.55	617.61	-12.83	13.81	-13.12	76.50	11.0
7	3650.50	205.05	5544.35	1893.85	438.29	-5.21	6.62	0.10	14706.27	1424.6
	3650.50	202.34	7662.00	4011.50	437.80	-5.16	6.61	0.09	32375.88	5325.9
	3650.50	205.13	9426.72	5776.22	438.15	-5.21	6.62	0.10	47763.64	10553.8
8	4804.87	321.39	8264.05	3459.18	1141.92	-10.24	-12.57	-0.14	409.39	81.1
	4803.57	322.13	9868.32	5064.75	1143.05	-10.18	-12.50	-0.10	611.95	121.4
9	4436.62	152.66	5547.61	1110.99	457.87	-9.83	-12.31	7.25	10.63	0.8
	5395.86	170.98	7593.49	2197.64	855.62	-14.83	22.08	-2.71	53.50	3.7
	5397.67	168.77	9639.38	4241.71	874.91	-14.88	22.09	-2.65	109.25	7.4
10	5652.58	330.37	8033.43	2380.85	701.13	-8.34	4.49	-11.69	1.98	0.6
	6801.12	194.28	10058.89	3257.77	1054.79	-10.89	10.10	-11.24	5.84	1.6
11	3932.94	215.43	5681.67	1748.72	669.74	-6.89	8.24	0.63	23841.97	4681.2
	3919.51	222.80	7630.18	3710.67	680.47	-6.99	8.35	0.85	57010.04	16165.6
	3923.98	220.05	9578.69	5654.71	678.18	-6.96	8.34	0.77	89492.17	32181.5
12	3650.50	68.57	5680.49	2029.99	964.32	-9.98	-12.47	3.26	100650.26	19921.6
	6531.11	99.78	7624.88	1093.77	1041.12	-9.12	-11.02	2.27	50732.19	8718.4
	3650.50	70.03	9569.27	5918.77	1029.02	-9.61	-12.19	3.23	308146.24	116366.7
13	3650.50	220.97	5969.30	2318.80	555.76	-8.57	3.11	2.75	44922.04	15913.6
	3650.50	219.50	7391.97	3741.47	564.95	-8.56	3.43	2.65	76038.17	30907.2
	3650.50	218.10	9525.99	5875.49	571.35	-8.55	3.72	2.57	123008.50	58697.1
14	6583.79	136.24	7529.57	945.78	309.54	-9.90	-15.77	-4.40	4.89	0.3
	6581.72	138.43	9874.18	3292.46	312.38	-9.87	-15.70	-4.16	19.67	1.3
15	3650.50	227.20	5583.43	1932.93	1359.20	-9.44	-11.63	-11.80	265233.42	174397.2
	3650.50	227.21	7397.08	3746.58	1359.50	-9.44	-11.63	-11.80	527916.98	424692.3
	3650.50	227.25	9210.74	5560.24	1360.55	-9.44	-11.63	-11.79	790680.51	682933.9
16	4578.23	60.07	5867.83	1289.60	1360.86	-8.78	-4.69	2.62	39109.10	5733.2
	4455.05	118.79	8298.70	3843.65	793.55	-9.69	11.57	-0.57	65299.94	27043.7
	4546.08	97.26	9514.13	4968.05	1804.38	-8.00	-4.63	2.20	187881.19	44490.0
17	5346.70	212.60	5566.21	219.52	273.45	-25.20	24.83	-3.26	30.66	2.5
	3867.85	411.59	8067.07	4199.22	407.68	-14.41	17.11	-4.25	76168.47	4546.1
	3864.13	417.78	9317.50	5453.37	418.41	-14.38	17.33	-4.48	105870.84	6119.9

*** The designation numbers correspond to the asteroids listed in Table 2.1.

Id^{***}	t_0 [d]	ToF [d]	t_{MOID} [MJD since 2000]	t_w [d]	m_d [d]	Δv_t [km/s]	Δv_n [km/s]	Δv_h [km/s]	δr [km]	$\|\Delta\mathbf{r}+\delta\mathbf{r}\|-\|\Delta\mathbf{r}\|$ [km]
	3755.42	424.18	5573.42	1818.00	872.68	4.70	1.17	-1.58	755.27	219.4
18	4131.45	336.26	7592.06	3460.61	1496.89	3.19	1.99	-1.31	1925.68	557.4
	4129.64	338.16	9322.33	5192.69	1496.07	3.19	2.03	-1.34	2965.54	863.3
	3650.50	201.18	6716.97	3066.47	668.09	-9.67	4.28	-0.53	266564.21	38923.2
19	3650.50	203.42	8138.22	4487.72	684.28	-9.63	3.62	-0.52	408070.55	75442.1
	3650.50	204.67	9559.48	5908.98	691.48	-9.62	3.26	-0.52	548972.26	123032.9
	3846.60	230.17	5723.91	1877.31	753.46	-2.96	-2.30	-8.95	37.72	13.0
20	3842.14	234.39	7755.70	3913.56	764.40	-2.89	-2.30	-8.70	84.18	29.3
	3865.47	105.14	9381.13	5515.66	648.50	-2.65	3.22	7.78	90.89	37.1
	3804.42	288.73	5629.83	1825.41	1578.00	-3.06	-7.03	0.10	24477.83	1051.0
21	3826.17	272.04	7737.97	3911.80	1536.69	-3.08	-7.13	0.15	54828.62	3768.4
	4795.22	308.28	9319.08	4523.86	2103.02	-3.17	-2.02	-0.16	96856.26	7416.7
	3753.67	283.60	6936.07	3182.40	1963.39	-9.36	-9.93	-0.07	52177.12	3830.9
22	3724.34	311.75	8417.98	4693.64	1936.20	-9.25	-9.76	-0.02	76581.96	8627.0
	3754.23	283.40	9899.90	6145.66	1954.74	-9.39	-9.99	-0.07	103984.39	16160.8
23	4108.27	595.86	8293.93	4185.66	347.87	-21.69	-23.22	-1.66	210.06	1.6
	4108.03	597.02	10151.47	6043.44	346.45	-21.67	-23.09	-1.63	311.42	2.3
	4638.90	146.75	6274.21	1635.31	465.31	-15.75	23.17	-1.52	250.69	2.7
24	4639.23	146.04	7702.81	3063.57	474.87	-15.83	23.23	-1.54	513.35	5.4
	6077.27	137.19	10560.01	4482.74	288.77	-19.62	26.95	-1.15	584.01	6.4
	5216.27	357.41	6144.63	928.36	596.31	-12.15	-16.67	-12.69	654.03	102.2
25	5950.28	307.64	7517.33	1567.04	735.93	-11.77	-15.09	-12.39	1555.50	204.2
	3774.30	434.60	9576.37	5802.07	303.65	-12.35	-19.21	-11.18	2491.86	543.1
26	6044.00	152.45	8036.66	1992.67	359.50	-19.42	26.10	8.57	53436.71	11541.4
	6058.42	141.37	9901.02	3842.60	278.23	-18.56	26.17	7.89	81765.09	20810.0
27	5844.80	240.64	7674.41	1829.61	588.33	-11.27	10.11	2.14	897.61	103.1
	7322.19	312.87	9245.58	1923.40	1034.88	-8.85	8.22	2.51	1128.88	238.4
	5483.00	166.08	5654.45	171.45	600.25	-9.33	9.06	4.28	2.55	0.5
28	3921.63	366.06	8311.08	4389.44	696.64	-7.07	5.40	4.15	10707.80	4942.5
	3919.12	369.63	9639.39	5720.27	713.03	-7.01	5.31	4.07	14551.53	6592.9
	3915.75	391.15	5785.14	1869.39	1537.58	-14.27	22.63	-2.96	5522.96	50.9
29	3905.58	401.40	8002.33	4096.75	1527.61	-14.46	22.84	-2.82	13908.93	329.1
	3907.39	399.72	9480.46	5573.07	1494.54	-14.66	23.04	-2.89	19345.68	641.5
	4654.83	160.20	5857.48	1202.65	595.10	-14.02	20.39	0.92	1123.71	47.6
30	4655.90	159.89	7998.45	3342.56	578.40	-13.89	20.25	0.90	3261.83	146.2
	4655.25	159.14	10139.43	5484.18	607.49	-14.13	20.49	0.91	5743.99	251.7

It should be noted that a number of solutions computed with the single-objective approach belong to the set of Pareto-optimal solutions of the multi-objective optimisation. As an example, Figure 2.28 shows the Pareto-optimal set for asteroid 2002VU17; the black points represent the solutions within an upper boundary of 5 years, the dark grey points the solutions with an upper boundary of 10 years, and the light grey points the solution with an upper boundary of 15 years. The three circles represent the Pareto-optimal solutions with the maximum deviation of each scenario; the three crosses are the optimal solutions from the single-objective optimisation with the maximum deviation of each scenario.

Figure 2.29 represents the distribution, for all the asteroids and for both analyses, of the components of the impact velocity in the orbit plane.

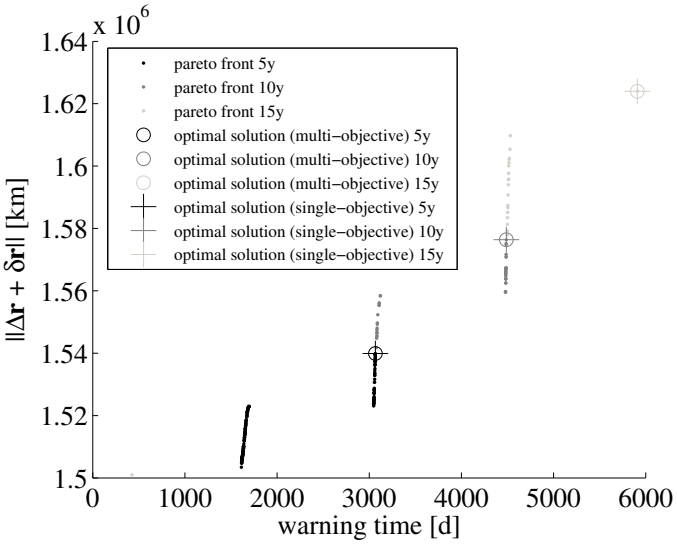

Figure 2.28: Pareto front for asteroid 2002VU17.

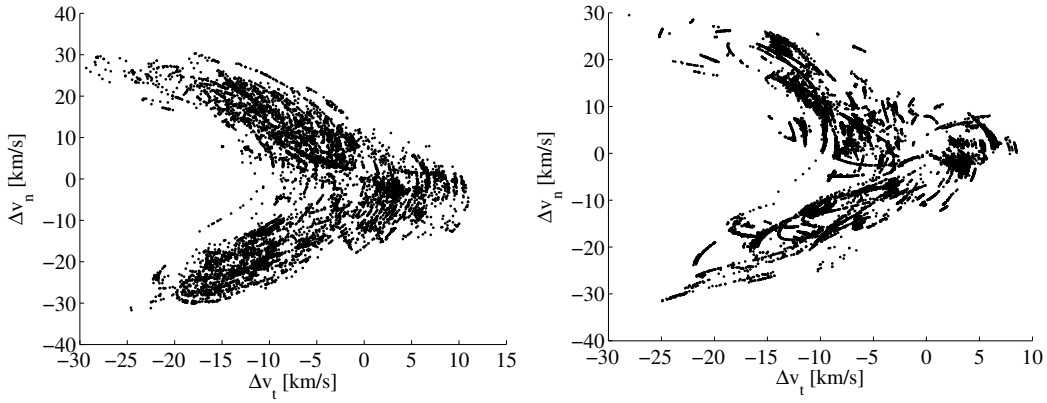

Figure 2.29: Optimal impact Δv distribution for direct impacts: a) results of the single-objective optimisation and b) results of the multi-objective optimisation.

Venus swing-by

Figure 2.29 shows that very-high-speed fuel-efficient impacts have both very high normal and tangential components with negative sign. High-speed direct impacts, therefore, correspond to trajectories that intersect almost perpendicularly the orbit of the NEO and not necessarily at the perihelion. Because this particular behaviour is due to the limitations on propellant consumption, one or more gravity-assist manoeuvres could improve the impact performance. Here, the effect of a single swing-by of Venus will be considered. Table 2.3 reports all the

solutions that show a significant improvement of the total deviation with respect to the direct transfer options.

Table 2.3: Optimal launch opportunities for transfers to selected asteroids via a single Venus swing-by as a result of the single-objective optimisation.

Id[†††]	t_0 [d]	ToF [d]	t_{MOID} [MJD since 2000]	t_w [d]	m_d [d]	Δv_t [km/s]	Δv_n [km/s]	Δv_h [km/s]	δr [km]	$\|\Delta\mathbf{r}+\delta\mathbf{r}\|-\|\Delta\mathbf{r}\|$ [km]
4	4516.93	247.64	5618.12	1101.19	609.91	-4.40	11.85	-3.49	32.36	**9.4**
	3881.90	1292.77	7658.52	3776.62	551.48	-4.86	11.88	-1.28	99.84	**28.8**
	3866.34	912.49	9290.84	5424.50	755.42	-4.69	11.01	-2.60	252.62	**57.2**
9	3901.67	648.33	5547.61	1645.93	508.23	-13.31	27.14	-4.44	15.25	**1.5**
	3899.06	647.96	7593.49	3694.43	592.22	-13.40	26.51	-4.82	51.91	**4.4**
	3901.41	648.51	9639.38	5737.97	510.18	-13.33	27.14	-4.47	76.53	**7.6**
11	3865.16	272.27	5681.67	1816.51	776.60	-6.37	6.56	0.40	24957.00	**4928.8**
	3917.58	220.53	7630.18	3712.60	717.81	-6.84	10.39	-0.40	58123.89	**16594.2**
	3918.67	218.93	9578.69	5660.02	719.28	-6.80	10.61	-0.41	91166.93	**32981.6**
14	4455.02	704.40	5966.50	1511.49	534.06	-15.21	-26.51	-2.50	12.45	**0.7**
	4540.25	622.35	7529.57	2989.32	306.22	-24.34	-32.83	1.04	32.57	**1.6**
	3805.78	1363.04	9874.18	6068.40	429.34	-21.45	-29.45	-1.42	73.47	**2.3**
20	4443.39	447.77	5723.91	**1280.52**	272.73	-8.75	-18.87	-8.33	20.13	6.2
	3950.95	832.02	7349.34	**3398.39**	460.33	-6.46	3.25	8.88	73.59	**30.4**
	5078.74	528.35	9381.13	**4302.39**	561.01	-5.88	6.81	8.25	124.05	**69.4**
26	3896.88	431.01	6172.31	2275.43	720.76	-13.63	16.04	13.56	71975.85	**12271.5**
	3871.68	454.34	8036.66	4164.98	781.25	-16.51	22.58	9.53	185251.39	**28983.5**
27	3929.37	574.96	6103.23	2173.86	553.06	-14.63	13.82	1.81	1050.20	**173.3**
	3921.14	589.63	7674.41	3753.26	689.31	-13.56	10.93	1.58	2496.01	**333.9**
	5629.76	433.82	9245.58	3615.83	517.10	-10.32	6.13	3.27	1318.43	279.8
29	3930.58	1120.13	5785.14	**1854.56**	403.36	-24.39	31.21	-1.28	1308.55	14.4
	4457.15	1349.65	8002.33	**3545.19**	563.93	-18.86	30.26	-1.23	5419.39	**354.5**

2.3. Summary

In this chapter, a simple analytical expression based on proximal motion equations is derived for the computation of the deflection of potentially hazardous asteroids. An analysis of the accuracy of the proposed analytical formulation has shown its accuracy for a wide range of orbit geometries and for different deviation strategies. This formulation represents an extension of all the approaches based on a variation of the mean motion of the asteroid. Furthermore, it is less computationally expensive than the approaches based on the use of the Lagrange coefficients. The proposed formulation is first used to predict the optimal

[†††] The designation numbers correspond to the asteroids listed in Table 2.1.

direction of the deflection $\delta\mathbf{v}$ that has to be applied to the NEO. The results presented in this chapter are in agreement with already existing results obtained with different techniques. This confirms the correctness of the approach and the validity of the basic assumptions that were made.

Moreover, a wide range of mission opportunities is analysed through a hybrid global search method. Optimal launch options for direct transfers and for transfers via a single Venus gravity-assist manoeuvre are identified for a selection of 30 asteroids with different orbital characteristics and different masses.

Though the assumed impacting spacecraft mass is quite small, it can be seen that remarkable deviations can be achieved with a reasonable time-to-MOID by producing a small $\delta\mathbf{v}$ along track. On the other hand, for very short times-to-MOID a more consistent $\delta\mathbf{v}$ is required, especially if the gravitational effects of the Earth are considered; in this case the direction of the optimal impulse depends on the time-to-MOID and the orbital parameters of the asteroid. The results obtained in this chapter show that the actual achievable change in the MOID can be significantly different from the deviation $\delta\mathbf{r}$ as a consequence of the modulus and direction of the MOID vector itself. Therefore, the actual MOID cannot be neglected, in general. Furthermore, it was shown that the ideal point of interception of the asteroid, when the transfer is considered, is not necessarily the pericentre of the orbit of the asteroid.

The importance of the transfer trajectory suggests that more complex sequences of gravity-assist manoeuvres and multi-impulse transfers may improve the results obtained in this chapter. The design of more efficient transfer trajectories is currently under investigation and will be the subject of a future work.

Chapter 3.

Low-thrust NEO deflection

This chapter focuses on the deflection of a near Earth object with a low-thrust strategy providing a continuous push on the threatening body over a certain interval of time. The displacement of the asteroid at the minimum orbit intersection distance from the Earth's orbit is computed through the proximal motion equations as a function of the variation of the orbital elements. In the general case, the variation of the orbital elements between the deviated and the nominal orbits is computed by numerical integration of Gauss' equations, considering the thrust acceleration of the deflection strategy as a perturbing acceleration.

Section 3.2 presents a semi-analytical solution of the asteroid deviation problem when a low-thrust action, inversely proportional to the square of the distance from the Sun, is applied to the asteroid. A set of semi-analytical formulae is derived to compute the variation of the elements: Gauss' planetary equations are averaged over one orbital revolution to give the secular variation of the elements, and their periodic components are approximated through a trigonometric expansion. Two formulations of the semi-analytical formulae, latitude and time formulation, are presented along with their accuracy against a full numerical integration of Gauss' equations. It is shown that the semi-analytical approach provides a significant saving in computational time while still maintaining a good accuracy.

Finally, some examples of deviation missions are presented as an application of the proposed semi-analytical theory. In particular, the semi-analytical formulae are used in conjunction with a multi-objective optimisation algorithm to find a set of Pareto-optimal mission options that minimises the asteroid warning time and the spacecraft mass while maximising the orbital deviation.

3.1. Asteroid deviation problem

Given the time of interception t_i of a generic NEO, the objective is to maximise the minimum orbit intersection distance from the Earth by applying a low-thrust deviation action, which consists of a continuous push along the asteroid's centre of mass* over a certain interval of time. In general, any deviation strategy generates a perturbation of the nominal orbit of the asteroid. The new orbit can be considered proximal to the unperturbed one (see Figure 3.1).

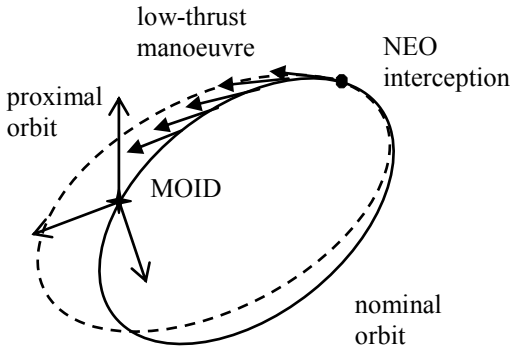

Figure 3.1: Low-thrust NEO deviation.

The proximal motion equations [115] can be again used to describe the variation of the NEO displacement at the MOID relative to its unperturbed position, after the low-thrust action. The nominal orbit of the NEO is taken as chief orbit and the perturbed orbit at the end of the low-thrust arc is considered the deputy orbit. Eqs. (2.1) that are recalled here for clarity are valid also in the low-thrust case:

$$\begin{aligned}
\delta s_r &\approx \frac{r_{\mathrm{MOID}}}{a}\delta a + \frac{ae\sin\theta_{\mathrm{MOID}}}{\eta}\delta M - a\cos\theta_{\mathrm{MOID}}\delta e \\
\delta s_\theta &\approx \frac{r_{\mathrm{MOID}}}{\eta^3}\left(1+e\cos\theta_{\mathrm{MOID}}\right)^2\delta M + r_{\mathrm{MOID}}\delta\omega + \\
&\quad + \frac{r_{\mathrm{MOID}}\sin\theta_{\mathrm{MOID}}}{\eta^2}\left(2+e\cos\theta_{\mathrm{MOID}}\right)\delta e + r_{\mathrm{MOID}}\cos i\delta\Omega \\
\delta s_h &\approx r_{\mathrm{MOID}}\left(\sin\theta^*_{\mathrm{MOID}}\delta i - \cos\theta^*_{\mathrm{MOID}}\sin i\delta\Omega\right)
\end{aligned} \tag{3.1}$$

* In this study, the deviation action is always considered aligned with the NEO centre of mass. The control issues related to the mechanics of moving an asteroid considering it as a rigid body, with spin properties, are not considered. On the other hand, in the results sections of this thesis margins on the total mission mass are added to take into account the propellant mass for the spacecraft control in proximity of the NEO. The reader can refer to [68] for more details on the mechanics of the NEO seen as a 6 degrees-of-freedom body.

where $\eta = \sqrt{1-e^2}$, θ_{MOID} indicates the true anomaly of the NEO at the MOID along the unperturbed orbit, and $\theta^*_{\text{MOID}} = \theta_{\text{MOID}} + \omega$ the corresponding argument of latitude. The variation in position $\delta\mathbf{r} = \begin{bmatrix}\delta s_r & \delta s_\theta & \delta s_h\end{bmatrix}^T$ is expressed in the radial-transversal-perpendicular-to-the-orbit-plane reference frame as function of the orbital parameters between the two orbits; in a matrix form:

$$\delta\mathbf{r}\left(t_{\text{MOID}}\right) = \mathbf{A}_{\text{MOID}}\delta\boldsymbol{\alpha}\left(t_{\text{MOID}}\right) \tag{3.2}$$

where $\delta\boldsymbol{\alpha}\left(t_{\text{MOID}}\right) = \begin{bmatrix}\delta a & \delta e & \delta i & \delta\Omega & \delta\omega & \delta M\end{bmatrix}^T$ is the vector of the orbit element difference at the MOID between the perturbed and the nominal orbit, and M is the mean anomaly. When a low-thrust deviation action is applied over the interval $\begin{bmatrix}t_i & t_e\end{bmatrix}$, where $t_e \le t_{\text{MOID}}$ is the time when the manoeuvre is ended, the total variation of the orbital parameters can be computed by integrating Gauss' planetary equations [71]:

$$\begin{aligned}
\frac{da}{dt} &= \frac{2a^2 v}{\mu_{\text{Sun}}} a_t \\
\frac{de}{dt} &= \frac{1}{v}\left[2\left(e+\cos\theta\right)a_t - \frac{r}{a}\sin\theta a_n\right] \\
\frac{di}{dt} &= \frac{r\cos\theta^*}{h} a_h \\
\frac{d\Omega}{dt} &= \frac{r\sin\theta^*}{h\sin i} a_h \\
\frac{d\omega}{dt} &= \frac{1}{ev}\left[2\sin\theta a_t + \left(2e + \frac{r}{a}\cos\theta\right)a_n\right] - \frac{r\sin\theta^*\cos i}{h\sin i} a_h \\
\frac{dM}{dt} &= n - \frac{b}{eav}\left[2\left(1+\frac{e^2 r}{p}\right)\sin\theta a_t + \frac{r}{a}\cos\theta a_n\right]
\end{aligned} \tag{3.3}$$

The low thrust strategy provides an acceleration $\mathbf{a}\left(t\right) = \begin{bmatrix}a_t & a_n & a_h\end{bmatrix}^T$, here expressed in a tangential-normal-binormal reference frame, such that a_t and a_n are the components of the acceleration in the plane of the osculation orbit, respectively, along the velocity vector and perpendicular to it, and a_h is the component perpendicular to the orbital plane. Note that the derivative of M in the

sixth equation of system (3.3) takes into account the instantaneous change of the orbit geometry at each instant of time $t \in [t_i \quad t_e]$ and the variation of the mean motion n due to the change in the semi-major axis along the thrust arc.

Letting $\boldsymbol{\alpha}(t) = [a \quad e \quad i \quad \Omega \quad \omega \quad M]^T$ be the vector of the orbital parameters, we define

$$\Delta\boldsymbol{\alpha} = \boldsymbol{\alpha}(t_e) - \boldsymbol{\alpha}(t_i) = [\Delta a \quad \Delta e \quad \Delta i \quad \Delta\Omega \quad \Delta\omega \quad \Delta M]^T$$

as the finite variation of the orbital elements with respect to the nominal orbit in the interval $[t_i \quad t_e]$, obtained from the numerical integration of Eqs. (3.3). It is important to point out that δM in Eqs. (3.1) must include the phase shift between the Earth and the asteroid. Therefore, because the mean anomalies at the MOID on the perturbed $\tilde{M}_{\text{MOID}}$ and on the nominal orbits M_{MOID} are computed as

$$\begin{aligned}
\tilde{M}_{\text{MOID}} &= M(t_e) + n_e(t_{\text{MOID}} - t_e) = M(t_i) + \Delta M + n_e(t_{\text{MOID}} - t_e) \\
&= n_i(t_i - t_p) + \Delta M + n_e(t_{\text{MOID}} - t_e) \\
M_{\text{MOID}} &= n_i(t_{\text{MOID}} - t_p)
\end{aligned}$$

where t_p is the passage at the pericentre, then the total variation in the mean anomaly between the proximal and the unperturbed orbit is

$$\delta M = \tilde{M}_{\text{MOID}} - M_{\text{MOID}} = (n_e - n_i)t_{\text{MOID}} + n_i t_i - n_e t_e + \Delta M \tag{3.4}$$

where n_i is the nominal angular velocity and

$$n_e = \sqrt{\frac{\mu_{\text{Sun}}}{(a + \Delta a)^3}}$$

The variation of the other orbital parameters in Eqs. (3.1) is simply $\delta a = \Delta a$, $\delta e = \Delta e$, $\delta i = \Delta i$, $\delta\Omega = \Delta\Omega$, $\delta\omega = \Delta\omega$.

If $\Delta\mathbf{r} = \begin{bmatrix} \Delta s_r & \Delta s_\theta & \Delta s_h \end{bmatrix}^T$ is the vector distance of the asteroid from the Earth at the MOID and $\delta\mathbf{r} = \begin{bmatrix} \delta s_r & \delta s_\theta & \delta s_h \end{bmatrix}^T$ is the variation given by Eqs. (3.1) at t_{MOID}, then the objective function for the maximum deviation problem is

$$\|\Delta\mathbf{r} + \delta\mathbf{r}\| = \sqrt{\left(\Delta s_r + \delta s_r\right)^2 + \left(\Delta s_\theta + \delta s_\theta\right)^2 + \left(\Delta s_h + \delta s_h\right)^2} \tag{3.5}$$

The proximal motion equations provide a very simple and general means to compute the variation of the MOID with good accuracy, without the need for further analytical developments.

Gauss' equations (3.3), together with Eq. (3.4), provide a way to compute the variation of the orbital elements between the nominal and the deviated orbits. The equations account both for the geometrical variation of the orbit and the secular change in the mean motion. To compute the effect of any low-thrust deflection strategy, Gauss' equations would have to be numerically integrated. However, in Section 3.2, we will restrict our attention to the case of a tangential push with the modulus inversely proportional to the square of the distance from the Sun. Note that if we integrate only the first term of the last of Eqs. (3.3), neglecting the variations of e, i, ω and Ω, and insert it into Eq. (3.4), we would get:

$$\delta M = \left(n_e - n_i\right) t_{\text{MOID}} + n_i t_i - n_e t_e + \int_{t_i}^{t_e} n\, dt \tag{3.6}$$

which is the secular change in the mean motion, already considered by other authors [68],[69]. The equivalence of Eq. (3.6) to what is already in the literature can be demonstrated as follows. Let us start by rewriting Eq. (3.6) as

$$\delta M = \left[n\left(t_{\text{MOID}} - t\right) \right]_{t_i}^{t_e} + \int_{t_i}^{t_e} n\, dt$$

and integrating by part

$$\delta M = \int_{t_i}^{t_e} \left(t_{\text{MOID}} - t\right) \frac{dn}{dt}\, dt \tag{3.7}$$

Now, the differential dn can be written as a function of da, and through the first of Gauss' equations (3.3) as a function of the time shift *dt*:

$$dn = \sqrt{\mu_{\text{Sun}}}\left(-\frac{3}{2}\right)a^{-5/2}da \qquad da = \frac{2a^2 v}{\mu_{\text{Sun}}}a_t\,dt$$

Hence, Eq. (3.7) becomes

$$\delta M = -\frac{3}{\sqrt{\mu_{\text{Sun}}}}\int_{t_i}^{t_e}\left(t_{\text{MOID}} - t\right)\frac{v}{\sqrt{a}}a_t\,dt$$

If we now use the superscript ^ to denote the time coordinates measured from the interception time t_i and we take the mean value of the semi-major axis out of the integral, we get:

$$\delta M = -\frac{3}{\sqrt{a\mu_{\text{Sun}}}}\int_0^{\hat{t}_e}\left(\hat{t}_{\text{MOID}} - \hat{t}\right) < \mathbf{v}, \mathbf{a}(\hat{t}) > d\hat{t}$$

which then can be translated from δM to the variation of the time to encounter $\delta\tau$, induced by the strategy deflection action $\mathbf{a}$, projected onto the velocity of the asteroid [69]:

$$\delta\tau = -\frac{3a}{\mu_{\text{Sun}}}\int_0^{\hat{t}_e}\left(\hat{t}_{\text{MOID}} - \hat{t}\right) < \mathbf{v}, \mathbf{a}(\hat{t}) > d\hat{t}$$

3.1.1. Analysis of the optimal thrust direction

An estimation of the optimal direction of the push can be driven from the maximum deviation analysis performed for the impulsive action case (see Section 2.1.1). The asteroid impulsive problem was written through the state transition matrix as the sensitivity of the current position vector at the MOID with respect to the velocity increase at the deviation time [see Eq. (2.8)]. The maximisation of $\left\|\delta\mathbf{r}\left(t_{\text{MOID}}\right)\right\|$ in Eq. (2.8) suggests that the optimal direction of the impulsive action is along the tangent direction, and this one is associated with the shift in time between the position of the asteroid and the Earth, rather than with a geometrical

variation of the MOID. This result is valid for Δt larger than a specific $\Delta t_{\text{NEO}} < 1 T_{\text{NEO}}$.

In the case of a low-thrust manoeuvre, as a first approximation, these results can be generalised by choosing the control vector at time *t* instantaneously tangent to the optimal impulsive $\delta \mathbf{v}_{opt}(t)$. This is equivalent to maximise

$$\delta \mathbf{r}\left(t_{\text{MOID}}\right) = \mathbf{A}_{\text{MOID}} \mathbf{G}_t \delta \mathbf{v}(t) = \mathbf{\Phi}(t) \delta \mathbf{v}(t)$$

for each instant of time $t \in \left[t_i \quad t_e\right]$, where $\mathbf{\Phi}(t)$ is the transition matrix that links the impulsive $\delta \mathbf{v}(t)$ at time *t* to the consequent deviation at t_{MOID}. $\mathbf{A}_{\text{MOID}}$ is the matrix in Eq. (3.2) and $\mathbf{G}_t$ is the matrix associated to the Gauss' equations written for finite differences; that is, the control acceleration is replaced by an instantaneous change in the asteroid velocity vector:

$$\delta \boldsymbol{\alpha}\left(t_{\text{MOID}}\right) = \mathbf{G}_t \delta \mathbf{v}(t)$$

In Section 3.2, to derive a semi-analytical formulation of the low-thrust asteroid deviation problem, we focus on low-thrust acceleration along the tangent direction. This is a valid assumption when we consider hazardous cases with a warning time longer than approximately $0.75 T_{\text{NEO}}$. For a better estimation of the optimal direction of thrust in the case of low-thrust propulsion, one can refer to the analysis by Song et al. [75]. Note that, for long times-to-MOID, the direction that maximises $\|\delta \mathbf{r}\|$ is also optimal for the maximisation of $\|\Delta \mathbf{r} + \delta \mathbf{r}\|$ and its projection into the *b*-plane[†].

[†] For an actual impact hazard $\|\Delta \mathbf{r}\|$ is less than the Earth radius.

3.2. Semi-analytical formulae for low-thrust deviation action

In this section, a set of semi-analytical formulae will be derived to calculate the total variation of the orbital parameters due to a low-thrust action. A continuous acceleration a_t is applied along the orbit track, with modulus given by

$$a_t = \frac{k_a}{r^2} \tag{3.8}$$

where r is the distance from the Sun and k_a is a time-invariant proportionality constant that has to be fixed according to the specification of the power system. The selection of this acceleration law does not represent a severe restriction to the mission design, in fact Eq. (3.8) describes any strategy that exploits the Sun as a power source: for example, a solar electric propulsion spacecraft that rendezvous with the NEO, anchors to its surfaces, and pushes, or a solar mirror that collects the energy from the Sun and focuses it onto the asteroid surface to ablate it. Moreover, if the formulae presented in the following are adopted to design a low-thrust trajectory, Eq. (3.8) represents the control acceleration due to a power-limited spacecraft.

Two formulations of the asteroid deviation problem, which make use of different independent variables for deriving the semi-analytical formulae, will be presented. The *latitude* formulation expresses the secular and periodic variation of the orbital parameters as function of the argument of latitude, whereas the *time* formulation introduces the time as independent variable. The use of latitude as independent variable allows deriving some elegant formulae that contain only two elliptic integrals to be solved numerically. The time formulation, although more complex and requiring the numerical solution of more terms, is necessary when dealing with the asteroid deviation problem. In fact the use of time as independent variable allows considering the component of the deviation associated to the shift in time between the passage of the Earth and the asteroid at the MOID.

3.2.1. Latitude formulation

Gauss' equations are written as a function of the true latitude θ^*:

$$\frac{d\boldsymbol{\alpha}}{d\theta^*} = \frac{d\boldsymbol{\alpha}}{dt}\frac{dt}{d\theta^*}$$

where, in case of zero-acceleration out-of-plane a_h,

$$\frac{d\theta^*}{dt} = \frac{h}{r^2} \tag{3.9}$$

where h is the orbital angular momentum. Under the hypothesis of planar tangential manoeuvre, Eqs. (3.3) become

$$\begin{aligned}
\frac{da}{d\theta^*} &= \frac{2a^2 v}{\mu_{\text{Sun}}}\frac{r^2}{h}a_t \\
\frac{de}{d\theta^*} &= \frac{1}{v}2\left(e+\cos\theta\right)\frac{r^2}{h}a_t \\
\frac{di}{d\theta^*} &= 0 \\
\frac{d\Omega}{d\theta^*} &= 0 \\
\frac{d\omega}{d\theta^*} &= \frac{1}{ev}2\sin\theta\frac{r^2}{h}a_t \\
\frac{dM}{d\theta^*} &= \left[n-\frac{b}{eav}2\left(1+\frac{e^2 r}{p}\right)\sin\theta a_t\right]\frac{r^2}{h}
\end{aligned} \tag{3.10}$$

Equations (3.10) are averaged over one period of the true anomaly θ [71], yielding the average rate of change of the orbital parameters:

$$\left(\frac{d\overline{\boldsymbol{\alpha}}}{d\theta^*}\right)^{\theta,2\pi} = \frac{1}{2\pi}\int_0^{2\pi}\frac{d\boldsymbol{\alpha}}{d\theta^*}d\theta$$

The total variation $\Delta\overline{\boldsymbol{\alpha}}$ of the orbital elements over one orbital period of θ^* can be approximated as:

$$\Delta\overline{\boldsymbol{\alpha}} \approx \int_0^{2\pi} \left(\frac{d\overline{\boldsymbol{\alpha}}}{d\theta^*} \right)^{\theta,2\pi} d\theta$$

if a zero variation in the anomaly of the pericentre is assumed (i.e., $d\theta^* \approx d\theta$). This assumption holds true when the deviation is calculated over one integer number of orbital revolutions, because the periodic variation of the anomaly of the pericentre ω is zero and the secular one is of order 10^{-11} rad for the level of acceleration used in this chapter. Thus, the variation of the orbital element over one revolution can be written as

$$\begin{aligned}
\Delta\overline{e} &= 2k_a \int_{\theta_0}^{\theta_0+2\pi} \frac{1}{h} \left((e+\cos\theta) \Big/ \sqrt{\mu_{\text{Sun}} \left(\frac{1+e^2+2e\cos\theta}{a(1-e^2)} \right)} \right) d\theta \\
\Delta\overline{a} &= \frac{2k_a}{\mu_{\text{Sun}}} \int_{\theta_0}^{\theta_0+2\pi} \frac{a^2}{h} \sqrt{\mu_{\text{Sun}} \left(\frac{1+e^2+2e\cos\theta}{a(1-e^2)} \right)} d\theta \\
\Delta\overline{i} &= 0 \\
\Delta\overline{\Omega} &= 0 \\
\Delta\overline{\omega} &= 2k_a \int_{\theta_0}^{\theta_0+2\pi} \frac{\sin\theta}{eh} \sqrt{\frac{1}{\mu_{\text{Sun}}} \left(\frac{a(1-e^2)}{1+e^2+2e\cos\theta} \right)} d\theta \\
\Delta\overline{M} &= \int_{\theta_0}^{\theta_0+2\pi} \left(\frac{n}{h} \left(\frac{a(1-e^2)}{1+e\cos\theta} \right)^2 - \frac{2bk_a}{eah} \sin\theta \sqrt{\frac{1}{\mu_{\text{Sun}}} \left(\frac{a(1-e^2)}{1+e^2+2e\cos\theta} \right)} + \right. \\
&\qquad \left. - \frac{2ebk_a}{ah} \frac{\sin\theta}{1+e\cos\theta} \sqrt{\frac{1}{\mu_{\text{Sun}}} \left(\frac{a(1-e^2)}{1+e^2+2e\cos\theta} \right)} \right) d\theta
\end{aligned} \tag{3.11}$$

By considering a and e constant within one revolution, the following analytical formulae can be derived after some algebraic manipulations (see Appendix A):

$$
\begin{aligned}
\Delta\bar{e} &= \left[\frac{2k_a}{h}\frac{(1+e)\chi}{ev}\left((1+e)\mathrm{E}\left[\frac{\theta}{2},\frac{4e}{(1+e)^2}\right] + (e-1)\mathrm{F}\left[\frac{\theta}{2},\frac{4e}{(1+e)^2}\right]\right)\right]_{\theta_0}^{\theta_0+2\pi} \\
\Delta\bar{a} &= \left[\frac{2a^2k_a}{\mu_{\mathrm{Sun}}h}\frac{2v}{\chi}\mathrm{E}\left[\frac{\theta}{2},\frac{4e}{(1+e)^2}\right]\right]_{\theta_0,\,e_0}^{\theta_0+2\pi,\,e_0+\Delta\bar{e}} \\
\Delta\bar{i} &= 0 \\
\Delta\bar{\Omega} &= 0 \\
\Delta\bar{\omega} &= \left[-\frac{2k_a}{eh}\frac{\left(1+e^2+2e\cos\theta\right)}{ev}\right]_{\theta_0,\,e_0}^{\theta_0+2\pi,\,e_0+\Delta\bar{e}} \\
\Delta\bar{M} &= \left[2\arctan\left(\sqrt{\frac{1-e}{1+e}}\tan\left(\frac{\theta}{2}\right)\right) - \frac{e\sqrt{1-e^2}\sin\theta}{1+e\cos\theta} + \right. \\
&\quad + \frac{2bk_a}{eah}\left(\frac{1+e^2+2e\cos\theta}{ve} + \right. \\
&\quad \left. \left. + e\frac{2\arctan\left(v\sqrt{a}\,/\sqrt{\mu_{\mathrm{Sun}}}\right)\sqrt{1+e^2+2e\cos\theta}}{v\sqrt{1-e^2}}\right)\right]_{\theta_0,\,e_0}^{\theta_0+2\pi,\,e_0+\Delta\bar{e}}
\end{aligned}
\tag{3.12}
$$

where

$$
v(\theta) = \sqrt{\mu_{\mathrm{Sun}}\frac{1+e^2+2e\cos\theta}{a\left(1-e^2\right)}}
$$

is the orbital velocity, and χ is defined as

$$
\chi(\theta) = \sqrt{\frac{1+e^2+2e\cos\theta}{(1+e)^2}}
$$

Equations (3.12) contain two elliptic integrals to be evaluated only once every orbital period:

$$
\mathrm{F}\left[\frac{\theta}{2},\frac{4e}{(1+e)^2}\right] \tag{3.13}
$$

where

$$\mathrm{F}\left[\phi,\lambda\right]=\int_0^{\phi}\frac{d\varphi}{\sqrt{1-\lambda\sin^2\varphi}}$$

is the incomplete elliptic integral of the first kind and

$$\mathrm{E}\left[\frac{\theta}{2},\frac{4e}{\left(1+e\right)^2}\right] \tag{3.14}$$

where

$$\mathrm{E}\left[\phi,\lambda\right]=\int_0^{\phi}\sqrt{1-\lambda\sin^2\varphi}\,d\varphi$$

is the incomplete elliptic integral of the second kind [71],[134]. Note that the integral kernels (3.12) to be evaluated in $\theta_0+2\pi$ and θ_0 are function only of the semi-major axis and the eccentricity.

The variation of the mean anomaly M strongly influences the consequent deviation, calculated through Eqs. (3.1). Hence, when the primitive function is evaluated in the upper limit $\theta_0+2\pi$, the value of the eccentricity is set equal to $e+\Delta\bar{e}$ to have a better approximation of $\Delta\bar{M}$ in Eqs. (3.12). This allows taking into account the secular variation $\Delta\bar{e}$ over one orbital revolution. Finally, the total variation of the orbital parameters over the thrust arc is determined by integrating Eqs. (3.12) with the Euler method with a step size of one orbital period (i.e., summing up Eqs. (3.12) over the number of revolutions n_{rev}, updating the value of a, e, E, F for each revolution).

$$\Delta\bar{\boldsymbol{\alpha}}_{n_{\mathrm{rev}}}=\sum_{j=1}^{n_{\mathrm{rev}}}\Delta\bar{\boldsymbol{\alpha}}_j\left(a,e,E,F\right)$$

where $\Delta\bar{\boldsymbol{\alpha}}_j\left(a,e,E,F\right)$ comes from the evaluation of Eqs. (3.12) within the integration boundaries $\left[\theta_0^*+\left(j-1\right)2\pi\quad\theta_0^*+j2\pi\right]$, with j an integer number and n_{rev} the number of full revolutions of θ^*.

Accuracy analysis

The accuracy of Eqs. (3.12) is assessed by computing the relative error on the achieved deviation $\delta\mathbf{r}$ between the numerical propagation of Gauss' equations and the semi-analytical formulae:

$$e_r = \frac{\left\| \delta\mathbf{r}_{\text{propagated}} - \delta\mathbf{r}_{\text{estimated}} \right\|}{\left\| \delta\mathbf{r}_{\text{propagated}} \right\|}$$

The deviation $\delta\mathbf{r}$ is calculated considering a push of the asteroid over the angular interval $\left[\theta_0^* \quad \theta_0^* + j2\pi \right]$, with j an integer number and by calculating the resulting displacement right at the end of the thrust arc. The vector $\delta\mathbf{r}_{\text{estimated}}$ is the deviation obtained by means of the analytical formulae (3.12), and $\delta\mathbf{r}_{\text{propagated}}$ is computed through the numerical integration of Gauss' equations (3.10):

$$\Delta\boldsymbol{\alpha} = \int_{\theta_0^*}^{\theta_0^* + j2\pi} \frac{d\boldsymbol{\alpha}}{d\theta^*} d\theta^*$$

Figure 3.2a represents the relative error on the computation of the deviation of Apophis when pushing over an increasing number of orbital revolutions and starting the deviation manoeuvre at different angular positions. In fact, the variation of the orbital parameters over one orbital revolution depends on where the manoeuvre starts along the orbit. In the legend, t_p is the time at the pericentre, t_i is the time when the deviation action commences, and T_{NEO} is the asteroid nominal orbital period. Figure 3.2b shows the relative error for an asteroid with higher eccentricity and inclination ($e = 0.73$, $i = 25$ deg). An adaptive step-size Runge-Kutta-Fehlberg integrator is used for the numerical integration, and the absolute and the relative tolerance are set to 1×10^{-16} and 2.3×10^{-14}, respectively, to obtain a relative error of the order of 10^{-5}. The value of k_a used for the following analyses is $k_a = 2.2\times10^5$ km^3/s^2 for asteroid Apophis (Figure 3.2a) and $k_a = 2\times10^4$ km^3/s^2 for asteroid 1979XB (Figure 3.2b). The reasons that led to these values will be explained in Section 3.3.2.

Other than the accuracy, an advantage of the analytical formulation is a significant reduction in the computational cost with respect to a numerical integration through a Runge-Kutta method. In fact, the CPU time[‡] required for the numerical propagation of Gauss' equations is one order of magnitude higher than that required for the computation of the analytical formulae, as reported in Table 3.1.

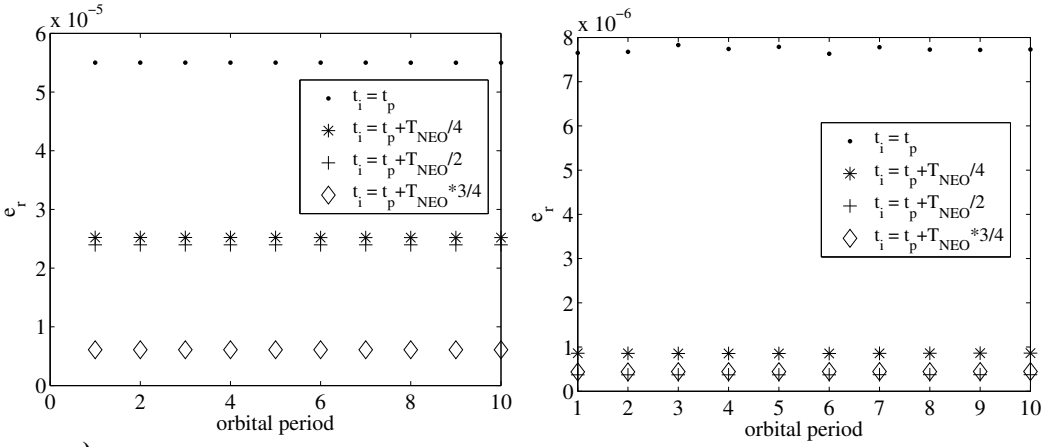

a) **b)**

Figure 3.2: Relative error on the deviation of a) asteroid Apophis and b) asteroid 1979XB.

Table 3.1: Computational time of the analytical and numerical approach.

Orbital periods	Time analytical [s]	Time numerical [s]	Percentage of saving in computational time (analytical/numerical)
1	4.3×10^{-3}	5.6×10^{-2}	92.3
2	6.1×10^{-3}	7.2×10^{-2}	91.5
3	6.8×10^{-3}	9.9×10^{-2}	93.1
4	9.3×10^{-3}	1.2×10^{-1}	92.2
5	1.2×10^{-2}	1.4×10^{-1}	91.7
6	1.3×10^{-2}	1.7×10^{-1}	92.0
7	1.6×10^{-2}	1.9×10^{-1}	91.7
8	1.9×10^{-2}	2.1×10^{-1}	91.1
9	2.0×10^{-2}	2.3×10^{-1}	91.2
10	2.2×10^{-2}	2.5×10^{-1}	91.2

3.2.2. Periodic variation of the orbital parameters

The analytical formulation in Eqs. (3.12) describes the mean variation of the Keplerian elements; hence, it gives a sufficiently accurate estimate of their variation over one full revolution of the true latitude. For smaller angular intervals, the periodic component of the perturbation must be included because its

[‡] Time calculated with a Pentium® 4 CPU at 3.00 GHz, using Mathworks Matlab v. 2007b.

variation is not zero. To this aim, an expression is derived to estimate the periodic component of semi-major axis, eccentricity and argument of the pericentre. The trend of a, e, and ω as functions of θ^* can be approximated by Eqs. (3.15):

$$\begin{aligned} a(\theta^*) &= a_i - C_a \sin\left(\theta_i^* - \theta_p^*\right) + \frac{\Delta\overline{a}}{2\pi}\left(\theta^* - \theta_i^*\right) + C_a \sin\left(\theta^* - \theta_p^*\right) \\ e(\theta^*) &= e_i - C_e \sin\left(\theta_i^* - \theta_p^*\right) + \frac{\Delta\overline{e}}{2\pi}\left(\theta^* - \theta_i^*\right) + C_e \sin\left(\theta^* - \theta_p^*\right) \\ \omega(\theta^*) &= \omega_i + C_\omega \cos\left(\theta_i^* - \theta_p^*\right) + \frac{\Delta\overline{\omega}}{2\pi}\left(\theta^* - \theta_i^*\right) - C_\omega \cos\left(\theta^* - \theta_p^*\right) \end{aligned} \tag{3.15}$$

where the first two terms are the initial condition for the secular evolution at point i (i.e., the point at which the deviation action commences), the third term indicates the secular variation obtained from Eqs. (3.12), and the fourth one is the periodic variation. The coefficients C_a, C_e and C_ω are the amplitudes of the periodic variation. Their value is set through a calibration process: Gauss' equations in Eqs. (3.10) are numerically integrated over one orbit of θ^*. With the vectors $\mathbf{a}_{\text{num},2\pi}$, $\mathbf{e}_{\text{num},2\pi}$, and $\boldsymbol{\omega}_{\text{num},2\pi}$ resulting from the numerical integration of Eqs. (3.10), we then have

$$\begin{aligned} \underset{\sim}{\mathbf{a}}_{2\pi} &= \mathbf{a}_{\text{num},2\pi} - \left(a_i + \frac{\Delta\overline{a}}{2\pi}\left(\theta^* - \theta_i^*\right)\right) \\ \underset{\sim}{\mathbf{e}}_{2\pi} &= \mathbf{e}_{\text{num},2\pi} - \left(e_i + \frac{\Delta\overline{e}}{2\pi}\left(\theta^* - \theta_i^*\right)\right) \\ \underset{\sim}{\boldsymbol{\omega}}_{2\pi} &= \boldsymbol{\omega}_{\text{num},2\pi} - \left(\omega_i + \frac{\Delta\overline{\omega}}{2\pi}\left(\theta^* - \theta_i^*\right)\right) \end{aligned} \tag{3.16}$$

from which the amplitudes of the periodic components can be computed as

$$\begin{aligned} C_a &= \frac{\max_{\theta^*}\left(\underset{\sim}{\mathbf{a}}_{2\pi}\right) - \min_{\theta^*}\left(\underset{\sim}{\mathbf{a}}_{2\pi}\right)}{2} \\ C_e &= \frac{\max_{\theta^*}\left(\underset{\sim}{\mathbf{e}}_{2\pi}\right) - \min_{\theta^*}\left(\underset{\sim}{\mathbf{e}}_{2\pi}\right)}{2} \\ C_\omega &= \frac{\max_{\theta^*}\left(\underset{\sim}{\boldsymbol{\omega}}_{2\pi}\right) - \min_{\theta^*}\left(\underset{\sim}{\boldsymbol{\omega}}_{2\pi}\right)}{2} \end{aligned} \tag{3.17}$$

where $\theta^* \in \left[\theta_i^* \quad \theta_i^* + 2\pi\right]$. Because Eqs. (3.16) come from a numerical integration, this calibration process is time-consuming. However, it needs to be performed once and for all, given the asteroid and the proportionality constant of the acceleration k_a. In fact, it was verified that for low-thrust action, the amplitude of the periodic components of the perturbation is almost constant over a number of integration periods that are sufficient to deviate the asteroid by a considerable distance.

Through the calibration process the second and the fourth terms in Eq. (3.15) can be determined. The former term is required to find the initial condition for the secular variation of the orbital parameters. For example, Figure 3.3 compares the semi-analytical expression of the eccentricity (bold solid line) with the numerical evolution (solid line) for asteroid Apophis. The dotted line represents the mean variation. Table 3.2 summarises the maximum of the relative error between the semi-analytical and the numerical integration of e, a, and ω, over 10 revolutions of θ^*, for low- (Apophis) and a high-elliptic asteroid (1979XB), respectively. The evolution of the relative error is also shown in Figure 3.4.

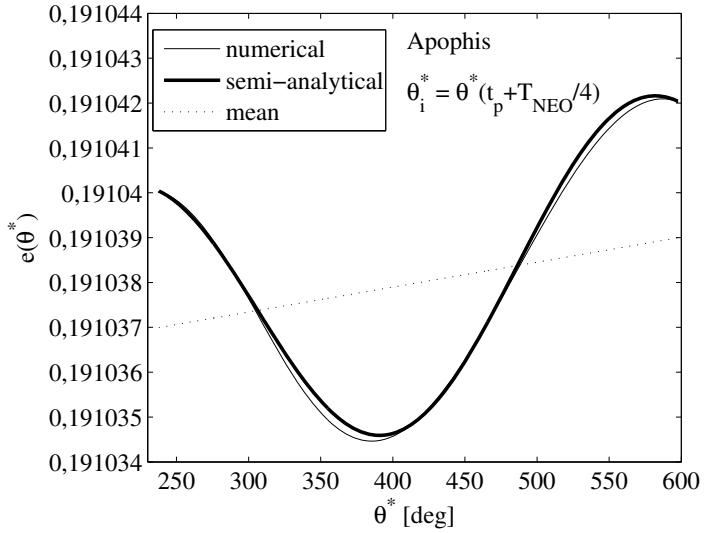

Figure 3.3: Semi-analytical expression of the eccentricity for asteroid Apophis.

Table 3.2: Maximum relative error between the numerical and semi-analytical integration.

	Asteroid Apophis	Asteroid 1979XB
Eccentricity	1.3×10^{-6}	1.4×10^{-7}
Semi-major axis	3.5×10^{-8}	$8.2e\times10^{-8}$
Anomaly of the pericentre	$6.9e\times10^{-7}$	6.6×10^{-8}

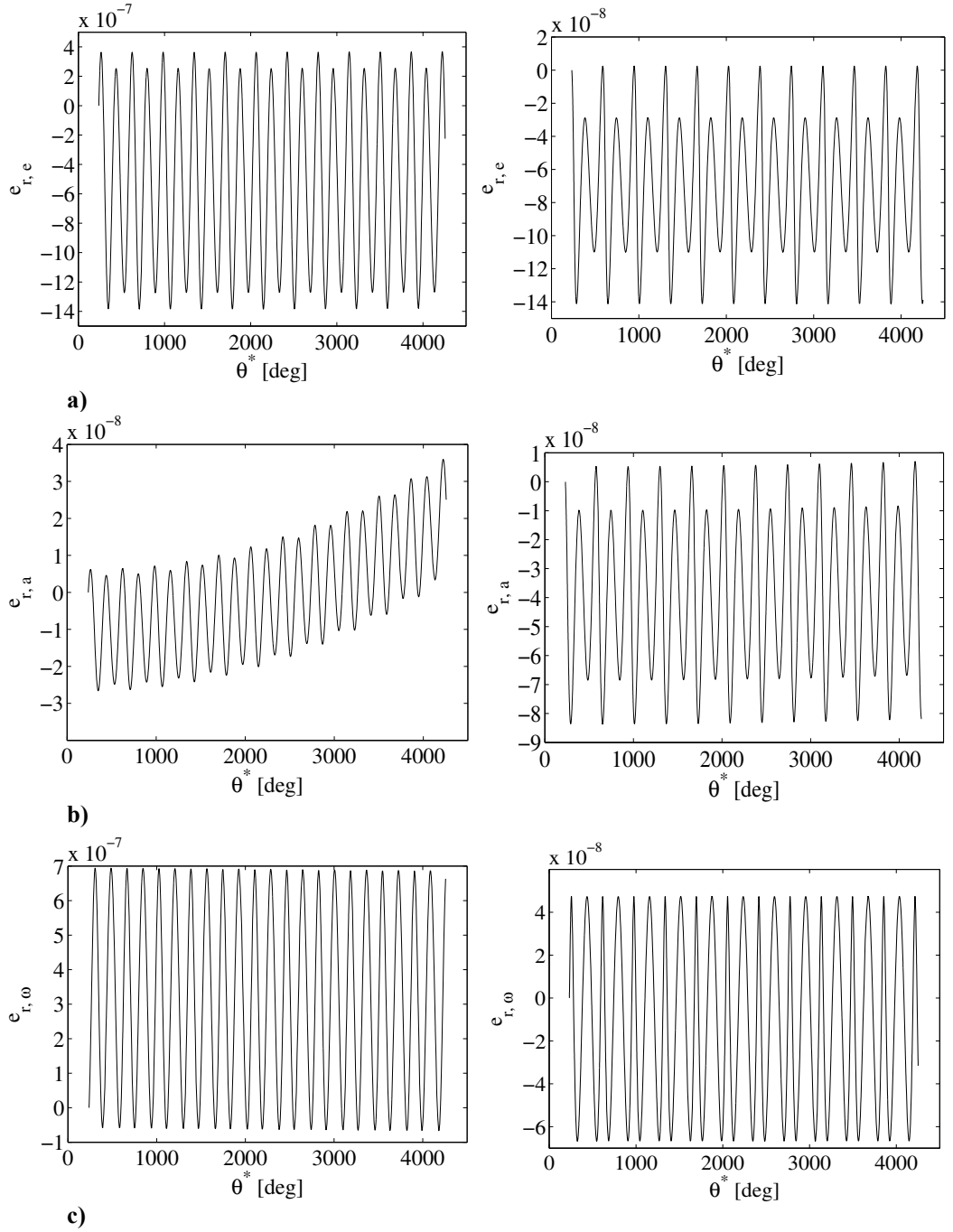

Figure 3.4: Relative error between the numerical and semi-analytical integration of a) the eccentricity, b) the semi-major axis, and c) anomaly of the pericentre for asteroid Apophis (left) and asteroid 1979XB (right).

To properly take into account the periodic variation of the mean anomaly within an interval smaller than one revolution, the corresponding Gauss' equation has to be integrated over θ^*:

$$\frac{dM}{d\theta^*} = \left[n - \frac{b}{eav} 2\left(1 + \frac{e^2 r}{p}\right) \sin\theta a_t \right] \frac{r^2}{h} \tag{3.18}$$

in which $e(\theta^*)$, $a(\theta^*)$, and $\omega(\theta^*)$ are expressed through Eqs. (3.15). The relative error on M with respect to the full integration of Eqs. (3.10) is represented in Figure 3.5.

Note that introducing the periodic terms allows for the computation of the evolution of the orbital elements starting from any angular position along the orbit. In fact, if the point when the deviation action commences [i.e., point i in Eqs. (3.15)] is different from the pericentre, the initial mean parameters are different from the initial osculating elements. The periodic terms ensure the required accuracy for a deviation manoeuvre starting and stopping at any angular position. This would have not been achieved by using other formulations [81]–[83] that account only for the secular variations.

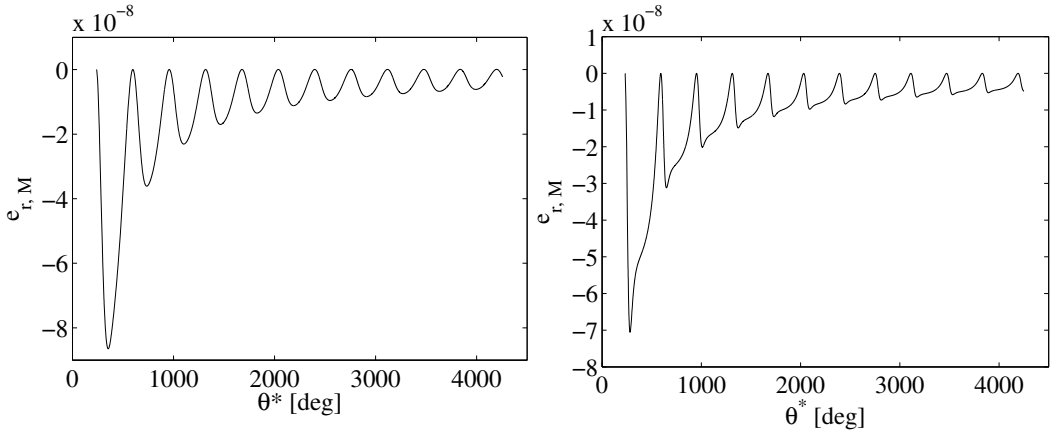

a) **b)**

Figure 3.5: Relative error between the numerical and semi-analytical integration of the mean anomaly for a) asteroid Apophis and b) asteroid 1979XB.

3.2.3. Time formulation

In some applications, the semi-analytical formulae introduced in Section 3.2.1 and 3.2.2 are enough to describe a low-thrust trajectory. The variation of the orbital parameters over an integer number of full revolutions of the angle θ^* can be calculated directly from Eqs. (3.12); for the last revolution, the periodic components are added to the secular variations through Eqs. (3.15). This approach, called *latitude formulation* in the following, does not use time as independent variable. It allows a considerable saving in computational time while

still providing good accuracy, comparable with a low-tolerance numerical integration.

However, the time is required when dealing with the asteroid deviation problem, because the component of the deviation associated to the shift in time has to be taken into account. In fact, the latitude formulation accounts only for the shift in position of the asteroid. Given the thrust arc $[t_i \quad t_e]$, we want to apply the described semi-analytical formulation to find the displacement of the asteroid after a given time. Equations (3.12) are used to compute the variation of the orbital elements over the number of full revolutions contained in the time interval $[t_i \quad t_e]$. For the remainder of the thrusting arc, the element differences are calculated using Eqs. (3.15) and (3.18). The interval $\Delta\theta^*$ corresponding to the time interval $[t_i \quad t_e]$ is computed by numerically integrating Eq. (3.9). Note that the terms corresponding to the secular variation of the parameters in Eqs. (3.15) are calculated updating $\Delta\overline{a}$, $\Delta\overline{e}$, and $\Delta\overline{\omega}$ at each orbital revolution.

Given the asteroid identification number id_{NEO} and the proportionality constant of the acceleration k_a, the calibration procedure gives the amplitude of the periodic component of *a*, *e* and ω (*step 0*). Once computed, the values of C_a, C_e, and C_ω are kept constant for every $t \in [t_i \quad t_e]$ and for the evaluation of the variation of the orbital elements over different time intervals, for a given asteroid (i.e., a given set of nominal orbital elements). The algorithm proceeds with the calculation of the upper limit on the number of revolutions contained in the interval $[t_i \quad t_e]$; the quotient of the division between $t_e - t_i$ and the nominal period of the asteroid is rounded to the nearest integer towards infinity[§] (*step 1*). In fact, due to the perturbation introduced by the low-thrust action, the time to perform a full revolution of θ^* is different from that of the unperturbed orbit. For each revolution, the value of the secular variation of the orbital parameters is computed with Eqs. (3.12) (*step 2*), updating *a* and *e* at each integration step

[§] The quotient of the division between t_e-t_i and the nominal period of the asteroid is rounded to the nearest integer towards infinity if the thrust is given in the direction of the velocity vector. Otherwise, if the thrust is given in the opposite direction with respect to the velocity vector, the period of the deviated orbit will decrease, hence the number of revolutions along the perturbed orbit may be greater than the number of revolutions along the nominal orbit.

(which is one period long) and recalculating the elliptic integrals in Eqs. (3.13) and (3.14). Once the secular variations are available (*step 3*), the value of $\Delta\theta^*$ corresponding to the thrust arc and the exact number of revolutions are computed through Eq. (3.9), with the orbital parameters computed through Eqs. (3.15). The secular variations of the parameters calculated in *step 2* are added up over the number of full revolutions (*step 4*), whereas the calculation of the variation of the orbital elements in the remainder of the thrust arc is performed through the evaluation of Eqs. (3.15) and the integration of Eq. (3.18) (*step 5*). Note that $a(\theta^*)$, $e(\theta^*)$, and $\omega(\theta^*)$, given by Eqs. (3.15), are calculated updating the values of $\Delta\overline{a}$, $\Delta\overline{e}$, and $\Delta\overline{\omega}$ at each revolution. The output of the algorithm is the total variation of the orbital elements over the interval $\left[t_i \quad t_e\right]$. The overall process is illustrated in Figure 3.6.

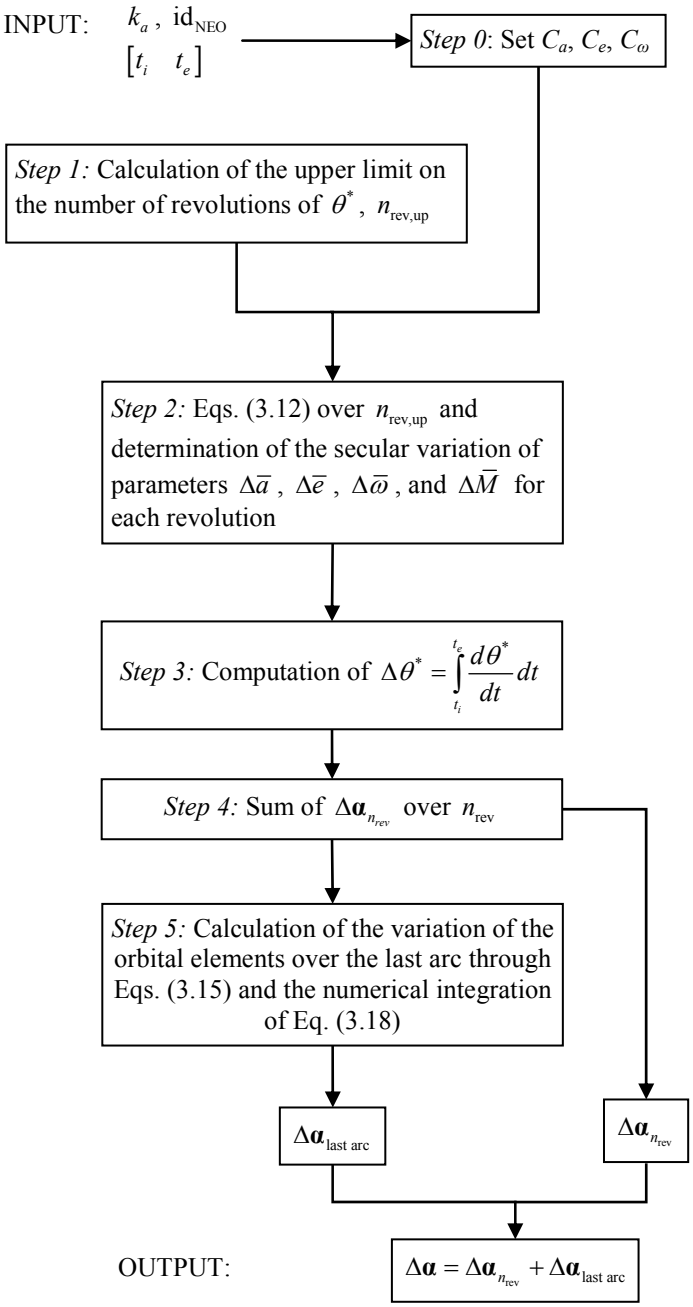

Figure 3.6: Time-formulation algorithm.

Accuracy analysis

The accuracy of the time formulation is verified by computing the relative error $e_{r,\ \mathrm{time\ formulation}}$ between the deviation $\delta\mathbf{r}_{\mathrm{estimated,\ tf}}$, calculated through the algorithm summarised in Figure 3.6, and the deviation $\delta\mathbf{r}_{\mathrm{propagated,\ tf}}$, computed with the numerical integration of Eqs. (3.3).

$$e_{r,\,\text{time formulation}} = \frac{\left\| \delta\mathbf{r}_{\text{propagated, tf}} - \delta\mathbf{r}_{\text{estimated, tf}} \right\|}{\left\| \delta\mathbf{r}_{\text{propagated, tf}} \right\|}$$

The relative error is computed for increasing values of the proportionality constant k_a. Figure 3.7a and 3.7b report $e_{r,\,\text{time formulation}}$ calculated with the nominal value of k_a (set in Section 3.3.2), $10\,k_a$ and $100\,k_a$, respectively, for asteroids Apophis and 1979XB. The values of $e_{r,\,\text{time formulation}}$ are plotted against the push time $t_e - t_i$, which was set equal to the time-to-MOID $\Delta t = t_{\text{MOID}} - t_i$ (i.e., $t_e = t_{\text{MOID}}$).

The high value of the relative error when $\Delta t < 1T_{\text{NEO}}$ is due to the approximation introduced with the periodic components of the orbital elements in Eqs. (3.15). For $\Delta t < 1T_{\text{NEO}}$, the difference between orbital elements of the perturbed and the nominal orbit $\delta\boldsymbol{\alpha}$ is of the same order of magnitude of the approximation error of the periodic components. As a consequence, the relative error difference of the orbital elements

$$e_{r,\,\delta\boldsymbol{\alpha}} = \frac{\delta\boldsymbol{\alpha}_{\text{propagated, tf}} - \delta\boldsymbol{\alpha}_{\text{estimated, tf}}}{\delta\boldsymbol{\alpha}_{\text{propagated, tf}}}$$

is high. In particular, the error on the assessment of the orbital parameters *a*, *e*, and ω affects the difference of mean anomaly, which significantly contributes to the terms in Eqs. (3.1). Figure 3.8 represents the relative error on δM for two asteroids.

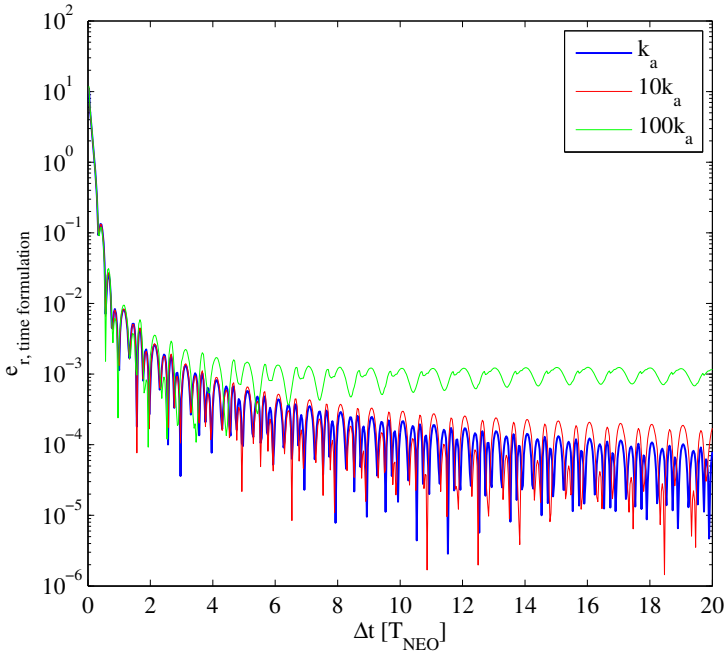

a)

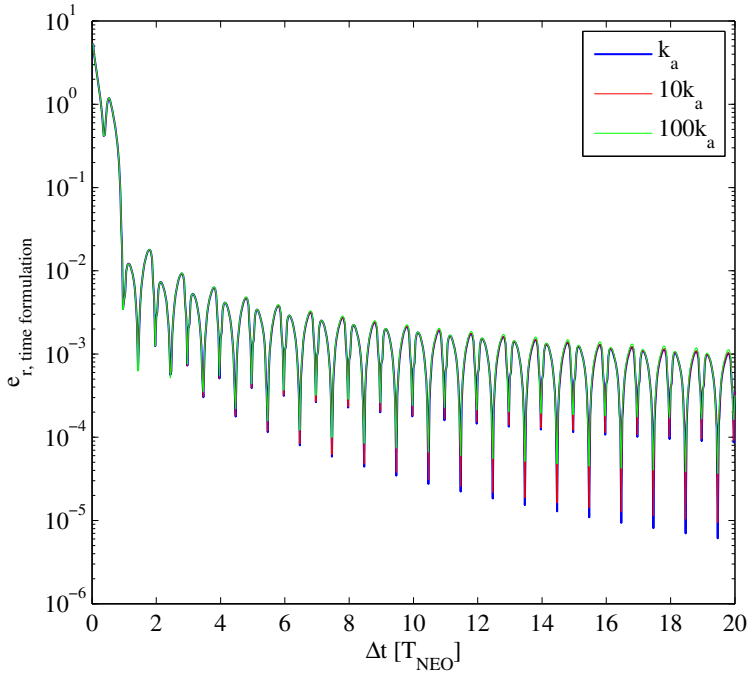

b)

Figure 3.7: Relative error of the time formulation for a) asteroid Apophis (k_a=2.2×10^5 km^3/s^2) and b) asteroid 1979XB (k_a=2×10^4 km^3/s^2).

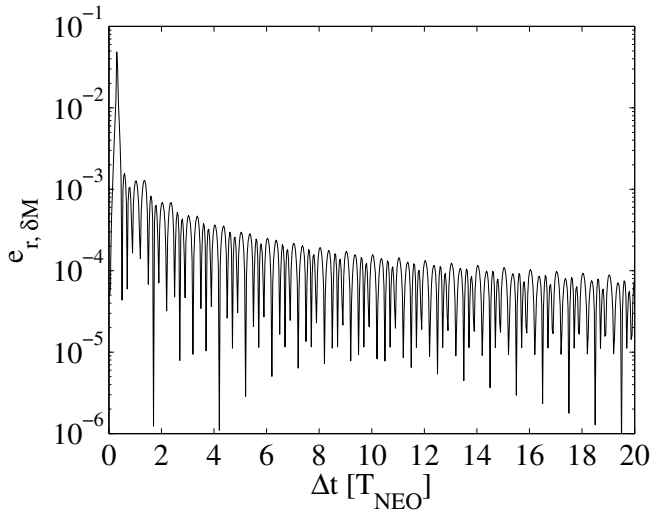

a)

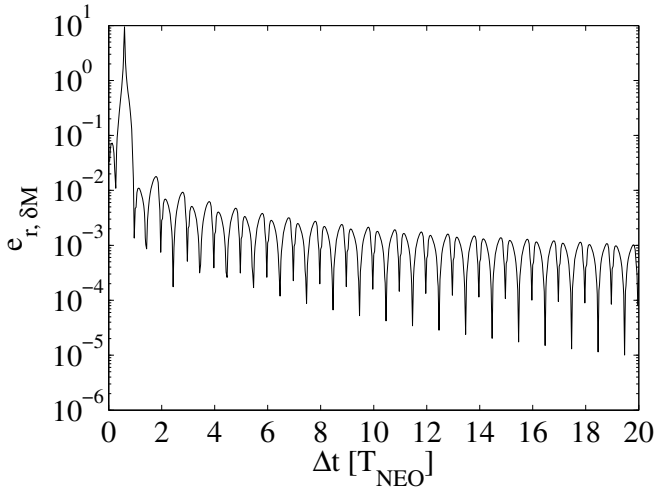

b)

Figure 3.8: Relative error on δM for a) asteroid Apophis and b) asteroid 1979XB.

Hence, the time formulation can be substituted to the numerical integration only for a thrust arc Δt longer than one orbital revolution (i.e., the relative error in Figure 3.7 is lower than 10^{-2}). On the other hand, when low-thrust strategies are selected, the thrust arc is, in general, longer than $1\,T_{\mathrm{NEO}}$. Figure 3.9 depicts the percentage of saving in computational time of the semi-analytical approach with time formulation, with respect to the numerical integration. When $\Delta t > 1T_{\mathrm{NEO}}$ the gain is around 40%, and it increases with the length of the push arc.

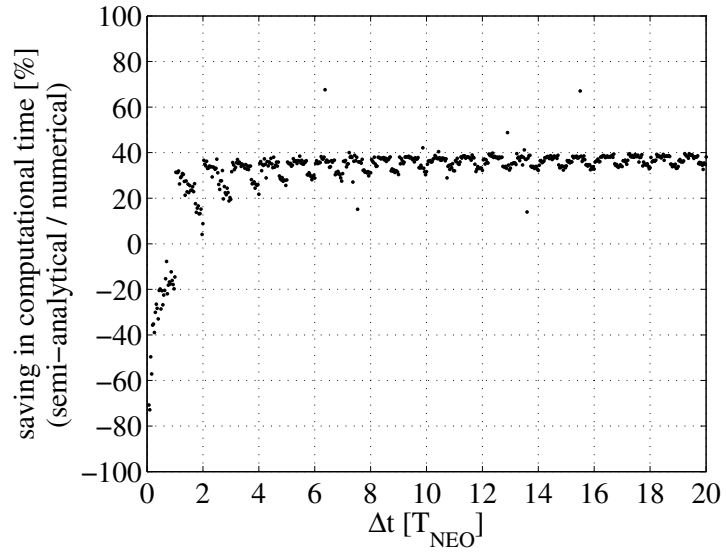

a)

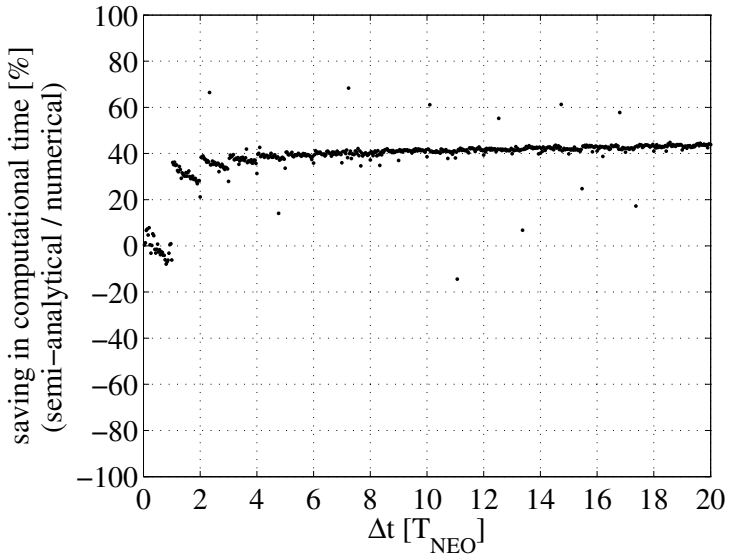

b)

Figure 3.9: Percentage of savings in computational time by using the semi-analytical time formulation with respect to the numerical integration of Gauss' equations. a) Asteroid Apophis and b) asteroid 1979XB.

3.3. Mission options for low-thrust deviation

In this section, the analysis of some NEO deviation missions is presented. The semi-analytical approach is used to compute the displacement of the position of the asteroid at the MOID point after a low-thrust deviation manoeuvre and a shape-based approach is adopted to model the transfer trajectory. A global search is performed over a wide range of launch dates and times of flight to find a set of

optimal solutions according to three criteria: the mass at launch, the warning time (i.e., elapsed time between time at launch and time at the MOID), and the total deviation. Each solution of the multi-objective global optimisation represents a complete mission design, which includes the transfer leg from the Earth to the asteroid interception, and the deflection manoeuvre over a finite period of time.

3.3.1. Targets selection

Four asteroids are selected, based on their orbital parameters: Apophis with low eccentricity and inclination and 1979XB with high eccentricity and high inclination ($e = 0.73$ and $i = 25.14$ deg). Castalia and Itokawa, with a mass of 1.4×10^{12} kg and 3.5×10^{10} kg respectively, are selected to analyse the influence of the mass of the asteroid. The orbital elements that are most significant for the following analysis are reported in Table 3.3, together with the minimum orbit intersection distance and the mass of the asteroid. The MOID Δr is calculated using the Earth's ephemerides on 27 January 2027 at 12:00 hrs, taken from analytic ephemerides which approximate JPL ephemerides de405[**]. As already pointed out, the actual MOID varies with time [132], due to the actual orbit of both the Earth and the asteroid. On the other hand, the aim of this work is not to reproduce any specific and realistic impact scenario, but rather to assess the performance of a low-thrust deviation action over a wide range of mission opportunities. A more accurate calculation of the MOID would produce a more precise estimation of the actual achievable deviation but would not invalidate the results in this dissertation.

Table 3.3: Asteroids orbital and physical parameters.

Asteroid	Semi-major axis [AU]	Eccentricity	Inclination [deg]	MOID [km]	Mass [kg]
Apophis	0.92	0.19	3.33	30,706	4.6×10^{10}
1979XB	2.35	0.73	25.14	3,725,733	4.4×10^{11}
Castalia	1.06	0.48	8.9	3,013,439	1.4×10^{12}
Itokawa	1.32	0.28	1.62	2,769,832	3.5×10^{10}

[**] Data available online at http://naif.jpl.nasa.gov/naif/pds.html [Retrieved 28 January 2009].

3.3.2. Spacecraft model and optimisation problem definition

As a reference case, we consider a spacecraft equipped with a solar mirror with a diameter of 100 m and a dry mass m_d [135] of 895 kg. The spacecraft is launched at time t_0 (selected in a range of 20 years before the possible collision), with maximum hyperbolic excess velocity of 3.5 km/s, and equipped with an engine delivering an unlimited thrust with an $I_{sp} = 3000$ s. Once the spacecraft has intercepted the asteroid, the low thrust deviation manoeuvre is performed from t_i up to the time at the MOID (i.e., $t_e = t_{\mathrm{MOID}}$); no propellant is assumed to be consumed during the deviation phase, but a 25% margin on the total wet mass is considered, to account for station-keeping and mirror deployment operations. Table 3.4 summarises the key parameters of the mission.

Table 3.4: Mission characteristics.

I_{sp}	3000 s
d_m	100 m
m_d	895 kg
Margin on m_0	25%
$v_{\infty,\max}$	3.5 km/s
$\left(t_{\mathrm{MOID}} - t_0\right)_{\max}$	20 y

The value of k_a is set according to the model of the solar collector developed in [126]. The value of k_a is chosen to obtain the same order of acceleration provided by a solar inflatable mirror, with a diameter d_m of between 100 and 110 m, along the range of distances from the Sun covered by the asteroid during its motion. Figure 3.10 compares the acceleration computed through the full model described in [126] against Eq. (3.8) over a feasible range of distances for asteroid Apophis. Between the orbit apocentre and pericentre, Eq. (3.8) (solid line) gives an acceleration comparable with that calculated through the full solar collector model (dashed lines). Note that Eq. (3.8) does not take into account the decrease of the mass of the asteroid due to the ablation of the material.

Table 3.5 reports the values of the acceleration constant k_a for each asteroid, together with the average of the thrust acceleration on the nominal orbit

of the asteroid, according to Eq. (3.8), the average of the Sun gravitational acceleration, and the ratio between the two accelerations.

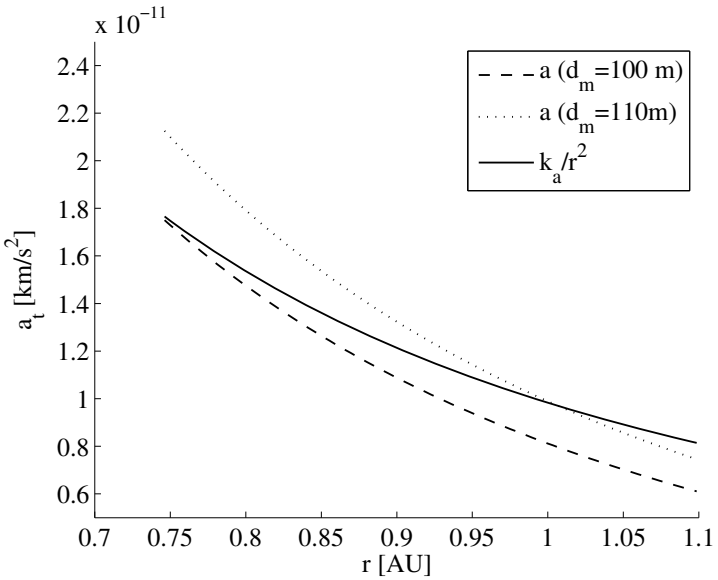

Figure 3.10: Magnitude of the acceleration for Apophis.

Table 3.5: Acceleration constant and average of the accelerations acting on the asteroid.

Asteroid	k_a [km^3/s^2]	Average thrust acceleration [km/s^2]	Average gravitational acceleration [km/s^2]	Acceleration ratio
Apophis	2.2×10^{5}	1.2×10^{-11}	6.8×10^{-8}	1.7×10^{-4}
1979XB	2.0×10^{4}	3.5×10^{-13}	9.0×10^{-9}	3.9×10^{-5}
Castalia	6.5×10^{3}	3.4×10^{-13}	4.8×10^{-8}	7.0×10^{-6}
Itokawa	2.0×10^{4}	5.5×10^{-12}	3.3×10^{-8}	1.6×10^{-5}

A multi-objective optimisation is performed to minimise the vector objective function:

$$\min\left(\left[\, m_0 \quad t_w \quad -\left(\|\Delta\mathbf{r}+\delta\mathbf{r}\|-\|\Delta\mathbf{r}\|\right)\right]\right) \tag{3.19}$$

with respect to the launch date, the time of flight and the hyperbolic excess velocity. In Eq. (3.19) m_0 is the wet mass of the spacecraft at the Earth:

$$m_0 = \left(m_d + m_p\right)\cdot 1.25 \tag{3.20}$$

where m_p is the propellant mass for the transfer, $t_w = t_{\mathrm{MOID}} - t_0$ is the warning time, and $\|\Delta\mathbf{r}+\delta\mathbf{r}\|$ is the total deviation to be maximised [see Eq. (3.5)]. Note that, from the analysis presented in Section 2.1.3 the strategies that aims at

maximising b^* are more accurate than the ones aiming at the maximisation of $\delta\mathbf{r}$. However, in the following, we use the latter strategy, because it provides good and reliable results for medium to long times-to-MOID and requires a lower computational cost[††].

Low-thrust transfer trajectory

The transfer trajectory is calculated through a shape-based method (see [118]). The low-thrust arc is obtained by shaping the trajectory through a set of pseudo-equinoctial elements[‡‡] and the required control to follow that trajectory is obtained through algebraic computation by an inverse method:

$$\mathbf{u} = \frac{d^2\mathbf{r}}{dt^2} + \mu_{\text{Sun}} \frac{\mathbf{r}}{r^3}$$

where $\mathbf{u}$ is the control acceleration vector and $\mathbf{r}$ the position vector in a Cartesian reference frame. An exponential shape is adopted, described by three shape parameters $\boldsymbol{\rho} = \begin{bmatrix} \rho_1 & \rho_2 & \rho_3 \end{bmatrix}^T$:

$$\breve{\boldsymbol{\alpha}} = \breve{\boldsymbol{\alpha}}_0 + \breve{\boldsymbol{\alpha}}_1 e^{\boldsymbol{\rho}(L-L_0)}$$

where $\breve{\boldsymbol{\alpha}}$ indicates the vector of pseudo-equinoctial non-singular elements. For further details on the trajectory model the reader can refer to [118],[136].

Because in this test case the dry mass of the spacecraft is set, the propellant mass required for the transfer trajectory is computed through the following expression:

$$m_p = m_d \left(\exp\left[\int_{L_0}^{L_f} \frac{\|\mathbf{u}\|}{I_{sp} g_0} \frac{dt}{dL} dL \right] - 1 \right) \tag{3.21}$$

[††] To have a precise estimate of the miss distance from the Earth, the projection on the b-plane of $\|\Delta\mathbf{r} + \delta\mathbf{r}\|$ should be computed. Here, however, we are not interested in computing the minimum distance from the Earth, rather to optimise the interception and deflection manoeuvres and we do not consider the Earth to be at the MOID point when the asteroid crosses it.

[‡‡] The elements are called pseudo-equinoctial because they do not always satisfy exactly Gauss' equations unless the thrust is zero.

where $L = \theta + \omega + \Omega$ indicates the true longitude that is used as independent variable in place of the time, and L_0 and L_f represent the initial and final true longitude of the trajectory. Additionally, the shape-based approach introduces the following constraint on the time of flight:

$$ToF = \int_{L_0}^{L_f} \frac{dt}{dL} dL$$

As a consequence, a constraint on the time of flight has to be included in the optimisation problem (3.19):

$$C_{ToF}: \quad \int_{L_0}^{L_f} \frac{dt}{dL} dL - ToF < 10 \text{ days} \tag{3.22}$$

The value of the parameter ρ_1, which is mostly responsible for the time of flight constraint satisfaction, is determined within an inner Newton loop of the shape-based trajectory-model generating algorithm, whereas the remaining two shape parameters are set as optimisation parameters, along with the launch date t_0, the time of flight ToF, the integer number of revolutions around the Sun n_{rev}, and the launch conditions. The design variables vector of the global optimisation is therefore:

$$\mathbf{x} = \begin{bmatrix} t_0 & ToF & n_{\text{rev}} & v_\infty & \alpha_{v_\infty} & \delta_{v_\infty} & \rho_2 & \rho_3 \end{bmatrix}$$

where the escape velocity vector provided by the launcher is fully determined by its magnitude v_∞, the in-plane angle α_{v_∞} measured from the tangent direction to the projection of the velocity vector $\mathbf{v}_\infty$ on the orbital plane, and the out-of-plane angle δ_{v_∞} between the velocity vector $\mathbf{v}_\infty$ and its projection on the orbital plane (measured from the orbital plane to $\mathbf{v}_\infty$). ρ_2 and ρ_3 are selected within the range $\begin{bmatrix} -0.5 & 0.5 \end{bmatrix}$, the number of integer revolution is chosen between 0 and 3, and the time of flight between 25 and 1500 days.

The solution of the multi-objective optimisation problem in Eq. (3.19) is found through a hybrid optimisation approach, blending a stochastic search with an automatic solution space decomposition technique [116],[133] (a more extensive explanation of the multi-criteria optimisation problem formulation will be given in Chapter 4).

3.3.3. Results

Apophis deviation mission

Figure 3.11 represents a set of launch opportunities for a deviation mission to Apophis, assuming that the asteroid is at the MOID on the 7th July 2027 (10,049 MJD2000). Note that the Earth is not at the MOID on the same date, because the aim of these test cases is to measure the achieved deviation, not to reproduce a real impact scenario.

The launch dates and transfer times in Figure 3.11 correspond to the set of Pareto-optimal solutions in Figure 3.12a. In Figure 3.11, we can see that a wide range of launch opportunities are available every year between 2010 and 2030, though the required transfer time might change significantly. In particular, we can identify two groups of solutions around 5000 MJD2000 and 7500 MJD2000 with a short transfer time, a scattered set of solutions with a transfer time between 500 and 600 days, and three groups of solutions with long transfer time. Note that we used a non-exhaustive[§§] stochastic search process; therefore, more solutions can exist in the same range of launch dates. In Figure 3.12a, the three axes represent the components of the objective function equation (3.19); the z axis contains the magnitude of the deviation $\|\delta\mathbf{r}\|$. The mass into space m_0, which is limited to 5000 kg in this analysis, is a function of the mass of propellant required to perform a transfer from the Earth to the asteroid. In the case of Apophis, a mission using a solar collector with a diameter of 100 m would achieve deviations of the order of 10^6 km, in a time range of 20 years of warning time, and solutions with 1000 days of warning time have a deviation of about 20,000 km.

[§§] The stochastic approach of the search process is non-exhaustive in the sense that it does not guarantee to find a feasible (or optimal) solution with probability 1, but it searches non-systematically until a specific stop criterion is satisfied.

The modulus of the achieved deviation is proportional to the length of the thrust interval $\Delta t = t_{\mathrm{MOID}} - t_i$ and has a periodic trend with the angular position of the point of interception, as shown in Figure 3.12b. The colour scale represents the value of the true anomaly (in degrees) at interception.

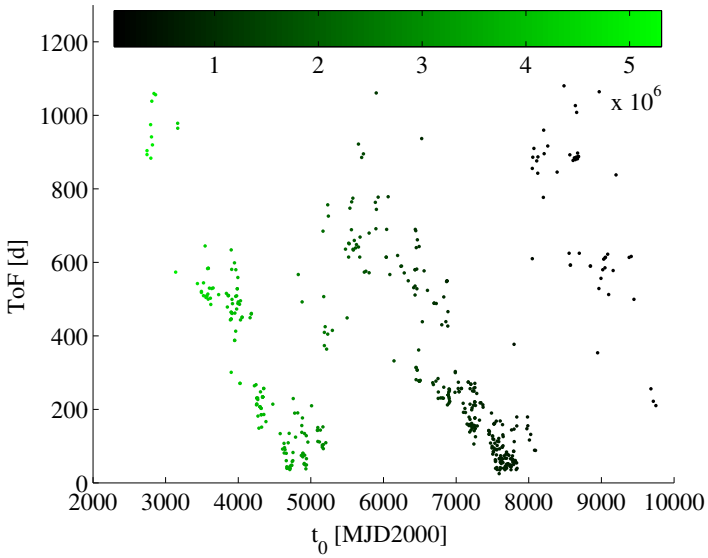

Figure 3.11: Launch opportunities for a deviation mission to Apophis. The colour scale represents the value of the achieved deviation at the MOID.

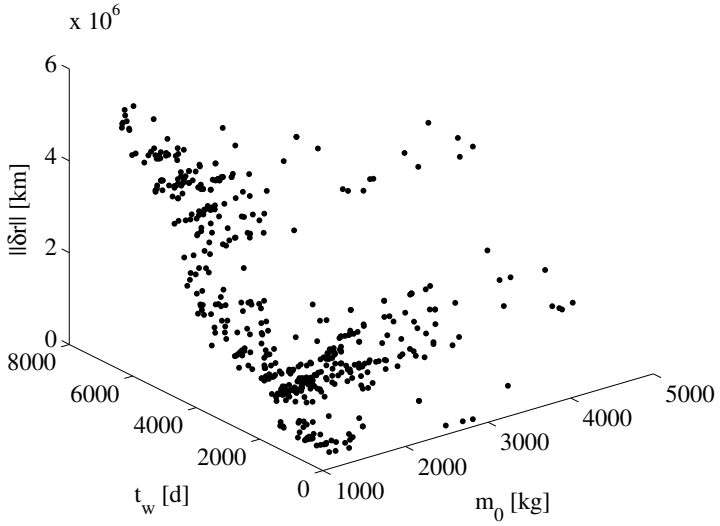

a) Pareto front for a deviation mission to Apophis.

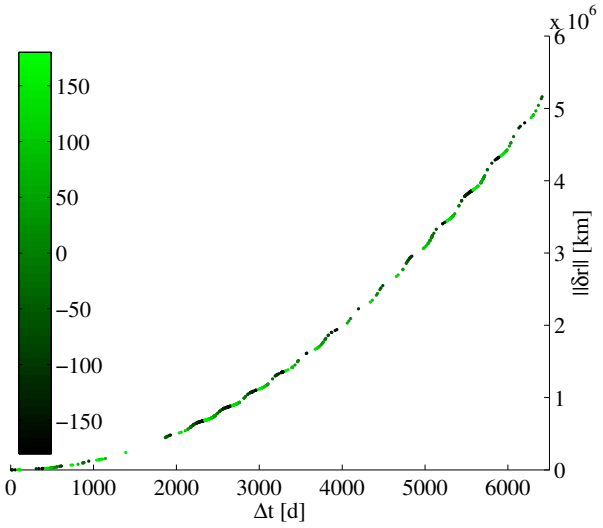

b)

Figure 3.12: Deviation mission to Apophis: a) Pareto front. Launch mass, warning time and magnitude of the deviation are represented on the three axes. b) Achieved deviation as a function of the time length of the thrust arc.

Neglecting the transfer phase and assuming the same value of the acceleration constant k_a, the sensitivity of the deviation to the in-plane orbital elements a and e of the nominal orbit of the asteroid can now be investigated. Several values of semi major-axis and eccentricity are considered, covering the range of in-plane elements for a group of 338 Aten asteroids from the JPL catalogue[***]. The range considered for semi-major axis in astronomical units is $0.64 < a < 0.99$, and the range for eccentricity is $0.013 < e < 0.89$. For each value of eccentricity and semi-major axis, the corresponding orbit is computed keeping the other orbital elements equal to the parameters of Apophis. The deviation is calculated for increasing values of the pushing time, from 1 day up to 20 years before the date at the corresponding MOID.

Figure 3.13a shows the different nominal orbits obtained starting from the orbital elements of Apophis by changing the value of the semi-major axis (see Apophis orbit in bold line, the Earth orbit in dashed line, the crosses indicate the MOID points), and Figure 3.13b the true anomaly of the MOID (the cross marker indicates Apophis case).

The modulus of the deviation of the asteroid at the MOID is displayed in Figure 3.14a as a function of the pushing time. Note that as a consequence of the

[***] Data available online at http://neo.jpl.nasa.gov/cgi-bin/neo_elem [Retrieved 05 August 2008].

acceleration law, which goes with the inverse of the distance from the Sun squared, the achievable deviation for a fixed warning time decreases with the increase of the nominal semi-major axis. This is clear if we analyse the first equation of Eqs. (3.3) and we substitute the value of the acceleration:

$$\frac{da}{dt} = \frac{2a^2 v}{\mu_{\text{Sun}}} \frac{k_a}{r^2}$$

In fact, this term is proportional to $a^{-1/2}$ and is the term that mostly influences the value of the deviation, because it contributes to the shift in time.

As we can appreciate from Figure 3.14b, the relative error with the precise numerical integration does not exceed 10^{-2}, which means that the accuracy of the analytical formulae is good in the selected range of values of the semi-major axis.

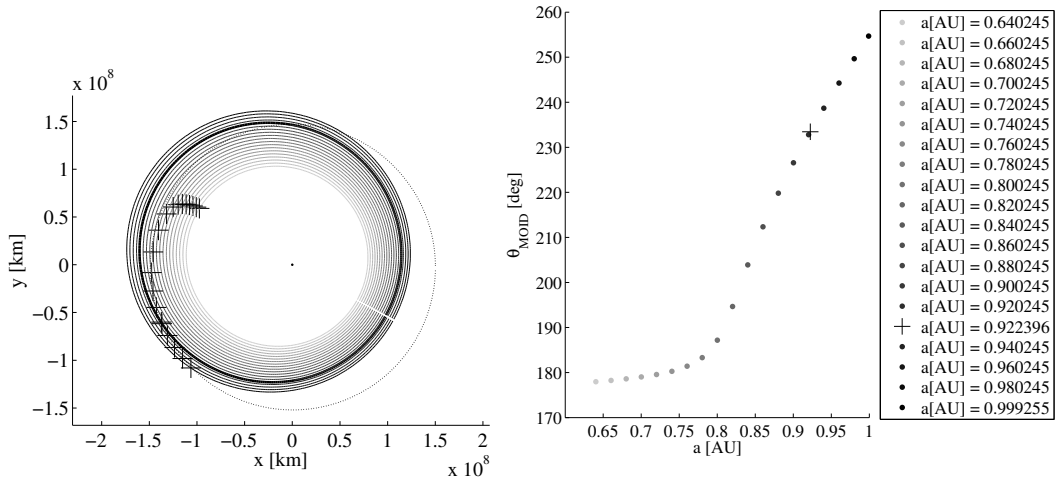

a) **b)**

Figure 3.13: Orbit and MOID characteristics for different values of semi-major axis starting from Apophis case: a) asteroid orbits and b) true anomaly of the MOID.

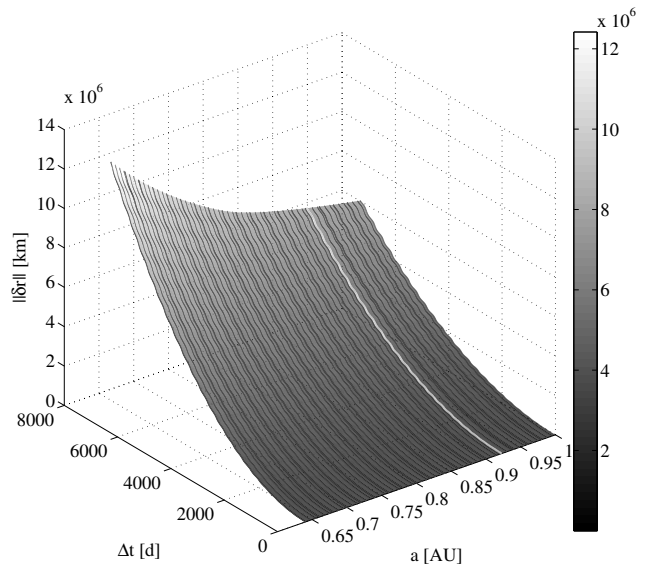

a)

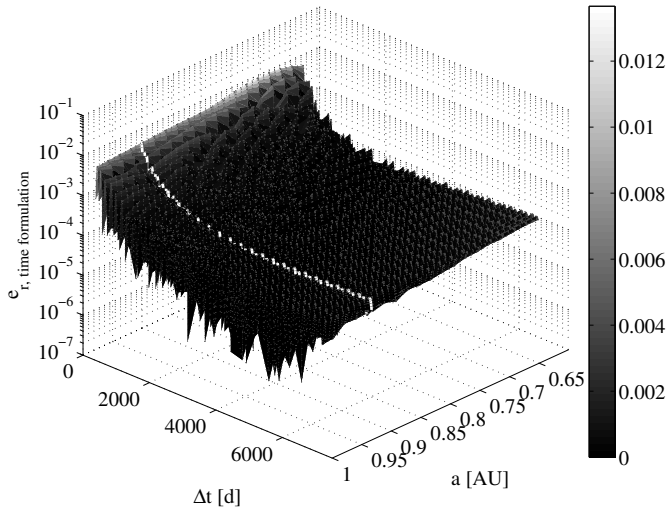

b)

Figure 3.14: Sensitivity of the deviation to the semi-major axis: a) deviation achieved for orbits with different values of semi-major axis and for increasing values of thrust interval and b) relative error for different values of semi-major axis. The white line represents Apophis case (a = 0.922 AU).

The sensitivity analysis to the eccentricity is shown in Figure 3.16. The resulting orbits and MOID obtained by changing the eccentricity are shown in Figure 3.15. The orbit of Apophis is the bold line in Figure 3.15a, and the Earth orbit is represented by the dashed line. In this case (see Figure 3.16a), for the same pushing time, the magnitude of the deviation increases, with the increase of the eccentricity. The fluctuations within the orbital period are also more visible. The local maxima correspond to an interception point prior to the pericentre.

Note that a good accuracy is also assured for different values of eccentricity within the range $0.013 < e < 0.89$. Figure 3.16b shows the relative error of the time formulation. Note that the accuracy of the time formulation is, in general, lower than the accuracy of the latitude formulation. In fact, the former needs a further operation, which is the determination of the value of $\Delta\theta^*$ corresponding to the thrust arc and the exact number of revolutions (see step 3 in Figure 3.6).

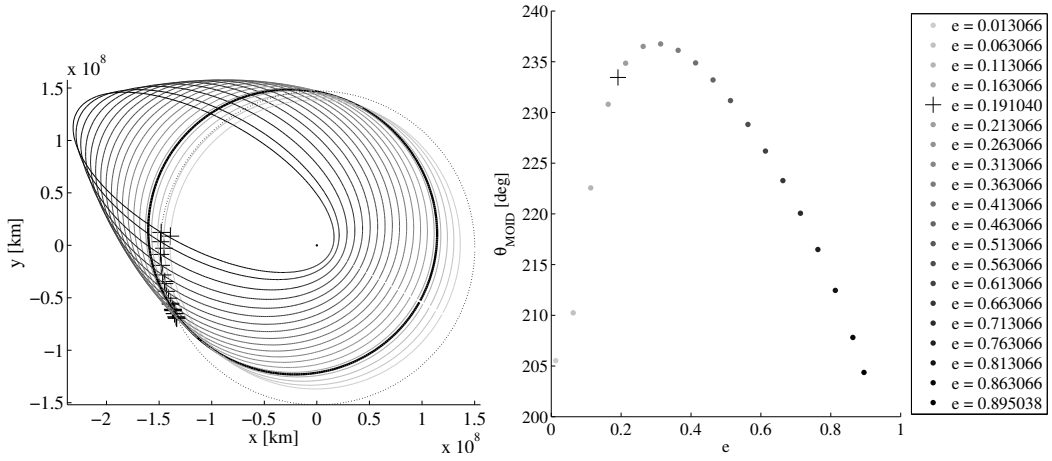

a) **b)**

Figure 3.15: Orbit and MOID characteristics for different values of eccentricity starting from Apophis case: a) asteroid orbits and b) true anomaly of the MOID.

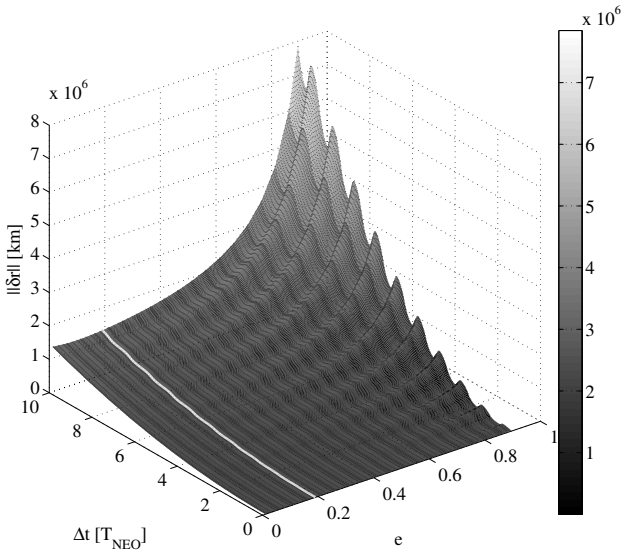

a)

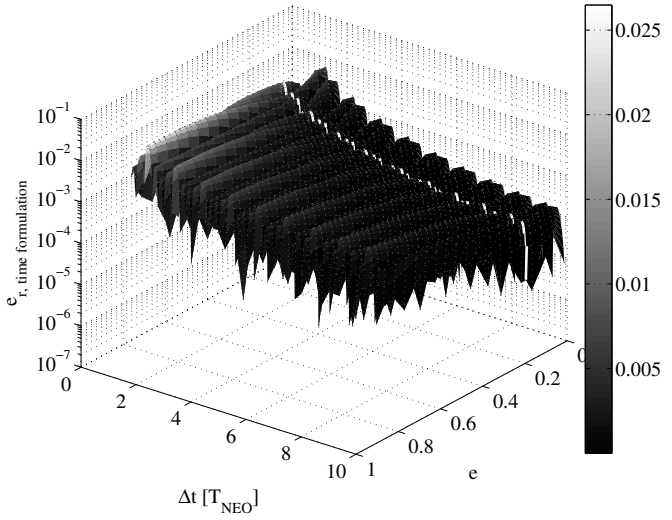

b)

Figure 3.16: Sensitivity of the deviation to the eccentricity: a) deviation achieved for orbits with different values of eccentricity and for increasing values of thrust interval and b) relative error for different values of eccentricities. The white line represents Apophis case (e = 0.191).

1979XB deviation mission

The launch opportunities for a deviation mission to asteroid 1979XB are represented in Figure 3.17. The NEO is at the MOID on the 20th May 2030 (11,097 MJD2000). In this case, the launch opportunities are grouped in single strips, with an average transfer time ranging between around 200 and 800 days. The corresponding set of Pareto-optimal solutions is shown in Figure 3.18a, which shows that the maximum achieved deviation is of the order of 10^5 km, because the mass of the asteroid is 4.4×10^{11} kg, significantly higher than the mass of Apophis.

The high eccentricity of the orbit of asteroid 1979XB emphasises the periodicity of the achievable deviation with Δt (see Figure 3.18b, in which the colour scale indicates the angular position at interception). The considerable step in the value of the deviation is in correspondence of an interception before the pericentre. This effect is amplified for this asteroid, because its orbit is highly elliptical.

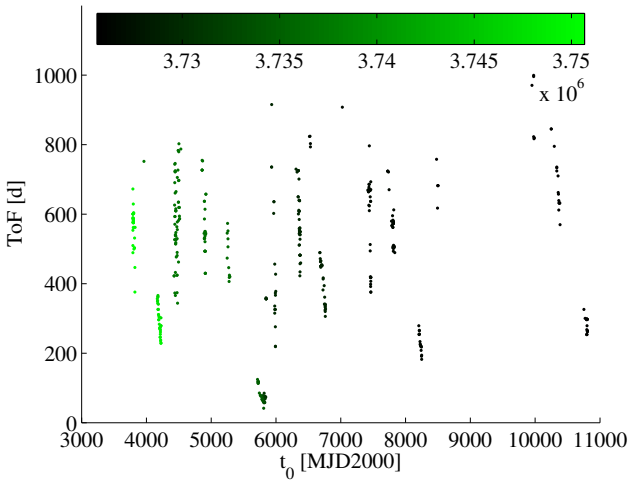

Figure 3.17: Launch opportunities for a deviation mission to 1979XB. The colour scale represents the value of the achieved deviation at the MOID.

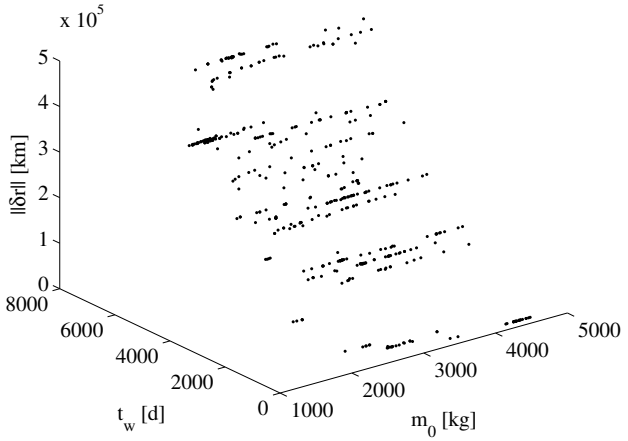

a)

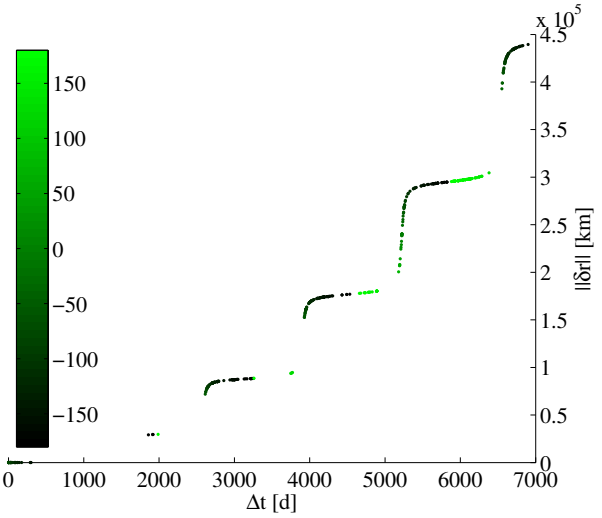

b)

Figure 3.18: Deviation mission to 1979XB: a) Pareto front. Launch mass, warning time and magnitude of the deviation are represented on the three axes. b) Achieved deviation as a function of the time length of the thrust arc.

The same analysis of sensitivity to the semi-major axis and the eccentricity is performed by computing the deviation for a range of *a* and *e* and by keeping the other parameters equal to that of 1979XB, which belongs to the Apollo class [5]. Although the range of the eccentricity is always $0.013 < e < 0.89$, for the semi-major axis a range of $1.0006 < a < 3.595$ AU is considered as the range of semi-major axis of the Apollo class, taken from the JPL catalogue[†††].

Figure 3.19a shows the different orbits (1979XB orbit in bold line and the Earth orbit in dashed line), and the position of the MOID for each orbit (cross markers). The corresponding true anomaly is depicted in Figure 3.19b (the cross is 1979XB θ_{MOID}). Because the inclination is quite high, the point of minimum distance with the Earth orbit identifies also the ascending or descending node of the asteroid.

Also in this case (see Figure 3.20a), the value of the deviation, for a fixed pushing time decreases with the increase of the semi-major axis (the 1979XB case is represented by a white line). The different shape with the orbital period with respect to Figure 3.14a is due to the higher eccentricity (e = 0.726). Finally, the accuracy is represented in Figure 3.20b. The relative error, despite being always under 3×10^{-2}, increases with the semi-major axis for fixed value of the pushing time.

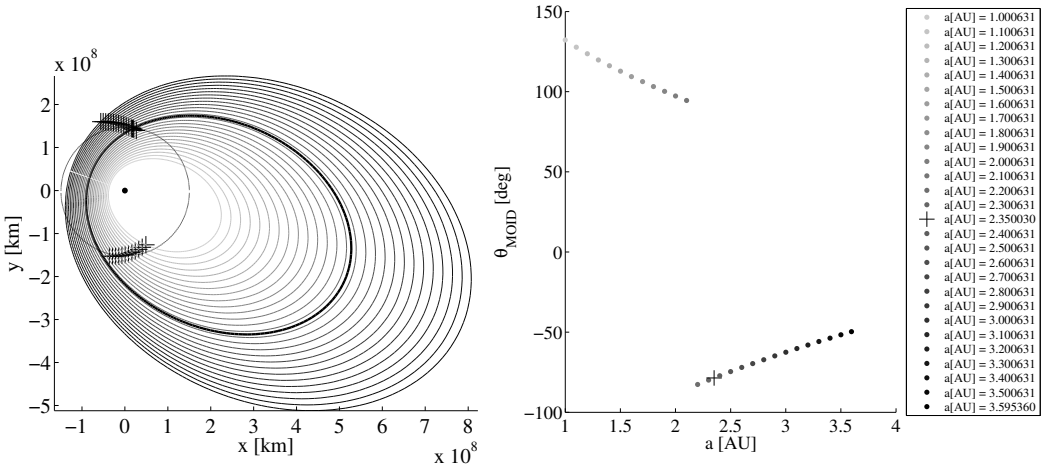

a) **b)**

Figure 3.19: Orbit and MOID characteristics for different values of semi-major axis starting from 1979XB case: a) asteroid orbits and b) true anomaly of the MOID.

[†††] Data available online at http://neo.jpl.nasa.gov/cgi-bin/neo_elem [Retrieved 05 August 2008].

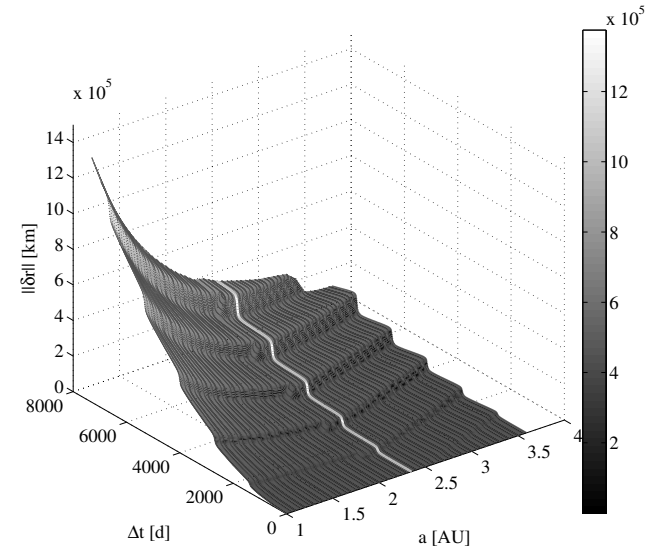

a)

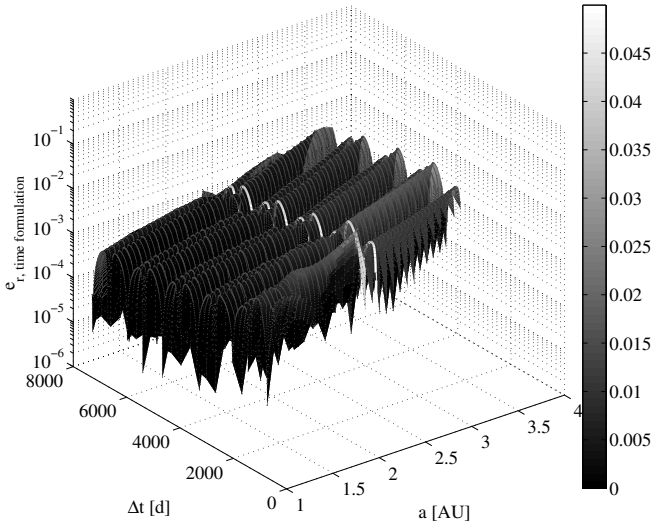

b)

Figure 3.20: Sensitivity of the deviation to the semi-major axis: a) deviation achieved for orbits with different values of semi-major axis and for increasing values of thrust interval and b) relative error for different values of semi-major axis. The white line represents 1979XB case (a = 2.350 AU).

The sensitivity to the eccentricity is depicted in Figure 3.22. Figure 3.21 shows the different orbits and MOID angular positions. In Figure 3.21a 1979XB orbit is the bold line and the Earth orbit is represented by the dashed line. In Figure 3.21b θ_{MOID} of asteroid 1979XB is the cross symbol.

As already observed in Figure 3.16a, for the same pushing time, the magnitude of the deviation increases with the increase of the eccentricity (see Figure 3.22a). Also in this case, a good accuracy is achieved for different values

of eccentricity within the range $0.013 < e < 0.89$. Figure 3.22b shows the relative error of the time formulation.

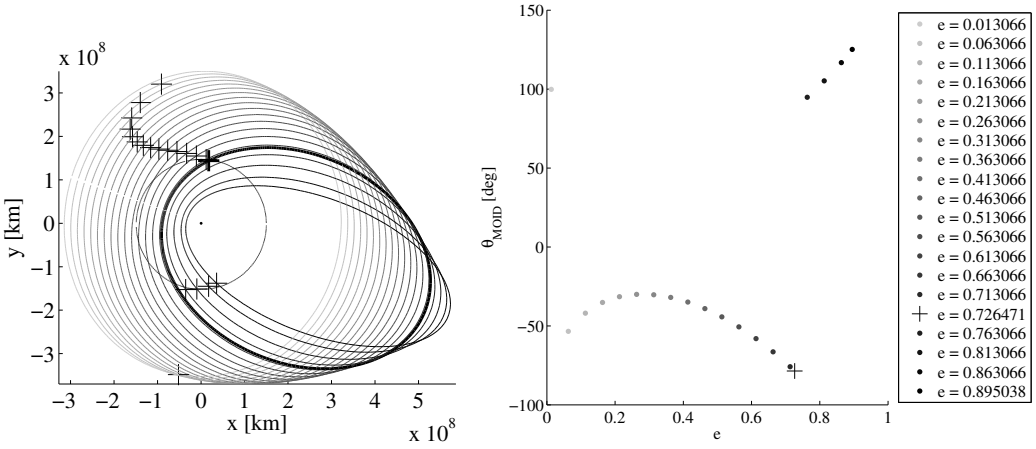

a) **b)**

Figure 3.21: Orbit and MOID characteristics for different values of eccentricity starting from 1979XB case: a) asteroid orbits and b) true anomaly of the MOID.

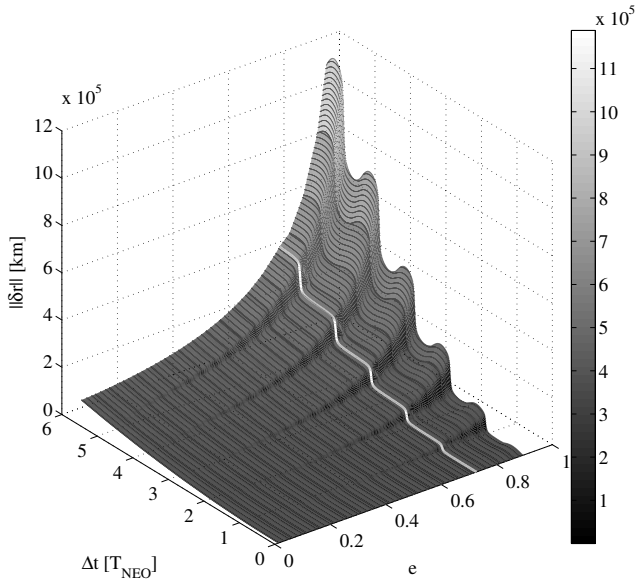

a)

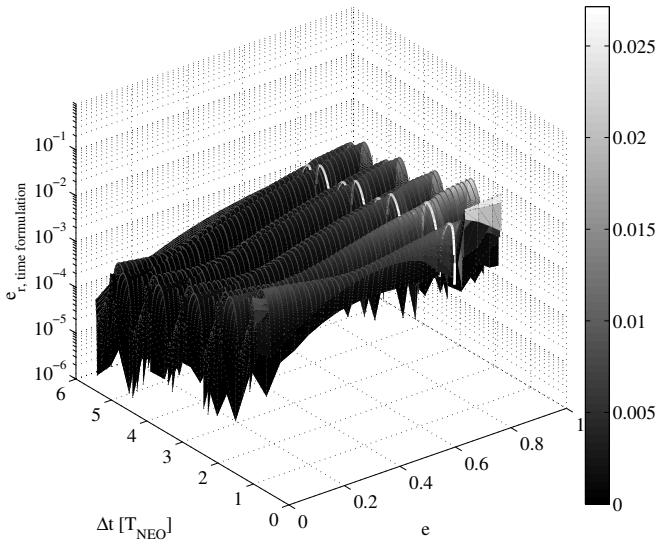

b)

Figure 3.22: Sensitivity of the deviation to the eccentricity: a) deviation achieved for orbits with different values of eccentricity and for increasing values of thrust interval and b) relative error for different values of eccentricity. The white line represents 1979XB case (e = 0.726).

Castalia deviation mission

A deviation mission to asteroid Castalia is designed, considering the asteroid at the MOID on the 17th June 2027 (10,029 MJD2000). Note that the favourable launch dates (Figure 3.23) recur with the synodic period between the Earth and the asteroid. The corresponding values of the initial mass, warning time, thrusting interval and magnitude of the achieved deviation are represented in Figure 3.24.

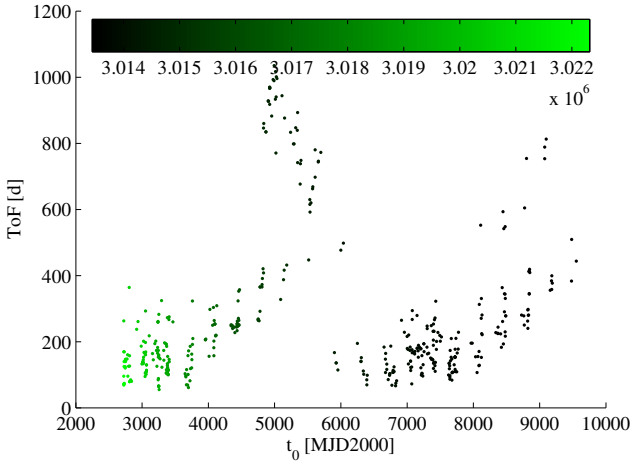

Figure 3.23: Launch opportunities for a deviation mission to Castalia. The colour scale represents the value of the achieved deviation at the MOID.

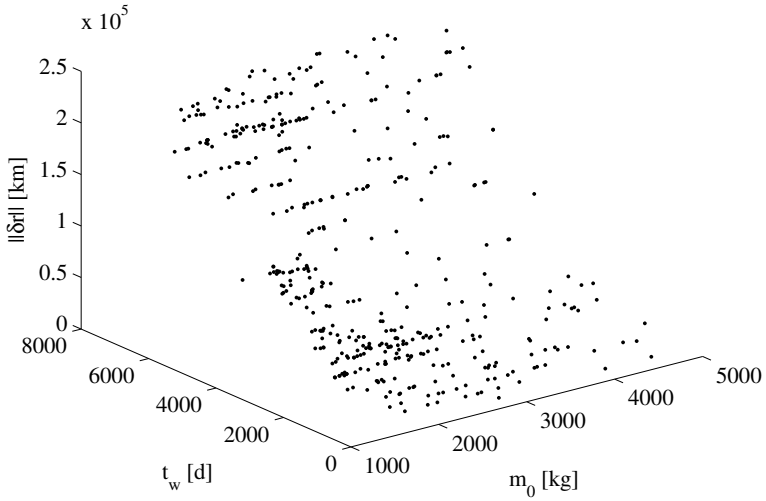

a)

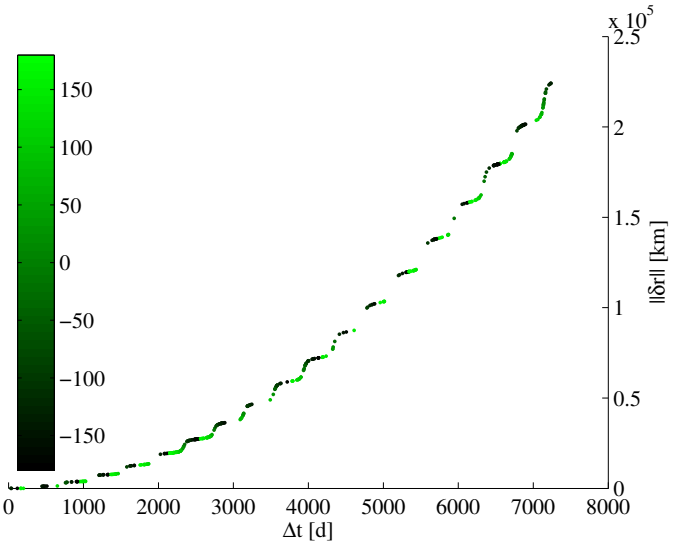

b)

Figure 3.24: Deviation mission to Castalia: a) Pareto front. Launch mass, warning time and magnitude of the deviation are represented on the three axes. b) Achieved deviation as a function of the time length of the thrust arc.

Itokawa deviation mission

A deviation mission to Itokawa is presented (see Figure 3.25), considering the MOID interception on the 20th July 2027 (10,072 MJD2000). The orbit of the asteroid is almost in the ecliptic plane and its pericentre is close to the Earth's orbit. The mass of the asteroid is 3.5×10^{10} kg, relatively small compared to the previous two cases, thus the Pareto front in Figure 3.25 contains remarkable solutions with initial masses of approximately 1300 kg. A recurrent feature of the Pareto front is the periodicity with the angular position of the interception (see Figure 3.26b).

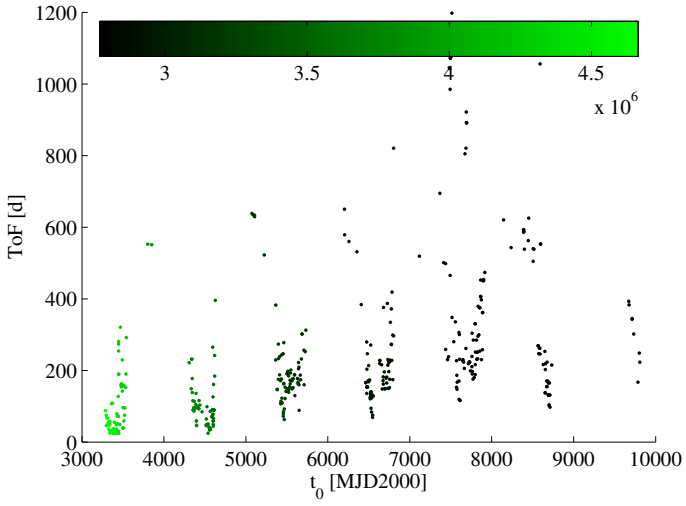

Figure 3.25: Launch opportunities for a deviation mission to Itokawa. The colour scale represents the value of the achieved deviation at the MOID.

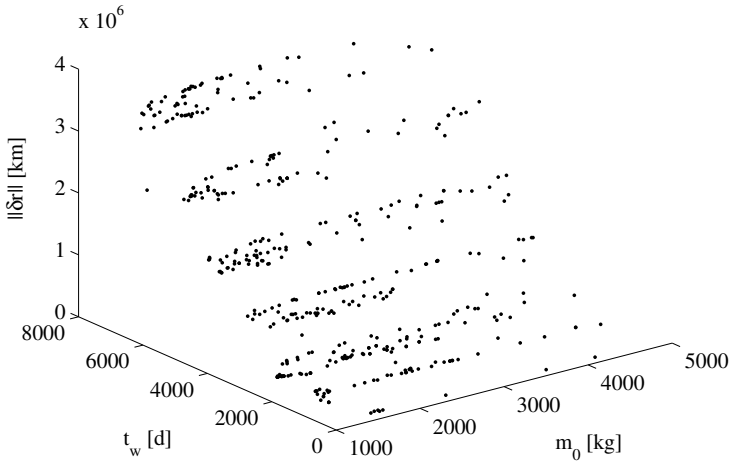

a)

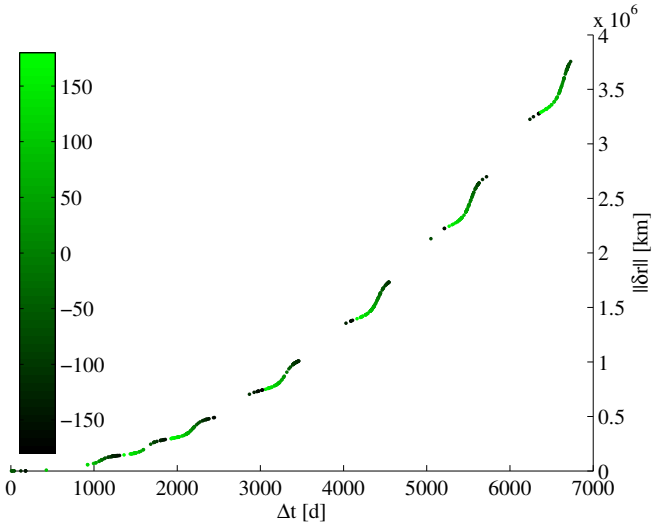

b)

Figure 3.26: Deviation mission to Itokawa: a) Pareto front. Launch mass, warning time and magnitude of the deviation are represented on the three axes. b) Achieved deviation as a function of the time length of the thrust arc.

3.4. Summary

In this chapter, a solution to the asteroid deviation problem in the case of a low-thrust deviating action is proposed. The proximal motion equations are used to compute the achieved deviation at the minimum orbit intersection distance, and semi-analytical formulae are derived to calculate the total variation of the orbital elements at the end of the thrust arc. The proposed semi-analytical formulation is proven to provide a significant savings in computational time with respect to the direct numerical integration of Gauss' equations. In particular, for the latitude formulation, the savings in computational time is up to 1 order of magnitude. The time formulation displays a lower savings, because the accuracy requirements are quite stringent for the specific application to NEO deviation. Nonetheless, for very expensive calculations, such as the generation of the Pareto sets that require several hundred of thousands of function evaluations, the semi-analytical formulae allow the generation of double the number of Pareto sets in the same computational time. Moreover, the gain in speed is not compensated by an equivalent loss in accuracy. The results in the chapter show that the relative error on the variation of the orbital elements is small for a push interval longer than one orbital period and remains small for long spirals. On the other hand, for shorter periods, numerical integration has to be used because it produces more accurate results. Finally, the proposed semi-analytical formulae are accurate for a wide range of values for eccentricities, semi-major axis and accelerations, suggesting their use for the fast generation of first guess solutions for long escape or capture spirals.

The chapter presents some applications of the semi-analytical formulation to the generation of sets of Pareto-optimal solutions for the design of mitigation missions to asteroid Apophis, 1979XB, Castalia, and Itokawa. For all the asteroids, a wide range of launch opportunities are found between 2010 and 2030, with an achieved deviation that grows above the Earth–Moon distance for warning times above 20 years. For shorter warning times, between 3 to 5 years, the achievable deviation is of the order of the radius of the geostationary orbit. The value of the achieved deviation presents a periodic trend with the true anomaly of the interception point; in particular, when the eccentricity of the asteroid is high,

an interception before the pericentre is significantly more effective than an interception after the pericentre.

Chapter 4.

Comparison of mitigation strategies for hazardous NEOs

Over the last few years, the possible scenario of an asteroid threatening to impact the Earth has stimulated an intense debate among the scientific community about possible deviation strategies [8]. This chapter presents a comparative assessment of some of the more feasible mitigation schemes proposed in the literature (i.e., kinetic impactor, nuclear interceptor, mass driver, solar collector, low-thrust attached propulsion, and gravity tug). A mathematical model of each strategy, which outputs the deflection action applied to the asteroid as a function of the mass available at the interception point, is implemented. The formulations described in Chapter 2 and Chapter 3 are used to translate the impulsive or low-thrust manoeuvre applied to the asteroid in a variation of its displacement at the point of minimum orbit intersection distance. The transfer trajectory from Earth to the interception of the target is modelled through preliminary design techniques.

For each deflection scheme, a multi-criteria optimisation method is adopted to construct a set of Pareto-optimal solutions that minimise both the mass of the spacecraft at launch and the warning time, while simultaneously maximising the deviation at the MOID. A dominance criterion is then defined and used to compare all the Pareto sets of the different mitigation schemes. This approach allows assessing the effectiveness of the strategies proposed in the literature, based on set of hundreds of potential missions, instead of choosing a single hypothetical mission case. In Appendix B the technology readiness of each strategy is evaluated and used to recompute a more realistic value for the required warning time.

4.1. NEO deflection strategies model

The effect of the various deviation strategies on the asteroid can be modelled either as an impulsive variation of its velocity (e.g., kinetic impactor, nuclear explosion, mass driver considered as a multi-impulsive strategy), or a slow-push on the asteroid with a continuous momentum change (e.g., solar collector, asteroid tug, gravity tractor). To evaluate the performance achievable with each deviation strategy, a set of mathematical models is exploited. Each model yields the total impulse imparted to the asteroid as a function of the mass available at the asteroid interception. The general form of the strategies model for an *impulsive* deviation strategy is

$$\delta \mathbf{v} = f\left(m_d, t_d, id_{\text{NEO}}\right) \tag{4.1}$$

and for a *low-thrust* deviation strategy is

$$\mathbf{a} = f\left(m_d, t_i, t_e, id_{\text{NEO}}\right) \tag{4.2}$$

where m_d is the mass of the spacecraft at the NEO interception, which is defined as the mass available, after the transfer Earth–asteroid, to alter the trajectory of the celestial body, and id_{NEO} is the asteroid identification number that is used to identify the orbital and physical properties of the NEO. The deflection manoeuvre is imparted to the NEO as an impulsive $\delta \mathbf{v}$ at t_d, or as a continuous acceleration $\mathbf{a}$ over the interval $\left[t_i \quad t_e\right]$ (where t_e is set equal to t_{MOID} in this analysis, with the exception of the attached spacecraft propulsion strategy).

The system design and the mathematical models of the deflection schemes, represented by Eq. (4.1) and Eq. (4.2), were developed by Sanchez, and a comprehensive explanation can be found in [126],[137]. In the following we will not describe the mathematical derivation of the models and the detailed explanation of the physical phenomena taken into account. However, all the strategies considered will be briefly introduced and qualitatively described to provide a good understanding of the deflection schemes and some of the assumptions made for the mathematical formulation. Particular emphasis will be

placed on the mass margin added (usually on the transformation from the mass of the spacecraft at the asteroid interception to the mass available for the power system) to emphasise the conservative approach, in accordance with other studies and some in-flight experimental data. Subsections 4.1.1 and 4.1.2 are also intended to explicit the interaction between the outputs of the action models and the formulation for computing the consequent deviation at the MOID.

Among the variety of NEO mitigation options proposed in the literature, six strategies are selected for this study, namely kinetic impactor, nuclear interceptor, mass driver, attached spacecraft propulsion, solar collector, and gravity tractor. However, the technique proposed in the following for the comparative assessment can be used to compare more strategies not included here.

4.1.1. Impulsive action

Kinetic impactor and nuclear interceptor represent the most common impulsive deviation strategies. Both schemes count on a spacecraft that intercepts the asteroid and impacts against it (i.e., kinetic impactor) or delivers a nuclear warhead which explodes in vicinity of it (i.e., nuclear interceptor). In both cases, the strategy performance is function of the transfer trajectory, not only in terms of the time in advance the asteroid is intercepted, but also because the direction of the deflecting impulse depends on the arrival condition of the spacecraft at the target object. Deflection through mass drivers, even if having an effect comparable to other low-thrust deflection strategies, can be modelled as a series of impulsive changes in the asteroid velocity.

Kinetic impactor

A spacecraft (or another small celestial body) is inserted into an orbit that intersects the asteroid course and will collide with the NEO at high relative velocity. This is the simplest concept of hazard mitigation, partially tested by the mission Deep Impact [28] and proposed for the ESA asteroid deflection precursor mission Don Quijote [37]. Through the collision, the asteroid linear momentum is modified; the spacecraft kinetic energy is transferred to the NEO, and this effect is enhanced by the ejection of surface material expelled as a consequence of crater formation after the impact.

The collision is modelled as a simple inelastic impact and a momentum enhancement factor γ is introduced to take into account the amplification of the momentum change due to the ejected materials. A conservative value of $\gamma = 2$ is chosen in this analysis [48],[138]. The variation of velocity imparted by the impactor spacecraft is given by Eq. (2.16) here reported:

$$\delta \mathbf{v} = \gamma \frac{m_d}{\left(m_{\text{NEO}} + m_d\right)} \Delta \mathbf{v}$$

where m_d is the mass of the spacecraft at the interception point and m_{NEO} the mass of the asteroid. The relative velocity of the spacecraft with respect to the asteroid at the deviation point $\Delta \mathbf{v}$ is computed from the solution of a Lambert's problem [71]. Consequently, the direction of the $\delta \mathbf{v}$ provided depends on the characteristics of the transfer trajectory. The variation in orbit geometry is computed with the first five equations in Eqs. (2.2) and Eq. (2.4), and the NEO deviation at the MOID is computed through Eq. (2.1).

Nuclear interceptor

Mitigation through nuclear detonation ensures the highest energy density compared to other options. The strategy considered in this study consists of a nuclear warhead that is detonated at a certain distance from the asteroid. The energy transferred to the asteroid is mainly carried by debris from the explosion, x-rays, gamma, and neutron radiation [139]. Because the neutron radiation is the most efficient in terms of material evaporation, a fusion device [126], which maximises this interaction, is selected. The total impulsive manoeuvre is composed by:

$$\delta \mathbf{v} = \delta \mathbf{v}_{\text{radiation}} + \delta \mathbf{v}_{\text{x-rays}} + \delta \mathbf{v}_{\text{debris}} + \delta \mathbf{v}_{\text{neutrons}}$$

and is directed along the spacecraft velocity vector with respect to the asteroid at the end of the interception transfer trajectory. The variation in orbit geometry is computed with the first five equations in Eqs. (2.2) and Eq. (2.4), and the NEO deviation at the MOID is computed through Eq. (2.1).

The mass of the nuclear device considered in this study is 30% of the dry mass of the spacecraft at the end of the transfer trajectory.

Mass driver

One or more spacecraft, equipped with a mass driver and drilling device, land and anchor to the asteroid surface. The NEO linear momentum is modified by the ejection of the surface material that is drilled out and accelerated away from the asteroid by an electromagnetic rail gun. In this way the spacecraft power is converted into kinetic energy, by exploiting in-situ resources [52],[140].

The total effect on the asteroid orbit can be described as a series of multi impulsive manoeuvres. The change in velocity of the asteroid for each shot is determined through the law of conservation of momentum:

$$\delta v_j = \frac{m_{\text{shot},j}}{m_{\text{NEO}}(t)} v_e \tag{4.3}$$

where $m_{\text{shot},j}$ is the mass expelled per shot by the mass driver device and v_e is the excess velocity of the ejected material, estimated to be 200 m/s, within the range 100–300 m/s given in the literature [67],[140]. The total mass of the NEO m_{NEO} decreases at every shot. The frequency of the shots is computed assuming that the spacecraft lands on the asteroid equator, the rotational axis of the body is perpendicular to its orbital plane, and such that the material is ejected every time the mass driver device is pointing along the optimal direction (see Section 2.1.1).

The mass expelled per shot $m_{\text{shot},j}$ depends on the total power converted from electric to kinetic, considered to be 30% of the available power (the remaining part represents mechanical losses) and 30% of the mass at the interception is allocated to the power system. The mathematical model of the mass driver provides the frequency of shots and the magnitude of each impulse δv_j that is given to the asteroid along the direction that optimises the instantaneous deflection. The mass driver is in operation from the interception time t_i up to t_e (where t_e is set equal to t_{MOID} in this analysis).

At each shot, the finite variation of the orbital elements of the asteroid is computed with Eqs. (2.2) and Eq. (2.4) substituting δv_j given by Eq. (4.3), and the new set of orbital parameters must be calculated before the subsequent impulsive action. The mean anomaly after each shot and before the following mass ejection is computed from the first of Eqs. (2.5) and Kepler's equation is solved for the osculating eccentric anomaly and the true anomaly, by the Newton method described in [71]. The deviation at the MOID, computed through Eq. (2.1) is a function of the total variation of the orbital parameters over the operational time.

4.1.2. Low-thrust action

All low-thrust actions need the rendezvous of a spacecraft with the hazardous object. By timing the pushing manoeuvre or controlling the hovering position, the deflection action acts along the optimal direction (see Section 3.1.1). Mitigation through in-situ spacecraft propulsion presents the issue of anchoring to the target surface, whereas solar collector and gravity tug do not require an attachment mechanism to the asteroid, hence are less influenced by its shape and spinning properties.

Attached spacecraft propulsion

Among the strategies to divert the orbit of the NEO, one option considers a spacecraft attached to the surface of the asteroid. The linear momentum of the hazardous object is perturbed by the thrust given by the propulsion system of the spacecraft. Any propulsion system could be exploited (e.g., electric or chemical engine, or non-conventional systems like solar sails).

In this study a spacecraft powered by an electrical engine is considered, because, compared to a chemical engine, it requires less propellant mass to achieve the same deviation of the asteroid. The system consists of two engines with $I_{sp} = 3000$ s situated at opposite spots along the equator of the asteroid. By a proper schedule of the thrusting period of each engine, a quasi-constant thrust with correct pointing can be obtained. A scattering factor takes into account the misalignment from the optimal thrust direction.

In this case, the mass of the spacecraft at the end of the transfer trajectory includes the system mass and the propellant mass for the deviation phase. The mass available for the power subsystem is 50% of the dry mass. The total variation of the NEO orbital elements is computed through the numerical integration of Eqs. (3.3) over the thrust interval and Eq. (3.4), with an acceleration along the direction defined in Section 3.1.1, with a magnitude given by the following expression

$$\left\|\mathbf{a}(t)\right\| = \frac{\left\|\mathbf{T}_{\text{engine}}\right\|}{m_{\text{NEO}} + m(t)}$$

where $\mathbf{T}_{\text{engine}}$ is the constant thrust provided by the attached engine, and $m(t)$ is the mass of the spacecraft. The mass consumption for the deflection phase is computed with the equation

$$\frac{dm}{dt} = -\frac{\left\|\mathbf{T}_{\text{engine}}\right\|}{I_{sp} g_0}$$

Sanchez at al. [126] showed that, fixing the available mass of the spacecraft system and the maximum period of time for the application of the low-thrust deflection manoeuvre $\left[t_i \quad t_{\text{MOID}}\right]$, thrusting continuously over the whole interval $\left[t_i \quad t_{\text{MOID}}\right]$ is not necessarily more efficient than thrusting for a shorter interval $\Delta t < t_{\text{MOID}} - t_i$ with higher levels of thrust. In fact, the comparison of the deviation achieved adopting the continuous-thrust strategy against the deviation by means of a scheduled-thrust strategy suggests a pushing manoeuvre that commences at t_i and stops after the last pericentre passage before 45% of the total available time. This result is implemented in the model used for the present analysis.

Solar collector

The use of solar ablation for mitigation of threatening NEOs was first proposed by Melosh [56]. A big inflatable mirror is used as light collector, focusing sunlight onto the surface of the asteroid. The high energy concentration over a limited area causes the ablation of the surface and the evaporating material

produces a gas jet that acts as the plum of exhaust gases of a conventional propulsion system.

The solar collector system design accounts for 30% of the dry mass of the spacecraft mass at rendezvous with the NEO for the inflatable structure and attachments. The model of the deviation strategy computes the evaporation flux dm_{NEO}/dt from the illuminated area of the asteroid surface, and from there it derives an expression for the magnitude of the deviating acceleration (its direction is specified in Section 3.1.1):

$$\left\|\mathbf{a}(t)\right\| = \frac{\sigma \cdot \dfrac{dm_{\mathrm{NEO}}}{dt} \cdot \bar{V}}{m_{\mathrm{NEO}}(t)} \tag{4.4}$$

where $\bar{V}$ is the average velocity of the particles in the evaporated jet and σ is a factor that takes into account the dispersion of the particles in the ejecta plume. Eq. (4.4) is substituted into Eqs. (3.3) and (3.4), and they are numerically integrated, together with the equations of the asteroid mass consumption on the surface due to sublimation, to compute the total variation of orbital parameters.

Gravity tractor

Another option that does not require the direct contact between the spacecraft and the NEO is the gravity tractor. The mutual gravitational attraction between the asteroid and the spacecraft can be exploited to move the NEO away from its orbit [54]. A spacecraft hovers at a constant distance from the asteroid, with a configuration such that the exhaust gases from the engine do not impinge the asteroid's surface. In this way there is an escape of mass from the NEO–spacecraft system and an acceleration acting on the asteroid given by

$$\left\|\mathbf{a}(t)\right\| = \frac{Gm(t)}{d^2} \tag{4.5}$$

where G is the universal gravity constant, d the hovering distance and m is the mass of the spacecraft that is computed through the equation

$$\frac{dm}{dt} = -\frac{\left\|\mathbf{T}_{\text{engine}}\right\|}{I_{sp} g_0}$$

where the total thrust of the engine has to counteract the gravitational pull, slanted by an angle ϕ between the pointing direction of the engines, and the line between the spacecraft and the NEO centre of mass.

$$\left\|\mathbf{T}_{\text{engine}}\right\| = \frac{G m_{\text{NEO}} m(t)}{d^2 \cos\phi}$$

Eq. (4.5) is substituted into Eqs. (3.3) and (3.4), and they are numerically integrated to compute the total variation of orbital parameters.

The gravity tractor model considers 50% of the spacecraft mass at the asteroid available for the power system.

4.2. Transfer trajectory

To perform a comparative assessment of the various deflection strategies, an entire mission from launch to final mitigation is modelled. The transfer trajectory determines the available mass at the target interception for sizing the deflection system; moreover, the arrival conditions at the end of the transfer path influence to various degrees the efficiency of the mitigation schemes.

The transfer trajectory is designed through different preliminary design techniques, considering a two-body problem, with the Earth and the asteroid as point masses with no gravity. The Earth ephemerides are computed through analytic ephemerides which approximate JPL ephemerides de405[*], and the ephemerides of the target asteroids are computed from their orbital elements.

A chemical engine with $I_{sp} = 315$ s is selected for mitigation missions by means of kinetic impactor and nuclear interceptor. The transfer trajectory is modelled through Lambert's problem [71], and the propellant mass is determined from Δv_0 at the Earth.

[*] Data available online at http://naif.jpl.nasa.gov/naif/pds.html [Retrieved 28 January 2009].

$$m_p = m_0\left(1-\exp\left[\frac{-\Delta v_0}{I_{sp}g_0}\right]\right)$$

For the remaining mitigation schemes (i.e., mass driver, attached spacecraft propulsion, solar collector, and gravity tractor) an electrical engine is selected with $I_{sp}=3000$ s. The trajectory is modelled through the shape-based method [118],[136], briefly described in Section 3.3.2. In this case the initial mass of the mission m_0 is selected as a parameter of the optimisation, hence the computation of the propellant mass in Eqs. (3.21) is substituted by the following expression

$$m_p = m_0\left(1-\exp\left[-\int_{L_0}^{L_f}\frac{\|\mathbf{u}\|}{I_{sp}g_0}\frac{dt}{dL}dL\right]\right)$$

where $L=\theta+\omega+\Omega$ indicates the true longitude, L_0 and L_f represent the initial and final true longitude of the trajectory, and $\mathbf{u}$ is the control acceleration vector.

In both cases, the spacecraft is assumed to be at time t_0 at the Earth with zero relative velocity and initial mass m_0. The mass available at the asteroid for performing the deflection phase is equal to m_0-m_p.

4.3. Multi-criteria optimisation problem formulation

The optimality of each strategy is defined through a number of criteria or objectives that have to be attained. Unlike single objective problems, multiple objective problems look for a set of optimal values rather than a single optimal one. The general problem is to find a set X of feasible solutions $\mathbf{x}$ such that the property $P(\mathbf{x})$ is true for all $\mathbf{x}\in X\subseteq D$:

$$X=\{\mathbf{x}\in D \mid P(\mathbf{x})\}$$

where the domain D is a hyper-rectangle defined by the upper and lower bounds on the components of the vector $\mathbf{x}$:

$$D = \left\{ x_i \mid x_i \in \left[b_i^l \quad b_i^u \right] \subseteq \mathbb{R},\ i = 1,...n \right\}$$

where the index *i* indicates the components of $\mathbf{x}$ and *n* is the total number of components. b_i^l and b_i^u indicate, respectively, the lower and the upper bound on the *i*-component.

All the solutions satisfying the property *P* are defined to be optimal with respect to *P* or *P*-optimal and *X* can be said to be a *P*-optimal set.

Multiple objective optimisation

In the case of multi-objective optimisation, if *P* is a dominance condition or Pareto optimality condition for the solution $\mathbf{x}$, then the solution is Pareto-optimal if $P(\mathbf{x})$ is true. According to the definition, a set of parameters is Pareto-optimal if there exists no other feasible vector of variables which would decrease some criterion without causing a simultaneous increase in at least one other criterion[†]. Each solution vector $\mathbf{x}_j$ is associated with a scalar dominance index $I_d(\mathbf{x}_j)$ such that:

$$I_d(\mathbf{x}_j) = \left| \left\{ k \mid k \in N_p \wedge \mathbf{x}_k \succ \mathbf{x}_j \right\} \right|$$

where the symbol $\left| \ \right|$ is used to denote the cardinality (i.e., number of elements) of a set, $\succ$ represents the dominance of the solution $\mathbf{x}_k$ over the solution $\mathbf{x}_j$, and N_p is the set of the indices of all the feasible solutions in the population.

The solution $\mathbf{x}_k$ dominates solution $\mathbf{x}_j$ if all the components of criteria or objectives vector $\mathbf{J}(\mathbf{x}_k)$ associated to $\mathbf{x}_k$ are better (i.e., lower in the case of a minimisation) than all the components of the criteria or objectives vector $\mathbf{J}(\mathbf{x}_j)$ associated to $\mathbf{x}_j$ (i.e., strong dominance).

[†] This definition is valid in the case of a minimisation. When a multi-objective maximisation is performed, a set of parameters is Pareto-optimal if there exists no other feasible vector of variables which would increase some criterion without causing a simultaneous decrease in at least one other criterion. Note that in Section 4.3 all the definitions will be given for a minimisation problem; in the case of a maximisation problem, all the definitions have to be accordingly changed.

$$\mathbf{x}_k \succ \mathbf{x}_j \Rightarrow \mathbf{J}_i\left(\mathbf{x}_k\right) < \mathbf{J}_i\left(\mathbf{x}_j\right) \ \forall \ i = 1,...m$$

where the index *i* indicates the components of $\mathbf{J}(\mathbf{x})$ and *m* is the total number of components of the vector objective function $\mathbf{J}(\mathbf{x})$.

The property $P(\mathbf{x})$ in this case simply defines non-dominated solutions:

$$X = \left\{\mathbf{x} \in D \mid I_d(\mathbf{x}) = 0\right\} \tag{4.6}$$

This definition gives not one unique solution, but a set of not-dominated solutions, that generate the Pareto front.

For constrained problems, the property $P(\mathbf{x})$ has to be true and all the solutions of the not-dominated set must be feasible, i.e., the constraint must be satisfied:

$$X_{\text{constrained}} = \left\{\mathbf{x} \in D \mid I_d(\mathbf{x}) = 0 \wedge \ C(\mathbf{x}) < 0\right\}$$

where $C(\mathbf{x}) < 0$ represent the constraint.

The search of the *P*-optimal sets *X*, for each strategy, is performed here through a multiagent-based search approach hybridised with a domain decomposition technique developed by Vasile [133].

Single objective optimisation

In the case of single-objective optimisation[‡], the set *X* contains all the solutions that are local minima or are below a given threshold. Because we are looking at local minima solutions, the property $P(\mathbf{x})$ is to be a local minimiser, or a solution $\mathbf{x}^*$ can be said to dominate the solution $\mathbf{x}$ if the associated value of the objective function $J(\mathbf{x}^*) < J(\mathbf{x})$.

$$\mathbf{x}^* \succ \mathbf{x} \Rightarrow J(\mathbf{x}^*) < J(\mathbf{x}) \tag{4.7}$$

For constrained problems, all the solution $\mathbf{x}^* \in X$ must also be feasible:

[‡] The single-objective optimisation is used in Section 2.2.3; however we include it in this subsection to introduce the formulation of the optimisation problem all at once.

$$C(\mathbf{x}^*) < 0$$

In order to construct the set *X*, a systematic sampling of the solution space along with a local minimisation started for each sampled point would be computationally expensive. Therefore, the problem is tackled through a more efficient domain decomposition technique hybridised with a stochastic global optimisation method [116],[117]. During the optimisation process, the overall domain is partitioned in smaller subdomains and in each of them a search is performed and the solutions found are saved in memory. The solutions stored in the archive are prevented to crowd in a single solution (feature controlled by a crowding parameter) to identify several local minima rather than only the global one. For these reasons, when the optimisation process is ended more than one single result is available.

Now property *P* may not identify a unique set, therefore we can define a global optimal set X_o such that all the elements of X_o dominates the elements of any other *X*.

$$X_o = \left\{ \mathbf{x}^* \in D \mid P(\mathbf{x}^*) \wedge \ \forall\ \mathbf{x} \in X \Rightarrow \mathbf{x}^* \succ \mathbf{x} \right\}$$

where the symbol $\succ$ represents the dominance of the solution $\mathbf{x}^*$ over the solution $\mathbf{x}$. Because we are looking at a minimum, the solution $\mathbf{x}^*$ is said to dominate the solution $\mathbf{x}$ if Eq. (4.7) is verified. In this case X_o would contain the global minimum or a set of global minima all with the same value of $J(\mathbf{x}^*)$.

4.4. Objective function definition

To define the optimality of each strategy a multiple objective minimisation is performed, according to three figures of merit[§]:

$$\min_{\mathbf{x}} \left[m_0 \quad t_w \quad -\|\Delta\mathbf{r} + \delta\mathbf{r}\| \right] \tag{4.8}$$

[§] Note that the three terms of Eq. (4.8) are properly scaled within the optimisation process.

The mass in space m_0 is the wet mass at the Earth after launch. Even if the strategies were modelled with a very conservative approach, an additional margin on the initial spacecraft mass was added to take into account the corrective manoeuvres required during both the transfer leg and the deflecting arc. The margins, reported in Table 4.1, are set considering the actual technology level of the different strategies. Note that the effective mass available for the transfer trajectory and the deflection manoeuvre is the total mass m_0 diminished by the percentage margin in Table 4.1, according to the strategy under consideration.

Table 4.1: Margins on the wet mass into orbit for the different deviation strategies.

Deviation strategies	Margin on the mass at launch
Kinetic impactor	5%
Nuclear interceptor	15%
Mass driver	25%
Attached spacecraft propulsion	25%
Solar collector	25%
Gravity tug	25%

The second component of the vector objective function Eq. (4.8) is the warning time $t_w = t_{\mathrm{MOID}} - t_0$ that is the interval between the launch date and the time at the MOID. The encounter time t_{MOID} is fixed as the first date the asteroid reaches the minimum orbit intersection distance from the Earth orbit after 1 January 2029 at 00:00 hrs (10,592.5 MJD2000). Note that the Earth is not necessarily at the MOID at t_{MOID}; on the other hand the aim of this analysis is to measure the achieved deviation and not to reproduce a real impact scenario.

The third component to be maximised is the total deviation at the MOID $\|\Delta\mathbf{r} + \delta\mathbf{r}\|$, where $\Delta\mathbf{r}$ is the MOID distance and $\delta\mathbf{r}$ is computed by means of Gauss' equations and relative motion equations, through the action model described in Section 4.1. As already stated, for the hypotheses of the proximal motion equations to hold true, the relative orbit radius δr must be small compared with the nominal orbit radius r. For this reason, the maximum acceptable deviation is set equal to the Earth–Moon distance, as this is considered a sufficient distance to ward off the threat of an impact. Note that the total deviation is chosen as figure of merit and not the ability of a particular deflection

strategy to avoid the keyholes [132]; in this case a smaller $\delta\mathbf{r}$ would be enough to produce significant results.

For the mass driver, low-thrust attached propulsion, solar collector, and gravity tug strategies the direction of the $\delta\mathbf{v}$ change or the acceleration is given in the direction that maximises the deviation $\delta\mathbf{r}$ and the sign of the optimal manoeuvre (i.e., $+\delta\mathbf{v}$ or $-\delta\mathbf{v}$) is chosen to maximise the total deviation at the MOID $\|\Delta\mathbf{r}+\delta\mathbf{r}\|$ (see Section 2.1.1).

The three figures of merit in Eq. (4.8) give an estimate of size, cost, time, and effectiveness of a mitigation mission; the initial mass strongly determines the required launch capabilities and the cost of the mission, the warning time is a measure of the time in advance the mission has to be planned, and the deviation achieved can be used to compare the effectiveness of the various strategies.

The problem is to find the Pareto-optimal set X given in Eq. (4.6), in other words, a set of non-dominated solutions according to the three criteria in Eq. (4.8). The general from of the solution vector $\mathbf{x}$ in the case of high-thrust transfer (modelled through Lambert's arc) is

$$\mathbf{x} = \begin{bmatrix} m_0 & t_0 & ToF & d_{tr} \end{bmatrix}$$

where m_0 is the mass at launch (comprehensive of mass margin), t_0 is the launch date, ToF the time of flight, and d_{tr} is an index equal to 0 or 1 identifying a direct or retrograde arc. In the case of a low-thrust transfer model (with the shape-based method described in Section 3.3.2) the solution vector also contains the number of revolutions around the Sun and the two shape parameters for the low-thrust arc[**].

$$\mathbf{x} = \begin{bmatrix} m_0 & t_0 & ToF & n_{\text{rev}} & \rho_2 & \rho_3 \end{bmatrix}$$

Note that the low-thrust transfer case requires also the satisfaction of the constraint on the time of flight given by Eq. (3.22) and reported here:

[**] The first shape parameter of the shape-based method is automatically determined inside the trajectory modelling algorithm.

$$C_{ToF}: \quad \int_{L_0}^{L_f} \frac{dt}{dL} dL - ToF < 10 \text{ days} \tag{4.9}$$

Each solution $\mathbf{x} \in X \subseteq D$ represents an entire mission, which launches from the Earth at t_0 with initial mass m_0, intersects the asteroid at $t_0 + ToF$ and performs an impulsive manoeuvre, or rendezvous with the asteroid at $t_0 + ToF$ and performs a low-thrust manoeuvre over a continuous pushing time $\Delta t = t_{MOID} - (t_0 + ToF)$ (except for the attached spacecraft propulsion strategy[††]).

The search for Pareto-optimal solutions is performed over a wide domain of initial masses to represent all different sizes of missions. The launch date is fixed between 1000 days and 20 years before the time at which the asteroid reaches the MOID, and the time of flight ranges within 25–1000 days. The boundaries of the solution vector $\mathbf{x}$ are reported in Table 4.2.

Table 4.2: Search domain for the multi-objective optimisation.

Element on the state vector	Lower bound	Upper Bound
Initial mass [kg]	100	100,000
Launch date	$t_{\text{MOID}} - 20$ years	$t_{\text{MOID}} - 1000$ days
Time of flight [d]	25	1000
Number of revolutions	0	3
Shape parameter ρ_2	–1	1
Shape parameter ρ_3	–1	1

4.5. Deflection mission options

The following section presents different scenarios for the mitigation of a number of selected asteroids. Fixed a target asteroid, the transfer trajectory to reach it from Earth is modelled through preliminary design techniques (see Section 4.2); subsequently, six deflection strategies (presented in Section 4.1) are applied to increase the displacement of the asteroid at the MOID. For each mitigation scheme, a set of Pareto-optimal deflection missions is computed according to the objective function in Eq. (4.8). The concept of dominance is proposed to perform a comparison of the various deflection strategies, according

[††] In the case of the attached spacecraft propulsion strategy: $\Delta t < t_{MOID} - (t_0 + ToF)$.

to the three criteria of the optimisation. In Appendix B the technology readiness of each system is included in the analysis, by adding to the warning time the time delay necessary for the required technology to be completely viable.

4.5.1. Targets selection

The effectiveness of a given deviation strategy depends on the orbital and physical characteristics of the NEO it is applied to; for this reason, four asteroids are chosen for the multi-criteria analysis (see Table 4.3 and Figure 4.1). Apophis belongs to the Aten class (i.e., with semi-major axis smaller than Earth's: $a < 1$ AU and apocentre distance $r_a > 0.983$ AU); because of the uncertainties on its orbit after the next encounter with Earth in 2029, it is often selected as a case study for the ongoing discussion on the available options for its deflection. The other asteroids selected for this study, Itokawa, Castalia, and 1979XB, belong to the Apollo class (i.e., Earth-crossing objects with semi-major axis larger than Earth's: $a > 1$ AU and pericentre distance $r_p < 1.017$ AU) group and differ for their mass and orbital elements. Other physical characteristics that influence the performances of the action models are the density and the rotational speed of the asteroid[‡‡]. The interested reader can refer to [126],[137] for further information on the asteroid model. Note that the nominal MOID of the Apollo class asteroids is quite big; this means that the three asteroids do not currently represent a real impact hazard to our planet. However, the aim of this analysis is to present a qualitative comparison of the different deflection strategies and not to reproduce a real impact scenario. The same technique presented in Section 4.3 can be applied to other study cases.

Table 4.3: Asteroids orbital and physical parameters.

Asteroid	Semi-major axis [AU]	Eccentricity	Inclination [deg]	MOID [km]	Mass [kg]
Apophis	0.92	0.19	3.33	30,706	4.6×10^{10}
Itokawa	1.32	0.28	1.62	2,769,832	3.5×10^{10}
Castalia	1.06	0.48	8.9	3,013,439	1.4×10^{12}
1979XB	2.35	0.73	25.14	3,725,733	4.4×10^{11}

[‡‡] A density of 2.5 g/cm^3 is taken for all the asteroids, whereas the rotational period of the four asteroids is respectively: 30.54 hrs for Apophis, 12.13 hrs for Itokawa, 4.07 hrs for Castalia, and 10 hrs for asteroid 1979XB.

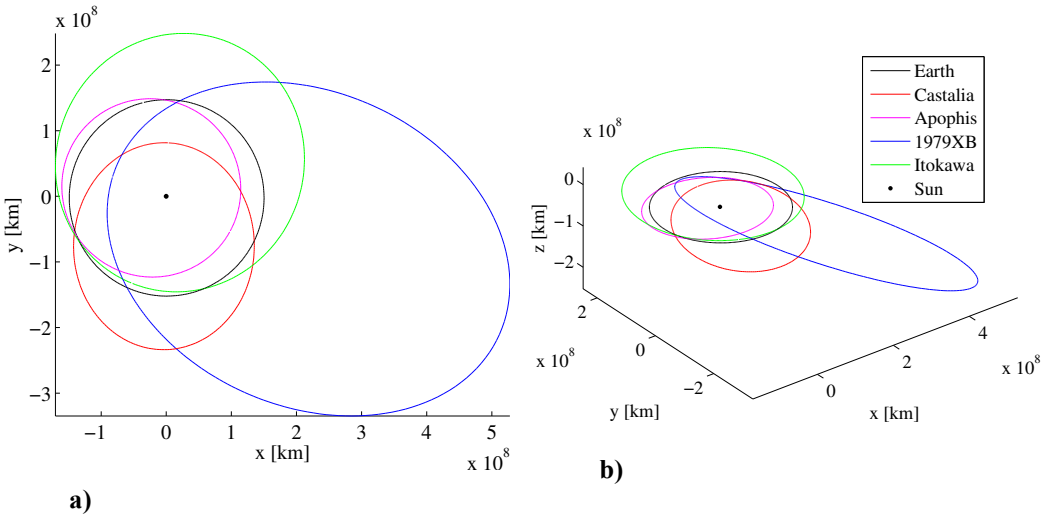

Figure 4.1: Orbit of the selected asteroids: a) 2D view, and b) 3D view.

4.5.2. Pareto fronts

A convenient representation of the result of each deflection strategy is the Pareto front, constituted by all the optimal solutions that have lower cost (i.e., lower mass and warning time and higher total deviation) than points corresponding to other choices of parameters. Figure 4.2–Figure 4.5 present the Pareto fronts for the mitigation of asteroid Apophis, Itokawa, Castalia, and 1979XB, respectively, by means of all the deflection schemes analysed. Each black dot represents a complete preliminary design for a mission that launches from Earth, intercepts the asteroid and applies a deflection manoeuvre. To improve the visualisation of the Pareto fronts, for each figure an interpolating surface has been generated from the scattered set of Pareto optimal solutions. The x and y axis represent the first two components of the cost function Eq. (4.8), initial mass m_0 and warning time t_w; on the z axis the deviation δr is reported.

The shape of the Pareto fronts is mostly dependent on the mitigation strategy used. NEO orbital characteristics, size and rotational period also model the surface of the Pareto front, sizing it and slightly changing the inclination and position in the criteria space. Some common features can be recognised in the Pareto fronts for all the asteroids, in particular the linear or quadratic increase of the deviation with the initial mass (directly related to the models of the strategies), and the periodicity along the warning time axis, which is related to the transfer trajectory and the angular position of the interception point where a variation of the asteroid velocity is more effective. Note that for low-thrust propulsion, the

concentration of the solutions along stripes on the t_w axis is due to the constraint of the time of flight in Eq. (4.9); in fact it was verified that the points are more spread if this constraint is relaxed (however, in that case the solutions would not be feasible).

Apophis deviation mission

The mitigation scenario considered for asteroid Apophis is identified by a close encounter with the Earth on the 14th April 2029 (10695.8 MJD2000).

Figure 4.2 presents the Pareto fronts for the mitigation of asteroid Apophis by means of all the deflection schemes analysed. The range of initial masses and warning times covered by the solutions in the Pareto fronts is similar for all strategies and depends on the boundaries on the optimisation parameter vector $\mathbf{x}$. The range of achievable deviation, on the other hand, gives an idea of the capability of each mitigation scheme.

The strategies that exhibit the best results for almost all the asteroids considered are the solar collector and the nuclear interceptor (see Figure 4.2e and b); in fact, they reach the limit set on the maximum deviation (equal to the Earth−Moon distance) for small values of the wet mass and warning time. Note that, the two schemes are completely different, as the deviation is achieved through a continuous thrust arc in the former case, or through an impulsive change of the linear momentum in the latter case. The mass driver strategy (see Figure 4.2c) shows a satisfactory performance, reaching the maximum deviation in some cases; even if this scheme is modelled as a multi-impulsive-action, its effect is analogous to a continuous thrust manoeuvre. Strategies like kinetic impactor, attached low-thrust propulsion, and gravity tractor present deviation ranges of one order of magnitude less than the one achievable with nuclear interceptor and solar collector; a deviation of approximately 10,000 km is reached for values of initial mass and warning time close to the maximum considered.

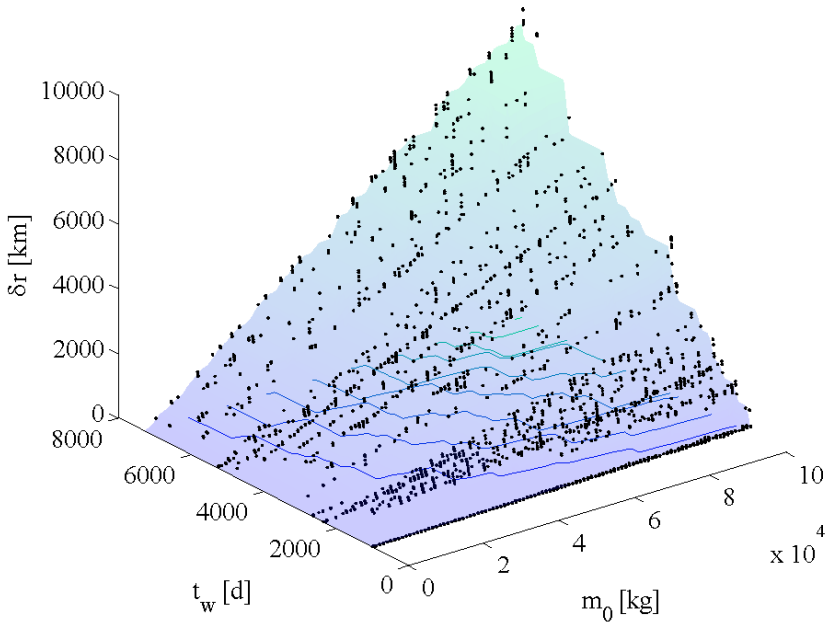

a) Pareto front for the deviation of asteroid Apophis through kinetic impactor.

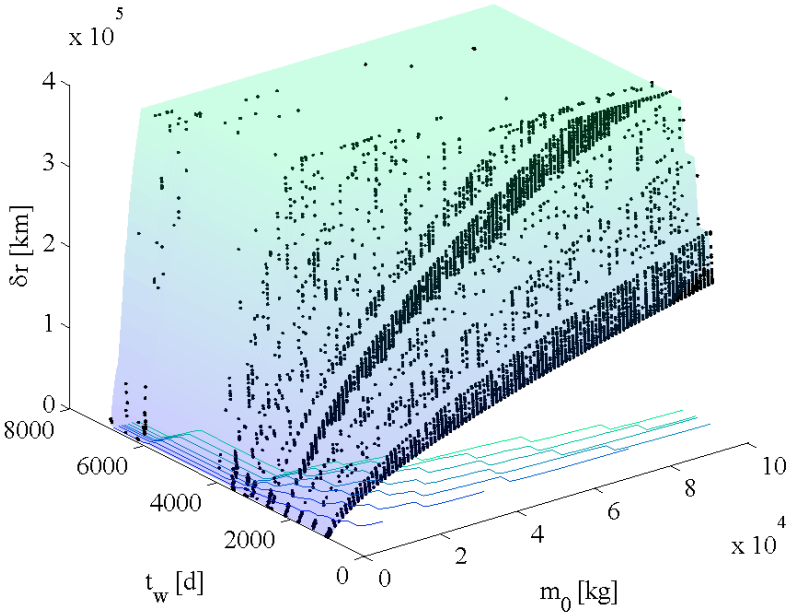

b) Pareto front for the deviation of asteroid Apophis through nuclear interceptor.

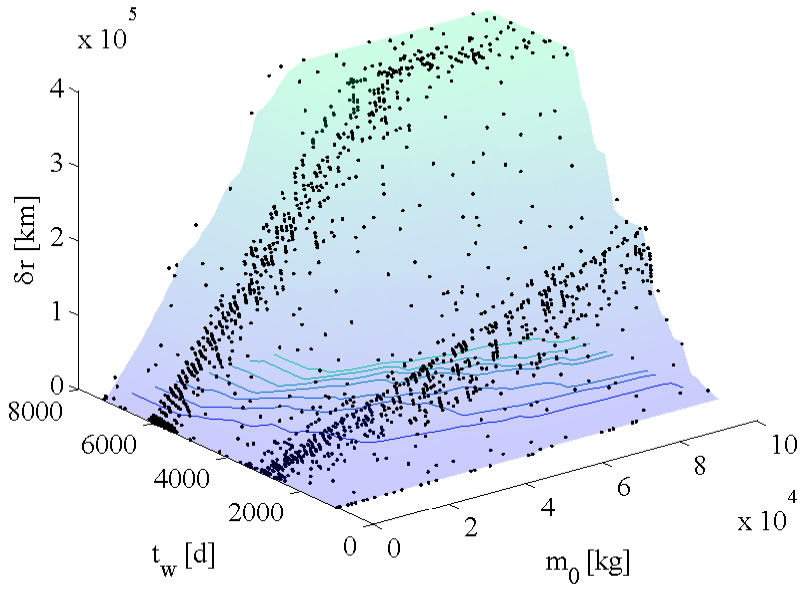

c) Pareto front for the deviation of asteroid Apophis through mass driver.

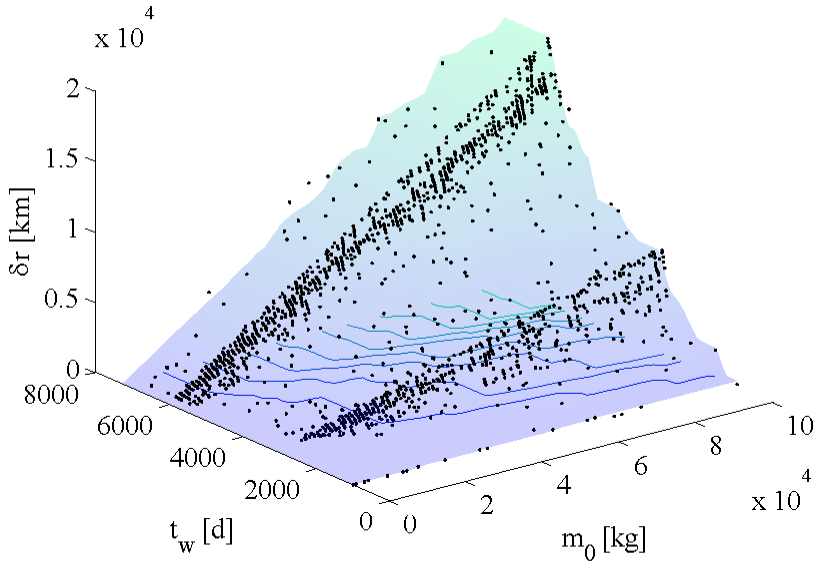

d) Pareto front for the deviation of asteroid Apophis through attached spacecraft propulsion.

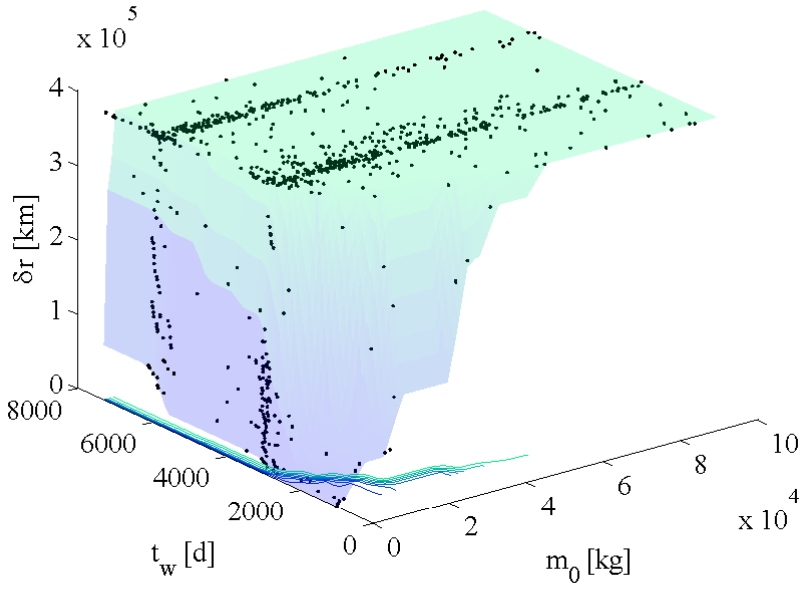

e) Pareto front for the deviation of asteroid Apophis through solar collector.

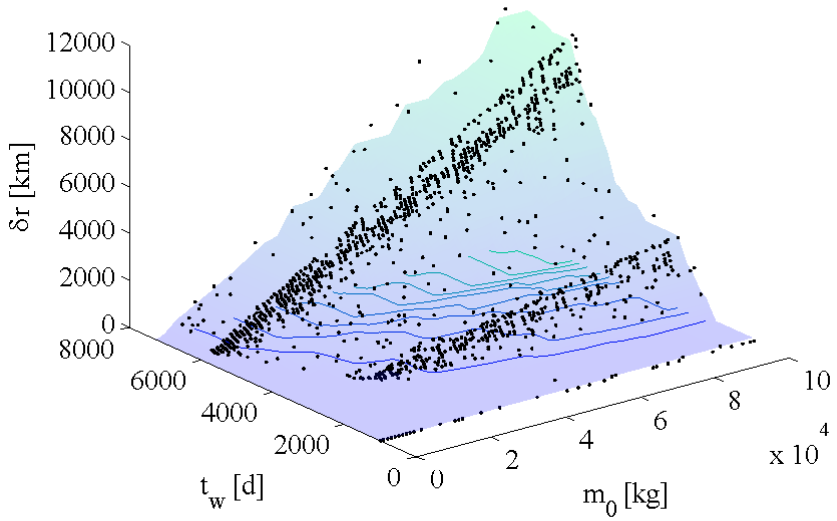

f) Pareto front for the deviation of asteroid Apophis through gravity tractor.

Figure 4.2: Pareto front for the deviation of asteroid Apophis through different strategies: a) kinetic impactor, b) nuclear interceptor, c) mass driver, d) attached spacecraft propulsion, e) solar collector, and e) gravity tractor.

Itokawa deviation mission

The asteroid Itokawa is at the MOID point on the 5th February 2029 (10,628 MJD2000). The Pareto fronts of the optimal solutions by means of the various deflection schemes are reported in Figure 4.3. The solar collector and nuclear interceptor reach also in this case the maximum limit set on the deviation, followed by the mass driver strategy. In all the Pareto fronts the stripes along the t_w axis are due to the choice of the best condition for the transfer trajectory and the interception point.

In this case few solutions exist for the kinetic impactor strategy for low value of masses and warning times. The reason is that, unlike the other strategies, the performance of kinetic impactor and nuclear interceptor are strongly related to the arrival condition at the asteroid. Since we optimise $\|\Delta\mathbf{r}+\delta\mathbf{r}\|$ instead of only $\|\delta\mathbf{r}\|$, the ideal optimal direction of the $\delta\mathbf{v}$ change is determined also in its sign (i.e., $+\delta\mathbf{v}$ or $-\delta\mathbf{v}$), but the real direction (when the transfer trajectory is included in the optimisation) could be far from the ideal one. In a real impact scenario $\|\Delta\mathbf{r}\|\approx 0$, hence the sign of the impulsive manoeuvre (but not its direction) is less influential because either $+\delta\mathbf{v}$ or $-\delta\mathbf{v}$ achieve a similar value of $\|\Delta\mathbf{r}+\delta\mathbf{r}\|$.

Due to the size and orbital elements of the asteroid Itokawa, the gravity tug is less performing than the low-thrust attached propulsion and kinetic impactor.

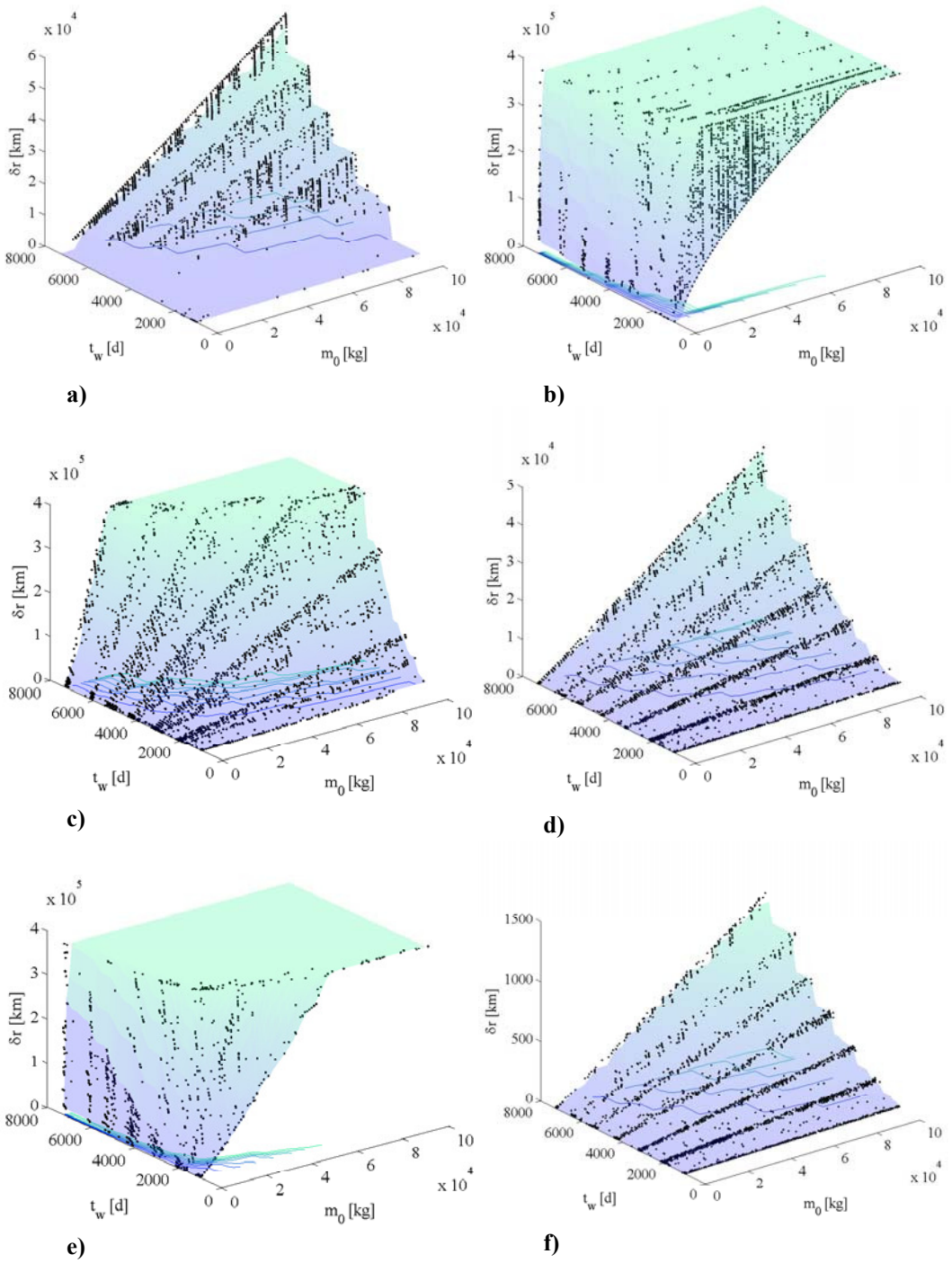

Figure 4.3: Pareto front for the deviation of asteroid Itokawa through different strategies: a) kinetic impactor, b) nuclear interceptor, c) mass driver, d) attached spacecraft propulsion, e) solar collector, and e) gravity tractor.

Castalia deviation mission

The mitigation scenario for asteroid Castalia considers the asteroid at the MOID on the 25th August 2029 (10,829 MJD2000). The Pareto fronts for all the deflection strategies are presented in Figure 4.4. The values of deflection achieved are generally lower than the other scenarios due to the high mass of the asteroid. For such a big asteroid only few strategies could be implemented to achieve a significant deflection. Its orbit is also considerably different from the Earth's and, for this set of orbital elements, chemical transfers (simply modelled as Lambert's arcs) do not allow meeting the most favourable conditions for an impulsive manoeuvre.

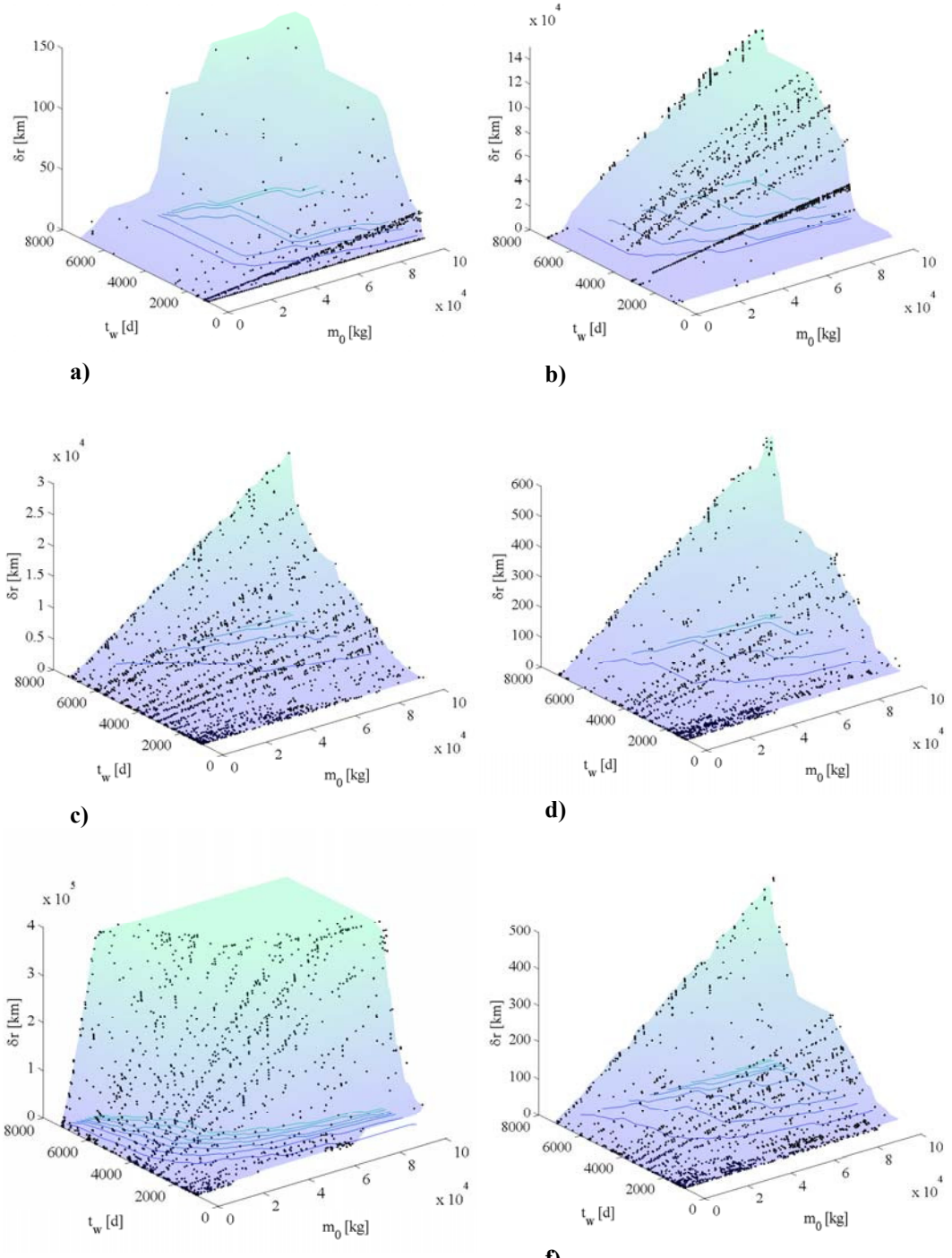

Figure 4.4: Pareto front for the deviation of asteroid Castalia through different strategies: a) kinetic impactor, b) nuclear interceptor, c) mass driver, d) attached spacecraft propulsion, e) solar collector, and e) gravity tractor.

1979XB deviation mission

Figure 4.5 presents the Pareto front for a set of mitigation missions to asteroid 1979XB, which is at the MOID on the 20th May 2030 (11,097 MJD2000). The kinetic impactor has higher performances than the low-thrust attached propulsion and gravity tug strategies; because of the high eccentricity and inclination, an intercepting trajectory is more efficient in term of propellant consumption than a rendezvous with high relative velocity.

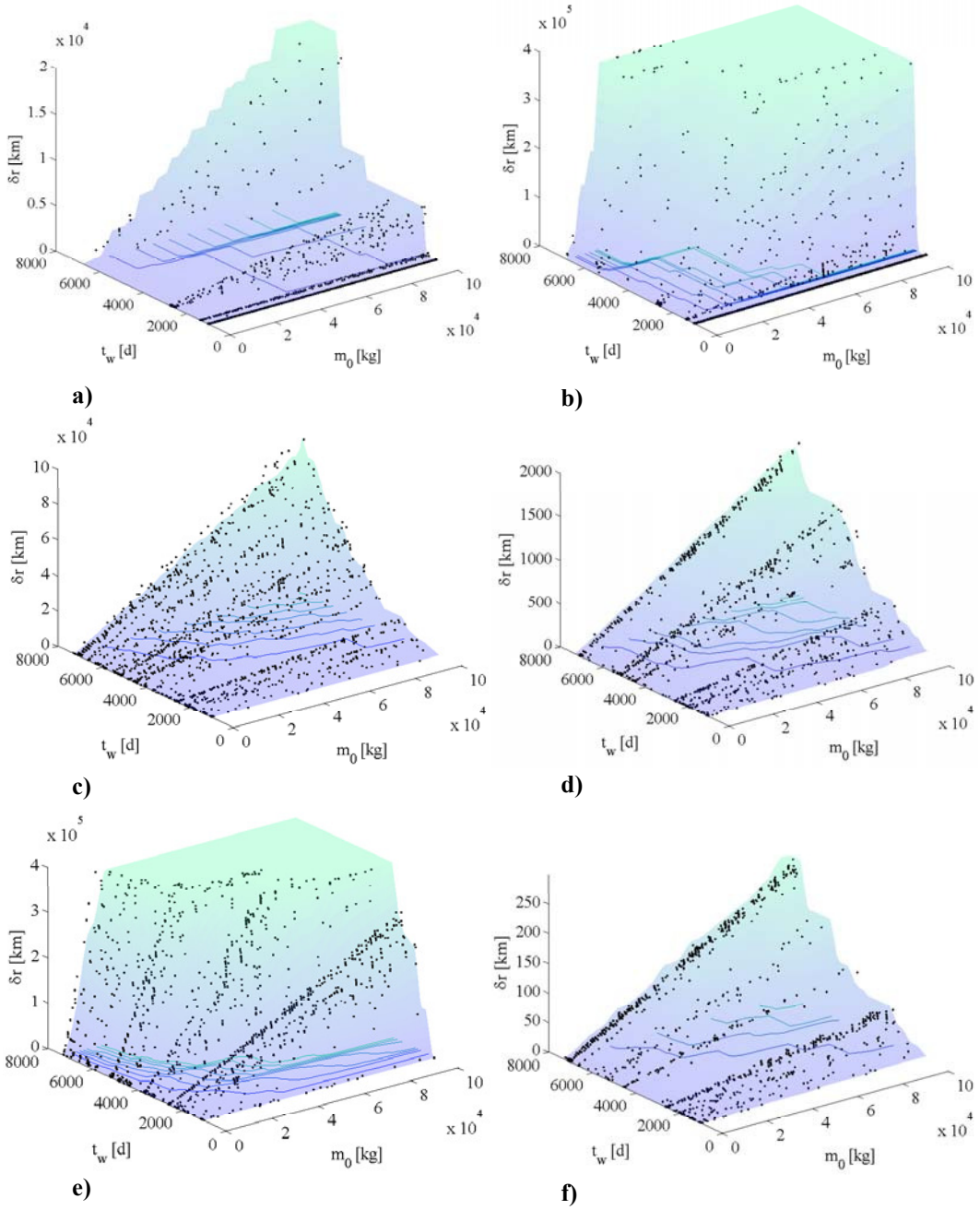

Figure 4.5: Pareto front for the deviation of asteroid 1979XB through different strategies: a) kinetic impactor, b) nuclear interceptor, c) mass driver, d) attached spacecraft propulsion, e) solar collector, and e) gravity tractor.

4.5.3. Multi-criteria analysis

The effectiveness and efficiency of each strategy are expressed through a set of Pareto-optimal points. To compare one strategy against the others we can define the concept of dominance of one Pareto set over another: an element (or solution belonging to the Pareto set) *k* of strategy *A* is said to be dominated by an element *j* of strategy *B* if all the components of the vectorial objective function $\mathbf{J}_j^B$ are better (smaller) than all the components of the vectorial objective function $\mathbf{J}_k^A$, where:

$$\mathbf{J}_k^A = \begin{bmatrix} J_{1,k}^A & J_{2,k}^A & \dots & J_{m,k}^A \end{bmatrix}^T$$

The dominance index $I_{d,A[B]}\left(\mathbf{x}_k^A\right)$ of an element *k* of strategy *A* with respect to strategy *B* is the cardinality of the set of elements of the Pareto front of strategy *B* that dominate the element *k*.

$$I_{d,A[B]}\left(\mathbf{x}_k^A\right) = \left|\left\{ j \mid j \in N_p^B \wedge \mathbf{x}_j^B \succ \mathbf{x}_k^A \right\}\right| \tag{4.10}$$

where the dominance symbol $\succ$ in Eq. (4.10) means that all the not equal components of $\mathbf{J}_j^B$ are better than the components of $\mathbf{J}_k^A$ (i.e., simple dominance):

$$\mathbf{x}_j^B \succ \mathbf{x}_k^A \Rightarrow \mathbf{J}_{i,j}^B \leq \mathbf{J}_{i,k}^A \ \forall\ i = 1,\dots m \tag{4.11}$$

If the dominance index $I_{d,A[B]}\left(\mathbf{x}_k^A\right)$ associated to an element *k* of strategy *A* is zero, it means that there is no element of the Pareto front of strategy *B* that dominates the element *k*.

We can say that strategy s_A dominates strategy s_B if the percentage of elements of *A* that are dominated (i.e., with dominance index $I_{d,A[B]}\left(\mathbf{x}^A\right)$ different than zero) by *B* is less than the percentage of the elements of *B* that are dominated by *A*.

$$d_k^{A[B]} = \begin{cases} 1 \text{ if } \; I_{d,A[B]}\left(\mathbf{x}_k^A\right) > 0 \\ 0 \text{ if } \; I_{d,A[B]}\left(\mathbf{x}_k^A\right) = 0 \end{cases}$$

$$s_A \succ s_B \Rightarrow \frac{1}{N_A}\sum_{k=1}^{N_A} d_k^{A[B]} < \frac{1}{N_B}\sum_{j=1}^{N_B} d_j^{B[A]}$$

where N_A is the total number of the solutions in the Pareto front of strategy s_A and N_B is the total number of solutions in the Pareto front of strategy s_B.

The dominance of the different strategies is shown in Table 4.4–Table 4.7 for the mitigation of asteroid Apophis, Itokawa, Castalia, and 1979XB, respectively. Chosen an asteroid, the numbers contained in the table are the percentages of dominance of one deviation strategy over another one. The value in each cell represents the percentage of elements of the strategy in the corresponding row that dominate over the elements of the strategy in the corresponding columns. For example in Table 4.4 (Apophis), 100% of the elements of the Pareto front of the nuclear interceptor dominate over the elements of the Pareto front of the mass driver mitigation strategy. Only 8% of the solutions of the Pareto front of the nuclear strategy dominate the elements of the solutions of the solar collector. The bold style in some cells of the tables indicates when one strategy clearly dominates over the other strategy in the corresponding column. In most of the cases, the sum of the percentage in a given cell with the percentage in the cell symmetric with respect to the diagonal is not 100 because the points on the Pareto set are not uniformly distributed, hence it could happen that 100% of points of one strategy are dominating only on a small fraction of points of the other set. Another reason is that the definition of dominance used in the comparison between two strategies is true also in the case of equality of two components [i.e., simple dominance, see Eq. (4.11)]. These figures have an inherent margin of error since the Pareto sets for each strategy are only composed of a finite and discrete number of elements. More accurate numbers can be computed by increasing the number of solutions, uniformly distributed, in each Pareto set.

Table 4.4: Strategy dominance for asteroid Apophis.

	Kinetic impactor	Nuclear interceptor	Mass driver	Attached propulsion	Solar Collector	Gravity Tractor
Kinetic impactor	–	0	1	17	0	78
Nuclear interceptor	**100**	–	**100**	**100**	8	**100**
Mass driver	**100**	0	–	**100**	0	**100**
Attached propulsion	100	0	0	–	0	**100**
Solar Collector	**100**	98	**100**	**100**	–	**100**
Gravity Tractor	74	0	0	0	0	–

Table 4.5: Strategy dominance for asteroid Itokawa.

	Kinetic impactor	Nuclear interceptor	Mass driver	Attached propulsion	Solar Collector	Gravity Tractor
Kinetic impactor	–	0	0	95	0	**100**
Nuclear interceptor	**100**	–	**100**	**100**	63	**100**
Mass driver	**100**	1	–	**100**	0	**100**
Attached propulsion	54	1	0	–	0	**100**
Solar Collector	**100**	64	**100**	**100**	–	**100**
Gravity Tractor	11	0	0	0	0	–

Table 4.6: Strategy dominance for asteroid Castalia.

	Kinetic impactor	Nuclear interceptor	Mass driver	Attached propulsion	Solar Collector	Gravity Tractor
Kinetic impactor	–	0	0	79[§§]	0	96[§§]
Nuclear interceptor	**100**	–	**100**	**100**	0	**100**
Mass driver	**100**	11	–	**100**	0	**100**
Attached propulsion	87	0	0	–	0	96
Solar Collector	**100**	**100**	**100**	**100**	–	**100**
Gravity Tractor	87	0	0	14	0	–

[§§] In this case, the numbers indicating the percentage dominance of the kinetic impactor over the low-thrust attached propulsion and the gravity tug are not very reliable, because the points of the Pareto front for the deflection mission of Castalia through kinetic impactor are concentrated in a small area of the range of masses and warning time.

Table 4.7: Strategy dominance for asteroid 1979XB.

	Kinetic impactor	Nuclear interceptor	Mass driver	Attached propulsion	Solar Collector	Gravity Tractor
Kinetic impactor	–	2	9	**76**	3	**99**
Nuclear interceptor	**100**	–	**100**	**100**	61	**100**
Mass driver	**97**	2	–	**100**	2	**100**
Attached propulsion	7	3	0	–	3	**100**
Solar Collector	**100**	25	**99**	**99**	–	**100**
Gravity Tractor	5	5	0	0	2	–

The comparison tables confirm the dominance of nuclear interceptor and solar collector strategies over the other options. The solar strategy is better performing than the nuclear interceptor for asteroids Apophis and Castalia, whereas the nuclear impactor achieves higher deviations (for the same values of masses and warning times) than the solar collector scheme for the asteroid 1979XB. In fact the orbit of asteroid 1979XB has high eccentricity and inclination; for this reason, it is hardly accessible for a rendezvous mission. Moreover, it goes far from the Sun, hence the exploitation of the solar radiation is less efficient. The mass driver system usually achieves better results over the whole domain than the kinetic impactor, low thrust attached propulsion and gravity tug strategies. The gravity tug strategy is usually dominated by all the other options; however it dominates the kinetic impactor over some regions of the domain in the case of Apophis, Itokawa and Castalia. In particular, the increased mass of Castalia (with respect to the other asteroids) penalises to a greater degree the kinetic impactor with respect to the gravity tug strategy, the reason for this being intrinsic to the system model [137]. The kinetic impactor has good performances for the Itokawa scenario, whereas it is particularly outperforming with respect to the low-thrust attached propulsion and the gravity tug in the case of asteroid 1979XB, because of its high eccentricity and inclination.

In Appendix B the multi-criteria analysis is performed considering as additional criterion the Technology Readiness Level (TRL) of each deflection strategy as a measure of the expected practicability in the near future.

4.6. Summary

In this chapter, different strategies to deviate dangerous NEOs are compared. The formulation described in Chapter 2 and Chapter 3 is used to compute the variation of the MOID due to a given impulsive or low-thrust deviation strategy. The performance of each strategy is evaluated in terms of warning time, wet mass of the spacecraft at the Earth, and achievable deviation at the MOID; a set of Pareto optimal solutions is computed according to these three criteria for each asteroid mitigation scenario. The sets of Pareto optimal solutions for each strategy are then compared by defining the dominance of one Pareto set over another. Moreover, in Appendix B, the technology readiness level of each system is taken into account by adding to the warning time the time needed to fully develop the required technology.

This preliminary comparison shows that the solar concentrator and nuclear interceptor are generally dominant. The solar collector strategy remains a competitive technology even after technology readiness considerations (see Appendix B). On the other hand, kinetic impactor can still be a very reasonable option for small asteroids, as it is able to achieve deviations of several Earth radii with an affordable mass. The definition of the TRL factor is, of course, arbitrary and is subject to the actual development of each specific piece of technology that composes a given strategy. However, for the kinetic impactor no technology development is required at present and it is therefore the only strategy already available. The percentage of dominance for the other methods, instead, is expected to change according to the future investment in one technology or the other.

On the other hand, it has to be noticed that NEO mitigation through impulsive action presents the risk of fragmentation of the asteroid in pieces that could still impact the Earth causing damage. A more accurate comparison would require taking into account the contingency of fragmentation of the asteroid due to an impulsive deflection action [51]. Moreover, a more complete reproduction of the actual Pareto sets would provide more accurate figures for the percentage of dominance and more criteria could be used for the multi-criteria optimisation, such as mission cost and robustness of the deflection action.

Finally the analysis presented in this chapter is limited to a small group of asteroids. A more exhaustive analysis comprising a larger group of asteroids is currently being performed and will give an indication on the most effective strategy for a given class of asteroids [126].

Chapter 5.

Optimal low-thrust trajectories to asteroids through an algorithm based on differential dynamic programming

In the previous chapters families of optimal solutions for potential deflection missions to NEOs have been generated, each one representing a complete mission with a specific launch date and transfer time. The global search for launch opportunities is performed using simplified models for the trajectory and considering a two-body dynamics; in particular the preliminary design of the low-thrust trajectory is performed through a shape-based approach [118],[136], which provides an estimation of the required propellant mass.

As a second stage, the first guess solutions of the Pareto fronts can be refined and the transfer trajectory can be designed using more accurate models of the dynamics. In this chapter, an optimisation algorithm based on Differential Dynamic Programming (DDP) is developed and applied to the design of rendezvous and fly-by trajectories to near Earth objects. Differential dynamic programming is a successive approximation technique that computes a feedback control law in correspondence of a fixed number of decision times. In this way the high dimensional problem characteristic of low-thrust optimisation is reduced into a series of small dimensional problems. The proposed method exploits the stage-wise approach to incorporate an adaptive refinement of the discretisation mesh within the optimisation process. A particular interpolation technique is used to preserve the feedback nature of the control law, thus improving robustness against some approximation errors introduced during the adaptation process. The algorithm implements global variations of the control law, which ensure a further increase in robustness. The results presented here show how the proposed

approach is capable of fully exploiting the multi-body dynamics of the problem; in fact, in one of the study cases, a fly-by of the Earth, which was not included in the first guess solution, is scheduled.

Section 5.1 introduces the classical DDP approach, whereas Section 5.2 and 5.3 present the modified method. The DDP algorithm is applied in Section 5.4 to refine the transfer trajectory of the solutions of one of the Pareto fronts presented in Chapter 3. Section 5.5 contains an analysis of some mission opportunities for the rendezvous and fly-by of a selected number of asteroids; for these transfers also the escape phase is considered, hence the three-body dynamics model is used. Some solutions with a long time of flight and a high number of spirals will also be presented.

5.1. Differential Dynamic Programming

Differential dynamic programming, firstly introduced by Jacobson and Mayne in 1969 [111], is a successive approximation technique for finding the optimal control of a non-linear system. It overcomes the issue of dimensionality linked to dynamic programming [112], by introducing in the optimisation process a linear-quadratic approximation of the cost function in the neighbourhood of the nominal trajectory.

Given a nominal control strategy, each iteration of DDP produces, through the backward propagation of the difference Bellman equation, a feedback control strategy which is forward propagated, to give an improved trajectory and a reduction in the cost function. The control laws, produced within successive iterations, approach the optimal control solution of the problem.

5.1.1. Differential dynamic programming for trajectory optimisation

The standard DDP technique works with two variable classes: the system state vector $\mathbf{s}(t)$ and the dynamic control vector $\mathbf{u}(t)$. A low-thrust trajectory is characterised by a continuous-time dynamics. However, for solving the low-thrust optimisation problem through DDP, the discrete-time approach is usually adopted;

the continuous-time problem is transcribed in a discrete-time system and approximated by difference equations. Given a sequence of controls $\{\mathbf{u}_k\}_{k=1}^{N}$, the resulting trajectory $\{\mathbf{s}_k\}_{k=1}^{N+1}$ is computed by the recursive formula:

$$\begin{aligned} &\mathbf{s}_{k+1} = \mathbf{f}(\mathbf{s}_k, \mathbf{u}_k; t_k) && k = 1, ..., N \\ &\mathbf{s}_1 = \overline{\mathbf{s}}_1 \end{aligned} \tag{5.1}$$

where $\overline{\mathbf{s}}_1$ is the initial condition at time t_1, which is assumed fixed and $\mathbf{f}$ is the discrete-time state transition function, which expresses the state vector at time $k+1$ as a function of state and control vector at the previous time step. We define $k = 1, ..., N$ as the stages of this problem, i.e., the decision times over which the control law is allowed to change.

The optimisation problem is described by a cost function to be minimised; we define the cost function of a trajectory with initial condition $\overline{\mathbf{s}}_1$ and control schedule $\{\mathbf{u}_k\}_{k=1}^{N}$ as:

$$J(\{\mathbf{u}_k\}; \overline{\mathbf{s}}_1) = \sum_{k=1}^{N} g(\mathbf{s}_k, \mathbf{u}_k; t_k) \tag{5.2}$$

where g represents the scalar stage-wise loss function of $(\mathbf{s}_k, \mathbf{u}_k; t_k)$. Eq. (5.2) corresponds to the integral term of the cost function for the continuous-time problem. The optimisation problem is to determine the sequence of control $\{\mathbf{u}_k\}_{k=1}^{N}$ that minimises Eq. (5.2) under certain constraints. The constraints considered at this point are equality constrains on the final state:

$$\boldsymbol{\varphi}(\mathbf{s}_{N+1}; t_{N+1}) = \mathbf{0} \tag{5.3}$$

where the final time t_{N+1} is supposed to be given explicitly. The constrained optimisation is converted into an unconstrained one by including Eq. (5.3) into the cost function in Eq. (5.2) through a time invariant set of Lagrange multipliers $\boldsymbol{\lambda}$ [120]:

$$J\left(\{\mathbf{u}_k\};\bar{\mathbf{s}}_1\right)=\sum_{k=1}^{N} g\left(\mathbf{s}_k,\mathbf{u}_k;t_k\right)+\boldsymbol{\lambda}^T\cdot\boldsymbol{\varphi}\left(\mathbf{s}_{N+1};t_{N+1}\right) \tag{5.4}$$

If we try to minimise Eq. (5.4) through dynamic programming, we need to apply Bellman's principle of optimality for discrete-time systems [111]:

$$V_k\left(\mathbf{s}_k\right)=\min_{\mathbf{u}_k}\left[g\left(\mathbf{s}_k,\mathbf{u}_k;t_k\right)+V_{k+1}\left(\mathbf{s}_{k+1}\right)\right] \tag{5.5}$$

Eq. (5.5) gives the optimal return function at stage *k,* $V_k\left(\mathbf{s}_k\right)$, defined as the cost $J\left(\{\mathbf{u}_k\};\mathbf{s}_k\right)$ associated to the segment of the trajectory starting at point $\mathbf{s}_k$, if the optimal control policy is employed (see Figure 5.1).

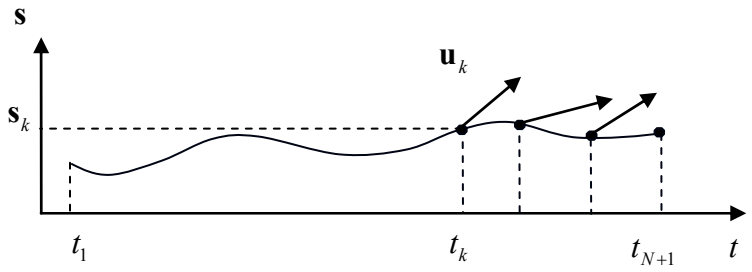

Figure 5.1: Dynamic programming approach.

The value of $V_k\left(\mathbf{s}_k\right)$ results from the minimisation of the optimal return function at stage $k+1$ added to the term of the *k*-stage-wise loss function *g*. Starting from the final condition at the end-point of the trajectory:

$$V_{N+1}\left(\mathbf{s}_{N+1}\right)=\boldsymbol{\lambda}^T\cdot\boldsymbol{\varphi}\left(\mathbf{s}_{N+1};t_{N+1}\right)$$

dynamic programming requires the solution of Eq. (5.5) from stage *N* backward to stage 1. The limitation of dynamic programming for continuous problem is the high dimensional problem resulting from the application of Eq. (5.5) to every stage *k*. In fact this is equivalent to finding a family of optimal solutions, one from each different initial point $\mathbf{s}_k, k=1,...,N$.

In order to overcome this computational limitation, *differential* dynamic programming applies the principle of optimality in the neighbourhood of a nominal trajectory. At each stage *k*, the full expression of the stage-wise cost

function *g* and the optimal return function from the next iteration onward V_{k+1} are replaced by their quadratic approximation about the current nominal control and trajectory.

The state and control vectors at each discretisation step can be written as a variation from their nominal values:

$$\begin{aligned} \mathbf{s}_k &= \overline{\mathbf{s}}_k + \delta\mathbf{s}_k \\ \mathbf{u}_k &= \overline{\mathbf{u}}_k + \delta\mathbf{u}_k \end{aligned} \tag{5.6}$$

where the superscript dash indicates the nominal conditions. With this notation, $\left\{\overline{\mathbf{u}}_k\right\}_{k=1}^{N}$ is the nominal control profile and $\left\{\overline{\mathbf{s}}_k\right\}_{k=1}^{N+1}$ the corresponding trajectory, obtained by the integration of Eqs. (5.1) under the nominal control $\left\{\overline{\mathbf{u}}_k\right\}_{k=1}^{N}$.

Said $QP[\cdot]$ the linear and quadratic part of the Taylor expansion of a generic function, differential dynamic programming reduces Eq. (5.5) to:

$$V_k\left(\overline{\mathbf{s}}_k + \delta\mathbf{s}_k\right) \simeq \min_{\delta u_k}\left[QP\left[g\left(\overline{\mathbf{s}}_k + \delta\mathbf{s}_k, \overline{\mathbf{u}}_k + \delta\mathbf{u}_k; t_k\right) + V_{k+1}\left(\overline{\mathbf{s}}_{k+1} + \delta\mathbf{s}_{k+1}\right)\right]\right] \tag{5.7}$$

Similarly to the procedure for solving Eq. (5.5), the solution of Eq. (5.7) is performed *backward* in time, from the final stage *N* to the initial stage 1, the boundary condition at t_{N+1} being:

$$V_{N+1}\left(\overline{\mathbf{s}}_{N+1} + \delta\overline{s}_{k+1}\right) \simeq QP\left[\boldsymbol{\lambda}^T \cdot \boldsymbol{\varphi}\left(\overline{\mathbf{s}}_{N+1} + \delta\overline{s}_{k+1}; t_{N+1}\right)\right]$$

The necessary requirement is that the new control sequence should produce small variations in the state vector such that the linear-quadratic approximation in Eq. (5.7) holds true. This may be achieved even with a big variation in the control action, as long as the time duration of this variation is small. This means that the new control $\mathbf{u}_k$ does not need to be restricted to the neighbourhood of $\overline{\mathbf{u}}_k$, therefore the second of Eqs. (5.6) can be modified as follows:

$$\mathbf{u}_k = \mathbf{u}_k^* + \delta\mathbf{u}_k \tag{5.8}$$

where the global variation in the nominal control $\bar{\mathbf{u}}_k$ to $\mathbf{u}_k^*$ is computed by minimising Eq. (5.7), where the nominal trajectory $\bar{\mathbf{s}}_k$ is substituted:

$$V_k\left(\bar{\mathbf{s}}_k\right) \simeq \min_{\mathbf{u}_k^*}\left[QP\left[g\left(\bar{\mathbf{s}}_k, \mathbf{u}_k; t_k\right) + V_{k+1}\left(\bar{\mathbf{s}}_{k+1}\right)\right]\right] \tag{5.9}$$

Therefore the linear-quadratic expansion of Eq. (5.5) is now evaluated about the point $\left(\bar{\mathbf{s}}_k, \mathbf{u}_k^*\right)$:

$$V_k\left(\bar{\mathbf{s}}_k + \delta\mathbf{s}_k\right) \simeq \min_{\delta u_k}\left[QP\left[g\left(\bar{\mathbf{s}}_k + \delta\mathbf{s}_k, \mathbf{u}_k^* + \delta\mathbf{u}_k; t_k\right) + V_{k+1}\left(\bar{\mathbf{s}}_{k+1} + \delta\mathbf{s}_{k+1}\right)\right]\right] \tag{5.10}$$

This hypothesis was implemented in an algorithm that employs global variations in the control, hence strong variations in the state [111],[120].

The necessary condition to minimise the right hand side of Eq. (5.10) is to set to zero its first derivative with respect to the control. This leads to the definition of a feedback strategy of the form:

$$\delta\mathbf{u}_k = \boldsymbol{\beta}_k \cdot \delta\mathbf{s}_k \tag{5.11}$$

The variation in control is expressed as a function proportional to the state variation. Eqs. (5.9) and (5.10) are computed backward in time for every stage $k = N,...,1$ and the coefficient $\boldsymbol{\beta}_k$ is constructed and stored in memory.

At this point, the trajectory is swept *forward* in time, for every stage $k = 1,...,N$: the successor control policy $\mathbf{u}_k$ is constructed and the new trajectory is propagated through the state transition function $\mathbf{f}$, with the initial condition $\bar{\mathbf{s}}_1$:

$$\begin{cases} \mathbf{u}_k = \mathbf{u}_k^* + \boldsymbol{\beta}_k\left(\mathbf{s}_k - \bar{\mathbf{s}}_k\right) \\ \mathbf{s}_{k+1} = \mathbf{f}\left(\mathbf{s}_k, \mathbf{u}_k; t_k\right) \\ \mathbf{s}_1 = \bar{\mathbf{s}}_1 \end{cases} \qquad k = 1,...,N$$

A posteriori we need to verify that the variations of the control do not break the assumption of linear-quadratic approximations in Eq. (5.10). To this purpose, a method was proposed by Jacobson and Mayne [111] and later refined by

Gershwin and Jacobson [120], to determine the section of the trajectory over which the new control strategy can be applied.

The nominal control is applied over an initial segment of the trajectory, up to step k_{lim}, afterwards the new strategy is adopted:

$$\mathbf{u}_k = \begin{cases} \overline{\mathbf{u}}_k & k = 1,...,k_{\text{lim}} - 1 \\ \mathbf{u}_k^* + \boldsymbol{\beta}_k \delta \mathbf{s}_k & k = k_{\text{lim}},...,N \end{cases} \tag{5.12}$$

The resulting control law and the associated trajectory are represented respectively in Figure 5.2 and Figure 5.3:

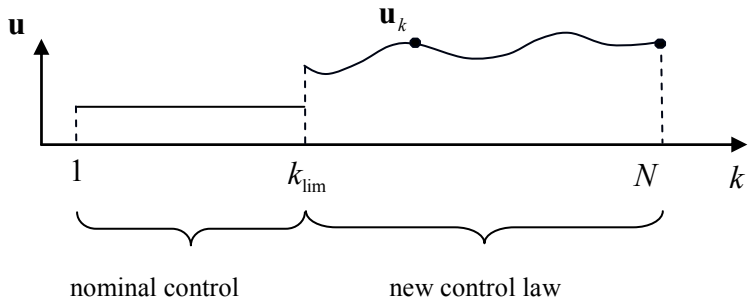

Figure 5.2: Control law schedule according to Jacobson's algorithm.

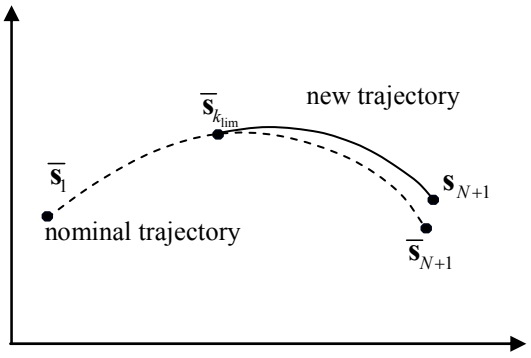

Figure 5.3: Trajectory associated to the control law in Eq. (5.12).

The guess value of k_{lim} is initially set to 1 and is progressively increased, until an improvement in the value of the cost function $J\left(\{\mathbf{u}_k\};\overline{\mathbf{s}}_1\right)$ with respect to its nominal value $J\left(\{\overline{\mathbf{u}}_k\};\overline{\mathbf{s}}_1\right)$ is registered. This procedure is called *step-size adjustment method*.

In summary, the core of the DDP technique consists in a backward recursion followed by a forward recursion. A nominal trajectory and control policy are

required as input and an improved control law and trajectory are provided as output, which ensures a decrease of the value of the cost function. Successive iterations of the backward and forward recursions produce control laws that progressively approximate the optimal control of the problem. Figure 5.4 depicts the history of the control magnitude during the convergence process for a direct transfer from Earth to Mars. The value of $k_{\lim}$ selected at the first iteration of the algorithm is close to the number of discretisation steps N and tends to 1 as convergence is reached.

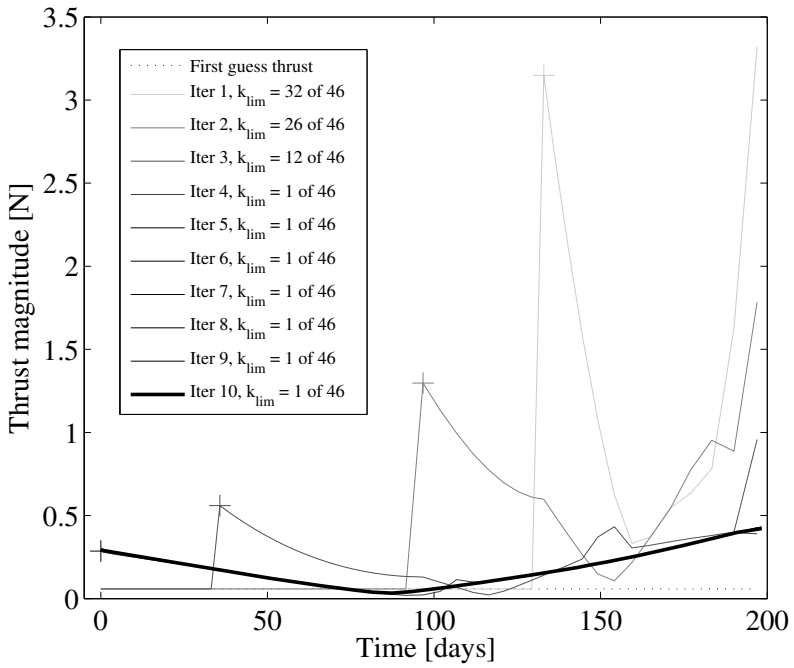

Figure 5.4: Control law during the convergence process. Direct transfer Earth to Mars, with a time of flight of 200 days.

The algorithm has quadratic convergence under the assumption that the Hessian matrix of the cost function is positive definite [141]−[143].

In the following subsections, the fundamental DDP algorithm is derived, in the case of end-point equality constraints. The purpose is to give a concise exposition of the original method upon which the one proposed here (see Section 5.2) is based on. We report it here because the algorithm derivation is useful to understand the algorithm itself and in order to summarise some part of the theory, presented in different references: the algorithm derivation with global control variations by Jacobson and Mayne [111], the end-point constraints algorithm by Gershwin and Jacobson [120], and the matrix algorithmic exposition by Yakowitz

and Rutherford [113]. For the entire demonstration the reader should turn to the source references.

The fundamental DDP algorithm

In this subsection we derive the fundamental DDP algorithm, for an unconstrained problem, starting from the general formulation presented in the previous section. Both sides of Eq. (5.10) are expanded in Taylor series about the point $\left(\overline{\mathbf{s}}_k, \mathbf{u}_k^*\right)$:

$$\begin{aligned}\frac{1}{2}\delta\mathbf{s}_k^T V_{ss}^k \delta\mathbf{s}_k + V_s^k \delta\mathbf{s}_k + \overline{V}_k\left(\overline{\mathbf{s}}_k\right) + \Theta_k \simeq \min_{\delta\mathbf{u}_k}\Big[\Theta_{k+1} + g\left(\overline{\mathbf{s}}_k, \overline{\mathbf{u}}_k; t_k\right) + \Delta\mathbf{g}_k + \\ + \mathbf{g}_s^k \delta\mathbf{s}_k + \mathbf{g}_u^k \delta\mathbf{u}_k + \frac{1}{2}\delta\mathbf{s}_k^T \mathbf{g}_{ss}^k \delta\mathbf{s}_k + \frac{1}{2}\delta\mathbf{u}_k^T \mathbf{g}_{uu}^k \delta\mathbf{u}_k + \delta\mathbf{u}_k^T \mathbf{g}_{us}^k \delta\mathbf{s}_k + \\ + \overline{V}_{k+1}\left(\overline{\mathbf{s}}_{k+1}\right) + V_s^{k+1}\delta\mathbf{s}_{k+1} + \frac{1}{2}\delta\mathbf{s}_{k+1}^T V_{ss}^{k+1}\delta\mathbf{s}_{k+1}\Big]\end{aligned} \tag{5.13}$$

where Θ_k is defined as the difference between the optimal return function obtained by applying $\left\{\mathbf{u}_j\right\}_{j=k}^N$ from the state $\overline{\mathbf{s}}_k$ until the end of the trajectory, and the nominal cost computed by using $\left\{\overline{\mathbf{u}}_j\right\}_{j=k}^N$ from the state $\overline{\mathbf{s}}_k$ until the end of the trajectory:

$$\Theta_k = V_k\left(\overline{\mathbf{s}}_k\right) - \overline{V}_k\left(\overline{\mathbf{s}}_k\right) \tag{5.14}$$

Analogously we define $\Theta_{k+1} = V_{k+1}\left(\overline{\mathbf{s}}_{k+1}\right) - \overline{V}_{k+1}\left(\overline{\mathbf{s}}_{k+1}\right)$, whereas $\Delta g_k = g\left(\overline{\mathbf{s}}_k, \mathbf{u}_k^*; t_k\right) - g\left(\overline{\mathbf{s}}_k, \overline{\mathbf{u}}_k; t_k\right)$. The left-hand side of Eq. (5.13) contains linear and quadratic terms of $\delta\mathbf{s}_k$ and the right-hand side contains linear and quadratic terms of $\delta\mathbf{s}_k$, $\delta\mathbf{u}_k$ and $\delta\mathbf{s}_{k+1}$, where:

$$\begin{aligned}\delta\mathbf{s}_{k+1} = \mathbf{s}_{k+1} - \overline{\mathbf{s}}_{k+1} = \mathbf{f}\left(\overline{\mathbf{s}}_k + \delta\mathbf{s}_k, \mathbf{u}_k^* + \delta\mathbf{u}_k; t_k\right) - \mathbf{f}\left(\overline{\mathbf{s}}_k, \overline{\mathbf{u}}_k; t_k\right) = \\ \Delta\mathbf{f}_k + \mathbf{f}_s^k \delta\mathbf{s}_k + \mathbf{f}_u^k \delta\mathbf{u}_k + \frac{1}{2}\delta\mathbf{s}_k^T \mathbf{f}_{ss}^k \delta\mathbf{s}_k + \frac{1}{2}\delta\mathbf{u}_k^T \mathbf{f}_{uu}^k \delta\mathbf{u}_k + \delta\mathbf{u}_k^T \mathbf{f}_{us}^k \delta\mathbf{s}_k\end{aligned} \tag{5.15}$$

with $\Delta\mathbf{f}_k = \mathbf{f}\left(\bar{\mathbf{s}}_k, \mathbf{u}_k^*; t_k\right) - \mathbf{f}\left(\bar{\mathbf{s}}_k, \bar{\mathbf{u}}_k; t_k\right)$. By substituting Eq. (5.15) into Eq. (5.13) and by grouping the terms of the same order, the resulting equation can be written in a matrix form:

$$\begin{aligned}\delta\mathbf{s}_k^T\mathbf{P}_k\delta\mathbf{s}_k + \mathbf{Q}_k\delta\mathbf{s}_k + \Theta_k \simeq \min_{\delta\mathbf{u}_k}\big[\,&\delta\mathbf{s}_k^T\mathbf{A}_k\delta\mathbf{s}_k + \delta\mathbf{u}_k^T\mathbf{C}_k\delta\mathbf{u}_k + \delta\mathbf{u}_k^T\mathbf{B}_k\delta\mathbf{s}_k + \\ &+\delta\mathbf{s}_k^T\mathbf{E}_k + \delta\mathbf{u}_k^T\mathbf{D}_k + \Theta_{k+1} + \Delta\mathbf{g}_k + \mathbf{Q}_{k+1}\Delta\mathbf{f}_k + \Delta\mathbf{f}_k^T\mathbf{P}_{k+1}\Delta\mathbf{f}_k\,\big]\end{aligned} \tag{5.16}$$

where some matrices are introduced for clarity purpose.

$$\begin{aligned}\mathbf{P}_k &= \frac{1}{2}V_{ss}^k && n\times n\\ \mathbf{Q}_k &= V_s^k && 1\times n\end{aligned}$$

denote the linear and quadratic part of the Taylor expansion of the optimal return function at stage *k*. The matrices $\mathbf{A}_k$, $\mathbf{B}_k$, $\mathbf{C}_k$, $\mathbf{D}_k$ and $\mathbf{E}_k$, instead, contain the derivatives of the stage-wise loss function *g* and the state transition function $\mathbf{f}$ at stage *k*, and the derivatives of the optimal return function of the next stage forward V_{k+1}. If $\mathbf{u}_k$ and $\mathbf{s}_k$ are respectively a $m\times 1$ and $n\times 1$ vector, we define $\mathbf{g}_u$ and $\mathbf{g}_s$ to be respectively the $1\times m$ and $1\times n$ gradient of the scalar cost function *g* with respect to the components of the control and the state vector; $\mathbf{g}_{uu}$, $\mathbf{g}_{ss}$ and $\mathbf{g}_{su}$ represent the block components of the Hessian matrix of *g* respectively of size $m\times m$, $n\times n$ and $n\times m$. Said $\mathbf{f}\left(\mathbf{s}_k, \mathbf{u}_k; t_k\right)$ the state transition matrix, we denote with $\mathbf{f}_u$ and $\mathbf{f}_s$ the Jacobian of $\mathbf{f}$ with respect to $\mathbf{u}$ and $\mathbf{s}$ of size $n\times m$ and $n\times n$ and with $\mathbf{f}_{uu}$, $\mathbf{f}_{ss}$ and $\mathbf{f}_{us}$ the blocks components of the Hessian matrix of $\mathbf{f}$ respectively of size $m\times m\times n$, $n\times n\times n$ and $n\times m\times n$. All the above quantities are evaluated at $\left(\bar{\mathbf{s}}_k, \mathbf{u}_k^*\right)$.

$$\mathbf{A}_k = \frac{1}{2}\left(\mathbf{g}_{ss}^k + \sum_{j=1}^{n} \left[V_s^{k+1} \right]_j \left[\mathbf{f}_{ss}^k \right]_j + \mathbf{f}_s^{kT} V_{ss}^{k+1} \mathbf{f}_s^k + \Delta \mathbf{f}_k V_{ss}^{k+1} \mathbf{f}_{ss}^k \right) \qquad n \times n$$

$$\mathbf{B}_k = \left(\mathbf{g}_{su}^k + \sum_{j=1}^{n} \left[V_s^{k+1} \right]_j \left[\mathbf{f}_{su}^k \right]_j + \mathbf{f}_s^{kT} V_{ss}^{k+1} \mathbf{f}_u^k + \Delta \mathbf{f}_k V_{ss}^{k+1} \mathbf{f}_{su}^k \right)^T \qquad m \times n$$

$$\mathbf{C}_k = \frac{1}{2}\left(\mathbf{g}_{uu}^k + \sum_{j=1}^{n} \left[V_s^{k+1} \right]_j \left[\mathbf{f}_{uu}^k \right]_j + \mathbf{f}_u^{kT} V_{ss}^{k+1} \mathbf{f}_u^k + \Delta \mathbf{f}_k V_{ss}^{k+1} \mathbf{f}_{uu}^k \right) \qquad m \times m \qquad (5.17)$$

$$\mathbf{D}_k = \left(\mathbf{g}_u^k + V_s^{k+1} \mathbf{f}_u^k + \Delta \mathbf{f}_k^T V_{ss}^{k+1} \mathbf{f}_u^k \right)^T \qquad m \times 1$$

$$\mathbf{E}_k = \left(\mathbf{g}_s^k + V_s^{k+1} \mathbf{f}_s^k + \Delta \mathbf{f}_k^T V_{ss}^{k+1} \mathbf{f}_s^k \right)^T \qquad n \times 1$$

Note that the last terms of the matrices $\mathbf{A}_k$, $\mathbf{B}_k$ and $\mathbf{C}_k$ have to be rewritten in order to represent a quadratic form respectively with respect to $(\delta \mathbf{s}_k, \delta \mathbf{s}_k)$, $(\delta \mathbf{s}_k, \delta \mathbf{u}_k)$ and $(\delta \mathbf{u}_k, \delta \mathbf{u}_k)$. Moreover the matrices $\mathbf{A}_k$, $\mathbf{C}_k$ are symmetric.
The constant part of Eq. (5.16) , instead, can be grouped in:

$$\Theta_k = \Theta_{k+1} + \Delta \mathbf{g}_k + \mathbf{Q}_{k+1} \Delta \mathbf{f}_k + \Delta \mathbf{f}_k^T \mathbf{P}_{k+1} \Delta \mathbf{f}_k \qquad (5.18)$$

with the final condition:

$$\Theta_{N+1} = 0 \qquad (5.19)$$

The value of $\mathbf{u}_k^*$ in Eq. (5.8) is computed by solving the minimisation problem on the right hand side of Eq. (5.9), which is equivalent to solving the right hand side of Eq. (5.16) for $\delta \mathbf{s}_k$ and $\delta \mathbf{u}_k$ set to zero:

$$\min_{\mathbf{u}_k^*} \left[\Delta \mathbf{g}_k + \mathbf{Q}_{k+1} \Delta \mathbf{f}_k + \Delta \mathbf{f}_k^T \mathbf{P}_{k+1} \Delta \mathbf{f}_k \right] \qquad (5.20)$$

As a consequence at $\mathbf{u}_k^*$ the following condition is satisfied:

$$\nabla_u \left[\Delta \mathbf{g}_k + V_s^{k+1} \Delta \mathbf{f}_k + \frac{1}{2} \Delta \mathbf{f}_k^T V_{ss}^{k+1} \Delta \mathbf{f}_k \right] = 0 \Rightarrow \mathbf{g}_u^k + V_s^{k+1} \mathbf{f}_u^k + \Delta \mathbf{f}_k^T V_{ss}^{k+1} \mathbf{f}_u^k = 0 \Rightarrow \mathbf{D}_k = 0$$

Once $\mathbf{u}_k^*$ is computed, Eq. (5.16) can be solved with respect to $\delta\mathbf{u}_k$. The necessary condition for the minimisation of Eq. (5.16) with respect to $\delta\mathbf{u}_k$ implies that:

$$2\mathbf{C}_k\delta\mathbf{u}_k + \mathbf{B}_k\delta\mathbf{s}_k = 0 \Rightarrow \delta\mathbf{u}_k = -\frac{1}{2}\mathbf{C}_k^{-1}\mathbf{B}_k\delta\mathbf{s}_k \tag{5.21}$$

Eq. (5.21) gives the coefficient $\boldsymbol{\beta}_k$ of the feedback control law in Eq. (5.11):

$$\boldsymbol{\beta}_k = -\frac{1}{2}\mathbf{C}_k^{-1}\mathbf{B}_k \qquad m\times n \tag{5.22}$$

The variation in control in Eq. (5.21) can be substituted back in Eq. (5.16) and by grouping the terms of the same order we obtain:

$$\begin{aligned}\mathbf{Q}_k &= \mathbf{E}_k^T \\ \mathbf{P}_k &= \mathbf{A}_k - \frac{1}{4}\mathbf{B}_k^T\mathbf{C}_k^{-1}\mathbf{B}_k\end{aligned} \tag{5.23}$$

with the final conditions:

$$\begin{aligned}\mathbf{Q}_{N+1} &= \left[\boldsymbol{\lambda}^T\cdot\boldsymbol{\varphi}\left(\bar{\mathbf{s}}_{N+1};t_{N+1}\right)\right]_s \\ \mathbf{P}_{N+1} &= \frac{1}{2}\left[\boldsymbol{\lambda}^T\cdot\boldsymbol{\varphi}\left(\bar{\mathbf{s}}_{N+1};t_{N+1}\right)\right]_{ss}\end{aligned} \tag{5.24}$$

Eqs. (5.20), (5.17), (5.18), (5.22), and (5.23) are computed backward in time for every stage $k = N,...,1$ with the final condition Eqs. (5.19) and (5.24) at stage N+1 and the coefficient $\{\boldsymbol{\beta}_k\}_{k=1}^N$ is stored in memory for the forward propagation.

DDP ensures an improvement at each iteration under the condition that the Hessian of the cost function, i.e., the matrix $\mathbf{C}_k$ is positive definite. In case this is not verified, different procedures can be applied (see [144],[111],[113],[145]). The one implemented in this work replaces the matrix $\mathbf{C}_k$, for the computation of Eq. (5.22), with the positive definite matrix

$$\tilde{\mathbf{C}}_k = \mathbf{C}_k + 2\left|\nu_{\min}\right|\mathrm{I}(m) \tag{5.25}$$

where $\nu_{\min}$ is the minimum eigenvalue of the matrix $\mathbf{C}_k$ and $\mathrm{I}(m)$ the identity matrix of size m. The condition on the matrix $\mathbf{C}_k$ is even more stringent; in fact, in order to achieve a sufficient descent direction at each iteration, the matrix $\mathbf{C}_k$ should also be far from being non-positive definite [146]; hence the active shift Eq. (5.25) is applied, also in case the minimum eigenvalue $\nu_{\min}$, although positive, is smaller than a given small positive value (10^{-6} is usually adopted).

Once the backward propagation is terminated, the trajectory is swept forward in time, for every stage $k = 1,...,N$; the new control policy is given by Eq. (5.12) and the corresponding trajectory is computed by Eq. (5.1). The value of $k_{\lim}$ in Eq. (5.12) has to be chosen such that the following condition is satisfied, c being a constant between 0 and 1.

$$J\left(\{\mathbf{u}_k\};\overline{\mathbf{s}}_1\right) - J\left(\{\overline{\mathbf{u}}_k\};\overline{\mathbf{s}}_1\right) \le c \cdot \Theta_{k_{\lim}} \tag{5.26}$$

where $J\left(\{\mathbf{u}_k\};\overline{\mathbf{s}}_1\right)$ is the value of the cost function associated to the new control law, computed with Eq. (5.4). Following to the definition in Eq. (5.14), $\Theta_{k_{\lim}}$ is used as a measure of the predicted change in cost applying the control law Eq. (5.12).

A single iteration of DDP is composed by the backward and the forward recursion that produce an improved control law and trajectory. A number of iterations follow one after the other, until the stopping condition

$$\Theta_1 < \Theta_{\text{out}} \tag{5.27}$$

is verified, being Θ_{out} a fixed threshold.

Treatment of the terminal equality constraints

The terminal constraints are added to the cost function through a set of Lagrange multipliers $\boldsymbol{\lambda}$ to give the Lagrange function in Eq. (5.4).

Here we follow the method proposed by Gershwin and Jacobson [120]. At first Eq. (5.4) is minimised fixing the value of the Lagrange multipliers $\overline{\boldsymbol{\lambda}}$. Successive iterations of DDP follow until the convergence criterion Eq. (5.27) is

satisfied. At this point a variation of $\delta\boldsymbol{\lambda}$ is allowed, in order to find a control law that decreases the constraints violation. Eq. (5.5) is now expanded not only in $\delta\mathbf{u}_k$ and $\delta\mathbf{s}_k$ but also in $\delta\boldsymbol{\lambda}$ about the point $\left(\bar{\mathbf{s}}_k, \mathbf{u}_k^*, \bar{\boldsymbol{\lambda}}\right)$, where $\bar{\boldsymbol{\lambda}}$ is considered to be the nominal value of the Lagrange multipliers:

$$\begin{aligned}
&\frac{1}{2}\delta\mathbf{s}_k^T V_{ss}^k \delta\mathbf{s}_k + \frac{1}{2}\delta\boldsymbol{\lambda}^T V_{\lambda\lambda}^k \delta\boldsymbol{\lambda} + \delta\mathbf{s}_k^T V_{s\lambda}^k \delta\boldsymbol{\lambda} + V_s^k \delta\mathbf{s}_k + V_\lambda^k \delta\boldsymbol{\lambda} + \bar{V}_k\left(\bar{\mathbf{s}}_k\right) + \Theta_k = \\
&= \Theta_{k+1} + g\left(\bar{\mathbf{s}}_k, \bar{\mathbf{u}}_k; t_k\right) + \Delta\mathbf{g}_k + \mathbf{g}_s^k \delta\mathbf{s}_k + \mathbf{g}_u^k \delta\mathbf{u}_k + \frac{1}{2}\delta\mathbf{s}_k^T \mathbf{g}_{ss}^k \delta\mathbf{s}_k + \\
&+ \frac{1}{2}\delta\mathbf{u}_k^T \mathbf{g}_{uu}^k \delta\mathbf{u}_k + \delta\mathbf{u}_k^T \mathbf{g}_{us}^k \delta\mathbf{s}_k + \bar{V}_{k+1}\left(\bar{\mathbf{s}}_{k+1}\right) + V_s^{k+1}\delta\mathbf{s}_{k+1} + \\
&+ \frac{1}{2}\delta\mathbf{s}_{k+1}^T V_{ss}^{k+1}\delta\mathbf{s}_{k+1} + V_\lambda^{k+1}\delta\boldsymbol{\lambda} + \frac{1}{2}\delta\boldsymbol{\lambda}^T V_{\lambda\lambda}^{k+1}\delta\boldsymbol{\lambda} + \delta\mathbf{s}_{k+1}^T V_{s\lambda}^{k+1}\delta\boldsymbol{\lambda}
\end{aligned} \tag{5.28}$$

Substituting Eq. (5.15) and grouping some terms, Eq. (5.28) can be written in a matrix form:

$$\begin{aligned}
&\delta\mathbf{s}_k^T \mathbf{P}_k \delta\mathbf{s}_k + \delta\boldsymbol{\lambda}^T \mathbf{R}_k \delta\boldsymbol{\lambda} + \delta\mathbf{s}_k^T \mathbf{S}_k \delta\boldsymbol{\lambda} + \mathbf{Q}_k \delta\mathbf{s}_k + \mathbf{Z}_k \delta\boldsymbol{\lambda} + \Theta_k = \\
&= \delta\mathbf{s}_k^T \mathbf{A}_k \delta\mathbf{s}_k + \delta\mathbf{u}_k^T \mathbf{C}_k \delta\mathbf{u}_k + \delta\mathbf{u}_k^T \mathbf{B}_k \delta\mathbf{s}_k + \delta\mathbf{s}_k^T \mathbf{E}_k + \delta\mathbf{u}_k^T \mathbf{D}_k + \\
&+ \delta\boldsymbol{\lambda}^T \mathbf{R}_{k+1} \delta\boldsymbol{\lambda} + \delta\mathbf{s}_k^T \mathbf{H}_k \delta\boldsymbol{\lambda} + \delta\mathbf{u}_k^T \mathbf{K}_k \delta\boldsymbol{\lambda} + \mathbf{Z}_{k+1}\delta\boldsymbol{\lambda} + \Theta_{k+1}
\end{aligned} \tag{5.29}$$

where more matrices are introduced for clarity; respectively on the left side:

$$\begin{aligned}
&\mathbf{Z}_k = V_\lambda^k && 1\times l \\
&\mathbf{R}_k = \frac{1}{2}\left(V_{\lambda\lambda}^k\right) && l\times l \\
&\mathbf{S}_k = V_{s\lambda}^k && n\times l
\end{aligned} \tag{5.30}$$

and on the right side.

$$\begin{aligned}
&\mathbf{R}_{k+1} = \frac{1}{2}\left(V_{\lambda\lambda}^{k+1}\right) && l\times l \\
&\mathbf{H}_k = \left(\mathbf{f}_s^{kT} V_{s\lambda}^{k+1}\right) = \mathbf{f}_s^{kT}\mathbf{S}_{k+1} && n\times l \\
&\mathbf{K}_k = \left(\mathbf{f}_u^{kT} V_{s\lambda}^{k+1}\right) = \mathbf{f}_u^{kT}\mathbf{S}_{k+1} && m\times l \\
&\mathbf{Z}_{k+1} = V_\lambda^{k+1} && 1\times l
\end{aligned} \tag{5.31}$$

Note that the variation of Lagrange multipliers is introduced only once an optimal control law has been found with $\boldsymbol{\lambda} = \overline{\boldsymbol{\lambda}}$; as a consequence, from Eq. (5.28) $\mathbf{u}_k^* \simeq \overline{\mathbf{u}}_k$ and hence $\Delta \mathbf{g}_k = 0$ and $\Delta \mathbf{f}_k = 0$. This is equivalent to using the small control variation algorithm [111]. Now, by differentiating Eq. (5.29) with respect to $\delta \mathbf{u}_k$ we obtain:

$$
\begin{aligned}
&2\mathbf{C}_k \delta \mathbf{u}_k + \mathbf{B}_k \delta \mathbf{s}_k + \mathbf{K}_k \delta \boldsymbol{\lambda} = 0 \Rightarrow \\
&\delta \mathbf{u}_k = -\frac{1}{2}\mathbf{C}_k^{-1}\mathbf{B}_k \delta \mathbf{s}_k - \frac{1}{2}\mathbf{C}_k^{-1}\mathbf{K}_k \delta \boldsymbol{\lambda}
\end{aligned}
$$

Hence the variation of the control contains also a term proportional to the variation of the multipliers:

$$
\delta \mathbf{u}_k = \boldsymbol{\beta}_k \delta \mathbf{s}_k + \boldsymbol{\gamma}_k \delta \boldsymbol{\lambda} \tag{5.32}
$$

The associated coefficient $\boldsymbol{\gamma}_k$ is computed during the backward recursion and stored in memory together with coefficient $\boldsymbol{\beta}_k$:

$$
\boldsymbol{\gamma}_k = -\frac{1}{2}\mathbf{C}_k^{-1}\mathbf{K}_k \qquad m \times l \tag{5.33}
$$

By substituting back Eq. (5.32) into Eq. (5.29) we obtain:

$$
\begin{aligned}
\mathbf{S}_k &= \mathbf{H}_k - \frac{1}{2}\mathbf{B}_k^T \mathbf{C}_k^{-1}\mathbf{K}_k \\
\mathbf{R}_k &= \mathbf{R}_{k+1} - \frac{1}{4}\mathbf{K}_k^T \mathbf{C}_k^{-1}\mathbf{K}_k \\
\mathbf{Z}_k &= \mathbf{Z}_{k+1}
\end{aligned} \tag{5.34}
$$

with the final conditions:

$$
\begin{aligned}
\mathbf{S}_{N+1} &= \boldsymbol{\varphi}_s \left(\overline{\mathbf{s}}_{N+1}; t_{N+1} \right)^T \\
\mathbf{R}_{N+1} &= \mathbf{0} \\
\mathbf{Z}_{N+1} &= \boldsymbol{\varphi} \left(\overline{\mathbf{s}}_{N+1}; t_{N+1} \right)
\end{aligned} \tag{5.35}
$$

The backward recursion is performed for every stage $k = N,...,1$, in which the same equations of the main DDP loop are solved, with the addition of Eqs. (5.31), (5.33), (5.34), and with the final condition Eqs. (5.35); the coefficients $\{\boldsymbol{\beta}_k\}_{k=1}^{N}$ and $\{\boldsymbol{\gamma}_k\}_{k=1}^{N}$ are stored in memory.

At this point we can determine the variation of Lagrange multipliers $\delta\boldsymbol{\lambda}$, by maximising Eq. (5.28) at t_1 and $\bar{\mathbf{s}}_1$, with respect to $\delta\boldsymbol{\lambda}$ (see [111]); this gives:

$$\delta\boldsymbol{\lambda} = -\frac{1}{2}\mathbf{R}_1^T\mathbf{Z}_1 \tag{5.36}$$

under the requirement that $\mathbf{R}_1$ is negative definite (hence invertible).

The new control law and trajectory are propagated for every stage $k = 1,..., N$:

$$\begin{cases} \mathbf{u}_k = \bar{\mathbf{u}}_k + \boldsymbol{\beta}_k\delta\mathbf{s}_k + \boldsymbol{\gamma}_k\delta\boldsymbol{\lambda} \\ \mathbf{s}_{k+1} = \mathbf{f}\left(\mathbf{s}_k, \mathbf{u}_k; t_k\right) \qquad\qquad k = 1,..., N \\ \mathbf{s}_1 = \bar{\mathbf{s}}_1 \end{cases} \tag{5.37}$$

Also in this case, $\delta\boldsymbol{\lambda}$ has to be verified not to exceed the range of validity of the linear-quadratic expansion, hence the constant $0 < \varepsilon \le 1$ is introduced in Eq. (5.36):

$$\begin{aligned} &\delta\boldsymbol{\lambda} = -\varepsilon\frac{1}{2}\mathbf{R}_1^T\mathbf{Z}_1 \qquad 0 < \varepsilon \le 1 \\ &\boldsymbol{\lambda} = \bar{\boldsymbol{\lambda}} + \delta\boldsymbol{\lambda} \end{aligned} \tag{5.38}$$

The value of ε is chosen, through a linear search method, so that the following condition is satisfied [120]:

$$\begin{aligned} &\left|J\left(\{\mathbf{u}_k\}, \boldsymbol{\lambda}(\varepsilon); \bar{\mathbf{s}}_1\right) - J\left(\{\bar{\mathbf{u}}_k\}, \bar{\boldsymbol{\lambda}}; \bar{\mathbf{s}}_1\right)\right| - \Theta_1 + \\ &+\frac{1}{2}\left(\varepsilon - \frac{1}{2}\varepsilon^2\right)\cdot\boldsymbol{\varphi}\left(\bar{\mathbf{s}}_{N+1}; t_{N+1}\right)^T\mathbf{R}_1^{-1}\boldsymbol{\varphi}\left(\bar{\mathbf{s}}_{N+1}; t_{N+1}\right) < reltol\left|J\left(\{\bar{\mathbf{u}}_k\}; \bar{\mathbf{s}}_1\right)\right| \end{aligned} \tag{5.39}$$

where *reltol* is a relative tolerance. Eq. (5.39) compares the actual improvement in the cost function to the one predicted through the linear-quadratic expansion. Moreover the change in $\boldsymbol{\lambda}$ has to reduce the violation of the terminal constraints:

$$\boldsymbol{\varphi}\left(\mathbf{s}_{N+1};t_{N+1}\right)-\boldsymbol{\varphi}\left(\overline{\mathbf{s}}_{N+1};t_{N+1}\right)<\mathbf{0} \tag{5.40}$$

5.2. Modified DDP method

When the optimisation problem is not very sensitive, for example when designing a two-body problem transfer, the conventional DDP technique, described in Section 5.1, can be applied to find the optimal control. However, if the problem involves more complex dynamics, such as escape or capture phases, or gravity assist manoeuvres, the propagation becomes a crucial point. In particular, the use of a time mesh fixed a priori can jeopardise the high fidelity representation of the problem; on the other hand, the coupling between the integration scheme and the optimisation process must be handled very carefully, in order not to compromise convergence.

The approach proposed in this paper uses a variable step integration method for the propagation of the dynamics and the integration mesh is refined at each iteration of DDP.

5.2.1. Discretisation scheme

The low-thrust continuous problem, characterised by the dynamic system

$$\begin{aligned}&\frac{d\mathbf{s}(t)}{dt}=\tilde{\mathbf{f}}\left(\mathbf{s}(t),\mathbf{u}(t);t\right) \qquad\qquad t\in\left[t_0 \quad t_f\right]\\&\mathbf{s}\left(t_0\right)=\overline{\mathbf{s}}_1\end{aligned} \tag{5.41}$$

where t_0 and t_f define the time interval, is approximated by difference equations as shown in Eq. (5.1), where the state transition function $\mathbf{f}$ represents the explicit scheme for the numerical approximation of Eq. (5.41):

$$\begin{aligned}&\mathbf{s}_{k+1}=\mathbf{f}\left(\mathbf{s}_k,\tilde{\mathbf{f}}\left(\mathbf{s}_k,\mathbf{u}_k;t_k\right);h_k\right) \qquad\qquad k=1,\ldots,N\\&\mathbf{s}_1=\overline{\mathbf{s}}_1\end{aligned} \tag{5.42}$$

where h_k is the discretisation step. Note that in the rest of the chapter the dependences of the function $\mathbf{f}$ were written in the simplified form:

$$\mathbf{f}\left(\mathbf{s}_k, \mathbf{u}_k; t_k\right) = \mathbf{f}\left(\mathbf{s}_k, \tilde{\mathbf{f}}\left(\mathbf{s}_k, \mathbf{u}_k; t_k\right); h_k\right)$$

In this thesis we use the discrete-time form of DDP; according to this approach, the N steps identify both the decision times of the trajectory (i.e., the points where the feedback control is computed) and the steps of the numerical propagation, as shown in Figure 5.5.

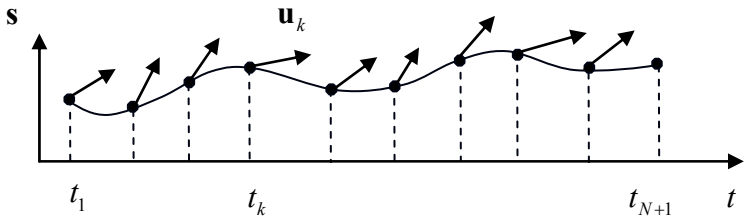

Figure 5.5: Trajectory discretisation within the optimisation problem.

In a previous application of the discrete-time DDP algorithm to orbital transfer, a fixed step size Euler integration scheme was used (see [120]). However, such a simple integration scheme is not appropriate when the dynamics becomes highly non-linear. In other more recent DDP-based approaches, the issue was solved by dividing the trajectory in a number of segments over which the thrust is constant [106],[109]. Within a single segment Whiffen integrates backward a system of coupled ordinary differential equations which are the integral form of the discrete-time DDP matrices, whereas Lantoine and Russel introduce a second order state transition matrix to map the propagation of the dynamics. In these approaches, decision times and integration steps do not coincide.

In this work, the classical discrete formulation is used (see Figure 5.5) but the mesh is discretised with a more accurate scheme than the one adopted by Gershwin and Jacobson [120]: a variable step-size Runge-Kutta-Fehlberg integration scheme, with a six stage pair of approximation of the fourth and fifth order [147][*]:

[*] A Runge-Kutta-Fehlberg integration scheme is selected because it provides higher accuracy than first order methods (such as the Euler method) by maintaining a single-step structure, however, with an increase of the number of function evaluations for each step.

$$\begin{aligned} \mathbf{s}_{k+1} &= \mathbf{f}\left(\mathbf{s}_k, \mathbf{u}_k; t_k\right) = \mathbf{s}_k + h_k \sum_{r=1}^{\sigma} \mathbf{b}_r \tilde{\mathbf{f}}_r \\ \tilde{\mathbf{f}}_r &= \tilde{\mathbf{f}}\left(\mathbf{s}_k + h_k \sum_{r=1}^{\sigma} \mathbf{a}_{j,r} \tilde{\mathbf{f}}_r, \mathbf{u}_k; t_k + \mathbf{c}_r h_k\right) \qquad j = 1,\ldots,\sigma; \quad \sigma = 6 \end{aligned} \tag{5.43}$$

where $\tilde{\mathbf{f}}$ is the continuous dynamics of the problem, $\mathbf{a}$, $\mathbf{b}$ and $\mathbf{c}$ the coefficient matrices of the integration scheme and h_k the length of the discretisation step.

Note that the integration scheme Eq. (5.43) is chosen to be explicit, as it allows the analytic evaluation of its derivatives which are required in the DDP procedure [in Eqs. (5.17) and Eqs. (5.31)].

The identity between decision times and integration steps increases the computational requirements but ensures high fidelity of the dynamics and allows varying the control at each integration step. Note that, if $\mathbf{u}_k$ is kept constant over a certain number of discretisation steps, Eq. (5.43) reduces to the trajectory model used by Whiffen and Lantoine (see Figure 5.6)[†].

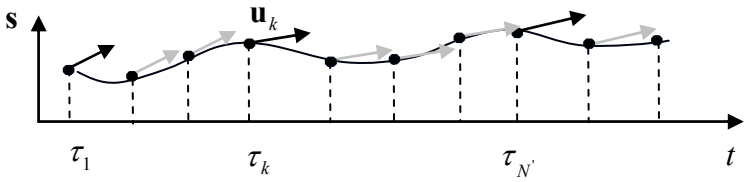

Figure 5.6: Trajectory discretisation in the Static/Dynamic Control approach. The grey arrows show that the control is kept constant within a segment.

5.2.2. Mesh definition

If the dynamic system Eq. (5.42) is not correctly integrated, the optimisation of the control law could lead to an incorrect solution. This is likely to occur if a fixed step size is used. For this reason, in the approach proposed in this thesis, the

[†] In the SDC approach the trajectory is divided in a number N' of constant-thrusted periods, and the dynamics is numerically integrated within each single period

$$\mathbf{s}_{k+1} = \mathbf{s}_k + \int_{\tau_k}^{\tau_{k+1}} \tilde{\mathbf{f}}\, dt \qquad k = 1,\ldots,N'$$

τ_k and τ_{k+1} indicate the decision times that are the points where the control is allowed to vary. Whiffen derives some Riccati-like equations that are the continuous form of Eqs. (5.17), without considering the terms linked to the global variations of control. These equations are backward integrated from the decision time τ_{k+1} up to the previous one τ_k, and, at that point, Eq. (5.21) is evaluated.

step-size of the integration scheme is adapted at each iteration of the DDP algorithm.

We define a nominal time-mesh grid $\{\bar{N}\}$ together with the first guess trajectory and control sequences $\{\bar{\mathbf{s}}_k\}_{k=1}^{\bar{N}+1}$ and $\{\bar{\mathbf{u}}_k\}_{k=1}^{\bar{N}}$. The backward and forward propagation of DDP are then executed with the nominal mesh. Once a value of $k_{\lim}$ is determined, according to condition Eq. (5.26), the trajectory selected for the next DDP iteration follows, within the range $[0 \quad k_{\lim}]$, the nominal path, while the segment of the trajectory $\{\mathbf{s}_k\}_{k=k_{\lim}}^{\bar{N}+1}$ implements the new control strategy $\{\mathbf{u}_k\}_{k=k_{\lim}}^{\bar{N}}$, according to Eq. (5.12). The segment $\{\mathbf{s}_k\}_{k=k_{\lim}}^{\bar{N}+1}$ of the trajectory is propagated through the adaptive-step integration algorithm and a new mesh $\{N\}$ is defined for $\{\mathbf{s}_k\}_{k=k_{\lim}}^{N+1}$ and $\{\mathbf{u}_k\}_{k=k_{\lim}}^{N}$.

In order to perform this operation, the control law, which is given on the original mesh points, needs to be interpolated in the new points required by the integration algorithm. Handling properly the interpolation is essential to preserve the DDP performances; in fact a bad interpolation could introduce errors which can results in rejecting the control computed by the DDP.

Two interpolation schemes were adopted in this study; the first one, called *complete interpolation* in the following, directly interpolates the control $\{\mathbf{u}_k\}_{k=k_{\lim}}^{\bar{N}}$ on the new mesh. Recalling Eq. (5.12), the complete interpolation technique interpolates the left hand side of Eq. (5.44):

$$\mathbf{u}_k = \mathbf{u}_k^* + \boldsymbol{\beta}_k \left(\mathbf{s}_k - \bar{\mathbf{s}}_k\right) \qquad k = k_{\lim},...,N \tag{5.44}$$

The second interpolation technique, although more computationally expensive, ensures a higher accuracy. Rather than interpolating the control computed on the nominal mesh through the forward recursion $\{\mathbf{u}_k\}_{k=k_{\lim}}^{\bar{N}}$, each term on the right hand side of Eq. (5.44), namely $\mathbf{u}_k^*$, $\boldsymbol{\beta}_k$, and $\bar{\mathbf{s}}_k$, is independently interpolated. In this way the feedback nature of the control variation computed by

the DDP is fully exploited: if the state $\{\mathbf{s}_k\}_{k=k_{\lim}}^{N+1}$ moves away from the one computed on the nominal mesh $\{\mathbf{s}_k\}_{k=k_{\lim}}^{\bar{N}+1}$, the term of the control $\boldsymbol{\beta}_k(\mathbf{s}_k - \bar{\mathbf{s}}_k)$ changes as a consequence. The piecewise cubic spline interpolation method is adopted [148]. We will call this technique as *term-wise interpolation*.

In some cases (see for example the transfer problem presented in Figure 5.4 and Sections 5.4 and 5.5.1) the complete interpolation technique is enough to reach convergence, whereas in more sensitive and complex cases, the complete interpolation introduces small errors in the interpolated control that, propagated through a sensitive dynamics, may result in an unrecoverable increase of the final constraints violation. For example for the transfer problem presented in Section 5.5.2, the term-wise interpolation technique was essential to reach the convergence. In particular, the section of the trajectory where the spacecraft passes close to the Earth's gravity field, highlighted in Figure 5.26 (see p. 193), showed to be very sensitive to the control profile and hence required a very high accuracy in the control law interpolation.

Once the new mesh is defined, an additional test is performed, to assess whether the refinement of the mesh did not introduce errors in the dynamics. The cost computed with the new mesh $J\left(\{\mathbf{u}_k\}_{k=1}^{N}; \bar{\mathbf{s}}_1\right)$ must not differ from the cost computed with the nominal mesh $J\left(\{\mathbf{u}_k\}_{k=1}^{\bar{N}}; \bar{\mathbf{s}}_1\right)$ by a predefined quantity:

$$J\left(\{\mathbf{u}_k\}_{k=1}^{N}; \bar{\mathbf{s}}_1\right) - J\left(\{\mathbf{u}_k\}_{k=1}^{\bar{N}}; \bar{\mathbf{s}}_1\right) < reltol_{mesh} \cdot J\left(\{\mathbf{u}_k\}_{k=1}^{\bar{N}}; \bar{\mathbf{s}}_1\right) \quad reltol_{mesh} \ll 1 \tag{5.45}$$

By using the term-wise interpolation technique, condition Eq. (5.45) was always satisfied[‡]. In the cases in which the complete interpolation technique is adopted, Eq. (5.45) is used as verification of the failure of the interpolation technique; when that occurs, the DDP mesh refinement is performed again, with the term-wise interpolation technique.

[‡] This was verified for all the results showed in Section 5.5.

Note that the mesh refinement during the optimisation process increases the computational time, but only in this way one can ensure that the algorithm convergences to a correct solution.

5.3. Algorithm

We now report a summary of the algorithm adopted in this work. The algorithm is composed by the following steps:

Initialisation

A nominal set of Lagrange multipliers $\bar{\boldsymbol{\lambda}}$ and a control law $\{\bar{\mathbf{u}}_k\}_{k=1}^{\bar{N}}$ is given as an input to the algorithm; the associated nominal trajectory $\{\bar{\mathbf{s}}_k\}_{k=1}^{\bar{N}+1}$ is propagated through Eq. (5.1), where $\bar{\mathbf{s}}_1$ has also been fixed. The first guess trajectory also determines the nominal mesh of the problem $\{\bar{N}\}$. The cost function $J\left(\{\bar{\mathbf{u}}_k\};\bar{\mathbf{s}}_1\right)$ associated to the nominal strategy and trajectory is evaluated through Eq. (5.4).

Moreover, the derivatives of the state transition function and the stage-wise loss function *g* are analytically computed.

Loop1: Control law loop

Step 1:

The parameters needed for starting the recursive computation of Eq. (5.16) are initialised at step $N+1$, through Eq. (5.19) and Eqs. (5.24), computed with the nominal value of the Lagrange multipliers $\bar{\boldsymbol{\lambda}}$.

Step 2: Backward propagation performed for each stage *k* from stage N to stage 1:

The nominal control $\bar{\mathbf{u}}_k$ is perturbed to the new nominal policy $\mathbf{u}_k^*$, by minimising Eq. (5.20). The local minimisation of Eq. (5.20) is performed numerically, through a subspace trust-region method, based on the interior-reflective Newton method [149],[150]. The analytical expression of the gradient is

supplied. The derivative of the state transition function and the stage-wise loss function g are evaluated at $\left(\overline{\mathbf{s}}_k, \mathbf{u}_k^*\right)$ and the matrices in Eq. (5.17) are constructed. Eq. (5.18) represents the forecast of the improvement in the cost function associated with stage k, whereas the matrices $\mathbf{Q}_k$ and $\mathbf{P}_k$ are computed through Eq. (5.23) and replaced to the one of the next step forward. The coefficient $\boldsymbol{\beta}_k$ is computed with Eq. (5.22) and stored in memory for the forward propagation. If the matrix $\mathbf{C}_k$ is not positive definite, Eq. (5.25) is used for the computation of $\boldsymbol{\beta}_k$:

$$\boldsymbol{\beta}_k = -\frac{1}{2}\tilde{\mathbf{C}}_k^{-1}\mathbf{B}_k \qquad m \times n$$

Step 3: Forward propagation performed from step 1 to step N:

The trajectory is propagated through Eq. (5.1), with the improved control law Eq. (5.12). The value of k_{lim} is determined through Eq. (5.26), to provide a decrease in the objective function, and to not exceed the range of accuracy of the linear-quadratic expansion. The constant c in Eq. (5.26) was set in a value between 0.5 and 0.1.

Step 4:

When a new control sequence $\left\{\mathbf{u}_k\right\}_{k_{\text{lim}}}^{\bar{N}}$ is selected, the corresponding leg of trajectory is integrated with the adaptive step integration method, by interpolating the control through the complete interpolation technique or the term-wise interpolation technique, and a new discretisation of the control is obtained $\left\{\mathbf{u}_k\right\}_{k_{\text{lim}}}^{N}$. The value of the cost function associated to the new discretisation and the value computed on the original mesh are compared through Eq. (5.45). The new mesh, together with the improved control law and the associated trajectory are set as the nominal conditions for the next DDP iteration (*Step 1*).

$$\left\{\bar{N}\right\} \leftarrow \left\{N\right\}$$
$$\left\{\bar{\mathbf{u}}_k\right\}_{k=1}^{\bar{N}} \leftarrow \left\{\mathbf{u}_k\right\}_{k=1}^{N}$$
$$\left\{\bar{\mathbf{s}}_k\right\}_{k=1}^{\bar{N}+1} \leftarrow \left\{\mathbf{s}_k\right\}_{k=1}^{N+1}$$
$$J\left(\left\{\bar{\mathbf{u}}_k\right\}_{k=1}^{\bar{N}}; \bar{\mathbf{s}}_1\right) \leftarrow J\left(\left\{\mathbf{u}_k\right\}_{k=1}^{N}; \bar{\mathbf{s}}_1\right)$$

Convergence Criterion:

The first loop of DDP is stopped when $k_{\lim} = 1$ and the increase of the cost function is under a small value, set for stability analysis:

$$\Theta_1 \le \Theta_{out} \cdot \max\left[1, \left|J\left(\left\{\mathbf{u}_k\right\}_{k=1}^{N}; \bar{\mathbf{s}}_1\right)\right|\right] \tag{5.46}$$

Usually Θ_{out} is set to be around 10^{-6} but it can be increased up to 10^{-4} if the problem is very sensitive in order to filter the numerical error introduced by the integration over a long time of flight.

Loop 2: Equality constraints loop

Step 5: Backward propagation performed for each stage k from stage N to backward until stage 1:

The matrices in Eq. (5.17) and Eq. (5.23) are constructed, together with the new matrices in Eq. (5.31) and Eq. (5.34) with the initial condition Eqs. (5.24) and Eq. (5.35). All the derivatives are now evaluated at point $\left(\bar{\mathbf{s}}_k, \bar{\mathbf{u}}_k, \bar{\boldsymbol{\lambda}}\right)$. Coefficients $\boldsymbol{\beta}_k$ and $\boldsymbol{\gamma}_k$ are computed through Eq. (5.22) and Eq. (5.33) and stored in memory for the forward propagation.

Step 6: Forward propagation performed from step 1 to step N:

The value of the Lagrange multiplier vector is updated with Eq. (5.38) and the new control law is propagated with Eq. (5.37). The value of ε is set according to condition Eq.(5.39).

Test on the final constraints

The violation of the constraints is updated and, if condition Eq. (5.40) is verified, the new value of $\boldsymbol{\lambda}$ is set as the nominal one, together with the control

sequence and trajectory; else ε is further decreased. The algorithm goes back to *Step 1* for further DDP iteration.

Stopping condition

The overall algorithm terminates at the end of loop 1, if condition Eq. (5.46) is satisfied and the constraints violation is under a required tolerance.

The overall algorithm is sketched in Figure 5.7:

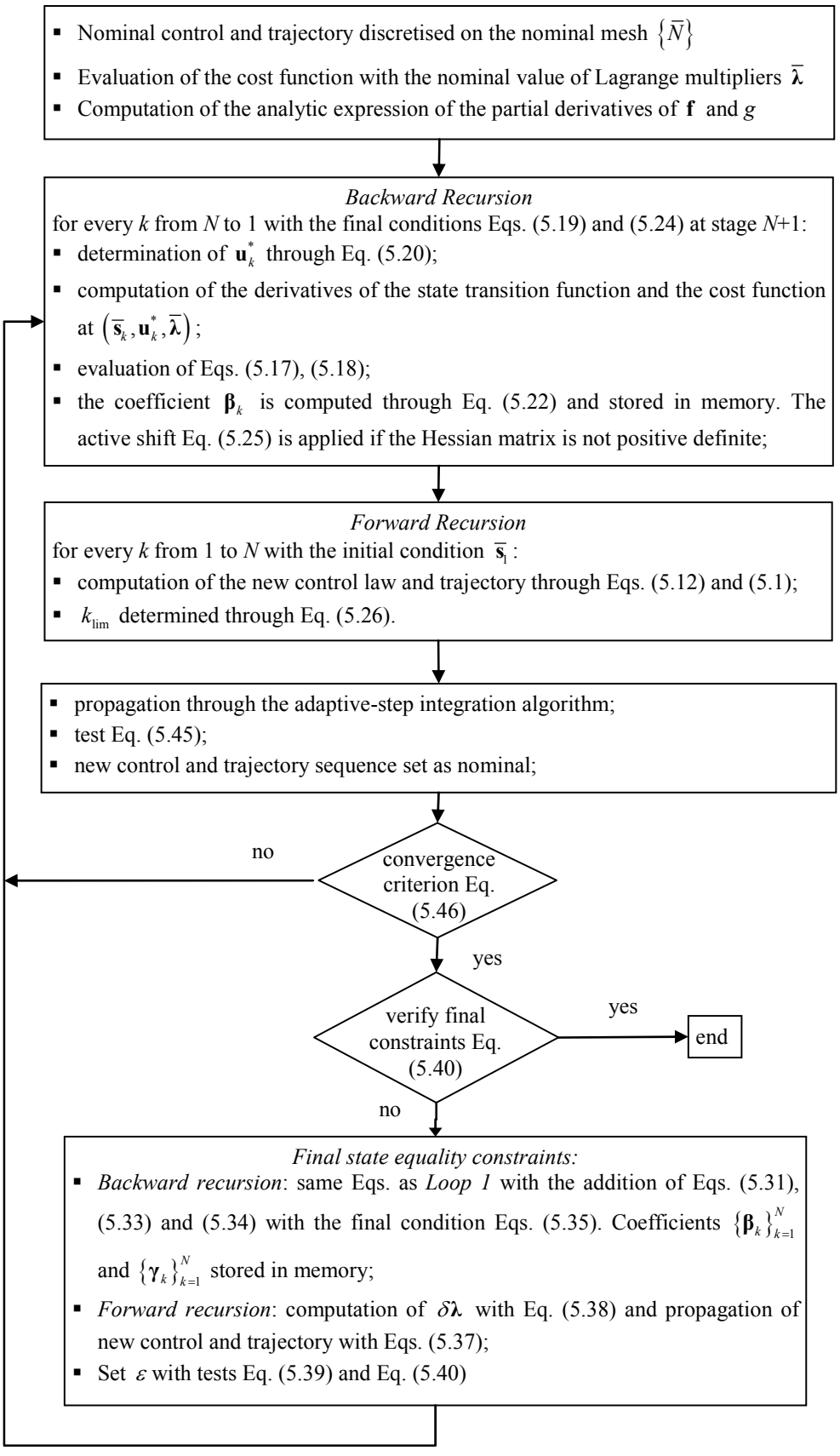

Figure 5.7: Modified DDP algorithm.

5.3.1. Heuristics to improve the convergence rate

As mentioned above, DDP has quadratic convergence if the Hessian matrix of the problem is positive definite, i.e., the problem is locally convex. Conversely for non-convex control problems, the convergence rate downgrades to linear [113]; this is a common difficulty in direct methods as well.

Within the DDP procedure, this can be diagnosed in different ways; the matrix $\mathbf{C}_k$ is not positive definite and the search for the local minimum $\mathbf{u}_k^*$ of Eq. (5.20) may fail in *Step 2* of the backward propagation.

Another common issue linked to the inaccuracy caused by the numerical approximation of the derivatives through finite-difference [146] is here avoided, because the derivatives of the cost function and the state transition function are analytically computed; this assures higher accuracy and allows saving computational time.

Moreover, the problem variables were scaled to have the same weight in the neighbourhood of the problem solution, thus preventing ill-conditioning of the Hessian matrix [146].

The cost function chosen for the constrained optimisation problem is the Lagrange function in Eq. (5.4). Eq. (5.4) is used both as cost function to be minimised and as a merit function to measure a progress of each iteration of DDP [151]. Both the expressions of the integral term $\sum_{k=1}^{N} g\left(\mathbf{s}_k, \mathbf{u}_k; t_k\right)$ and the equality constraints $\varphi\left(\mathbf{s}_{N+1}; t_{N+1}\right)$ were chosen to be quadratic forms. For this reason, numerical instability may occur if, in the equality constraints loop, any component of the Lagrange multiplier $\boldsymbol{\lambda}$ becomes negative.

Different heuristics were introduced in order to improve the convergence rate or to speed up the optimisation process. When the search of the local minimum $\mathbf{u}_k^*$ of Eq. (5.20) fails, in *Step 2* of the backward propagation, the nominal control $\bar{\mathbf{u}}_k$ is used in place of $\mathbf{u}_k^*$, in the following of the *k*-iteration. As a consequence the new control is restricted to be in the neighbourhood of the nominal strategy, according to:

$$\mathbf{u}_k = \overline{\mathbf{u}}_k + \boldsymbol{\beta}_k \delta \mathbf{s}_k$$

Anyway, only a limited number of iterations are allowed to fail in the search of the control $\mathbf{u}_k^*$. After a fixed number of iterations fail, the backward propagation is broken, and the value of $k_{\lim}$ for initialising the step-size adjustment method is set equal to the last value of the index k. In this case, the algorithm with global control variations showed to be very efficient, because, if at a given iteration k of the backward propagation the problem is locally non-convex, we do not need to terminate the backward propagation up to *Step 1*.

Another heuristic is adopted when, in the equality constraints loop, any component of the Lagrange multiplier $\boldsymbol{\lambda}$ becomes negative. The negative component itself is set to zero and the value of the integral term of the objective function $\sum_{k=1}^{N} g\left(\mathbf{s}_k, \mathbf{u}_k; t_k\right)$ is multiplied by a weight parameter $\tilde{w}$:

$$\tilde{w} = \frac{\boldsymbol{\lambda}^T \cdot \boldsymbol{\varphi}\left(\mathbf{s}_{N+1}; t_{N+1}\right)}{\tilde{\boldsymbol{\lambda}}^T \cdot \boldsymbol{\varphi}\left(\mathbf{s}_{N+1}; t_{N+1}\right)}$$

where $\boldsymbol{\lambda}$ indicates the original Lagrange vector, and $\tilde{\boldsymbol{\lambda}}$ is the modified one, where the negative component is set to 0.

The end-point constraints loop may terminate without a decrease of the constraints violation, if condition Eq. (5.39) and Eq. (5.40) are never satisfied for any value of ε. If this occurs, rather than stopping the process, a trial value of $\boldsymbol{\lambda}$ is set and the algorithm continues with *Loop 1*.

$$\boldsymbol{\lambda} = \overline{\boldsymbol{\lambda}} + \frac{10 \cdot \left(\overline{\boldsymbol{\lambda}}^T \cdot \varphi\left(\mathbf{s}_{N+1}; t_{N+1}\right)\right)}{\sum_{j=1}^{l} \varphi_j^2} \cdot \varphi\left(\mathbf{s}_{N+1}; t_{N+1}\right)$$

Finally an important consideration on the convergence rate of the process can be made. The algorithm with global control variations usually converges faster than the traditional small control variations algorithm [113], especially when far from the optimal solution.

This was verified on the design of the trajectories presented in Section 5.5. With the small control variations algorithm, it was necessary to resort to a continuation technique on the specific impulse, whereas it was possible to find directly the final solution with the global control variations algorithm. However, the convergence of the global control variations algorithm becomes slower, as the value of Θ_1 decreases. This is handled by switching to the small control variations algorithm, when close to the convergence within the first DDP loop, and switching back to the global control variation algorithm, once the value of $\boldsymbol{\lambda}$ is modified by the end-point constrains loop.

5.4. Local refinement of low-thrust trajectories

The intent of this section is to show the application of the algorithm based on DDP to the local refinement of the low-thrust transfer trajectories presented in Chapter 3 and Chapter 4. In particular, the deflection mission scenario of asteroid Apophis will be considered.

As in Section 3.3, a set of missions are computed for the interception and deflection of asteroid Apophis via a low-thrust powered spacecraft and a solar concentrator strategy. The interception and the deflection phase are optimised together through a global search [116],[133] and the low-thrust transfer is preliminary designed with a shape-based method [118]. The low-thrust transfer is modelled considering the Sun as the only gravitational body (i.e., two-body problem), assuming zero velocity at the Earth's sphere of influence[§]. Moreover, a 25% of margin is added to the spacecraft mass at launch. Although the very same approach of Section 3.3 is here used for the trajectory model and the global search of optimal solutions, the parameters of the mission scenario are slightly different from the parameters presented in Section 3.3; hence we report them here for clarity[**] (see Table 5.1). A spacecraft equipped with a solar mirror with a

[§] In Section 3.3, instead, a maximum hyperbolic excess velocity of 3.5 km/s was allowed.

[**] Note that a different choice of mission parameters such as the specific impulse, the relative velocity at the Earth, and the time at the MOID does not alter the purpose of this section. The DDP-based algorithm can be applied to perform the local refinement of all the low-thrust transfer options presented in Chapter 3 and Chapter 4.

diameter of 100 m and a dry mass m_d of 895 kg is considered [135]. The spacecraft is launched at a time t_0, selected in a range of 20 years before the possible collision, and is equipped with an engine delivering an unlimited thrust with a constant specific impulse of $I_{sp} = 3250$ s [88].

Table 5.1: Mission characteristics.

I_{sp}	3250 s
d_m	100 m
m_d	895 kg
Margin on m_0	25%
$v_{\infty,\max}$	0 km/s
$\left(t_{\text{MOID}} - t_0\right)_{\max}$	20 y

The result of the global search to identify candidate solutions for an interception and deviation mission to Apophis is reported in Figure 5.8. The asteroid is assumed at the MOID on the 15th May 2036 (13,284 MJD2000). The three axes of the Pareto front are related to the components of the objective function in Eq. (3.19), respectively the initial mass m_0, the warning time t_w, and the magnitude of the deviation $\|\delta\mathbf{r}\|$. Note that, being the final mass at the asteroid interception fixed, the initial mass depends on the propellant mass for the transfer leg. As already pointed out at page 95, a mission making use of a solar collector of 100 m achieves deviations of the order of 10^6 km, in a time range of 20 years, whereas solutions with 1000 days of warning time have a deviation of about 20,000 km.

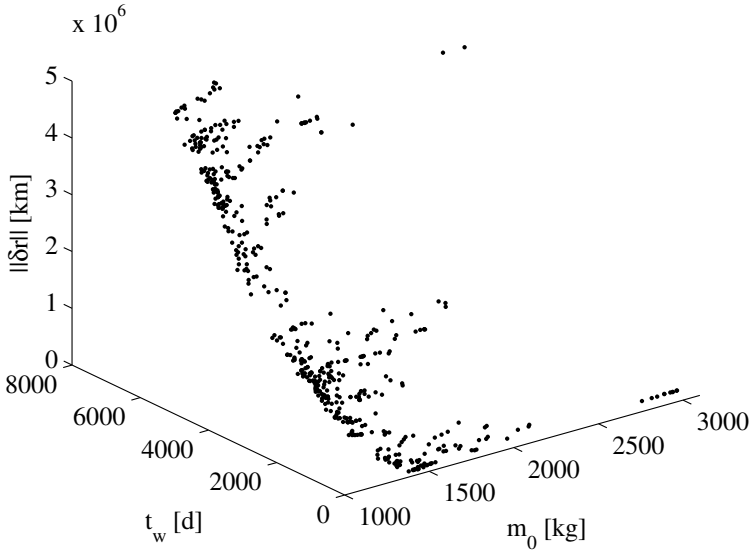

Figure 5.8: Pareto front for a deviation mission to asteroid Apophis.

To verify the propellant mass estimation computed through the global search, 80 solutions of the 500 points of the Pareto set in Figure 5.8 were locally optimised with the DDP-based method. The two-body dynamics is used to describe the motion of the spacecraft:

$$\begin{cases} \dfrac{d\mathbf{r}}{dt} = \mathbf{v} \\ \dfrac{d\mathbf{v}}{dt} = -\dfrac{\mu_{\text{Sun}}}{\|r\|^3}\mathbf{r} + \dfrac{\mathbf{T}}{m} \\ \dfrac{dm}{dt} = -\dfrac{\|\mathbf{T}\|}{I_{sp} g_0} \end{cases}$$

where μ_{Sun} is the Sun gravitational constant, I_{sp} the engine specific impulse, and g_0 the standard free-fall. The variables of the problem are the state vector $\mathbf{s}(t) = \{\mathbf{r} \quad \mathbf{v} \quad m\}^T$, made of position, velocity (expressed in a Sun-centred Cartesian reference frame) and mass of the spacecraft, and the control vector, made of the three components of thrust along the coordinate directions $\mathbf{u}(t) = \mathbf{T}$. The cost function used for the minimisation through DDP is

$$J\left(\{\mathbf{T}_k\}; \overline{\mathbf{s}}_1\right) = \sum_{k=1}^{N} \frac{1}{2} w \mathbf{T}_k^T \mathbf{T}_k \cdot h_k + \boldsymbol{\lambda}^T \cdot \left(\mathbf{s}_{N+1} - \mathbf{s}_{\text{target}}\right)^2 \tag{5.47}$$

where w is a weight factor and $h_k = t_{k+1} - t_k$ the integration interval at step k. The second term of Eq. (5.47) includes the rendezvous condition at the asteroid through the Lagrange multipliers vector $\boldsymbol{\lambda}$. The time constraints of each mission are set equal to the launch dates found through the global search; therefore, the locally optimised solutions have the same launch date and time of flight as the Pareto points, but a different thrust profile [i.e., the optimal thrust profile for the minimisation of Eq. (5.47)] and a different propellant mass. Figure 5.9 highlights the point of the Pareto set which were refined with the DDP-based algorithm. The black points belong to the original set of solutions and the red points are the corresponding solutions after the local optimisation. The propellant mass is determined by the DDP-based algorithm starting from the first guess solution, then the initial mass is computed with Eq. (3.20). In most of the cases, the initial mass required to achieve the same asteroid deviation decreases with the refinement of the solution.

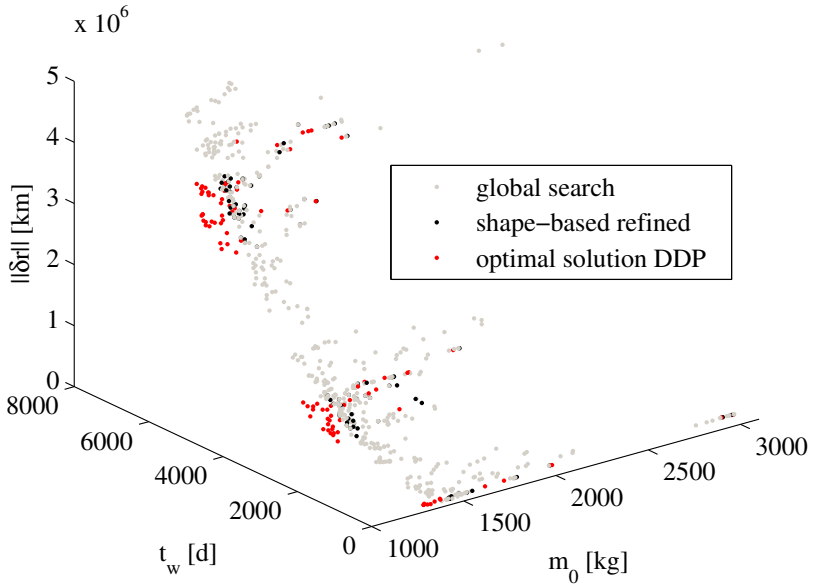

Figure 5.9: Points of the Pareto front locally optimised through the DDP method.

Figure 5.10 reports the percentage of propellant mass saved by the local optimisation of the trajectory, defined as

$$\frac{m_{p,\text{prelimiminary design}} - m_{p,\text{DDP optimised}}}{m_{p,\text{DDP optimised}}} \cdot 100$$

where $m_{p,\text{prelimiminary design}}$ is the propellant mass estimated with the shape-based method. In most of the cases the optimisation through the DDP method allows a significant saving in propellant mass. However, some solutions present an increased propellant mass with respect to the preliminary design case; this is due to the different objective function used within the DDP algorithm. In fact the integral term of the cost function in Eq. (5.47) is equivalent to

$$J_g = \int_{t_0}^{t_0+ToF} \left\|\mathbf{T}(t)\right\|^2 dt$$

where $\left\|\mathbf{T}(t)\right\|$ is the magnitude of the thrust vector function of time. Instead, the first term of the cost function in Eq. (3.19) indicates a minimisation of the propellant mass that, disregarding the constant coefficients *w*, is equivalent to

$$J_g = \int_{t_0}^{t_0+ToF} \left\|\mathbf{T}(t)\right\| dt \tag{5.48}$$

If the local optimisation was performed with the objective function in Eq. (5.48), all the solutions would present a decrease of the propellant mass[††].

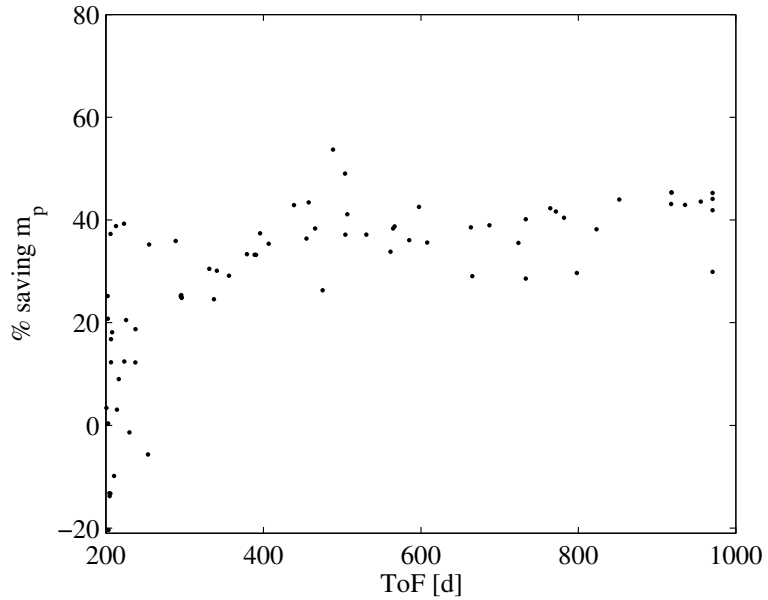

Figure 5.10: Percentage of propellant mass saved through the local optimisation of the solutions.

[††] The minimisation according to the cost function in Eq. (5.48) would require the DDP-based algorithm with constraints on the control function. This will be subject of future work.

The preliminary design of the trajectory for the construction of the Pareto front does not include the transfer leg for escaping the Earth gravity field. In fact it was assumed the initial position of the spacecraft to be out of the sphere of influence of the Earth, with a zero relative velocity and a margin of 25% was added on the total wet mass. An estimation of the propellant mass needed for the Earth escape, will be provided in the next section.

5.5. Asteroid rendezvous and fly-by missions

The algorithm presented in the previous sections is now applied to the optimisation of low-thrust trajectories to fly-by and rendezvous of near-Earth objects. The whole trajectory is described in an Earth inertial reference frame, centred in the Earth with the *x* axis in the γ-point direction and the *z* axis normal to the ecliptic plane, in the direction of the orbit angular momentum of the Earth (the *y* axis completes the reference frame). The variables of the problem are the state vector $\mathbf{s}(t)=\{\mathbf{r} \quad \mathbf{v} \quad m\}^T$, comprising position, velocity and mass of the spacecraft and the control vector, of the three components of thrust along the coordinate directions $\mathbf{u}(t)=\mathbf{T}$. The equations governing the motion of the spacecraft are:

$$\begin{cases} \dfrac{d\mathbf{r}}{dt}=\mathbf{v} \\ \dfrac{d\mathbf{v}}{dt}=-\dfrac{\mu_{\text{Earth}}}{\|r\|^3}\mathbf{r}-\mu_{\text{Sun}}\left(\dfrac{\mathbf{r}_{\text{Sun-s/c}}}{\|\mathbf{r}_{\text{Sun-s/c}}\|^3}-\dfrac{\mathbf{r}_{\text{Sun-Earth}}}{\|\mathbf{r}_{\text{Sun-Earth}}\|^3}\right)+\dfrac{\mathbf{T}}{m} \\ \dfrac{dm}{dt}=-\dfrac{\|\mathbf{T}\|}{I_{sp}g_0} \end{cases} \tag{5.49}$$

where μ_{Earth} and μ_{Sun} are, respectively, the Earth and Sun gravitational constant. $\mathbf{r}$ is the position vector with respect to the Earth inertial reference frame, $\mathbf{r}_{\text{Sun-Earth}}$ is the position vector of the Earth in a Sun-centred inertial reference frame and $\mathbf{r}_{\text{Sun-s/c}}$ is:

$$\mathbf{r}_{\text{Sun-s/c}} = \mathbf{r}_{\text{Sun-Earth}} + \mathbf{r}$$

The state vector of the Earth $\mathbf{s}_{\text{Sun-Earth}}$ was taken from analytic ephemerides which approximate JPL ephemerides de405[‡‡].

The terminal conditions at the asteroid, either rendezvous or fly-by, are included in the cost function through a quadratic term. In the case of a rendezvous mission the terminal constraints are:

$$\varphi\left(\mathbf{s}_{N+1}; t_{N+1}\right) = \begin{Bmatrix} \left(x_{N+1} - x_{\text{target}}\right)^2 \\ \left(y_{N+1} - y_{\text{target}}\right)^2 \\ \left(z_{N+1} - z_{\text{target}}\right)^2 \\ \left(v_{x,N+1} - v_{x,\text{target}}\right)^2 \\ \left(v_{y,N+1} - v_{y,\text{target}}\right)^2 \\ \left(v_{z,N+1} - v_{z,\text{target}}\right)^2 \end{Bmatrix}$$

whereas in the case of fly-by are:

$$\varphi\left(\mathbf{s}_{N+1}; t_{N+1}\right) = \begin{Bmatrix} \left(x_{N+1} - x_{\text{target}}\right)^2 \\ \left(y_{N+1} - y_{\text{target}}\right)^2 \\ \left(z_{N+1} - z_{\text{target}}\right)^2 \end{Bmatrix}$$

where $\mathbf{s}_{\text{target}} = \{x_{\text{target}} \quad y_{\text{target}} \quad z_{\text{target}} \quad v_{x,\text{target}} \quad v_{y,\text{target}} \quad v_{z,\text{target}}\}^T$ is the state vector representing the position of the asteroid at the final time of the trajectory. For measuring the constraints satisfaction, the infinity norm of the error in position $\left\|\mathbf{r} - \mathbf{r}_{\text{target}}\right\|_\infty$ and velocity $\left\|\mathbf{v} - \mathbf{v}_{\text{target}}\right\|_\infty$ is required to be under a given tolerance; specifically an absolute tolerance of 10,000 km is set for the positions and 0.01 km/s for the velocities.

The integral term of the cost function instead is selected to be the integral of the square of the norm of the thrust vector:

[‡‡] Data available online at http://naif.jpl.nasa.gov/naif/pds.html [Retrieved 28 January 2009].

$$g\left(\mathbf{s}_k,\mathbf{u}_k;t_k\right)=\frac{1}{2}w\mathbf{T}_k^T\mathbf{T}_k\cdot h_k \tag{5.50}$$

being w a weight factor and $h_k=t_{k+1}-t_k$ the integration interval at step k. In summary the cost function of the problem is:

$$J\left(\left\{\mathbf{T}_k\right\};\overline{\mathbf{s}}_1\right)=\sum_{k=1}^{N}\frac{1}{2}w\mathbf{T}_k^T\mathbf{T}_k\cdot h_k+\boldsymbol{\lambda}^T\cdot\left(\mathbf{s}_{N+1}-\mathbf{s}_{\text{target}}\right)^2$$

Generation of a first guess solution

A first guess is generated by patching together two low-thrust arcs with fixed thrust aligned to the velocity vector: one inside the sphere of influence of the Earth (i.e., until the distance from the Earth reaches the radius of the Earth's sphere of influence) and one from the Earth to the asteroid. The first guess solution is a function of a reduced set of parameters: the departure time from the Earth and the angular position on a fixed parking orbit, the time of flight, and the thrust magnitude out of the Earth's sphere of influence. The thrust magnitude of the spiralling-out phase is set outwith the optimisation. Thus, a global search for optimal first guesses is performed using Differential Evolution [152]. The objective for the global search is to minimise the error in distance (for a fly-by mission) or in distance and velocity (for rendezvous mission) between the state of the spacecraft and the target position at the final time:

fly-by: $$J_{\text{global search}}=\sum_{i=1}^{3}\frac{\left|\mathbf{r}_{N+1,i}-\mathbf{r}_{\text{target},\,i}\right|-r_{ref}}{r_{ref}}$$

rendezvous: $$J_{\text{global search}}=\sum_{i=1}^{3}\frac{\left|\mathbf{r}_{N+1,i}-\mathbf{r}_{\text{target},\,i}\right|-r_{ref}}{r_{ref}}+\sum_{i=1}^{3}\frac{\left|\mathbf{v}_{N+1,i}-\mathbf{v}_{\text{target},\,i}\right|-v_{ref}}{v_{ref}}$$

where $r_{ref}=10,000$ km and $v_{ref}=0.01$ km/s.

In the following three trajectories will be presented, the first two are rendezvous transfers to asteroid Apophis, the third one is a fly-by of asteroid 2002 AA29. In each of the three cases, the first guess is of course non optimal from an optimal control point of view and does not satisfy the terminal constraints; therefore the DDP algorithm is used to compute a locally optimal and feasible

trajectory. The two transfers to Apophis presented are quite different for initial orbit around the Earth, thrust magnitude, time of flight and mass of the spacecraft. In the second case (Section 5.5.2) being the initial orbit elliptical, the escape phase from the Earth is particularly sensitive to the three-body dynamics and the optimal solution differs pretty much from the first guess solution. In fact a fly-by of the Earth is scheduled, by the DDP algorithm, which was not included in the first guess trajectory. The transfer trajectory to asteroid 2002 AA29 (Section 5.5.3) presents also some interesting features, in correspondence of the passage in vicinity of the Lagrangian point L2.

5.5.1. Rendezvous with asteroid Apophis

The problem is to design an optimal low-thrust trajectory to rendezvous the asteroid Apophis, starting from an initial circular orbit (with the radius equal to the GEO), lying on the Earth equatorial plane. The spacecraft has an initial mass of 500 kg and is equipped with an engine capable of delivering a variable thrust at a fixed specific impulse $I_{sp} = 3250$ s. A first guess solution for the transfer is computed with the global search procedure illustrated in the preceding section. The departure date and transfer time were imported from the first guess. Table 5.2 summarises the main mission parameters.

Table 5.2: Mission characteristics.

Initial mass	500 kg
Specific impulse	3250 s
Departure date	19 August 2023 (8630.95 MJD2000)
Time of flight	990.4 days
Initial orbit radius	42,328 km

The optimal solution found has a propellant mass consumption of 133.15 kg and the thrust profile represented in Figure 5.11. The first guess (dashed line) is obtained with tangential thrust 0.15 N until exiting the Earth's sphere of influence and 0.0109 N afterwards. The value of the thrust magnitude outside the Earth's sphere of influence was imported from the first guess. The thrust evolution has an oscillatory behaviour with the spiralling-out from the Earth and the oscillation of the x and y-components are higher that the one along the z-axis (see Figure 5.12) The mass evolution follows approximately the first guess solution along the spiralling-out phase, whereas moves away from the first guess solution when out

of the Earth gravitation (see Figure 5.13). Note that the optimal solution has a mass consumption higher than the first guess because the constraints are satisfied under the required tolerance. The constraints violation in km and km/s of the first guess solution is:

$$\left|\mathbf{s}_{N+1} - s_{\text{target}}\right|_{\text{first guess}}^{T} = \left[3,708,314 \quad 9,936,689 \quad 8,362,980 \quad 0.51 \quad 3.09 \quad 0.038\right]$$

whereas it is under the required tolerance for the optimal solution:

$$\left|\mathbf{s}_{N+1} - s_{\text{target}}\right|_{\text{optimal}}^{T} = \left[4210.7 \quad 8089 \quad 1481.4 \quad 0.006 \quad 0.0045 \quad 0.00006\right]$$

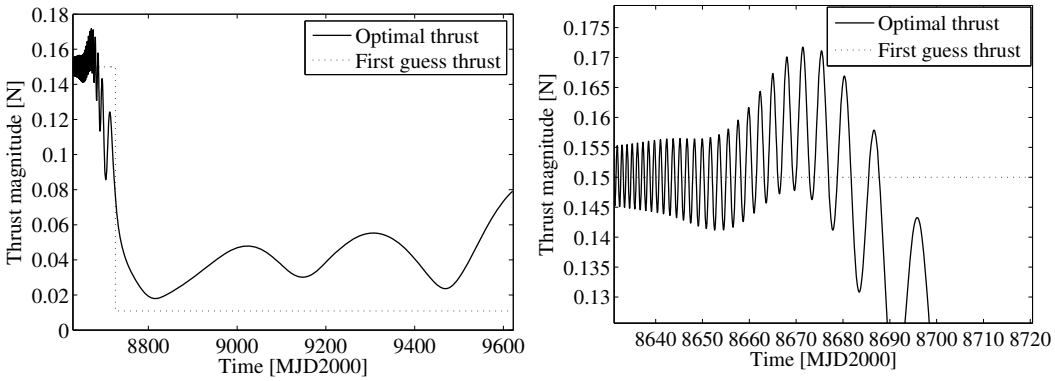

a) **b)**

Figure 5.11: Thrust magnitude. The dashed line represents the first guess solution provided to the DDP algorithm, the continuous line is the optimal thrust profile. a) Entire trajectory and b) close-up on the escape phase.

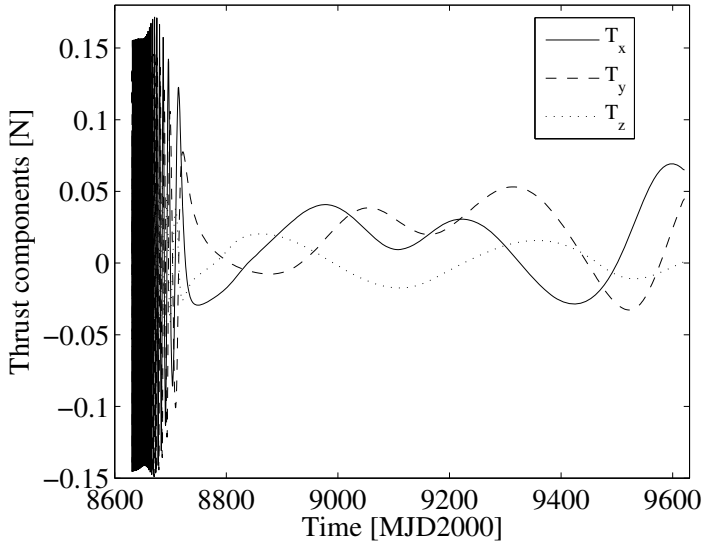

Figure 5.12: Time evolution of the thrust components.

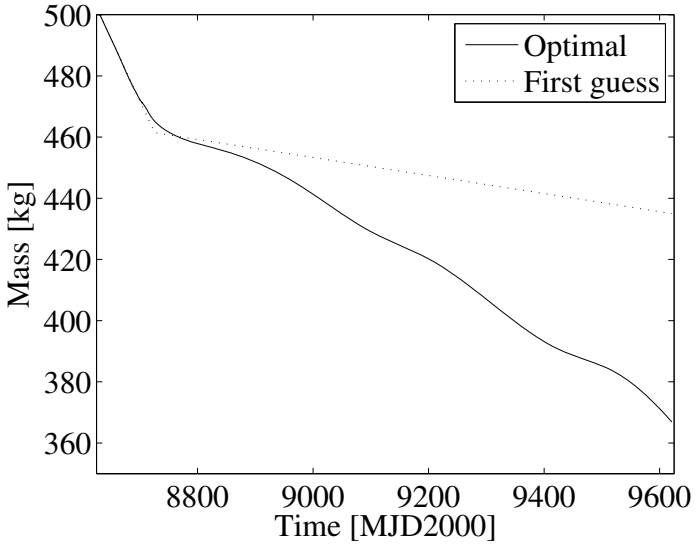

Figure 5.13: Mass. The dashed line represents the first guess solution; the continuous line is the optimal profile.

The transfer trajectory (see Figure 5.14) is represented in the Earth inertial system, the reference frame used for the optimisation process. Approximately thirty spirals are needed, with the level of thrust depicted in Figure 5.11, to escape the Earth's gravity field[§§].

Figure 5.15 shows the trajectory represented in the Sun inertial reference frame, and Figure 5.16 represents the time evolution of semi-major axis, inclination and eccentricity, during the escape phase (computed with respect to the Earth relative system, until the semi-major axis becomes negative and the eccentricity becomes smaller than 1).

[§§] The optimisation of the whole trajectory with the DDP algorithm required 3003 integration steps. Eight complete loops of the algorithm (see Figure 5.7) were needed, with an equivalent computational time of around 20 hours with a code written in Matlab®, on an AMD Athlon(tm) 64 Processor 3500+ @ 0.99GHz machine.

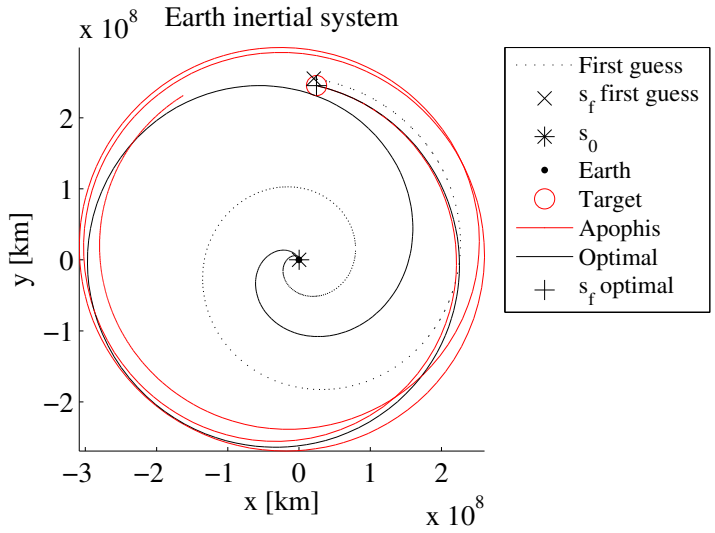

a)

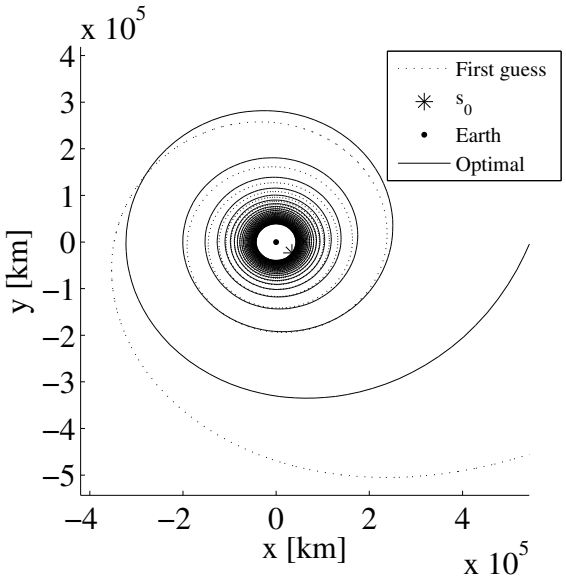

b)

Figure 5.14: Rendezvous trajectory to Apophis represented in the Earth inertial reference frame. a) Entire trajectory and b) close-up on the escape phase.

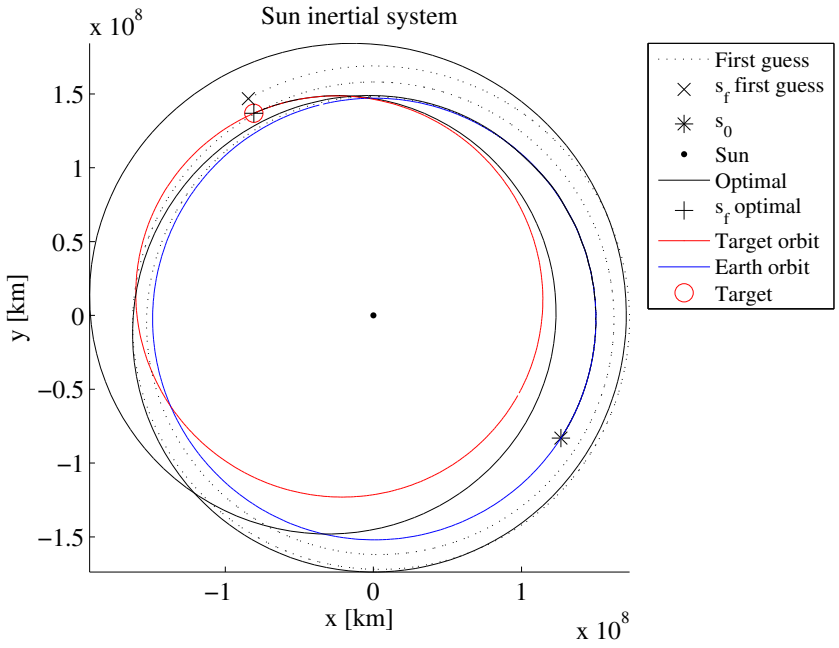

Figure 5.15: Trajectory to Apophis rendezvous. Transfer in the Sun inertial reference frame. The dashed line represents the first guess transfer solution; the continuous line is the optimal trajectory. Apophis and Earth orbit are represented respectively in red and blue continuous lines.

The optimal solution is characterised by a monotonic increase of the semi-major axis (see Figure 5.16a).

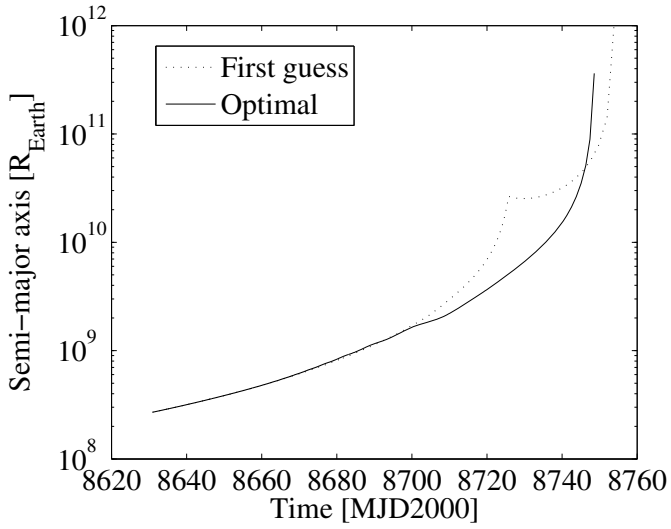

a) Evolution of the semi-major axis during the escape phase (expressed in Earth radii).

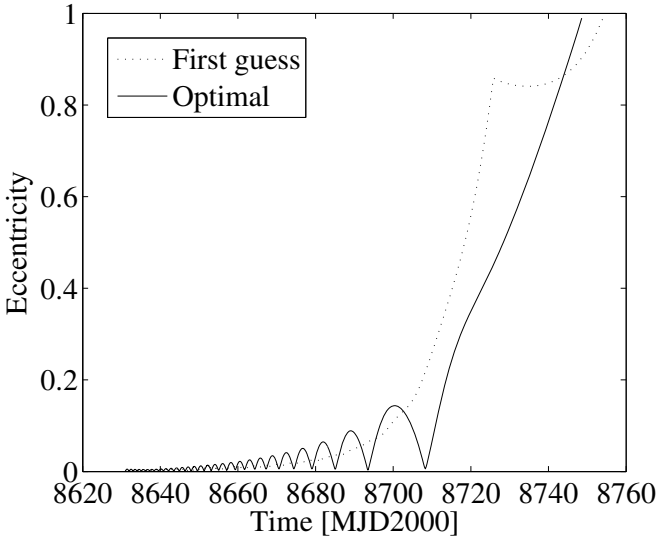

b)

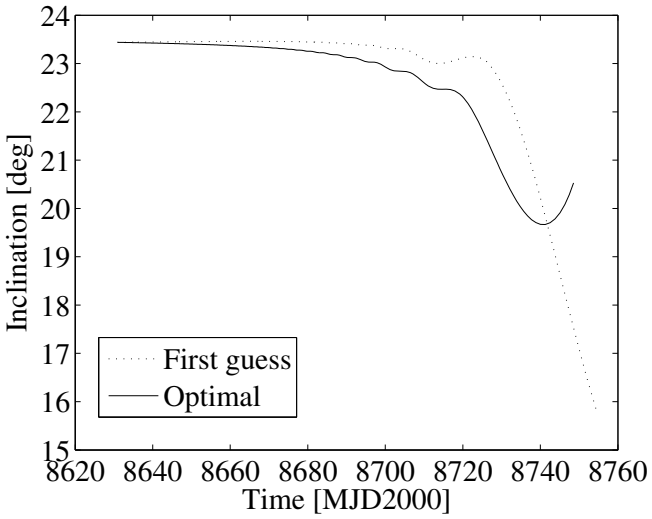

c)

Figure 5.16: Evolution of the Keplerian elements during the escape phase. The dashed line represents the first guess solution; the continuous line is the optimal profile. a) Semi-major axis expressed in Earth radii, b) eccentricity and c) inclination.

We then studied the evolution of the objective function for different times of flight, in the range of [700 1450] days. The result is reported in Figure 5.17.

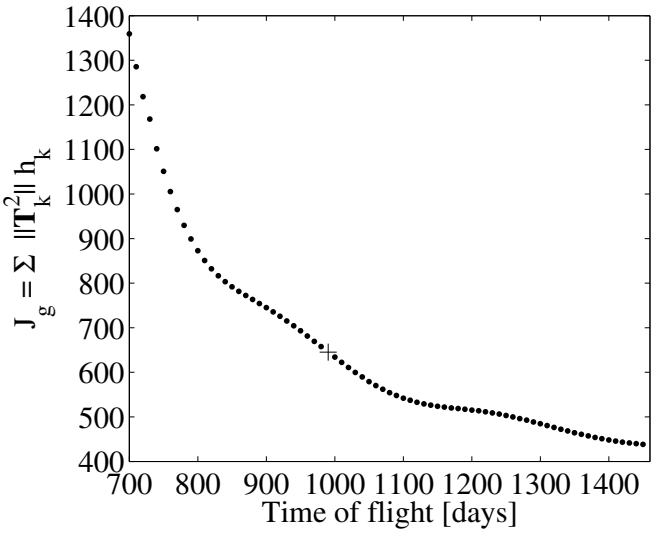

Figure 5.17: Time of flight sensitivity. The integral term of the cost function (normalised to the weight parameter *w*) is represented on the *y* axis. Each point represents an optimised transfer (with final constraints satisfied) with a given time of flight. The cross shows the result corresponding to the solution fully presented in this section.

The same trajectory was computed considering an initial mass of 1350 kg and keeping the other parameters equal to the values in Table 5.2, in order to give an estimation of the propellant mass needed for the Earth escape for the heliocentric trajectories computed in Section 5.4. The magnitude of the thrust vector is reported in Figure 5.18 and the mass of the spacecraft is shown in Figure 5.19. It has been computed that, for a mission with these characteristics, the propellant mass needed to exit the sphere of influence of the Earth is about 100 kg and the time of flight of the transfer is increased of 100 days with respect to the time for performing only the heliocentric leg. This implies that, if the escape phase from the Earth gravity field is taken into account in the Pareto fronts in Section 5.4, the additional propellant mass can be accounted for in the 25% of mass margin. However, an increase of the warning time has to be considered.

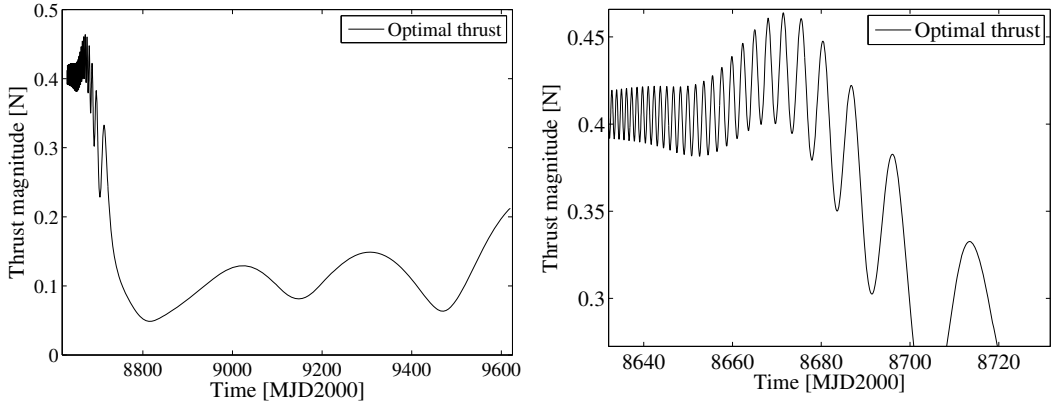

a) **b)**

Figure 5.18: Thrust magnitude for the mission with m_0 = 1350 kg. The dashed line represents the first guess solution provided to the DDP algorithm, the continuous line is the optimal thrust profile. a) Entire trajectory and b) close-up on the escape phase.

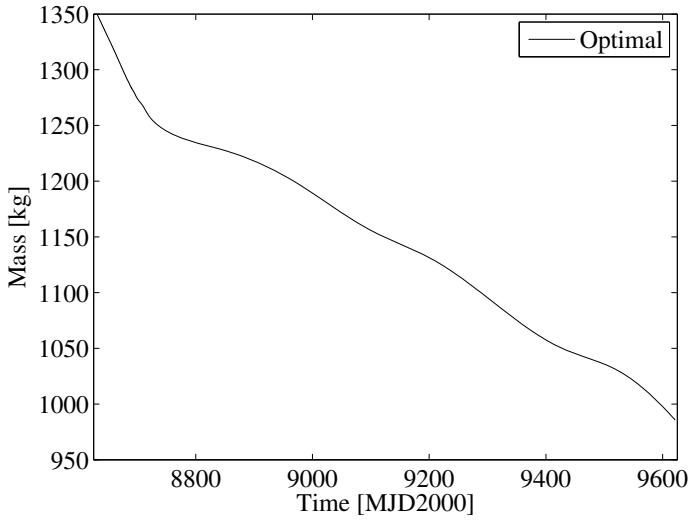

Figure 5.19: Mass for the mission with m_0 = 1350 kg. The dashed line represents the first guess solution; the continuous line is the optimal profile.

5.5.2. Rendezvous with asteroid Apophis from a geostationary transfer orbit

Another mission to asteroid Apophis is studied, with departure from a Geostationary Transfer Orbit (GTO). The arrival date at the asteroid is fixed on the 19th August 2033 (12283.5 MJD2000), based on the analysis of missions to deviate asteroid Apophis in Section 5.4. In fact, this launch date allows having 1000 days before the possible impact of the asteroid with the Earth on the 15 May 2036. The spacecraft, with initial mass of 1300 kg, is equipped with a low-thrust engine able to deliver a variable thrust at a fixed specific impulse of 3250 s.

The parking orbit of this transfer is a Geostationary Transfer Orbit (GTO) with an inclination of 23 deg with respect to the ecliptic; the transfer orbit injection point is fixed at the pericentre of the GTO and a midday launch is considered. The parking orbit parameters are reported in Table 5.3 and the other mission parameters are summarised in Table 5.4; the value of the time of flight and the magnitude of the thrust out of the sphere of influence of the Earth are fixed from the first guess solution. The DDP algorithm is used to find the solution to the optimal control problem and to satisfy the final constraints. The constraints violation in km and km/s of the first guess solution is:

$$\left|\mathbf{s}_{N+1} - s_{\text{target}}\right|_{\text{first guess}}^{T} = \left[20,041,710 \quad 60{,}297.6 \quad 1{,}954{,}650 \quad 3.07 \quad 1.5 \quad 1.19\right]$$

whereas it is under the required tolerance in the optimal solution:

$$\left|\mathbf{s}_{N+1} - s_{\text{target}}\right|_{\text{optimal}}^{T} = \left[24 \quad 3.4 \quad 24.7 \quad 0.00046 \quad 0.0086 \quad 0.0017\right]$$

Table 5.3: Parking orbit parameters.

Apocentre height	35950 km
Pericentre height	500 km
Inclination	23.44 deg
Anomaly of the ascending node	0 deg
Anomaly of the pericentre	185.24 deg (midday launch)
True anomaly	0 deg (pericentre)

Table 5.4: Mission characteristics.

Initial mass	1300 kg
Specific impulse	3250 s
Departure date	28 September 2029 (10,862.6 MJD2000)
Time of flight	1420.9 days

The optimal solution found has a propellant mass consumption of 336.95 kg; the optimal solution has a higher mass consumption because the final constraints are satisfied (see Figure 5.20). The thrust profile is represented in Figure 5.21 and Figure 5.22. The first guess (dashed line) is obtained with tangential thrust 1 N until exiting the Earth's sphere of influence and 0.0374 N afterwards. The oscillatory behaviour of the thrust with the spiralling-out from the Earth (see Figure 5.21b) causes small oscillations of the instantaneous eccentricity around the initial value, whereas the eccentricity of the first guess solution

(obtained with tangential thrust) decreases with time. This can be appreciated in Figure 5.23, which represents the evolution of the eccentricity with respect to the time and in Figure 5.24 which contains a close-up of the spiralling-out phase.

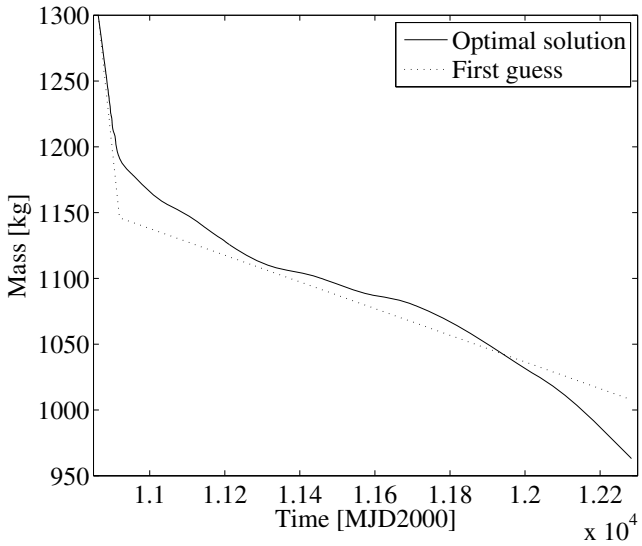

Figure 5.20: Mass. The dashed line represents the first guess solution; the continuous line is the optimal profile.

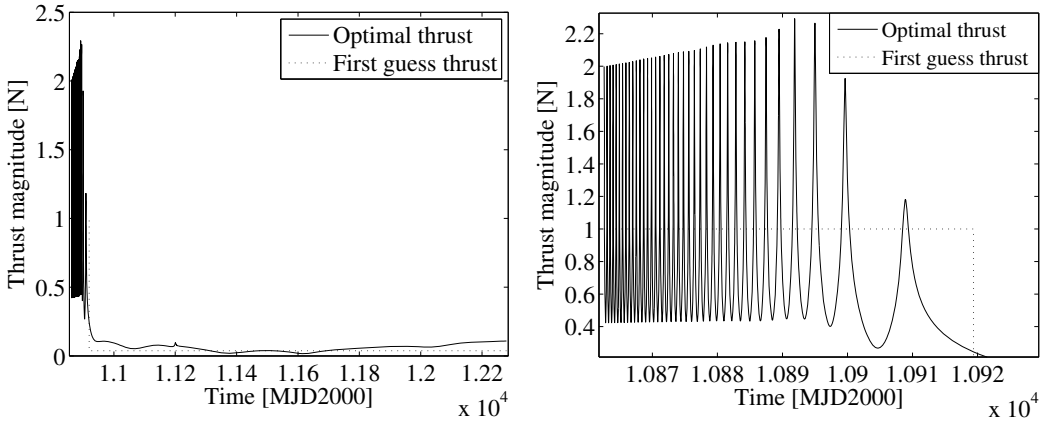

a) **b)**

Figure 5.21: Thrust magnitude. The dashed line represents the first guess solution provided to the DDP algorithm, the continuous line is the optimal thrust profile. a) Entire trajectory and b) close-up on the escape phase.

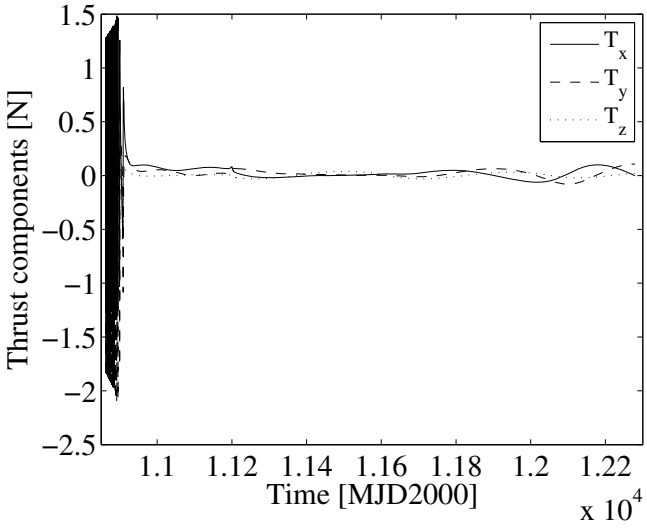

Figure 5.22: Time evolution of the thrust components.

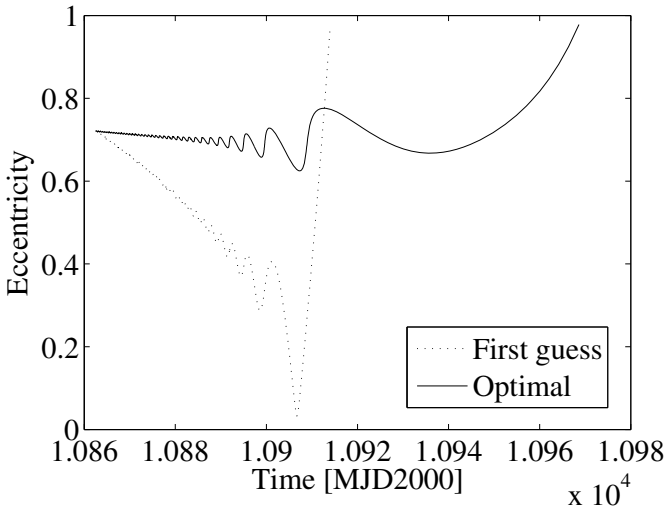

Figure 5.23: Evolution of the instantaneous eccentricity with time during the spiralling-out phase. The dashed line represents the first guess, the continuous line is the optimal solution.

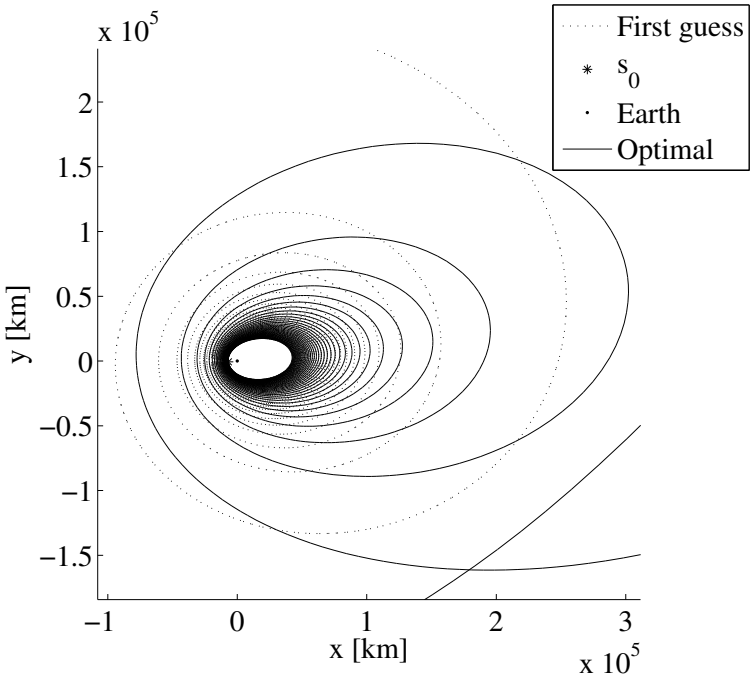

Figure 5.24: Close-up on the escape phase. The dashed line represents the first guess, the continuous line is the optimal solution.

Figure 5.25 shows the whole transfer trajectory in the Earth inertial reference frame (see Figure 5.25a) and in the Sun inertial reference frame (see Figure 5.25b). The dashed line is the first guess solution; the continuous line is the optimal solution. The solution found through the DDP algorithm presents a fly-by of the Earth that was not imposed in the first guess solution. The fly-by is indicated in Figure 5.25b with a cross and is shown in Figure 5.26 in the Earth inertial reference frame. The first guess solution progressively escapes away from the Earth gravity; the optimal solution instead goes far from the Earth and comes closer again to exploit the gravitational pull of the Earth for reaching the heliocentric transfer injection conditions.

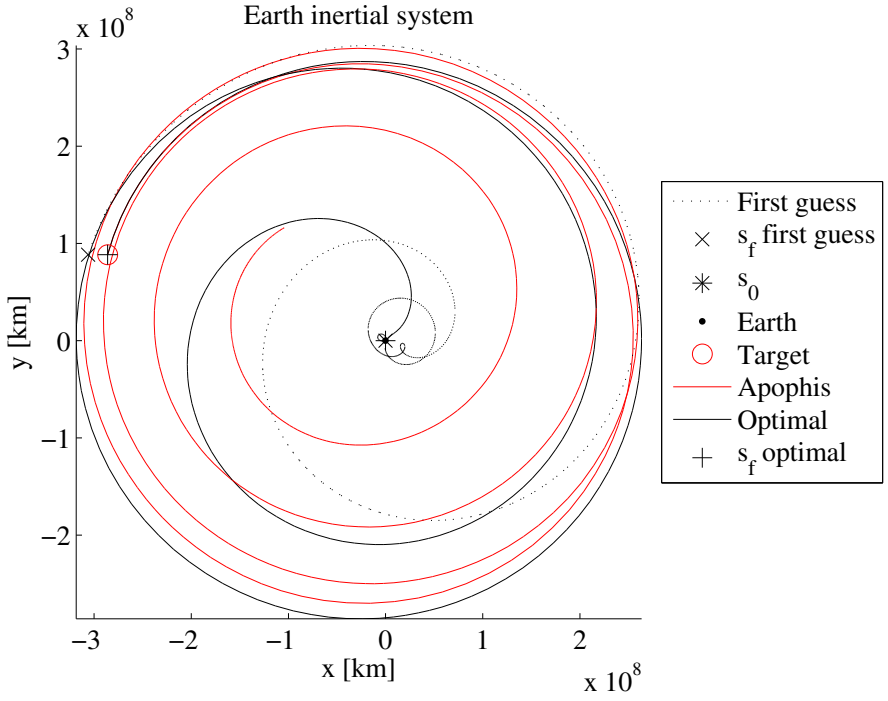

a)

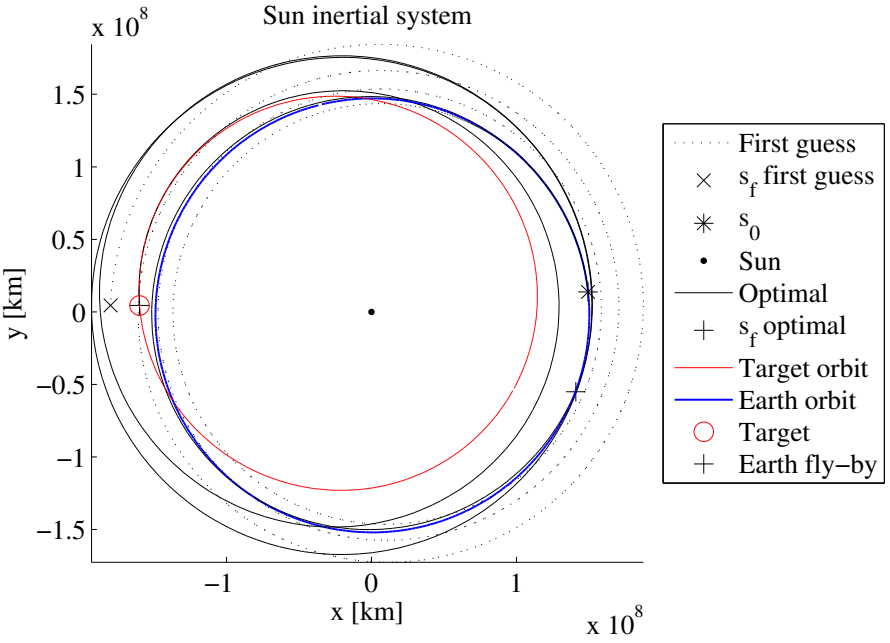

b)

Figure 5.25: Trajectory to Apophis rendezvous. The dashed line represents the first guess transfer solution; the continuous line is the optimal trajectory. a) Transfer in the Earth inertial reference frame. The circle represents the target position, the cross is the final state of the optimal trajectory. b) Transfer in the Sun inertial reference frame. Apophis and Earth orbit are represented respectively in red and blue continuous lines.

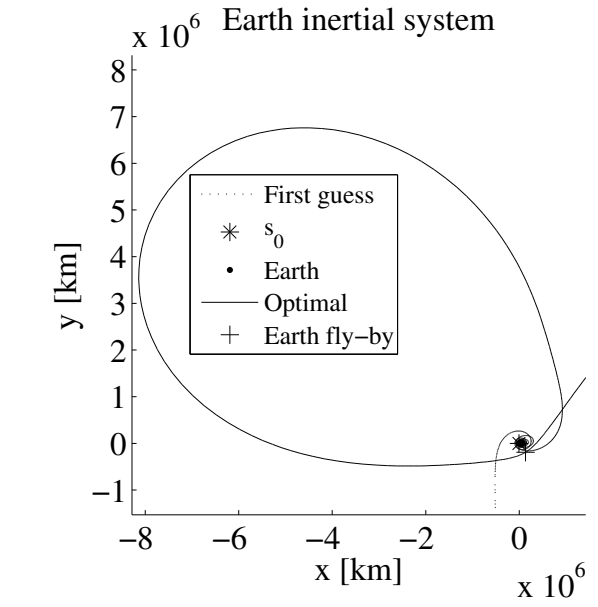

a)

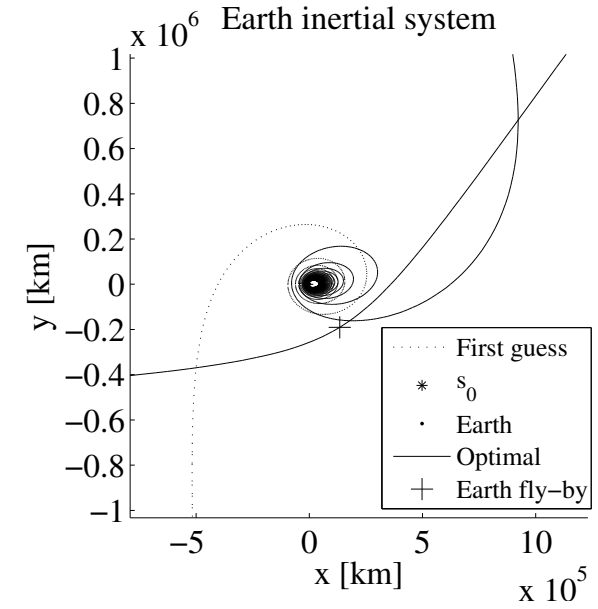

b)

Figure 5.26: Fly-by of the Earth. The cross represents the pericentre of the hyperbola with respect to the Earth. a) Fly-by phase and b) close-up of the passage from the pericentre of the hyperbola.

Figure 5.27 and Figure 5.28 are shown to demonstrate the presence of the fly-by phase. Figure 5.27 depicts the evolution of the thrust magnitude and the velocity magnitude during the fly-by phase, Figure 5.28 shows the in-plane angle α and the out-of-plane angle δ of the velocity with respect to the inertial reference frame centred at the Earth.

The peak in all the graphs in Figure 5.27 and Figure 5.28, in fact, is in correspondence of the passage from the pericentre (cross symbol in the figures). The velocity magnitude is almost unchanged at the entrance and exit from the fly-

by (see Figure 5.27b); whereas the in-plane and out-of plane angles, which represent the direction of the velocity vector, have a quasi-instantaneous change in correspondence of the pericentre passage (see Figure 5.28). In correspondence of the pericentre passage, a peak of the optimal control thrust is scheduled; this allows the following escape from the Earth (see Figure 5.27a).

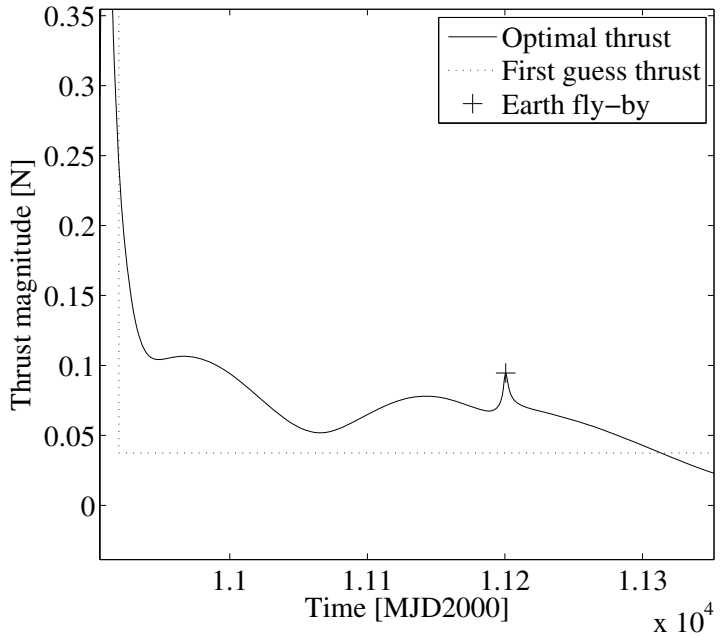

a)

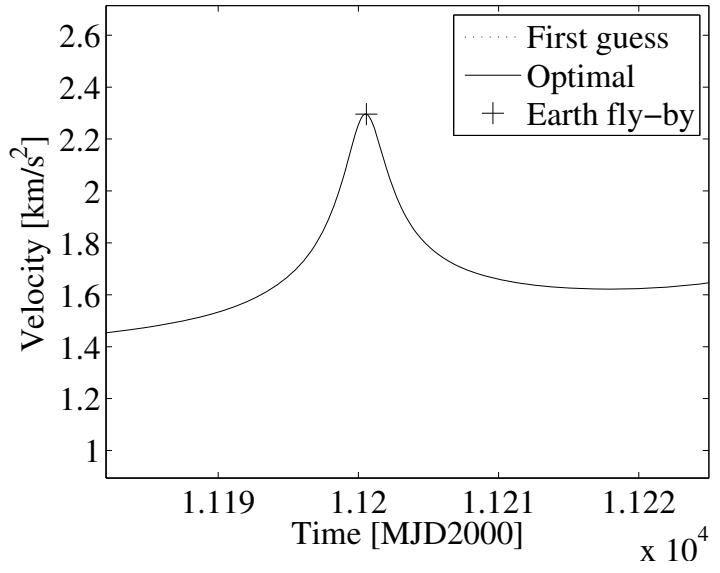

b)

Figure 5.27: Evolution of the thrust and velocity magnitude during the fly-by. The dashed line represents the first guess solution; the continuous line is the optimal profile. The cross symbol is in correspondence of the pericentre passage. a) Thrust magnitude and b) velocity magnitude with respect to the Earth.

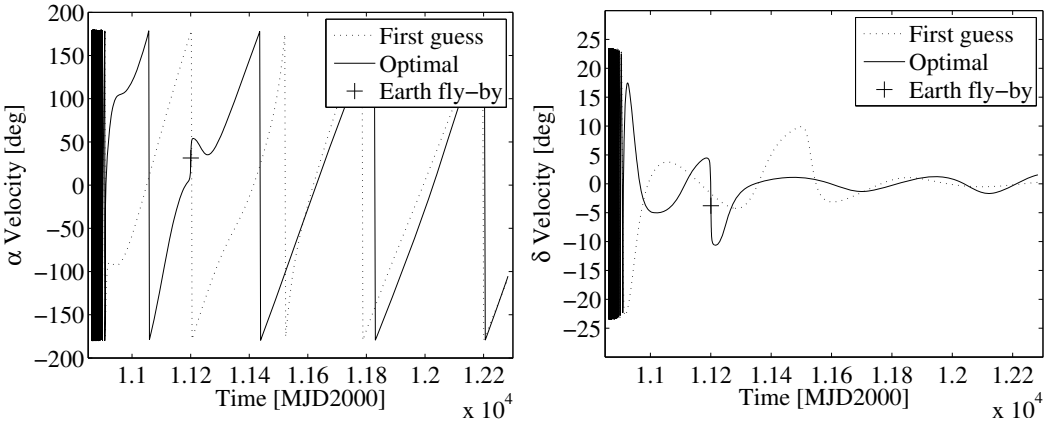

Figure 5.28: Evolution of the angles of the velocity vector with respect to the Earth inertial reference frame, during the fly-by. The dashed line represents the first guess solution; the continuous line is the optimal profile. The cross symbol is in correspondence of the pericentre passage. a) In-plane angle of the velocity vector and b) out-of-plane angle of the velocity vector.

5.5.3. Fly-by of asteroid 2002 AA29

Asteroid 2002 AA29 is a near Earth asteroid characterised by a "horseshoe orbit" with a full revolution of 95 years (see Figure 5.29). The latest nearest approach of the asteroid to the Earth was in January 2003, after that it reversed its direction once again[***]. A mission to the fly-by of 2002 AA29 is studied, with its parameters reported in Table 5.5. The initial orbit is circular (with the radius equal to the GEO) on the Earth equatorial plane.

Table 5.5: Mission characteristics.

Initial mass	500 kg
Specific impulse	2500 s
Departure date	27 April 2003 (1,212.2 MJD2000)
Time of flight	256.6 days
Initial orbit radius	42,328 km

The trajectory in the Sun inertial reference frame is depicted in Figure 5.30, whereas Figure 5.31 reports the thrust magnitude with a close-up on the spiralling-out from the Earth[†††]. The dashed line shows the magnitude of the first guess thrust: a constant thrust of 0.15 N is planned until a distance equal to the

[***] http://neo.jpl.nasa.gov/2002aa29.html [Retrieved 28 August 2009].

[†††] The optimisation of the whole trajectory (composed of around thirty spirals for the escape phase and the heliocentric leg) with the DDP algorithm required 2754 integration steps. One complete loops of the algorithm (see Figure 5.7) was needed, with an equivalent computational time of around 17 hours with a code written in Matlab®, on an AMD Athlon(tm) 64 Processor 3500+ @ 0.99GHz machine.

Earth's sphere of influence is reached; afterwards a constant thrust of 0.0088 N is applied along the direction of the velocity around the Sun. The continuous line in Figure 5.31 is the optimal solution computed through the DDP method. Figure 5.32 represents the time evolution of the thrust components and Figure 5.33 shows the mass of the spacecraft. The propellant mass needed for the asteroid interception is 49.3 kg.

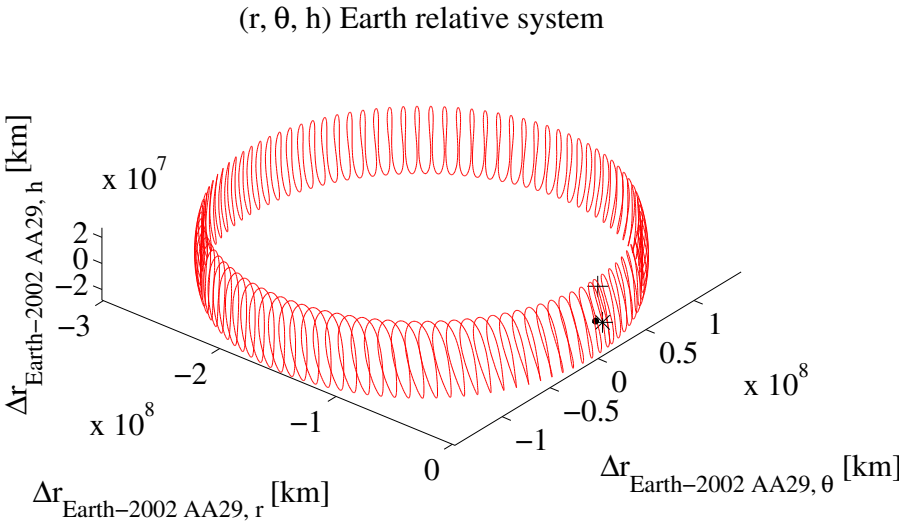

Figure 5.29: Trajectory of asteroid 2002 AA29 relative motion with respect to the Earth.

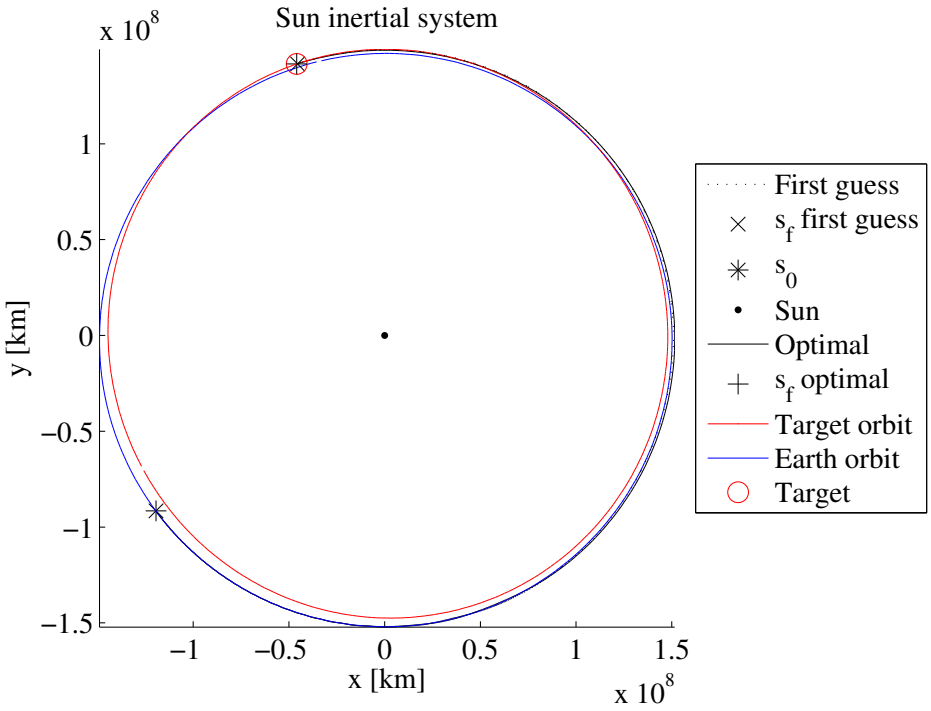

Figure 5.30: Transfer trajectory to 2002 AA29 fly-by in the Sun inertial reference frame. The dashed line represents the first guess transfer solution; the continuous line is the optimal trajectory. 2002 AA29 and Earth orbit are represented respectively in red and blue continuous lines.

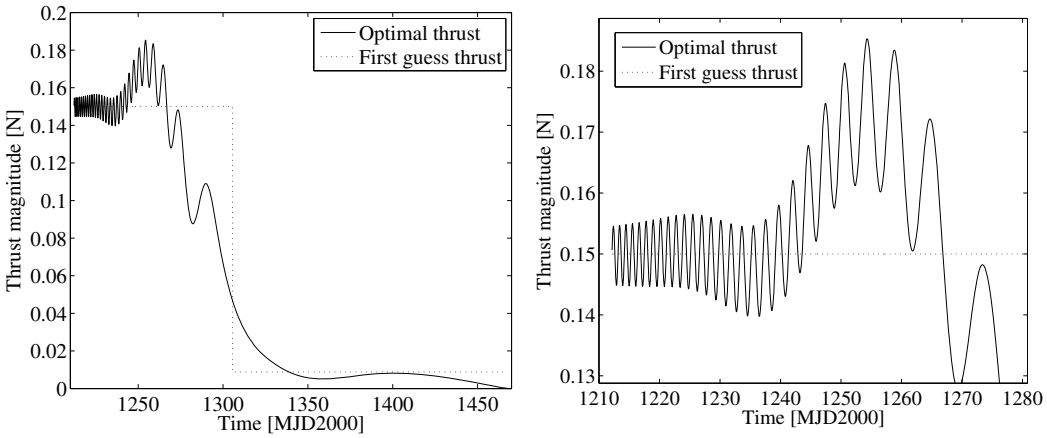

a) **b)**

Figure 5.31: Thrust magnitude. The dashed line represents the first guess solution provided to the DDP algorithm, the continuous line is the optimal thrust profile. a) Entire trajectory and b) close-up on the escape phase.

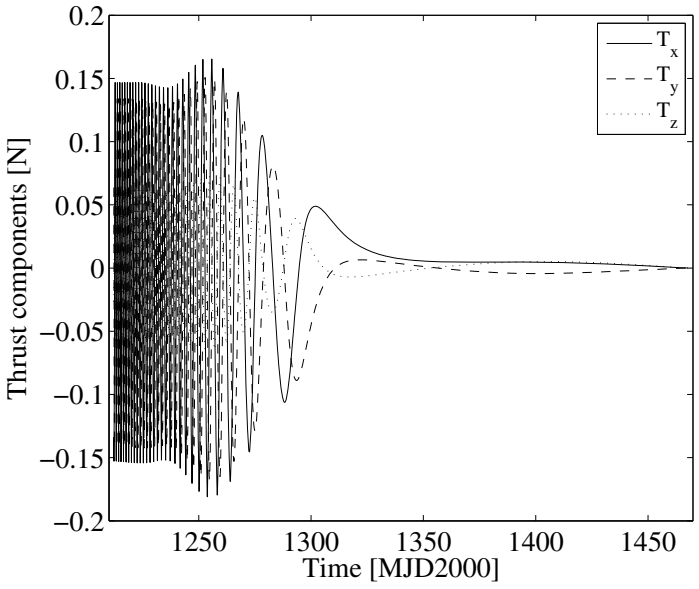

Figure 5.32: Time evolution of the thrust components.

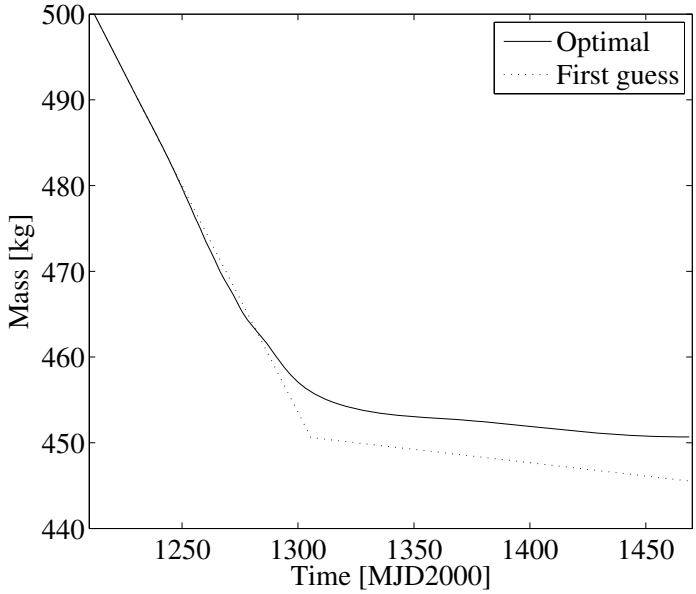

Figure 5.33: Mass. The dashed line represents the first guess solution; the continuous line is the optimal profile

Figure 5.34 represents the trajectory in the Earth inertial reference frame. The tolerance required for the fly-by of the asteroid is a maximum error of 10,000 km on the components of the relative position with respect to the asteroid. No constraints on the velocity are imposed; hence the spacecraft intercepts the asteroid with a relative velocity of 5.56 km/s. The dashed line represents the first guess trajectory which has a constraints violation on the three components of the position of $\Delta\mathbf{r} = \{390,574 \quad 24,805 \quad -908.6\}^T$ km, the continuous line indicates the optimal solution for the trajectory, with a violation of the position at the asteroid of $\Delta\mathbf{r} = \{\text{-}8278.5 \quad \text{-}5982.5 \quad \text{-}1803.1\}^T$ km. The red line describes the motion of 2002 AA29 with respect to the Earth inertial system.

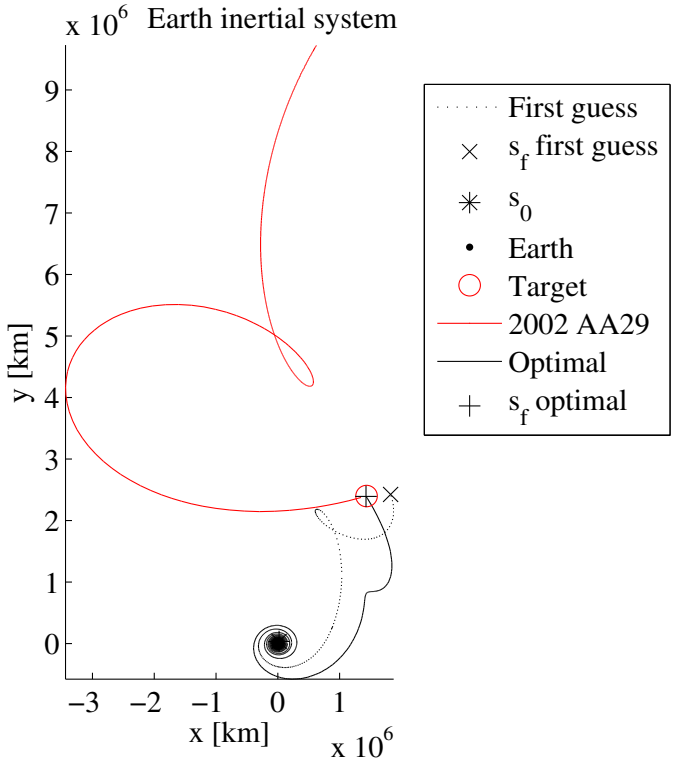

a)

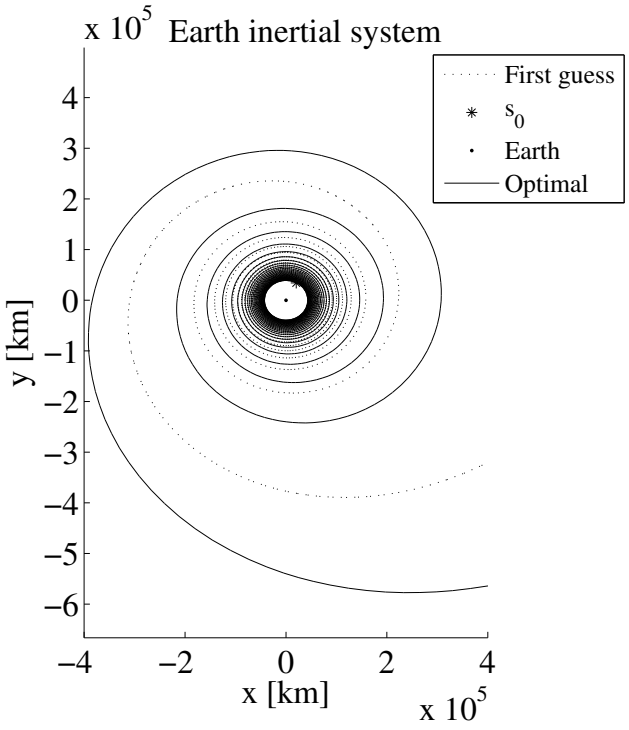

b)

Figure 5.34: Trajectory to 2002 AA29 fly-by represented in the Earth inertial reference frame. a) Entire trajectory and b) close-up on the escape phase.

Figure 5.35 reports the trend of the instantaneous Keplerian elements (computed with respect to the Earth relative system) along the trajectory until the

escape from the Earth (i.e., semi-major axis becomes negative and eccentricity becomes bigger than 1). The escape occurs slightly before for the optimal trajectory than the first guess one.

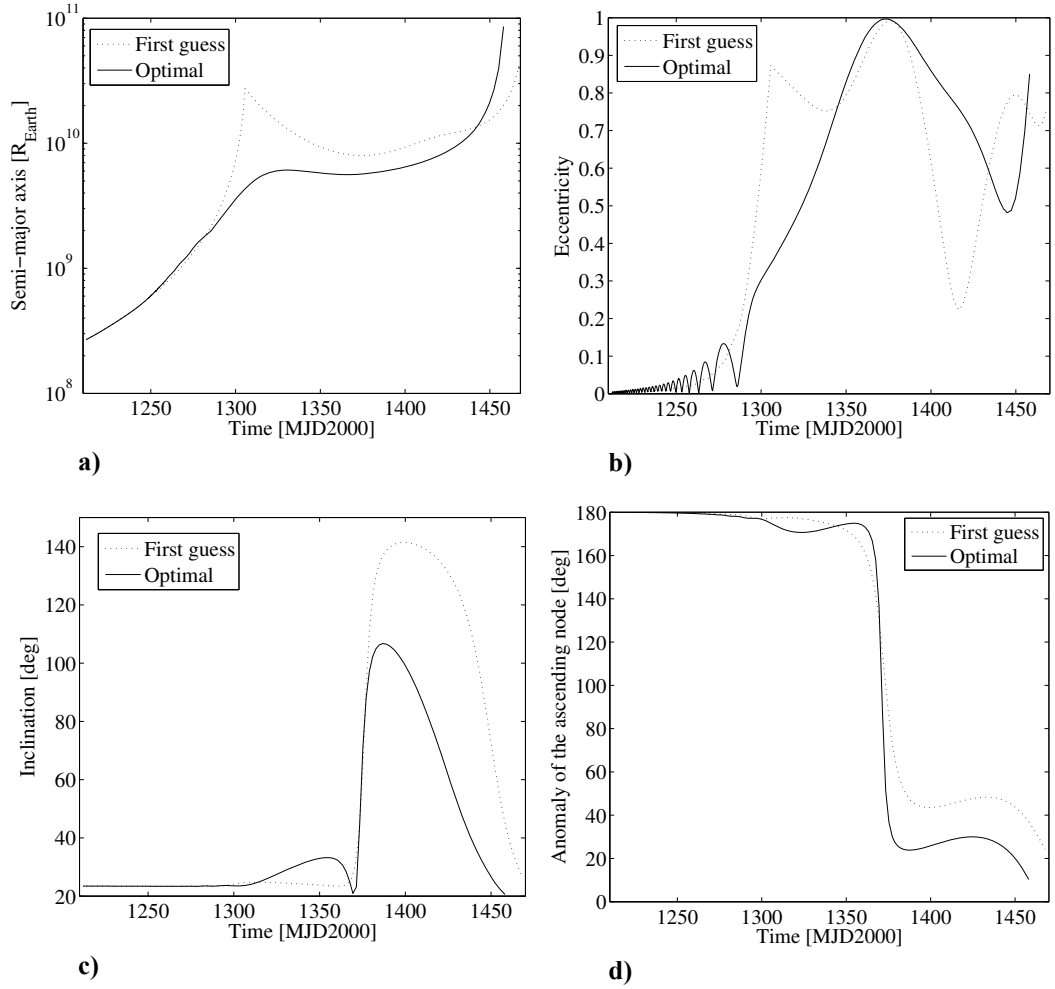

Figure 5.35: Evolution of the Keplerian elements during the escape phase. The dashed line represents the first guess solution; the continuous line is the optimal profile. a) Semi-major axis, b) eccentricity, c) inclination, and d) anomaly of the ascending node.

As can be seen from Figure 5.35, there is a sudden change of the orbital elements, especially inclination and anomaly of the ascending node, in a range of 20 days between 1370 and 1390 MJD2000. This occurs when the spacecraft passes in vicinity of the Lagrangian point L2, as can be appreciated from Figure 5.36. When passing in the vicinity of L2, a small change in the direction of the thrust vector (see Figure 5.37) produces a big variation of the orbital elements.

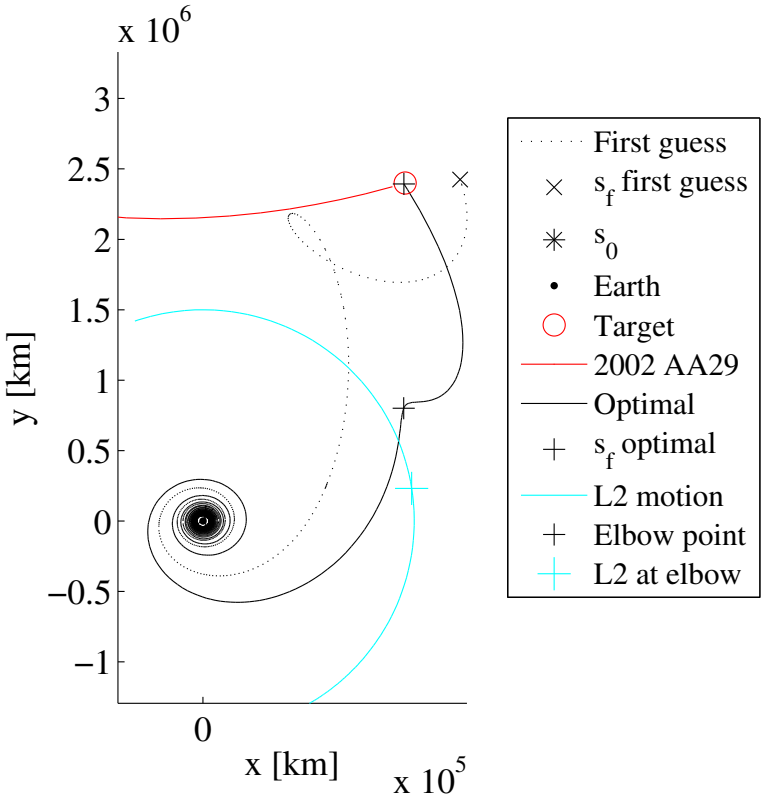

Figure 5.36: Lagrange point passage. The cross highlights the position of the Lagrange point L2 when the trajectory changes its inclination.

Figure 5.37 shows the angles of the thrust vector, the in-plane right ascension angle (Figure 5.37a), taken from the tangential direction along the velocity vector to the projection of the thrust vector on the orbital plane, and the out-of-plane declination angle (Figure 5.37b) from the projection of the thrust vector on the orbital plane up to the thrust vector itself.

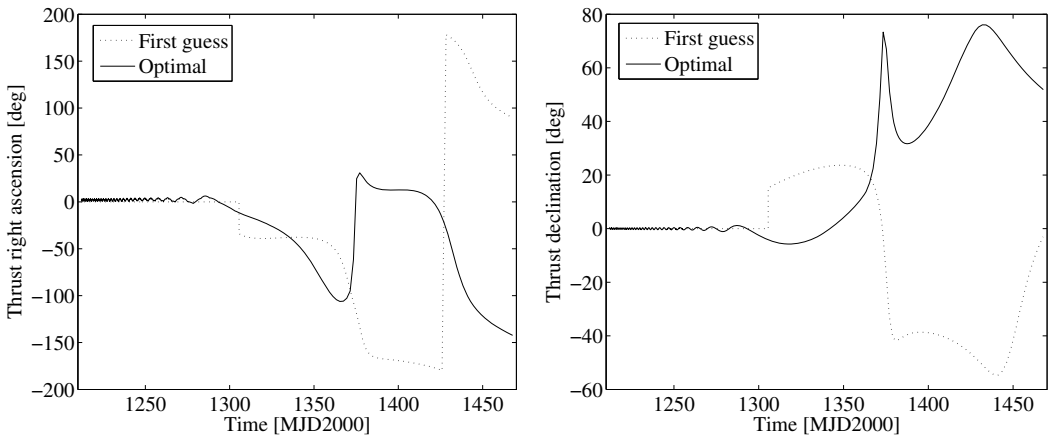

a) **b)**

Figure 5.37: Angles of the thrust vector. The dashed line represents the first guess solution; the continuous line is the optimal profile. a) Right ascension and b) declination.

Finally Figure 5.38 represents the components of the acceleration acting on the spacecraft, in the first guess (dashed line) and optimal (continuous line) solution. The components represented are respectively the acceleration due to the Earth's gravity field a_E (black lines), the disturbing components due to the interaction between Sun-Earth and Sun-spacecraft a_d (bold black lines), and the acceleration produced by the engines, a_T (bold grey lines). Focusing on the acceleration magnitude (Figure 5.38a) it can be noticed that around 1370 MJD2000, the acceleration component due to the Sun becomes bigger than the Earth's gravitation. Figure 5.38b, c and b, instead, contain the x, y and z components of the acceleration.

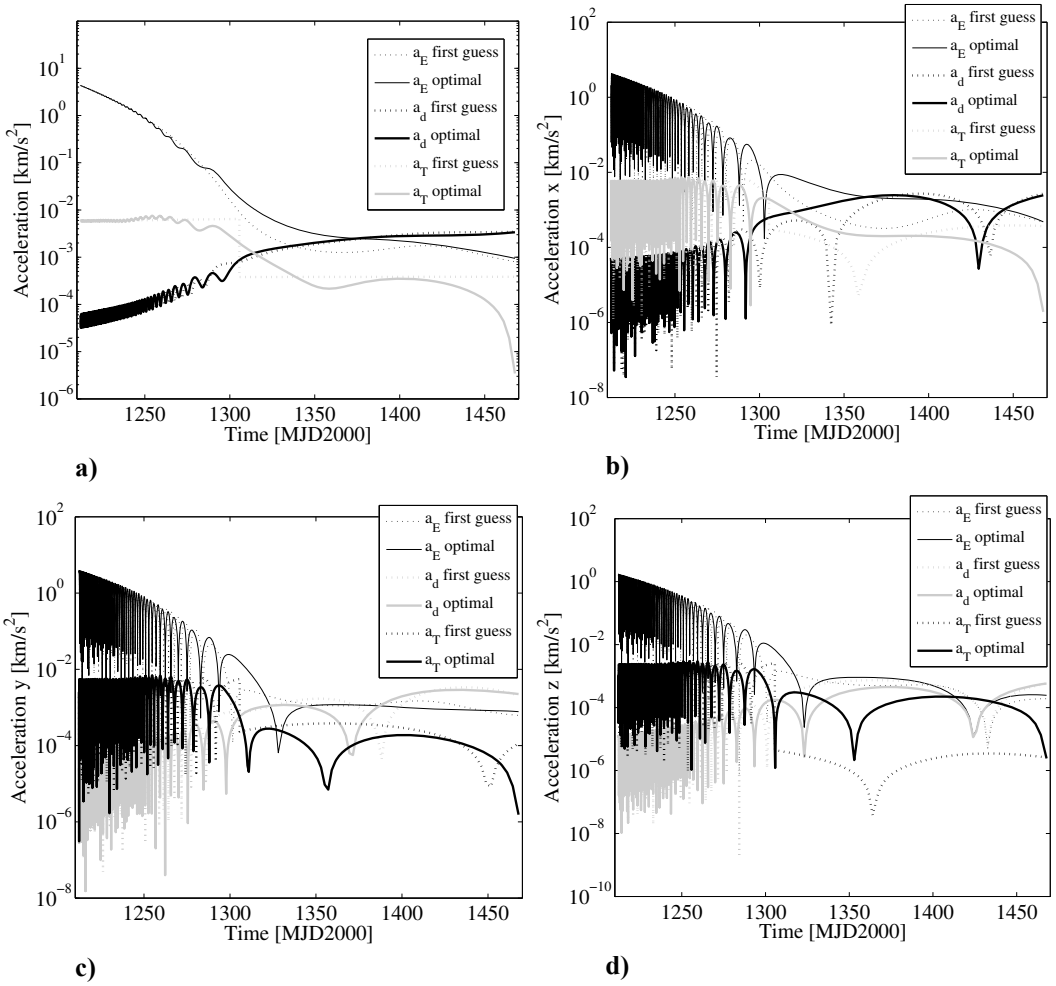

Figure 5.38: Acceleration components. The dashed line represents the first guess solution, the continuous line is the optimal solution. The black line indicates the acceleration due to the Earth's gravity field, the black bold line indicates the disturbing acceleration due to the Sun and the bold grey line indicates the thrust acceleration. a) Acceleration magnitude, b) x component of the acceleration, c) y component of the acceleration, and d) z component of the acceleration.

5.6. Summary

This chapter presents a modified Differential Dynamic Programming algorithm for the optimisation of low-thrust trajectories. The principal advantage of the proposed algorithm is that the problem is discretised in a number of decision steps, so that the optimisation process requires the solution of a great number of small dimensional problems (one for each stage). The stage-wise approach allows the use of an accurate adaptive integration of the dynamics during the optimisation process. The main advantage is that high fidelity dynamic model can be used. A Runge-Kutta-Fehlberg integration scheme is incorporated in the DDP scheme, together with a particular interpolation technique that preserves the feedback nature of the control variation. This particular technique improves the robustness of the algorithm against some approximation errors that are introduced during the adaptation process. A further increase in robustness is obtained by the use of global control variations, which showed to be more appropriate than the small control variations algorithm for the solution of the problems presented in this chapter.

In particular, the case of a transfer to asteroid Apophis, starting from a Geostationary Transfer Orbit around the Earth, demonstrates as differential dynamic programming is able to introduce an additional fly-by, not included in the first guess solution.

Chapter 6.
Conclusions

A crucial issue related to the safety of our planet is the danger represented by small celestial bodies such as comets or asteroids, which travel along orbits that may intercept the Earth and cause catastrophic impacts. This research responds to the requirement of hazard mitigation and proposes methodologies for the design of optimal trajectories for the interception and deflection of Near Earth Objects.

In this chapter an overview of the work done is provided, and the main results of this thesis are summarised and commented. On the base of the findings of this study, an outline of future works and some recommendations are given.

6.1. Summary and findings of the thesis

The design of a mitigation mission requires the definition of two phases, namely, the interception transfer leg from the Earth to the asteroid and subsequently the deflection phase, during which a low-thrust or impulsive action is applied to the target body to continuously or quasi-instantaneously deflect its orbit and increase the minimum orbit intersection distance with the Earth.

The first objective is to find a general formulation of the asteroid deviation problem, characterised by broad applicability and high accuracy. In Chapter 2 and 3, the asteroid deviation problem has been formulated making use of the linearised relative motion equations for general elliptic orbits, considering the nominal orbit of the asteroid as the chief orbit, and its new obit after the deflection manoeuvre as the proximal orbit to the unperturbed one. These equations express the displacement of the target celestial body at the minimum orbit intersection distance, as a function of the variation of the orbital elements between its perturbed course after the deflection manoeuvre, and the nominal unperturbed

orbit. The relative motion formulation has general applicability for any impulsive or low-thrust deviation manoeuvre, whose effect can be described as a variation of orbital parameters. The classical Keplerian elements representation has been used, and their variation is computed through Gauss' equations. In the case of an impulsive action, Gauss' equations have been written in the form of finite differences (Chapter 2), whereas, when a low-thrust manoeuvre is applied on the target body for a certain period of time, the equations have been numerically integrated (Chapter 3). In both cases, an expression for the variation of the mean anomaly, which takes into account the change in the orbit geometry and the phase shift between the Earth and the NEO due to a variation in the mean motion, was found.

The validity conditions of the relative motion formulation have been discussed in Chapter 2, and the accuracy analysis performed has shown the correctness of the proposed approach for a wide range of orbit eccentricities (covered by a large number of asteroids characterised by different sets of orbital parameters). This formulation represents an extension of other expressions that consider only the change in the asteroid orbital period due to a variation in the mean motion; unlike those approaches, the proposed formulation is able to describe a strategy producing an action in any direction (i.e., not only in the direction tangent to the motion). Furthermore, it is less computationally expensive than more general methods based on the analytical propagation of the perturbed trajectory by using the Lagrange coefficients, because it does not require the solution of the time equation for the evaluation of the deviation. On the other hand, it is conceptually and computationally equivalent to the approach that uses the fundamental perturbation matrix to propagate only the variation of position and velocity, instead of the complete orbit. Conversely, the proximal motion formulation expressed in Keplerian elements variation benefits from the direct relation between the deflection manoeuvre and the variation of the geometrical characteristics of the orbit of the NEO.

In Chapter 2 the transition matrix form of the relative motion equations and Gauss' equations for impulsive deflection has been exploited to study the optimal direction for maximum deviation strategies. The *b*-plane representation has been used to take into account the final motion of the asteroid in the Earth's sphere of

influence. In an actual impact scenario, in which the Earth is at the MOID and $\Delta r \approx 0$, the impact parameter b^* can be used as a good estimate of the minimum distance between the asteroid and the Earth. This has been verified by comparing the projection of the deviation on the *b*-plane with the deviation computed by numerical propagation of the perturbed motion (after an impulsive $\delta\mathbf{v}$ is imparted to the asteroid) in the three-body dynamics model.

The analysis of the results on the *b*-plane has shown that the effective deviation, considering the Earth's gravity, is smaller compared to the deviation computed in the two-body problem; this implies an increase of the $\delta\mathbf{v}$-requirement due to the gravitational effects of the Earth. This is in accordance with the results found by Ross et al. [73]. Furthermore, the b^*-parameter maximisation strategy suggests, for short times-to-MOID, a different optimal direction than the one found through the $\delta\mathbf{r}$-parameter maximisation. Instead, for a certain time-to-MOID $\Delta t_{\mathrm{NEO}} < 1T_{\mathrm{NEO}}$, which is different for every asteroid, the maximisation of the b^*-parameter and the maximisation of the deviation lead to the same conclusion on the optimal deflection strategy.

Some interesting considerations can be drawn from the analysis of the deviation components in the *b*-plane, given that the ξ-component represents the shortest distance between the Earth and the asteroid (hence it is strictly related to the geometrical variation of the MOID), whereas the ζ-component is a measure of the time shift between the asteroid and the Earth passage at the MOID [131]. The latter component constitutes the main contribution to the total resulting deviation achieved by a manoeuvre tangent to the velocity. In fact, an impulse in the tangential direction produces a secular and periodic variation of the ζ-component and a periodic variation of the ξ-component, whereas a strategy given in a direction normal to the motion produces a purely periodic variation of both the ζ- and ξ-component. The secular variation of the ζ-component demonstrates that only an impulse in the tangential direction has an effect that increases if the manoeuvre is imparted more than one orbital period in advance. A velocity change in a direction normal to the motion, instead, has an effect that overlaps for more than one orbital period in advance, although it can represent the optimal option for short times-to-MOID. This is in accordance with Conway's

results [70] and supports the assumption made in the existing literature of tangential direction for long times-to-MOID. Moreover, we gave a physical interpretation to the η-component, which is linked to the time difference between the instant when the actual minimum distance from the Earth is reached (considering the three-body problem dynamics) and the expected time at the MOID (estimated with a two-body approach).

The angular position of the deflecting manoeuvre along the unperturbed orbit also plays an important role; in fact a manoeuvre applied at the pericentre confirms to be the most efficient in maximising the consequent deviation.

Chapter 3 focused on NEO deviation through low-thrust strategies. In the general case of continuous acceleration acting on the threatening body, the numerical integration of Gauss' equations is necessary. In the case of a low-thrust deviating acceleration inversely proportional to the square of the distance from the Sun, a set of semi-analytical formulae has been derived, which only requires the evaluation of two elliptic integrals for every orbital revolution. Unlike other semi-analytical formulations, the periodic variation of the orbital elements has also been modelled. In fact, it was verified that considering the secular variation alone is not enough to describe with high accuracy the displacement at the MOID; this because high precision is required in determining the change in mean anomaly. The periodic terms ensure the required accuracy for a deviation manoeuvre starting at any angular position along the orbit of the NEO; this would have not been achieved by using other formulae that account only for the secular variations. The accuracy of the latitude and time formulations proposed has been extensively shown, through comparison of numerical data against semi-analytical prediction, for a range of values of the eccentricity, semi-major axis and proportionality constant of the acceleration.

The semi-analytical approach that was proposed allows reducing the computational time to 40% against the full numerical propagation of Gauss' equations. This is not particularly important when one single solution is computed, but represents a huge benefit if thousands of solutions have to be computed, for example when constructing a Pareto front.

The second objective of this study is to develop a fundamental optimal control theory and apply it to the interception of hazardous asteroids. In this vein,

a novel approach adopted in this work has encompassed the interception and the deflection phases as inseparable at the stage of preliminary design of a mitigation mission; in fact the mass and time requirements are highly influenced by the transfer leg for reaching the asteroid's orbit. At the same time, unlike existing literature, which is mainly focused either on the analysis of optimal deflection or on the study of a selected mission case, our study is aimed at finding several mission options rather than focusing on a single mission scenario.

A wide variety of mitigation missions, which maximise the total deviation at the MOID, while minimising the mass at launch and the warning time, has been computed. A hybrid global approach has been used to perform a multi-criteria optimisation that identifies sets of Pareto-optimal solutions [116]. The global search has been performed over a wide domain of mission parameters, such as launch date, time of flight, and geometrical characteristics of the transfer. At this stage, preliminary design techniques have been adopted for modelling the interception trajectory.

Chapter 2 presented a wide range of mission opportunities for asteroid mitigation through kinetic impact strategy. Thirty near Earth asteroids, with different masses and orbital elements, were selected, and for those targets optimal launch opportunities for direct transfers and transfer via Venus fly-by were identified. The results show that, with current technologies, a reasonably small spacecraft impactor of 1000 kg can obtain remarkable deviation in a limited time range. Another finding of the mission simulations is that the direction of the impact velocity moves away from the theoretical optimal direction, when we consider the interception transfer leg and real case scenario for which $\Delta r \neq 0$. In fact, the component of the velocity normal to the motion in the orbital plane becomes more significant. Therefore the actual MOID can not be neglected in general. Moreover, when the transfer leg is optimised, the optimal interception point is not necessarily the pericentre and for highly inclined asteroid is, as expected, close to the orbit nodes.

In Chapter 3 further mission opportunities, for deflection missions to four selected asteroids, have been computed. At the same time, these results represent an exemplificative application of the semi-analytical formulation for low-thrust deviation, derived in the first part of the chapter. The mission design assumes a

solar collector which focuses the Sun light onto the asteroid, causing the ablation of its surface; however, the acceleration law hypothesised for the analytical developments, could be alternatively used to model a low-thrust attached propulsion device with solar power system. The Pareto fronts presented show that deviation of the order of the radius of the geostationary obit can be reached with 3 to 5 years warning time, whereas for longer warning times the achievable deviation can increase to the Earth–Moon distance. The modulus of the achieved deviation is proportional to the length of the thrusting interval and has a periodic trend with the true anomaly of the interception point; in particular, when the eccentricity of the asteroid is high, an interception before the pericentre is significantly more effective than an interception after the pericentre.

Further mission options have been proposed in Chapter 4; the results presented define a wide variety of deflection mission opportunities for a number of selected asteroids, over a wide range of possible launch dates. The purpose of this chapter is also to qualitatively assess the more feasible mitigation strategies proposed in the literature and currently discussed in the international panel debate about asteroid mitigation. The design approach explained in Chapter 2 and 3 has been adopted to construct a number of Pareto sets, each one making use of a different deviation strategy. The launch mass, warning time and total deviation have been used as figures of merit for the multi-objective optimisation. The concept of *dominance*, borrowed from multi-objective optimisation, has been exploited to compare different solutions belonging to various Pareto fronts, obtained using the three criteria chosen for selecting the optimal points. With respect to the existing literature, an analytical method has been used to compare different options. The proposed approach allows assessing the effectiveness of a mitigation strategy, based on set of hundreds of potential missions, rather than choosing a single hypothetical mission case. Moreover, the technology readiness of each strategy has been considered by adding to the warning time the man-years necessary to develop the required technology (Appendix B). A preliminary comparison has been driven from the Pareto fronts and the comparison tables have been presented in Chapter 4. Solar collector and nuclear interceptor are, in general, the dominant strategies, because they reach values of deviation of the order of the Earth–Moon distance for relatively small values of the initial mass

and the warning time. Moreover, the solar collector system remains competitive also after evaluating the solutions according to their technology readiness. Kinetic impactor showed to be a feasible option to deviate asteroid of small dimensions, such as asteroid Apophis, because no technology development is required. However, the risk of fragmentation has to be carefully considered when dealing with impulsive strategies.

The second objective of the research presented in this thesis is addressed on two levels; in Chapter 2, 3 and 4 a large number of asteroid interception options has been identified, through a global search over an extended search domain. In Chapter 5 a selected number of solutions has been locally refined, by using a high fidelity model for the trajectory design. Among the methods for trajectory optimisation available in the literature, the technique of Differential Dynamic Programming has been investigated. The stage-wise feature of DDP has been exploited to develop a method for low-thrust trajectory optimisation that is capable of adjusting the discretisation mesh at each iteration of the convergence process. An interpolation technique has been studied to compute the thrust vector on the refined mesh, without jeopardizing the feedback nature of the control law. For this reason, when solving a problem, that is particularly sensitive to the dynamics, the interpolation of the control vector is performed separately on each term that constitutes the complete control law. Moreover, the use of the algorithm with global control variations has ensured a further increase in robustness. The results section of Chapter 5 firstly focuses on the transfer solutions identified through the global search introduced in the previous chapters. A number of solutions belonging to a Pareto front for a low-thrust mission to asteroid Apophis has been locally refined with the DDP-based algorithm, and the saving in propellant mass with respect to the preliminary design shown. Three trajectories have then been presented, as an application of the DDP-based algorithm to more complex case studies. The trajectories have been modelled in the three-body dynamics, considering the Earth and the Sun as gravitational bodies; both the escape leg, starting from an Earth-centred parking orbit, and the heliocentric leg to the asteroid interception have been optimised, without making use of the patched conic approach. In particular, the results presented for a rendezvous mission to asteroid Apophis, starting from an elliptical orbit around the Earth, shows how the

DDP-based approach is able to schedule an Earth fly-by, not included in the first guess solution, in order to optimise the escape trajectory.

To summarise, the aim of this dissertation is to provide a significant progress in the design of trajectories for interception and deflection missions to Near Earth Objects. The main findings are represented by theoretical developments validated through a large set of numerical results:

- A semi-analytical formulation for modelling the asteroid deviation problem has been provided, underpinned by general validity (for both impulsive and low-thrust deviation) and high accuracy.
- An approach to the design of NEO mitigation missions has been performed; the two fundamental phases of the mission (i.e., interception and deflection phase) have been combined and a multi-criteria optimisation approach allowed computing thousands of launch options. The analysis is therefore more general and extended to several different case scenarios.
- A method based on Differential Dynamic Programming has been proposed and developed for the local refinement of low-thrust transfer trajectories, with particular emphasis on the high fidelity of the trajectory (important for *n*-body dynamics application) and the robustness of the technique.
- A wide variety of mission options has been presented and analysed for mitigation mission to a number of asteroids and adopting different deflection strategies.
- A preliminary multi-criteria comparison among the deflection strategies proposed in the literature has been performed, and an approach for the analytic comparison of the efficiency of different options, according to several criteria, has been suggested.
- Some refined low-thrust trajectories are shown, which include the escape transfer leg from the Earth.

6.2. Limitations

The formulation proposed for the solution of the asteroid deflection problem has been shown to have general applicability for several deviation strategies and

the approach presented can be applied to compute the achievable deflection of any objects within the NEO class (i.e., both near Earth asteroids and comets). However, it has to be noted that in Chapter 2 and Chapter 3 the proximal motions equations and Gauss' equations have been written in their Keplerian-elements form that limits the application to eccentricities $0 < e < 1$.

The asteroid displacement following a deflection manoeuvre has been computed using the two-body problem assumption and the *b*-plane representation has been adopted to compute the effective deviation considering Earth's motion; moreover, as shown in Section 2.1.3, the strategies that aims at maximising b^* are more accurate than the ones aiming at the maximisation of $\delta\mathbf{r}$. The *b*-plane model is valid provided that the manoeuvre is imparted before entering the Earth's sphere of influence. Otherwise, a more accurate model, hinging on the three-body dynamics, should be used to get a more precise estimation of the deviation.

The prediction of the orbit deviation by a low-thrust action requires, in general, the numerical integration of Gauss' equations. In this thesis we derived a semi-analytical solution in the case of tangential acceleration, inversely proportional to the square of the distance from the Sun; the proposed solution can model the effects of a deviation scheme based on a solar electric propulsion spacecraft, or a solar collector. Other strategies, such as attached nuclear electric propulsion or gravity tug, are characterised by different thrust laws; hence, further mathematical developments are needed to obtain a semi-analytical formulation for these cases too.

The results presented in this dissertation show how the transfer trajectory strongly influences the outcome of the overall mitigation mission to a selected asteroid, because the total mass and warning time requirements are highly influenced by the orbital elements of the asteroid to be intercepted. This suggests that more complex sequences of gravity assist-manoeuvres may improve the design of the transfer leg. Moreover, a better estimate of the propellant mass for the transfer phase can be obtained considering the constraint on the maximum thrust level. This additional constraint should be taken into account in the global search of Pareto-optimal solutions and also in the refinement of the low-thrust trajectory, by solving a constrained optimal control problem.

6.3. Remarks for future work

The formulation of the asteroid deviation problem can be easily extended to the most general representation of either circular, elliptical, hyperbolic, and parabolic orbits, by using the non-singular equinoctial elements [71]. Besides avoiding singularities for zero eccentricity and inclination, this would allow broadening the study to Near Earth Comets.

Further studies are required for the precise determination of the optimal direction of a low-thrust deflection manoeuvre (in this thesis the simplifying hypothesis of tangential thrust has been used). A numerical estimation of the optimal thrusting angle has been provided by Song et al. [75], but a semi-analytical solution could be found by superimposing the effects of the thrust components along the principal directions.

The latitude and time formulation developed in Chapter 3 for low-thrust asteroid deflection can have a significantly broader application for the fast generation of first guess solutions for low-thrust trajectories. We are currently studying an approach for the global search of low-thrust trajectories including the escape phase from the Earth. In particular, the whole transfer trajectory is divided into three legs:

- The first leg (i.e., spiralling-out leg) is modelled in the two-body problem, considering the Earth as the only gravitational body. The escape spiral is computed through the semi-analytical technique presented in Chapter 3.
- The second part of the trajectory describes the escape segment. For this leg the third-body effect can not be neglected; thus, the trajectory is numerically integrated, under the assumption of tangential thrust with constant magnitude, until the spacecraft escapes from the Earth.
- The third leg represents the heliocentric phase to reach the target body. The two-body approximation is adopted in this case and the transfer design makes use of a shape-based method, with exponential shape of the pseudo-equinoctial elements [118].

The semi-analytical technique used for the generation of the first leg ensures a saving in computational time with respect to the full numerical integration;

hence it allows the extensive search of solutions over extended domains. The accuracy of the whole model has been verified, comparing it to the full propagation of the trajectory in the three body problem. Figure 6.1 shows a comparison between the solution provided by the approximated model (blue line) and the numerical integration of the transfer in the three-body problem (red line). Figure 6.1a represents the whole trajectory in the Earth centred reference plane and Figure 6.1b contains a close up of the escape phase.

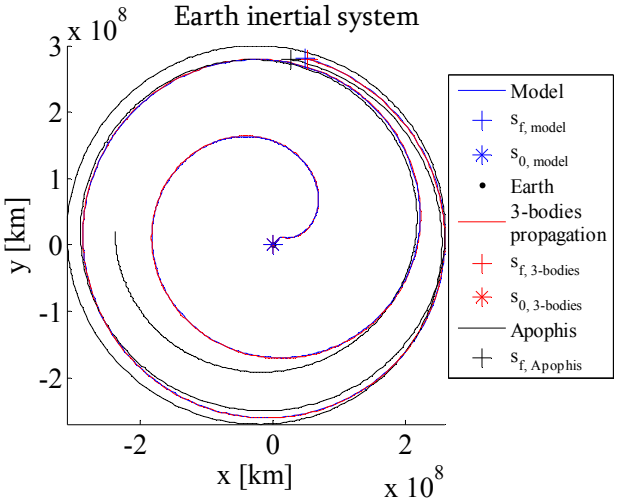

a)

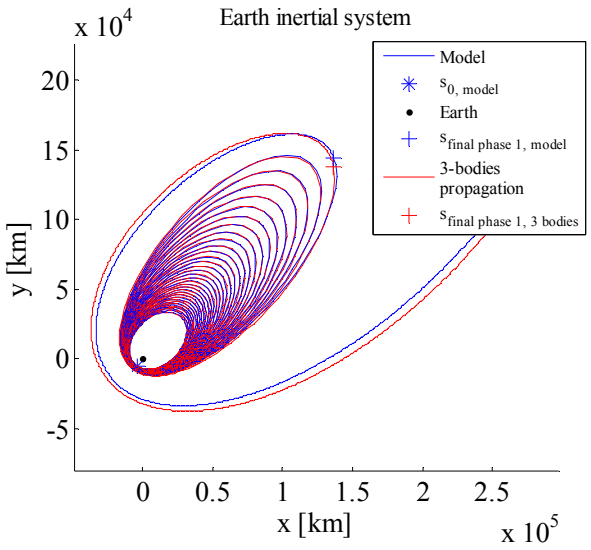

b)

Figure 6.1: Comparison between the approximated low-thrust model and the numerical integration in the three-body problem (Earth inertial system): a) transfer to Apophis, and b) Earth escape phase.

The method used in Chapter 4 for the preliminary comparison among different deviation strategies could be used to include other mitigation options in

the analysis. For a second phase of the mitigation mission definition, more complex models could be used for the trajectory design and the strategy actions. Moreover, the results of the comparison can be improved by computing a greater number of solutions for each Pareto front.

Finally, the DDP-based method presented in Chapter 5 achieved, in the author's opinion, promising results. For this reason, an improved version of the algorithm is under development to solve bang-bang control problems (maximisation of the final mass of the spacecraft), and also optimise static parameters, such as the time of flight and the initial conditions.

References

[1] NASA homepage: http://ssd.jpl.nasa.gov/?body_count [Retrieved: 27 February 2009].

[2] Committee on Planetary and Lunar Exploration, "The Exploration of Near Earth Objects", National Academy Press, Washington, D.C., 1998, available at http://www.nap.edu/catalog.php?record_id=6106 [Retrieved: 28 April 2009].

[3] Seboldt W., Reichert M., Hanowski N. and Novara M., "A Review of the Long-Term Options for Space Exploration and Utilisation", *ESA Bulletin*, Vol. 101, Feb. 2000.

[4] Chapman C. R. and Morrison D., "Impacts on the Earth by Asteroids and Comets: Assessing the Hazard", *Nature*, Vol. 367, No. 6458, Jan. 1994, pp. 33–40, doi: 10.1038/367033a0.

[5] NASA Near Earth Object Program homepage: http://neo.jpl.nasa.gov/neo/ [Retrieved: 24 May 2009].

[6] "Near-Earth Object Survey and Deflection Analysis of Alternatives, Report to Congress", NASA, March 2007, available at http://neo.jpl.nasa.gov/neo/report2007.html [Retrieved: 23 February 2009].

[7] "Protecting the Earth from Asteroids and Comets", AIAA Position Paper, Oct. 2004, available at http://www.planetarydefense.info/resources/pdf/Asteroids-Final.pdf [Retrieved: 23 February 2009].

[8] "Summary and Recommendations from the 2007 Planetary Defense Conference", held on 5–8 March 2007 in Washington, D.C., 25 April 2007, http://www.aero.org/conferences/planetarydefense/2007papers/WhitePaperFinal.pdf [Retrieved: 28 April 2009].

[9] "Report of the Task Force on Potentially Hazardous Near Earth Objects", British National Space Centre, Sept. 2000, available at http://www.spacecentre.co.uk/neo/report.html [Retrieved: 28 April 2009].

[10] Morrison D. (editor), "The Spaceguard Survey: Report of the NASA International Near-Earth-Object Detection Workshop", NASA Jet Propulsion Laboratory, Washington, D.C., 1992.

[11] Stokes G. H. and Yeomans D. K., "Study to Determine the Feasibility of Extending the Search for Near-Earth Objects to Smaller Limiting Diameters", NASA Report of the Near-Earth Object Science Definition Team, Aug. 2003.

[12] Sentry risk table homepage: http://neo.jpl.nasa.gov/risk/ [Retrieved: 24 May 2009].

[13] NEODyS homepage: http://newton.dm.unipi.it/neodys/index.php?pc=0 [Retrieved: 28 April 2009].

[14] Binzel R. P., "The Torino Impact Hazard Scale", *Planetary and Space Science*, Vol. 48, No. 4, April 2000, pp. 297–303, doi: 10.1016/S0032-0633(00)00006-4.

[15] Chesley S. R., Chodas P. W., Milani A., Valsecchi G. B. and Yeomans D. K., "Quantifying the Risk Posed by Potential Earth Impacts", *Icarus*, Vol. 159, No. 2, Oct. 2002, pp. 423–432, doi: 10.1006/icar.2002.6910.

[16] Shoemaker E. M., "Asteroid and Comet Bombardment of the Earth", *Annual Review of Earth and Planetary Sciences*, Vol. 11, 1983, pp. 461–494, doi: 10.1146/annurev.ea.11.050183.002333.

[17] Earth Impact Database homepage, 2009: http://www.unb.ca/passc/ImpactDatabase/ [Retrieved: 11 February 2009].

[18] Alvarez L. W., Alvarez W., Asaro F. and Michel H. V., "Extraterrestrial Cause for the Cretaceous-Tertiary Extinction", *Science*, Vol. 208, No. 4448, June 1980, pp. 1095–1108, doi: 10.1126/science.208.4448.1095.

[19] Swisher C. C. III, Grajales-Nishimura J. M., Montanari A., Margolis S. V., Claeys P., Alvarez W., Renne P., Cedillo-Pardoa E., Maurrasse F. J.-M. R., Curtis G. H., Smit J. and McWilliams M. O., "Coeval $^{40}Ar/^{39}Ar$ Ages of 65.0 Million Years Ago from Chicxulub Crater Melt Rock and Cretaceous-Tertiary Boundary Tektites", *Science*, Vol. 257, No. 5072, Aug. 1992, pp. 954–958, doi: 10.1126/science.257.5072.954.

[20] Sharpton V. L., Burke K., Camargo-Zanoguera A., Hall S. A., Lee D. S., Marin L. E., Suaarez-Reynoso G., Quezada-Muneton J. M., Spudis P. D.

and Urrutia-Fucugauchi J., “Chicxulub Multiring Impact Basin: Size and Other Characteristics Derived from Gravity Analysis”, *Science*, Vol. 261, No. 5128, Sept. 1993, pp. 1564–1567, doi: 10.1126/science.261.5128.1564.

[21] Rabinowitz D., Helin E., Lawrence K. and Pravdo S., “A Reduced Estimate of the Number of Kilometre-sized Near-Earth Asteroids”, *Nature*, Vol. 403, No. 6766, Jan. 2000, pp. 165–166, doi: 10.1038/35003128.

[22] Chyba C. F., Thomas P. J. and Zahnle K. J., “The 1908 Tunguska Explosion: Atmospheric Disruption of a Stony Asteroid”, *Nature*, Vol. 361, No. 6407, Jan. 1993, pp. 40–44, doi: 10.1038/361040a0.

[23] Tunguska homepage, University of Bologna, http://www-th.bo.infn.it/tunguska/ [Retrieved: 17 February 2009].

[24] Halley E., *A Synopsis of the Astronomy of Comets* (*Astronomiæ Cometicæ Synopsis*), London, printed for John Senex, 1705.

[25] Comet Shoemaker-Levy 9 Collision with Jupiter, NASA Goddard Space Flight Center, http://nssdc.gsfc.nasa.gov/planetary/comet.html [Retrieved: 17 February 2009].

[26] Giorgini J. D., Benner L. A. M., Ostro S. J., Nolan M. C. and Busch M. W., “Predicting the Earth encounters of (99942) Apophis”, *Icarus*, Vol. 193, No. 1, Jan. 2008, pp. 1–19, doi: 10.1016/j.icarus.2007.09.012.

[27] Giotto mission (ESA) homepage, 2006: http://www.esa.int/science/giotto [Retrieved: 23 February 2009].

[28] Deep Impact mission (NASA) homepage: http://deepimpact.jpl.nasa.gov/ [Retrieved: 23 February 2009].

[29] NEAR-Shoemaker mission (NASA) homepage: http://near.jhuapl.edu [Retrieved: 23 February 2009].

[30] Deep Space 1 mission (NASA) homepage: http://nmp.jpl.nasa.gov/ds1/ [Retrieved: 23 February 2009].

[31] Rayman M. D., Varghese P., Lehman D. H. and Livesay L. L., “Results from the Deep Space 1 Technology Validation Mission”, *Acta Astronautica*, Vol. 47, No. 2–9, July–Nov. 2000, pp. 475–487, doi: 10.1016/S0094-5765(00)00087-4.

[32] Galileo mission (NASA) homepage: http://www2.jpl.nasa.gov/galileo/ [Retrieved: 23 February 2009].

[33] Stardust mission (NASA) homepage: http://stardust.jpl.nasa.gov/top.html [Retrieved: 23 February 2009].

[34] Rosetta mission (ESA) homepage: http://www.esa.int/SPECIALS/Rosetta/ [Retrieved: 23 February 2009].

[35] Hayabusa mission (JAXA) homepage: http://www.muses-c.isas.ac.jp/ [Retrieved: 23 February 2009].

[36] Dawn mission (NASA) homepage: http://dawn.jpl.nasa.gov/, http://www-ssc.igpp.ucla.edu/dawn/ [Retrieved: 23 February 2009].

[37] Don Quijote mission (ESA) homepage: http://www.esa.int/gsp/completed/neo/donquijote.html [Retrieved: 23 February 2009].

[38] "A reference mission for diminishing the threat from near-Earth objects", CDF Study Report NEO2, CDF-39(A), ESA/ESTEC, Aug. 2005.

[39] Gritzner C., Häntschel G. and Fasoulas S., "NEO-MIPA, Near-Earth Object Hazard Mitigation Publication Analysis", Final Report, EUROSPACE, 19 Jan. 2001.

[40] Carusi A., Valsecchi G. B., D'Abramo G. and Boattini A., "Deflecting NEOs in Route of Collision with the Earth", *Icarus*, Vol. 159, No. 2, 2002, pp. 417–422, doi: 10.1006/icar.2002.6906.

[41] McInnes C. R., "Deflection of Near-Earth Asteroids by Kinetic Energy Impacts from Retrograde Orbits", *Planetary and Space Science*, Vol. 52, No. 7, 2004, pp. 587–590, doi: 10.1016/j.pss.2003.12.010.

[42] Dachwald B. and Wie B., "Solar Sail Kinetic Energy Impactor Trajectory Optimization for an Asteroid-Deflection Mission", *Journal of Spacecraft and Rockets*, Vol. 44, No. 4, July–Aug. 2007, pp. 755–764, doi: 10.2514/1.22586.

[43] Izzo D., Bourdoux A., Walker R. and Ongaro F., "Optimal trajectories for the impulsive deflection of near earth objects", *Acta Astronautica*, Vol. 59, No. 1–5, July 2006, pp. 294–300, doi: 10.1016/j.actaastro.2006.02.002.

[44] "Project Icarus", M.I.T. Report No. 13, The M.I.T. Press, Cambridge, MA, 1968.

[45] Smith P. L., Barrera M. J., Campbell E. T., Feldman K. A., Peterson G. E. and Smit G. N., "Deflecting a Near Earth Object with Today's Space

Technology", AIAA Planetary Defense Conference, Orange County, CA, AIAA Paper 2004-1447, Feb. 2004.

[46] Treaty on Principles Governing the Activities of States in the Exploration and Use of Outer Space, including the Moon and Other Celestial Bodies: http://www.unoosa.org/oosa/SpaceLaw/outerspt.html [Retrieved: 22 June 2009].

[47] Sagan C. and Ostro S. J., "Dangers of asteroid deflection", *Nature*, Vol. 368, No. 6471, April 1994, pp. 501–501, doi: 10.1038/368501a0.

[48] Tedeschi W. J., Remo J. L., Schulze J. F. and Young R. P., "Experimental Hypervelocity Impact Effects on Simulated Planetesimal Materials", *International Journal of Impact Engineering*, Vol. 17, No. 4–6, 1995, pp. 837–848, doi: 10.1016/0734-743X(95)99904-6.

[49] Solem J. C., "Interception of Comets and Asteroids on Collision Course with Earth", *Journal of Spacecraft and Rockets*, Vol. 30, No. 2, 1993, pp. 222–228.

[50] Housen K. R. and Holsapple K. A., "Impact cratering on porous asteroids", *Icarus*, Vol. 163, No. 1, May 2003, pp. 102–119, doi: 10.1016/S0019-1035(03)00024-1.

[51] Sanchez J. P., Vasile M. and Radice G., "Consequences of Asteroid Fragmentation during Impact Hazard Mitigation", *Journal of Guidance, Control and Dynamics*, Vol. 33, No. 1, Jan.–Feb. 2010, pp.126–143, doi: 10.2514/1.43868.

[52] Olds J., Charania A. and Schaffer M. G., "Multiple Mass Drivers as an Option for Asteroid Deflection Missions," 2007 Planetary Defense Conference, Washington, D.C., Paper 2007 S3-7, March 2007.

[53] Ivashkin V. V. and Smirnov V. V., "An analysis of some methods of asteroid hazard mitigation for the Earth", *Planetary and Space Science*, Vol. 43, No. 6, June 1995, pp. 821–825, doi: 10.1016/0032-0633(94)00225-G.

[54] Lu E. T. and Love S. G., "Gravitational Tractor for Towing Asteroids", *Nature*, Vol. 438, No. 7065, Nov. 2005, pp. 177–178, doi: 10.1038/438177a.

[55] Melosh H. J. and Nemchinov I. V., "Solar asteroid diversion", *Nature*, Vol. 366, No. 6450, Nov. 1993, pp. 21–22, doi: 10.1038/366021a0.

[56] Melosh, H. J., Nemchinov, I. V. and Zetzer, Y. I., "Non-Nuclear Strategies for Deflecting Comets and Asteroids". In: *Hazards due to Comets and Asteroids*, edited by Gehrels T., University of Arizona Press, Arizona, Tucson, 1994, pp. 1111–1132.

[57] Maddock C., Sanchez J. P., Vasile M. and Radice G., "Comparison of Single and Multi-Spacecraft Configurations for NEA Deflection by Solar Sublimation", *American Institute of Physics*, Conference Proceedings of New Trends in Astrodynamics and Applications III, 16–18 Aug. 2006, Princeton, New Jersey, Vol. 886, 2007, pp. 303–316, doi: 10.1063/1.2710064.

[58] Vasile M., "A multi-mirror solution for the deflection of dangerous NEOs", *Communications in Nonlinear Science and Numerical Simulation*, Vol. 14, No. 12, Dec. 2009, pp. 4139-4152, doi: 10.1016/j.cnsns.2008.09.005.

[59] Ivashkin V. V., "Possibility of Using Laser Action on a Celestial Body Approaching the Earth", *Physics - Doklady*, Vol. 49, No. 8, Aug. 2004, pp. 476–479, doi: 10.1134/1.1795961.

[60] "Space Laser for the Earth Defence from Asteroid-Comets Hazard", Russian Funds, 2004, available at http://www.rufund.org/Docs/laser/Doclad_laser_ENG.pdf [Retrieved: 28 April 2009].

[61] Spitale J. N., "Asteroid Hazard Mitigation using the Yarkovsky Effect", *Science*, Vol. 296, No. 5565, April 2002, p. 77, doi: 10.1126/science.1069577.

[62] Canavan G. H., Solem J. C. and Rather J. D. G., "Near-Earth Object Interception Workshop". In: *Hazards due to Comets and Asteroids*, edited by Gehrels T., University of Arizona Press, Arizona, Tucson, 1994, pp. 93–124.

[63] Hall C. D. and Ross I. M., "Dynamics and Control Problems in the Deflection of Near-Earth Objects", *Advances in the Astronautical Sciences*, Conference Proceedings of AAS/AIAA Astrodynamics 1997, 4–7 Aug. 1997, Sun Valley, Idaho, Vol. 97, 1997, Paper AAS 97-640, pp. 613–631.

[64] Adams R. B., Alexander R., Bonometti J., Chapman J., Fincher S., Hopkins R., Kalkstein M. and Polsgrove T., "Survey of Technologies Relevant to Defense From Near Earth Objects", NASA, NASA/TP-2004-213089, July

2004, available at http://www.nss.org/resources/library/planetarydefense/2004-SurveyOfTechnologiesRelevantToDefenseFromNEOs-NASA.pdf [Retrieved: 20 April 2009].

[65] Rogers G. and Izenberg N., ”Comparison of the Efficiency of Various Asteroid Hazard Mitigation Techniques”, White Paper, NASA NEO Workshop, Vail, Colorado, 26–28 June 2006.

[66] Kahle R., Hahn G. and Kührt E., “Optimal Deflection of NEOs en Route of Collision with the Earth”, *Icarus*, Vol. 182, No. 2, 2006, pp. 482–488, doi: 10.1016/j.icarus.2006.01.005.

[67] Ahrens T. J. and Harris A. W., “Deflection and Fragmentation of Near-Earth Asteroids”, *Nature*, Vol. 360, No. 6403, Dec. 1992, pp. 429–433, doi: 10.1038/360429a0.

[68] Scheeres D. J. and Schweickart R. L., “The Mechanics of Moving Asteroids”, 2004 Planetary Conference: Protecting Earth from Asteroids, Orange County, California, AIAA Paper 2004-1446, Feb. 2004.

[69] Izzo D., “Optimization of Interplanetary Trajectories for Impulsive and Continuous Asteroid Deflection”, *Journal of Guidance, Control, and Dynamics*, Vol. 30, No. 2, March–April 2007, pp. 401–408, doi: 10.2514/1.21685.

[70] Conway B. A., “Near-Optimal Deflection of Earth-Approaching Asteroids”, *Journal of Guidance, Control, and Dynamics*, Vol. 24, No. 5, 2001, pp. 1035–1037, doi: 10.2514/2.4814.

[71] Battin R. H., *An Introduction to the Mathematics and Methods of Astrodynamics*, AIAA Education Series, AIAA, Reston, VA, 1999.

[72] Park S.-Y. and Ross I. M., “Two-Body Optimization for Deflecting Earth-Crossing Asteroids”, *Journal of Guidance, Control, and Dynamics*, Vol. 22, No. 3, May–June 1999, pp. 415–420.

[73] Ross I. M., Park S.-Y. and Porter S. D. V., “Gravitational Effects of Earth in Optimizing Δv for Deflecting Earth-Crossing Asteroids”, *Journal of Spacecraft and Rockets*, Vol. 38, No. 5, Sept.–Oct. 2001, pp. 759–764, doi: 10.2514/2.3743.

[74] Park S.-Y. and Mazanek D. D., "Mission Functionality for Deflecting Earth-Crossing Asteroids/Comets", *Journal of Guidance, Control, and Dynamics*, Vol. 26, No. 5, Sep.–Oct. 2003, pp. 734–742, doi: 10.2514/2.5128.

[75] Song Y.-J., Park S.-Y. and Choi K.-H., "Optimal Deflection of Earth-Crossing Objects Using a Power Limited Spacecraft", 17th AAS/AIAA Space Flight Mechanics Meeting, Sedona, AZ, American Astronautical Society Paper 07-147, 2007.

[76] Lawden D., "Rocket Trajectory Optimization: 1950–1963", *Journal of Guidance, Control, and Dynamics*, Vol. 14, No. 4, Jul.–Aug. 1991, pp. 705–711, doi: 10.2514/3.20703.

[77] Tsien H. S., "Take-Off from Satellite Orbit", *Journal of the American Rocket Society*, Vol. 23, No. 4, Jul.–Aug. 1953, pp. 233–236.

[78] Benney D. J., "Escape from a Circular Orbit Using Tangential Thrust", *Jet Propulsion*, Vol. 28, No. 3, March 1958, pp. 167–169.

[79] Boltz F., "Orbital Motion Under Continuous Radial Thrust", *Journal of Guidance, Control, and Dynamics*, Vol. 14, No. 3, May–June 1991, pp. 667–670, doi: 10.2514/3.20690.

[80] Boltz F., "Orbital Motion Under Continuous Tangential Thrust", *Journal of Guidance, Control, and Dynamics*, Vol. 15, No. 6, Nov.–Dec. 1992, pp. 1503–1507, doi: 10.2514/3.56583.

[81] Kechichian J. A., " Orbit Raising with Low-Thrust Tangential Acceleration in Presence of Earth Shadow", *Journal of Spacecraft and Rockets*, Vol. 35, No. 4, July–Aug. 1998, pp. 516–525, doi: 10.2514/2.3361.

[82] Gao Y. and Kluever C. A., "Analytic Orbital Averaging Technique for Computing Tangential-Thrust Trajectories", *Journal of Guidance, Control, and Dynamics,* Vol. 28, No. 6, Nov.–Dec. 2005, pp. 1320–1323, doi: 10.2514/1.14698.

[83] Petropoulos A. E., "Some Analytic Integrals of the Averaged Variational Equations for a Thrusting Spacecraft", *The Interplanetary Network Progress Report*, Jet Propulsion Laboratory, California Inst. Of Technology, Rept. 42-150, Pasadena, CA, 2002, pp. 1–29.

[84] Racca G. D., "New Challenges to Trajectory Design by the Use of Electric Propulsion and Other New Means of Wandering in the Solar System",

Celestial Mechanics and Dynamical Astronomy, Vol. 85, No. 1, 2003, pp. 1–24, doi: 10.1023/A:1021787311087.

[85] Betts J. T., "Survey of Numerical Methods for Trajectory Optimization", *Journal of Guidance, Control, and Dynamics*, Vol. 21, No. 2, March–April 1998, pp. 193–207, doi: 10.2514/2.4231.

[86] Von Stryk O. and Bulirsch R., "Direct and Indirect Methods for Trajectory Optimization", *Annals of Operations Research*, Vol. 37, No. 1, Dec. 1992, pp. 357–373, doi: 10.1007/BF02071065.

[87] Conway B., Chilan C. and Wall B., "Evolutionary principles applied to mission planning problems", *Celestial Mechanics and Dynamical Astronomy*, Vol. 97, No. 2, 2007, pp. 73–86, doi: 10.1007/s10569-006-9052-7.

[88] Betts J. T. and Erb S. O., "Optimal Low Thrust Trajectories to the Moon", *SIAM Journal on Applied Dynamical Systems*, Vol. 2, No. 2, 2003, pp. 144–170.

[89] Enright P. J. and Conway B. A., "Optimal finite-thrust spacecraft trajectories using collocation and nonlinear programming", *Journal of Guidance, Control, and Dynamics*, Vol. 14, No. 5, Sept.–Oct. 1991, pp. 981–985, doi: 10.2514/3.20739.

[90] Scheel W. A. and Conway B. A., "Optimization of Very-Low-Thrust, Many-Revolution Spacecraft Trajectories", *Journal of Guidance, Control, and Dynamics*, Vol. 17, No. 6, Nov.–Dec. 1994, pp. 1185–1192, doi: 10.2514/3.21331.

[91] Kluever C. A., "Optimal Low-Thrust Interplanetary Trajectories by Direct Method Techniques", *Journal of the Astronautical Sciences*, Vol. 45, No. 3, Jul.–Sep. 1997, pp. 247–262.

[92] Pontryagin L. S., Boltyanskii V. G., Gamkrelidze R. V. and Mishenko E. F., *The Mathematical Theory of Optimal Processes*, Wiley (Interscience), New York, 1962.

[93] Ranieri C. L. and Ocampo C. A., "Indirect Optimization of Spiral Trajectories", *Journal of Guidance, Control, and Dynamics*, Vol. 29, No. 6, Nov.–Dec. 2006, pp. 1360–1366, doi: 10.2514/1.19539.

[94] Colasurdo G. and Casalino L., "Trajectories towards Near-Earth-Objects Using Solar Electric Propulsion", *Advances in the Astronautical Sciences*, Vol. 103, 1999, (AAS 99-339), pp. 593–608.

[95] Casalino L., Colasurdo G. and Pastrone D., "Optimal Low-Thrust Escape Trajectories Using Gravity Assist", *Journal of Guidance, Control, and Dynamics*, Vol. 22, No. 5, Sep.–Oct. 1999, pp. 637–642.

[96] Tang S. and Conway B. A., "Optimization of Low-Thrust Interplanetary Trajectories Using Collocation and Nonlinear Programming", *Journal of Guidance, Control, and Dynamics*, Vol. 18, No. 3, May–Jun. 1995, pp. 599–604, doi: 10.2514/3.21429.

[97] Herman A. L. and Spencer D. B., "Optimal, Low-Thrust Earth-Orbit Transfers Using Higher-Order Collocation Methods", *Journal of Guidance, Control, and Dynamics*, Vol. 25, No. 1, Jan.–Feb. 2002, pp. 40–47, doi: 10.2514/2.4873.

[98] Vasile M. and Bernelli-Zazzera F., "Targeting a Heliocentric Orbit Combining Low-Thrust Propulsion and Gravity Assist Manoeuvres", Operational Research in Space & Air, Vol. 79, ISBN 1-4020-1218-7, Book Series in Applied Optimization, Kluwer Academic Press, 2003.

[99] Vasile M. and Bernelli-Zazzera F., "Optimizing Low-Thrust and Gravity Assist Maneuvres to Design Interplanetary Trajectories", *The Journal of the Astronautical Sciences*, Vol. 51, No. 1, Jan.–March 2003, pp. 13–35.

[100] Guelman M., "Earth-to-Moon Transfer with a Limited Power Engine", *Journal of Guidance, Control, and Dynamics*, Vol. 18, No. 5, Sept.–Oct. 1995, pp.1113–1138.

[101] Vadali S. R., Nah R. S., Braden E. and Johnson Jr. I. L., "Fuel-Optimal Planar Earth–Mars Trajectories Using Low-Thrust Exhaust-Modulated Propulsion", *Journal of Guidance, Control, and Dynamics*, Vol. 23, No. 3, May–June 2000, pp. 476–482, doi: 10.2514/2.4553.

[102] Nah R. S., Vadali S. R. and Braden E., "Fuel-Optimal, Low-Thrust, Three-Dimensional Earth–Mars Trajectories", *Journal of Guidance, Control, and Dynamics*, Vol. 24, No. 6, Nov.–Dec. 2001, pp. 1100–1107, doi: 10.2514/2.4844.

[103] Ranieri C. L. and Ocampo C. A., "Optimization of Roundtrip, Time-Constrained, Finite Burn Trajectories via an Indirect Method", *Journal of Guidance, Control, and Dynamics*, Vol. 28, No. 2, March–April 2005, pp. 306–314, doi: 10.2514/1.5540.

[104] Pierson B. L. and Kluever C. A., "Three-Stage Approach to Optimal Low-Thrust Earth-Moon Trajectories", *Journal of Guidance, Control, and Dynamics*, Vol. 17, No. 6, Nov.–Dec. 1994, pp. 1275–1282, doi: 10.2514/3.21344.

[105] Kluever C. A. and Pierson B. L., "Optimal Low-Thrust Three-Dimensional Earth-Moon Trajectories", *Journal of Guidance, Control, and Dynamics*, Vol. 18, No. 4, July–Aug. 1995, pp. 830–837, doi: 10.2514/3.21466.

[106] Whiffen G. J., "Static/Dynamic Control for Optimizing a Useful Objective", United States Patent No. 6496741, Dec. 2002.

[107] Whiffen G. J. and Sims J. A., "Application of a Novel Optimal Control Algorithm to Low-Thrust Trajectory Optimization", AAS/AIAA Space Flight Mechanics Meeting, Santa Barbara, California, 11–15 Feb. 2001, Paper AAS 01-209.

[108] Whiffen G. J. and Sims J. A., "Application of the SDC Optimal Control Algorithm To Low-Thrust Escape and Capture Including Fourth-Body Effects", 2nd International Symposium on Low-Thrust Trajectories, Toulouse, France, 18–20 June 2002.

[109] Lantoine G. and Russel R. P., "A Hybrid Differential Dynamic Programming Algorithm for Low-Thrust Optimization", AIAA/AAS Astrodynamics Specialist Conference and Exhibit, 18–21 Aug. 2008, Honoululu, Hawaii, AIAA-2008-6615.

[110] Olympio J. T., "Algorithm for Low-Thrust Optimal Interplanetary Transfers with Escape and Capture Phases", AAS/AIAA Astrodynamics Specialist Conference and Exhibit, 18–21 Aug. 2008, Honoululu, Hawaii, AIAA-2008-7363.

[111] Jacobson D. H. and Mayne D. Q., *Differential Dynamic Programming*, American Elsevier, New York, 1969.

[112] Bellman R., *Dynamic Programming*, Princeton University Press, Princeton, New Jersey, 1957.

[113] Yakowitz S. and Rutherford B., "Computational Aspects of Discrete-Time Optimal Control", *Applied Mathematics and Computation*, Vol. 15, 1984, pp. 29–45.

[114] Bertsekas D. P., *Dynamic Programming and Optimal Control*, 3rd Edition, Athena Scientific, Belmont, 2005–2007.

[115] Schaub H. and Junkins J. L., *Analytical Mechanics of Space Systems*, AIAA Education Series, AIAA, 2003, pp. 592–623.

[116] Vasile M., "A Behavioral-Based Meta-Heuristic for Robust Global Trajectory Optimization", IEEE Congress on Evolutionary Computation (CEC 2007), Inst. of Electrical and Electronics Engineers, Piscataway, NJ, 25–28 Sept. 2007, pp. 2056–2063.

[117] Vasile M. and Locatelli M., "A Hybrid Multiagent Approach for Global Trajectory Optimization", *Journal of Global Optimization*, Vol. 44, No. 4, Aug. 2009, pp. 461–479, doi: 10.1007/s10898-008-9329-3.

[118] De Pascale P. and Vasile M., "Preliminary Design of Low-Thrust Multiple Gravity-Assist Trajectories", *Journal of Spacecraft and Rockets*, Vol. 43, No. 5, Sept.–Oct. 2006, pp. 1065–1076, doi: 10.2514/1.19646.

[119] Vasile M. and De Pascale P., "Preliminary Design of Multiple Gravity-Assist Trajectories", *Journal Of Spacecraft and Rockets*, Vol. 43, No. 4, July–Aug. 2006, pp. 794–805, doi: 10.2514/1.17413.

[120] Gershwin S. B. and Jacobson D. H., "A Discrete-Time Differential Dynamic Programming with Application to Optimal Orbit Transfer", *AIAA Journal*, Vol. 8, No. 9, Sept. 1970, pp. 1616–1626.

[121] Vasile M. and Colombo C., "Optimal Impact Strategies for Asteroid Deflection", *Journal of Guidance, Control and Dynamics*, Vol. 31, No. 4, July–Aug. 2008, pp. 858–872, doi: 10.2514/1.33432.

[122] Colombo C. and Vasile M., "Optimal Trajectories for NEO Deflection", 58th International Astronautical Congress, Hyderabad, India, 24–28 Sept. 2007, IAC-07-C1.4.02.

[123] Colombo C., Vasile M. and Radice G., "Semi-Analytical Solution for the Optimal Low-Thrust Deflection of Near Earth Objects", *Journal of Guidance, Control and Dynamics*, Vol. 32, No. 3, May–June 2009, pp. 796–809, doi: 10.2514/1.40363.

[124] Sanchez J. P., Colombo C., Vasile M. and Radice G., "A Multi-criteria Assessment of Deflection Methods for Dangerous NEOs", *American Institute of Physics*, Conference Proceedings of New Trends in Astrodynamics and Applications III, 16–18 Aug. 2006, Princeton, New Jersey, Vol. 886, 2007, pp. 317–333, doi: 10.1063/1.2710065.

[125] Colombo C., Sanchez J. P., Vasile M. and Radice G., "A Comparative Assessment of Different Deviation Strategies for Dangerous NEO", 57th International Astronautical Congress, Valencia, 2–6 Oct., Spain, 2006, IAC-06-A3.5.8.

[126] Sanchez J. P., Colombo C., Vasile M. and Radice G., "Multi-Criteria Comparison among Several Mitigation Strategies for Dangerous Near Earth Objects", *Journal of Guidance, Control and Dynamics*, Vol. 32, No. 1, Jan.–Feb. 2009, pp. 121–142, doi: 10.2514/1.36774.

[127] Colombo C., Vasile M. and Radice G., "Optimal Low-thrust Trajectories to Asteroids through an Algorithm based on Differential Dynamic Programming", *Celestial Mechanics and Dynamical Astronomy*, Vol. 105, Nos. 1–3, Nov. 2009, pp. 75–112, doi: 10.1007/s10569-009-9224-3.

[128] Colombo C., Vasile M. and Radice G., "Interception and Deviation of Near Earth Objects via Solar Collector Strategy", 59th International Astronautical Congress, Glasgow, United Kingdom, 29 Sept.–3 Oct. 2008, IAC-08-A3.I.06.

[129] Gronchi G. F. and Michel P., "Secular Orbital Evolution, Proper Elements, and Proper Frequencies for Near-Earth Asteroids: A Comparison between Semianalytic Theory and Numerical Integrations", *Icarus*, Vol. 152, No. 1, 2001, pp. 48–57, doi: 10.1006/icar.2001.6609.

[130] Öpik E. J., *Interplanetary Encounters*, Elsevier, New York, 1976.

[131] Bourdoux A., Izzo D., "Characterization and hazard mitigation of resonant returning Near Earth Objects", Final Stage Report, ACT internal report: ACT-RPT-4100-AB-CHMRRNEO05.

[132] Valsecchi G. B., Milani A., Gronchi G. F. and Chesley S. R., "Resonant Returns to Close Approaches: Analytical Theory", *Astronomy and Astrophysics*, Vol. 408, No. 3, 2003, pp. 1179–1196, doi: 10.1051/0004-6361:20031039.

[133] Vasile M., "Robust Mission Design Through Evidence Theory and Multi-Agent Collaborative Search", *Annals of the New York Academy of Sciences*, Conference Proceedings of New Trends in Astrodynamics and Applications II, 3–5 June 2005, Princeton, New Jersey, Vol. 1065, No. 1, pp. 152–173, doi: 10.1196/annals.1370.024.

[134] Carlson B. C., "Computing Elliptic Integrals by Duplication", *Numerische Mathematik*, Vol. 33, No. 1, 1979, pp. 1–16, doi: 10.1007/BF01396491.

[135] Kahle R., Kuhrt E., Hahn G. and Knollenberg J., "Physical Limits of Solar Collectors in Deflecting Earth-Threatening Asteroids", *Aerospace Science and Technology*, Vol. 10, No. 3, 2006, pp. 256–263, doi: 10.1016/j.ast.2005.12.004.

[136] Vasile M., De Pascale P. and Casotto S., "On the Optimality of a Shape-Based Approach based on Pseudo-Equinoctial Elements", *Acta Astronautica*, Vol. 61, No. 1–6, June–Aug. 2007, pp. 286–297, doi: 10.1016/j.actaastro.2007.01.017.

[137] Sanchez J. P., "Asteroid hazard mitigation: deflection models and mission analysis", Ph.D. Thesis, University of Glasgow, 2009, available at http://theses.gla.ac.uk/888/ [Retrieved: 26 June 2009].

[138] Holsapple K. A., "The Scaling of Impact Processes in Planetary Science", *Annual Review of Earth and Planetary Sciences*, Vol. 21, May 1993, pp. 333–373. doi: 10.1146/annurev.ea.21.050193.002001.

[139] Hammerling P. and Remo J. L., "NEO Interaction with Nuclear Radiation", *Acta Astronautica*, Vol. 36, No. 6, 1995, pp. 337–346. doi: 10.1016/0094-5765(95)00111-5.

[140] Olds J., Charania A., Graham M. and Wallace J., "The League of Extraordinary Machines: A Rapid and Scalable Approach to Planetary Defense against Asteroid Impactors", Vol. 1, NASA Inst. For Advanced Concepts, CP-NIAC 02-02, Atlanta, Apr. 2004.

[141] Murray D. M., "Differential Dynamic Programming for the Efficient Solution of Optimal Control Problems", Ph.D. Dissertation, Department of Mathematics, University of Arizona, University Microfilm Inc., Tucson, 1978.

[142] Murray D. M. and Yakowitz, S. J., "Differential Dynamic Programming and Newton's Method for Discrete Optimal Control Problem", *Journal of Optimization Theory and Applications*, Vol. 43, 1984, pp. 395–414, doi: 10.1007/BF00934463.

[143] Yakowitz S., "Theoretical and Computational Advances in Differential Dynamic Programming", *Control and Cybernetics*, Vol. 17, No. 2–3, 1988, pp. 173–189.

[144] Mayne D. A., "A Second Order Gradient Method for Determining Optimal Trajectories for Nonlinear Discrete-Time Systems", *International Journal on Control*, Vol. 3, 1966, pp. 85–95.

[145] Liao L. and Shoemaker C. A., "Advantages of Differential Dynamic Programming over Newton's Method for Discrete-Time Optimal Control Problems", Technical Report Cornell University, July 1992, available at http://ecommons.library.cornell.edu/handle/1813/5474 [Retrieved: 24 April 2009].

[146] Gill P. E., Murray W. and Wright M. H., *Practical Optimization*, Academic Press, 1981.

[147] Dormand J. R. and Prince P. J., "A family of embedded Runge-Kutta Formulae", *Journal of Computational and Applied Mathematics*, Vol. 6, March 1980, pp. 19–26.

[148] De Boor C., *A Practical Guide to Splines*, Springer-Verlag, 1978.

[149] Coleman T. F. and Li Y., "An Interior Trust Region Approach for Nonlinear Minimization Subject to Bounds", *SIAM Journal on Optimization*, Vol. 6, No. 2, May 1996, pp. 418–445, doi: 10.1137/0806023.

[150] Coleman T. F. and Li Y., "On the Convergence of Interior-Reflective Newton Methods for Nonlinear Minimization Subject to Bounds", *Mathematical Programming*, Vol. 67, No. 1, Oct. 1994, pp. 189–224, doi: 10.1007/BF01582221.

[151] Betts J. T., *Practical Methods for Optimal Control using Nonlinear Programming*, SIAM, Philadelphia, 2001.

[152] Price K., Storn R. and Lampinen J., *Differential Evolution - A Practical Approach to Global Optimization*, Springer, Berlin, 2005.

[153] Spiegel M. R., *Schaum's Mathematical Handbook of Formulas and Tables*, Second Edition, McGraw-Hill Companies, 1998.

[154] Mankins J. C., "Approaches to Strategic Research and Technology (R&T) Analysis and Road Mapping", *Acta Astronautica*, Vol. 51, Nos. 1–9, 2002, pp. 3–21, doi: 10.1016/S0094-5765(02)00083-8.

[155] Moorhouse D. J., "Detailed Definitions and Guidance for Application of Technology Readiness Levels", *Journal of Aircraft*, Vol. 39, No. 1, 2002, pp. 190–192, doi: 10.2514/2.2916.

[156] Angel R., Burge J., Hege K., Kenworthy M. and Woolf N., "Stretched Membrane with Electrostatic Curvature (SMEC): A New Technology for Ultra-Lightweight Space Telescopes", UV, *Optical and IR Space Telescopes and Instruments*, Vol. 4013, Society of Photo-Optical Instrumentation Engineers, Bellingham, WA, 2000, pp. 699–705.

Appendix A.

Secular variation of orbital elements due to low-thrust manoeuvre

In this appendix the derivation of Eq. (3.12) is showed, starting from Eqs. (3.11).

A.1. Secular variation of eccentricity over one orbital revolution

We consider the first of Eqs. (3.11)

$$\Delta\bar{e} = 2k_a \int_{\theta_0}^{\theta_0+2\pi} \frac{1}{h}\left((e+\cos\theta) \Big/ \sqrt{\mu_{\text{Sun}}\left(\frac{1+e^2+2e\cos\theta}{a(1-e^2)}\right)} \right) d\theta$$

and we take out of the integral sign the gravitational constant and the orbital parameters a, e, and h, which are considered constant within one revolution of the true anomaly:

$$\Delta\bar{e} = \frac{2k_a}{h\sqrt{\mu_{\text{Sun}}}}\sqrt{a(1-e^2)} \int_{\theta_0}^{\theta_0+2\pi} \frac{e+\cos\theta}{\sqrt{1+e^2+2e\cos\theta}} d\theta$$

We now focus only on the integral term and we first solve the indefinite integral:

$$\int \frac{e+\cos\theta}{\sqrt{1+e^2+2e\cos\theta}}d\theta = \frac{1}{2e}\int \frac{2e^2+2e\cos\theta+1-1}{\sqrt{1+e^2+2e\cos\theta}}d\theta =$$
$$= \frac{1}{2e}\int \frac{e^2+2e\cos\theta+1+e^2-1}{\sqrt{1+e^2+2e\cos\theta}}d\theta =$$
$$= \frac{1}{2e}\int \left(\frac{1+e^2+2e\cos\theta}{\sqrt{1+e^2+2e\cos\theta}} + \frac{e^2-1}{\sqrt{1+e^2+2e\cos\theta}} \right) d\theta =$$
$$= \frac{1}{2e}\int \sqrt{1+e^2+2e\cos\theta}\, d\theta - \frac{1-e^2}{2e}\int \frac{1}{\sqrt{1+e^2+2e\cos\theta}}d\theta =$$
$$= \frac{1+e}{2e}\int \sqrt{\frac{1+e^2+2e\cos\theta}{(1+e)^2}}\, d\theta - \frac{1-e}{2e}\int \sqrt{\frac{(1+e)^2}{1+e^2+2e\cos\theta}}d\theta$$

recalling that $1-e^2=(1+e)(1-e)$ and that $0\le e<1$. According to the double angle formulae

$$\cos(2\alpha)=1-2\sin^2\alpha$$

where α is a generic angle; we substitute the term $\cos\theta$ within the two integrals:

$$\int \frac{e+\cos\theta}{\sqrt{1+e^2+2e\cos\theta}}d\theta =$$
$$= \frac{1+e}{2e}\int \sqrt{\frac{1+e^2+2e\left(1-2\sin^2(\theta/2)\right)}{(1+e)^2}}\, d\theta - \frac{1-e}{2e}\int \sqrt{\frac{(1+e)^2}{1+e^2+2e\left(1-2\sin^2(\theta/2)\right)}}d\theta =$$

If we perform the change of variables:

$$\phi = \frac{\theta}{2}, \qquad d\phi = \frac{d\theta}{2}$$

we obtain

$$\int \frac{e+\cos\theta}{\sqrt{1+e^2+2e\cos\theta}}d\theta =$$
$$= \frac{1+e}{e}\int \sqrt{\frac{1+e^2+2e-4e\sin^2\phi}{(1+e)^2}}\, d\phi - \frac{1-e}{e}\int \sqrt{\frac{(1+e)^2}{1+e^2+2e-4e\sin^2\phi}}d\phi$$

After some algebraic manipulation we get:

$$\begin{aligned}
&\int \frac{e+\cos\theta}{\sqrt{1+e^2+2e\cos\theta}}\,d\theta = \\
&\quad = \frac{1+e}{e}\int \sqrt{\frac{(1+e)^2-4e\sin^2\phi}{(1+e)^2}}\,d\phi - \frac{1-e}{e}\int \sqrt{\frac{(1+e)^2}{(1+e)^2-4e\sin^2\phi}}\,d\phi = \\
&\quad = \frac{1+e}{e}\int \sqrt{1-\frac{4e}{(1+e)^2}\sin^2\phi}\,d\phi - \frac{1-e}{e}\int \sqrt{\frac{1}{1-\frac{4e}{(1+e)^2}\sin^2\phi}}\,d\phi
\end{aligned}$$

The two integrals identify, respectively, the incomplete integral of the second and the first kind, with $\lambda = \frac{4e}{(1+e)^2}$:

$$\begin{aligned}
\mathrm{E}[\phi,\lambda] &= \int_0^{\phi} \sqrt{1-\lambda\sin^2\varphi}\,d\varphi \\
\mathrm{F}[\phi,\lambda] &= \int_0^{\phi} \frac{d\varphi}{\sqrt{1-\lambda\sin^2\varphi}}
\end{aligned} \tag{A.1}$$

Hence:

$$\begin{aligned}
&\int \frac{e+\cos\theta}{\sqrt{1+e^2+2e\cos\theta}}\,d\theta = \\
&\quad = \frac{1}{e}\left[(1+e)\,\mathrm{E}\left[\phi,\frac{4e}{(1+e)^2}\right] - (1-e)\,\mathrm{F}\left[\phi,\frac{4e}{(1+e)^2}\right]\right] + c
\end{aligned}$$

where c is a constant. The change of eccentricity within one revolution is therefore:

$$\Delta\bar{e} = \frac{2k_a}{h\sqrt{\mu_{\mathrm{Sun}}}}\frac{\sqrt{a(1-e^2)}}{e}\left[(1+e)\,\mathrm{E}\left[\frac{\theta}{2},\frac{4e}{(1+e)^2}\right] - (1-e)\,\mathrm{F}\left[\frac{\theta}{2},\frac{4e}{(1+e)^2}\right]\right]_{\theta_0}^{\theta_0+2\pi} \tag{A.2}$$

Eq. (A.2) can be reordered as the second of Eqs. (3.12)

$$\Delta\bar{e} = \left[\frac{2k_a}{h} \frac{(1+e)\chi}{ev} \left((1+e)\mathrm{E}\left[\frac{\theta}{2}, \frac{4e}{(1+e)^2} \right] + (e-1)\mathrm{F}\left[\frac{\theta}{2}, \frac{4e}{(1+e)^2} \right] \right) \right]_{\theta_0}^{\theta_0+2\pi}$$

introducing the orbital velocity v and the quantity χ defined as:

$$v(\theta) = \sqrt{\mu_{\mathrm{Sun}} \frac{1+e^2+2e\cos\theta}{a(1-e^2)}}, \chi(\theta) = \sqrt{\frac{1+e^2+2e\cos\theta}{(1+e)^2}}$$

Note that the elliptic integrals Eqs. (A.1) are computed numerically, using a vectorised implementation of Carlson's duplication algorithm given in [134].

A.2. Secular variation of semi-major axis over one orbital revolution

The variation of the semi-major axis is derived analogously to the eccentricity. We consider the second of Eqs. (3.11):

$$\Delta\bar{a} = \frac{2k_a}{\mu_{\mathrm{Sun}}} \int_{\theta_0}^{\theta_0+2\pi} \frac{a^2}{h} \sqrt{\mu_{\mathrm{Sun}} \left(\frac{1+e^2+2e\cos\theta}{a(1-e^2)} \right)} d\theta$$

that can be rewritten taking out of the integral sign the quantities a, e, h that are considered constant within one revolution of true anomaly:

$$\Delta\bar{a} = \frac{2k_a a^2 \sqrt{\mu_{\mathrm{Sun}}}}{\sqrt{a}\mu_{\mathrm{Sun}} h} \int_{\theta_0}^{\theta_0+2\pi} \sqrt{\frac{1+e^2+2e\cos\theta}{(1+e)(1-e)}} d\theta$$

The indefinite integral can be simplified following the same procedure for finding Eq. (A.2):

$$\int\sqrt{\frac{1+e^2+2e\cos\theta}{(1+e)(1-e)}}\,d\theta=\int\sqrt{\frac{1+e^2+2e\left(1-2\sin^2\theta/2\right)}{(1+e)(1-e)}}\,d\theta=$$
$$=\int\sqrt{\frac{1+e^2+2e\left(1-2\sin^2\phi\right)}{(1+e)(1-e)}}\,2d\phi=$$
$$=\sqrt{\frac{1+e}{1-e}}2\int\sqrt{\frac{1+e^2+2e-4e\sin^2\phi}{(1+e)^2}}\,d\phi=$$
$$=\sqrt{\frac{1+e}{1-e}}2\int\sqrt{1-\frac{4e}{(1+e)^2}\sin^2\phi}\,d\phi$$

Also in this case we can identify the elliptic integral of the second kind:

$$\int\sqrt{\frac{1+e^2+2e\cos\theta}{(1+e)(1-e)}}\,d\theta=\sqrt{\frac{1+e}{1-e}}2\mathrm{E}\left[\phi,\frac{4e}{(1+e)^2}\right]+c$$

The variation of semi-major axis over one orbital revolution is therefore:

$$\Delta\overline{a}=\left[\frac{2k_a a^2\sqrt{\mu_{\mathrm{Sun}}}}{\sqrt{a}\mu_{\mathrm{Sun}}h}\sqrt{\frac{1+e}{1-e}}2\mathrm{E}\left[\phi,\frac{4e}{(1+e)^2}\right]\right]_{\theta_0}^{\theta_0+2\pi}$$

and introducing v and χ we obtain the second of the Eqs. (3.12):

$$\Delta\overline{a}=\left[\frac{2a^2k_a}{\mu_{\mathrm{Sun}}h}\frac{2v}{\chi}\mathrm{E}\left[\frac{\theta}{2},\frac{4e}{(1+e)^2}\right]\right]_{\theta_0}^{\theta_0+2\pi}$$

A.3. Secular variation of anomaly of the pericentre over one orbital revolution

The variation of the anomaly of the pericentre is derived from the fifth of Eqs. (3.11):

$$\Delta\bar{\omega} = 2k_a \int_{\theta_0}^{\theta_0+2\pi} \frac{\sin\theta}{eh}\sqrt{\frac{1}{\mu_{\text{Sun}}}\left(\frac{a(1-e^2)}{1+e^2+2e\cos\theta}\right)}\,d\theta =$$

$$= \frac{2k_a}{eh}\frac{\sqrt{a(1-e^2)}}{\sqrt{\mu_{\text{Sun}}}}\int_{\theta_0}^{\theta_0+2\pi}\frac{\sin\theta}{\sqrt{1+e^2+2e\cos\theta}}\,d\theta =$$

$$= -\frac{2k_a}{eh}\frac{\sqrt{a(1-e^2)}}{\sqrt{\mu_{\text{Sun}}}}\frac{1}{e}\int_{\theta_0}^{\theta_0+2\pi}\frac{1}{2}\frac{-2e\sin\theta}{\sqrt{1+e^2+2e\cos\theta}}\,d\theta =$$

$$= \left[-\frac{2k_a}{eh}\frac{\sqrt{a(1-e^2)}}{\sqrt{\mu_{\text{Sun}}}}\frac{1}{e}\sqrt{1+e^2+2e\cos\theta}\right]_{\theta_0}^{\theta_0+2\pi}$$

which gives the change of the anomaly of the pericentre given by Eqs. (3.12):

$$\Delta\bar{\omega} = \left[-\frac{2k_a}{eh}\frac{\left(1+e^2+2e\cos\theta\right)}{ev}\right]_{\theta_0}^{\theta_0+2\pi}$$

A.4. Secular variation of the mean anomaly over one orbital revolution

Finally the derivation of the variation of the mean anomaly is shown. The last of Eqs. (3.11) can be written distinguishing three terms that we solve separately:

$$\Delta\bar{M} = \Delta\bar{M}_1 + \Delta\bar{M}_2 + \Delta\bar{M}_3$$

$$\Delta\bar{M} = \int_{\theta_0}^{\theta_0+2\pi}\left(\frac{n}{h}\left(\frac{a(1-e^2)}{1+e\cos\theta}\right)^2 - \frac{2bk_a}{eah}\sin\theta\sqrt{\frac{1}{\mu_{\text{Sun}}}\left(\frac{a(1-e^2)}{1+e^2+2e\cos\theta}\right)} + \right.$$
$$\left. -\frac{2ebk_a}{ah}\frac{\sin\theta}{1+e\cos\theta}\sqrt{\frac{1}{\mu_{\text{Sun}}}\left(\frac{a(1-e^2)}{1+e^2+2e\cos\theta}\right)}\right)d\theta$$

The first term can be written in the form

$$\Delta\bar{M}_1 = \int_{\theta_0}^{\theta_0+2\pi}\frac{n}{h}\left(\frac{a(1-e^2)}{1+e\cos\theta}\right)^2 d\theta = \frac{n}{h}a^2(1-e^2)\int_{\theta_0}^{\theta_0+2\pi}\frac{(1-e^2)}{(1+e\cos\theta)^2}\,d\theta$$

The indefinite integral can be solved with some algebraic manipulations [153] and recalling that $1=\cos^2\theta+\sin^2\theta$:

$$\begin{aligned}\int\frac{(1-e^2)}{(1+e\cos\theta)^2}d\theta &= \int\frac{1-e^2+e\cos\theta-e\cos\theta}{(1+e\cos\theta)^2}d\theta = \\ &= \int\left(\frac{-e^2-e\cos\theta}{(1+e\cos\theta)^2}+\frac{1+e\cos\theta}{(1+e\cos\theta)^2}\right)d\theta = \\ &= -\int\frac{e\cos\theta+e^2(\cos^2\theta+\sin^2\theta)}{(1+e\cos\theta)^2}d\theta+\int\frac{1}{1+e\cos\theta}d\theta = \\ &= -\int\frac{e\cos\theta(1+e\cos\theta)+e\sin\theta\cdot e\sin\theta}{(1+e\cos\theta)^2}d\theta+\int\frac{1}{1+e\cos\theta}d\theta = \\ &= -\frac{e\sin\theta}{1+e\cos\theta}+\int\frac{1}{1+e\cos\theta}d\theta\end{aligned}$$

The remaining integral can be solved by substitution and exploiting the relation

$$\cos(2\alpha)=\cos^2\alpha-\sin^2\alpha$$

where α is a generic angle.

$$\begin{aligned}\int\frac{1}{1+e\cos\theta}d\theta &= \int\frac{1}{1+e\left(\cos^2(\theta/2)-\sin^2(\theta/2)\right)}d\theta = \\ &= \int\frac{1}{\cos^2(\theta/2)+\sin^2(\theta/2)+e\left(\cos^2(\theta/2)-\sin^2(\theta/2)\right)}d\theta = \\ &= \int\frac{1}{\cos^2(\theta/2)(1+e)+\sin^2(\theta/2)(1-e)}d\theta = \\ &= \int\frac{1}{1+\frac{1-e}{1+e}\frac{\sin^2(\theta/2)}{\cos^2(\theta/2)}}\frac{1}{(1+e)\cos^2(\theta/2)}d\theta = \\ &= \int\frac{1}{1+\frac{1-e}{1+e}\tan^2(\theta/2)}\frac{1}{(1+e)\cos^2(\theta/2)}d\theta\end{aligned} \tag{A.3}$$

The substitution adopted is:

$$\phi=\sqrt{\frac{1-e}{1+e}}\tan(\theta/2), \qquad d\phi=\sqrt{\frac{1-e}{1+e}}\frac{1}{2\cos^2(\theta/2)}$$

The integral in Eq. (A.3) becomes:

$$\begin{aligned}\int \frac{1}{1+e\cos\theta}\,d\theta &= \frac{2}{\sqrt{1-e^2}}\int \frac{1}{1+\phi^2}\,d\phi = \\ &= \frac{2}{\sqrt{1-e^2}}\arctan(\phi) = \\ &= \frac{2}{\sqrt{1-e^2}}\arctan\left(\sqrt{\frac{1-e}{1+e}}\tan\left(\frac{\theta}{2}\right)\right)\end{aligned}$$

The first term of the variation of mean anomaly is therefore

$$\Delta\bar{M}_1 = \left[\frac{n}{h}a^2(1-e^2)\left(-\frac{e\sin\theta}{1+e\cos\theta}+\frac{2}{\sqrt{1-e^2}}\arctan\left(\sqrt{\frac{1-e}{1+e}}\tan\left(\frac{\theta}{2}\right)\right)\right)\right]_{\theta_0}^{\theta_0+2\pi}$$

which after simplification gives

$$\Delta\bar{M}_1 = \left[2\arctan\left(\sqrt{\frac{1-e}{1+e}}\tan\left(\frac{\theta}{2}\right)\right)-\frac{e\sqrt{1-e^2}\sin\theta}{1+e\cos\theta}\right]_{\theta_0}^{\theta_0+2\pi}$$

The second term can be easily solved:

$$\begin{aligned}\Delta\bar{M}_2 &= -\frac{2bk_a}{eah}\frac{\sqrt{a(1-e^2)}}{\sqrt{\mu_{\text{Sun}}}}\int_{\theta_0}^{\theta_0+2\pi}\frac{\sin\theta}{\sqrt{1+e^2+2e\cos\theta}}\,d\theta = \\ &= +\frac{2bk_a}{eah}\frac{\sqrt{a(1-e^2)}}{\sqrt{\mu_{\text{Sun}}}}\frac{1}{e}\int_{\theta_0}^{\theta_0+2\pi}\frac{1}{2}\frac{-2e\sin\theta}{\sqrt{1+e^2+2e\cos\theta}}\,d\theta \\ &= \left[\frac{2bk_a}{eah}\frac{\sqrt{a(1-e^2)}}{\sqrt{\mu_{\text{Sun}}}}\frac{1}{e}\sqrt{1+e^2+2e\cos\theta}\right]_{\theta_0}^{\theta_0+2\pi} = \\ &= \left[\frac{2bk_a}{eah}\frac{1+e^2+2e\cos\theta}{ve}\right]_{\theta_0}^{\theta_0+2\pi}\end{aligned}$$

and the integral in the third term:

$$\Delta\bar{M}_3 = -\frac{2ebk_a}{ah}\frac{\sqrt{a(1-e^2)}}{\sqrt{\mu_{\text{Sun}}}}\int_{\theta_0}^{\theta_0+2\pi}\frac{\sin\theta}{(1+e\cos\theta)\sqrt{1+e^2+2e\cos\theta}}\,d\theta$$

can be solved by variable substitution:

$$\phi = \sqrt{1+e^2+2e\cos\theta}, \qquad \frac{d\phi}{d\theta} = -\frac{e\sin\theta}{\phi}$$

such that

$$e\cos\theta = \frac{\phi^2 - 1 - e^2}{2}$$

$$\begin{aligned}
\int \frac{\sin\theta}{(1+e\cos\theta)\sqrt{1+e^2+2e\cos\theta}}\,d\theta &= -\frac{1}{e}\int \frac{-e\sin\theta}{(1+e\cos\theta)\sqrt{1+e^2+2e\cos\theta}}\,d\theta \\
&= -\frac{1}{e}\int \frac{2}{1-e^2+\phi^2}\,d\phi \\
&= -\frac{2}{e}\int \frac{1}{(1-e^2)\left(1+\dfrac{\phi^2}{1-e^2}\right)}\,d\phi = \\
&= -\frac{2}{e\sqrt{1-e^2}}\int \frac{1}{\sqrt{1-e^2}}\frac{1}{1+\left(\dfrac{\phi}{\sqrt{1-e^2}}\right)^2}\,d\phi = \\
&= -\frac{2}{e\sqrt{1-e^2}}\arctan\left[\frac{\phi}{\sqrt{1-e^2}}\right] = \\
&= -\frac{2}{e\sqrt{1-e^2}}\arctan\left[\frac{\sqrt{1+e^2+2e\cos\theta}}{\sqrt{1-e^2}}\right]
\end{aligned}$$

Hence the third term is:

$$\Delta\bar{M}_3 = \frac{2ebk_a}{ah}\frac{\sqrt{a(1-e^2)}}{\sqrt{\mu_{\text{Sun}}}}\frac{2}{e\sqrt{1-e^2}}\arctan\left[\frac{\sqrt{1+e^2+2e\cos\theta}}{\sqrt{1-e^2}}\right]$$

which after simplification gives:

$$\Delta\bar{M}_3 = \left[\frac{2bk_a}{ah}2\arctan\left[\frac{\sqrt{1+e^2+2e\cos\theta}}{\sqrt{1-e^2}}\right]\frac{\sqrt{1+e^2+2e\cos\theta}}{v\sqrt{1-e^2}}\right]_{\theta_0}^{\theta_0+2\pi}$$

Hence the total variation of mean anomaly is:

$$\Delta\bar{M} = \left[2\arctan\left(\sqrt{\frac{1-e}{1+e}}\tan\left(\frac{\theta}{2}\right)\right) - \frac{e\sqrt{1-e^2}\sin\theta}{1+e\cos\theta} + \right.$$
$$+ \frac{2bk_a}{eah}\left(\frac{1+e^2+2e\cos\theta}{ve} + \right.$$
$$\left.\left. + e\frac{2\arctan\left(v\sqrt{a}/\sqrt{\mu_{\text{Sun}}}\right)\sqrt{1+e^2+2e\cos\theta}}{v\sqrt{1-e^2}}\right)\right]_{\theta_0}^{\theta_0+2\pi}$$

Appendix B.

Influence of the technology readiness level on the multi-criteria analysis

As an additional criterion to the multi-criteria analysis performed in Section 4.5.3, we consider the Technology Readiness Level (TRL) of each method as a measure of the expected practicality in the near future. The standard definition of TRL from [154],[155] (reported in Table B.1) consists of a number from 1 to 9 defining the level of maturity and development of a certain space system, from its concept up to the system flight validation. For each mitigation scheme a certain TRL interval has been determined, taking into account past missions and available experiments* and is presented in Table B.2. To have a conservative approach, the decision of the TRL interval was done considering the part of the required technology with the lowest TRL.

Despite the fact that no mission to test this technology is flying yet, the technology for the kinetic impactor has been considered to be fully developed, hence a range TRL 7–8 is assigned. Examples of this technology are the Deep Impact mission [28] and the asteroid deflection precursor mission Don Quijote, currently under study at the ESA [37]. The use of nuclear in space is banned by the Outer Space Treaty [46], but the effects of a nuclear explosion have already been studied. Hence an interval of TRL 6–8 is assigned, mainly because the environment in which the technology would be used is completely different from that for which it was designed and tested. An important issue for impulsive strategies, like kinetic impactor and nuclear interceptor, is the high precision required on the direction of the Δv, because the deflecting action is assumed to be applied in one single manoeuvre. On the other hand, it is also possible to schedule

* As already stated in Section 4.4, an additional margin on the initial spacecraft mass is also added, according to the level of development of the required technology.

a series of manoeuvres one after the other to increase the robustness of these options. The low-thrust attached technology has been considered to be at an intermediate stage where the critical function and characteristics have been demonstrated. However, the thrusting requirement are higher than the existing engines and the anchoring system has to be considered, even if it has been already studied, on a smaller scale, for missions like Rosetta [34] and Hayabusa [35]. Hence, an interval of TRL between 4 and 6 was assigned. Solar Collector and Mass Drivers are assumed to be, respectively, at TRL 2–3 and 2–4 because they would require a substantial redesign of existing technologies. The main issues for the solar collector are the control of the spacecraft in formation with the asteroid, adaptive optics, and autonomous pointing [58]; the mass driver strategy instead requires anchoring system, mining technologies and high power generation. Basic experiments with these technologies have already been performed; examples are the deployment of inflatable structures [156], or the autonomous drilling of planetary surfaces. Finally, deviation through gravity tractor would require control of the spacecraft in proximity of the asteroid and a nuclear power generation, hence it is considered at a TRL interval 3–5. A more detailed discussion on the TRL assignment is provided in [126].

Table B.1 : Technology readiness levels.

TRL	Technology readiness
1	Basic principles observed and reported
2	Technology concept and/or application formulated
3	Analytical and experimental critical function and/or characteristic proof-of-concept
4	Component and/or breadboard validation in laboratory environment
5	Component and/or breadboard validation in relevant environment
6	System/subsystem model or prototype demonstration in relevant environment (ground or space)
7	System prototype demonstration in space environment
8	Actual system competed and flight-qualified through test and demonstration (ground or space)
9	Actual system flight-proven through successful mission operations

Table B.2 : TRL for the different mitigation schemes.

Mitigation strategy	TRL range
Kinetic impactor	7–8
Nuclear interceptor	6–8
Mass driver	2–4
Attached low-thrust propulsion	4–6
Solar collector	2–3
Gravity tractor	3–5

To take into account the technology readiness in the multi-criteria analysis, the TRL factor is translated into a measure of man-years for developing the required technology Δt_{TR}. Hence, the launch of a mitigation mission is subjected to a time delay, necessary for the required technology to be validated, demonstrated and flight-qualified. The definition of warning time is modified to be:

$$t_{w,\,\mathrm{TR}} = t_{\mathrm{MOID}} - t_0 + \Delta t_{\mathrm{TR}}$$

The mapping between the TRL and the period for development is done through the logistic function [126]:

$$\Delta t_{\mathrm{TR}} = \frac{a}{1+\exp\left[-\frac{\Lambda - t_c}{\tau}\right]} + b \tag{B.1}$$

where Δt_{TR} is the man-years required to take a technology from TRL 1 to TRL Λ and t_c represents the turning point for the development of the technology when it starts to be tested in relevant environment. The coefficients a, b and τ were chosen so that:

$$\begin{aligned} &\Delta t_{\mathrm{TR}}(\Lambda = 2) = 0 \\ &\Delta t_{\mathrm{TR}}(\Lambda = 9) = 15 \\ &\Delta t_{\mathrm{TR}}(\Lambda = 7) - \Delta t_{\mathrm{TR}}(\Lambda = 4) = 10 \end{aligned} \tag{B.2}$$

The last condition in Eq. (B.2) means that 10 man-years are necessary to develop a technology from the breadboard validation in laboratory environment up to the system prototype demonstration in space environment. The value of Δt_{TRL} corresponding to the TRL [according to the logistic function in Eq. (B.1)] are reported in Table B.3[†].

[†] No strategy is considered to be at TRL 1.

Table B.3 : TRL mapping into required time to fully develop the required technology.

TRL	Δt_{TR} [man-year]
2	15
3	13.9233
4	11.5392
5	7.7077
6	3.8762
7	1.4921
8	0.4154
9	0

The date at which the asteroid is at the MOID is kept fixed for all the strategies applied to a given asteroid to analyse the effects of each scheme for the same MOID. As a consequence, the effect of the technology readiness level is to increase the warning time corresponding to the same deviation the strategy would achieve without considering the TRL. All the points of the Pareto fronts are shifted along the t_w axis and those points, whose $t_{w,\,\mathrm{TRL}}$ becomes bigger than the maximum warning time without considering TRL, are eliminated from the comparison. For warning times less than the minimum time for developing a certain strategy, the corresponding deflection is zero. The Pareto fronts of Eq. (4.8) are modified as follow:

$$\mathbf{J} = \left[m_0 \quad t_w + \Delta t_{\mathrm{TR}} \quad -\|\Delta\mathbf{r} + \delta\mathbf{r}\| \right]$$

Table B.4–Table B.7 show the results of the multi-criteria comparison considering the TRL for the strategies applied to the mitigation of the selected asteroids. By comparing Table B.4–Table B.7 with Table 4.4–Table 4.7, few preliminary considerations can be drawn. The first consideration is that when the technology readiness level is considered, the kinetic impactor becomes competitive since its Pareto front encloses parts of the criteria domain that the other strategies are not able to cover; this is a direct consequence of the translation along the t_w axis. The nuclear interceptor still dominates over the other strategies and becomes dominant over the solar collector for all the asteroids analysed. On the other hand, even after the technology readiness filtering, the solar mirror strategy remains particularly competitive over all the strategies with the exception of nuclear interceptor. For example, for the case of asteroid Apophis, the solar collector passes from a percentage of dominance over the nuclear interceptor of

98% without considering TRL (see Table 4.4) to 4–3% when TRL is added (see Table B.4). The mass driver scheme cannot be completely discarded, because it has a satisfactory behaviour. Finally the technology readiness analysis reveals the impracticability of the low-thrust attached device. In fact, the achieved results are comparable with the kinetic impactor, despite the more complex technology of the low-thrust system.

Table B.4 : Strategy dominance for asteroid Apophis considering the technology readiness level.

	Kinetic impactor	Nuclear interceptor	Mass driver	Attached propulsion	Solar Collector	Gravity Tractor
Kinetic impactor	–	28–0	96–86	100–63	91–87	100
Nuclear interceptor	100	–	100	100	100	100
Mass driver	77–99	0	–	100–99	3–4	100
Attached propulsion	0–88	0	6–59	–	5–60	100
Solar Collector	96–97	4–3	96–97	100	–	100
Gravity Tractor	0	0	83–9	13–1	83–90	–

Table B.5 : Strategy dominance for asteroid Itokawa considering the technology readiness level.

	Kinetic impactor	Nuclear interceptor	Mass driver	Attached propulsion	Solar Collector	Gravity Tractor
Kinetic impactor	–	2–0	100–63	100	63	100
Nuclear interceptor	100	–	100	100	100	100
Mass driver	73–98	0	–	100–99	0–31	100
Attached propulsion	52–38	0–1	94–49	–	94–75	100
Solar Collector	100	0	100	100	–	100
Gravity Tractor	1–4	0	31–39	0	31–72	–

Table B.6 : Strategy dominance for asteroid Castalia considering the technology readiness level.

	Kinetic impactor	Nuclear interceptor	Mass driver	Attached propulsion	Solar Collector	Gravity Tractor
Kinetic impactor	–	81–2	99–97	100–97	98	100
Nuclear interceptor	100	–	100	100	100–99	100
Mass driver	70–88	0	–	88–64	0–47	100–95
Attached propulsion	20–61	0–2	77–93	–	75–96	100
Solar Collector	100	15–24	100	100	–	100
Gravity Tractor	0–57	0	48–38	0	48–65	–

Table B.7 : Strategy dominance for asteroid 1979XB considering the technology readiness level.

	Kinetic impactor	Nuclear interceptor	Mass driver	Attached propulsion	Solar Collector	Gravity Tractor
Kinetic impactor	–	69–3	100	100	100–99	100
Nuclear interceptor	100	–	100	100	100	100
Mass driver	3–21	0	–	87–96	47	95–99
Attached propulsion	0	0	61–50	–	71–73	100
Solar Collector	62–85	0	69–86	63–86	–	65–86
Gravity Tractor	0	0	49–42	0	65–94	–